Tailoring spatiotemporal dynamics with DNA circuits

Adrien Padirac

▶ **To cite this version:**

Adrien Padirac. Tailoring spatiotemporal dynamics with DNA circuits. Molecular Networks [q-bio.MN]. Université Claude Bernard - Lyon I, 2012. English. NNT : . tel-00856610

HAL Id: tel-00856610
https://theses.hal.science/tel-00856610

Submitted on 2 Sep 2013

HAL is a multi-disciplinary open access archive for the deposit and dissemination of scientific research documents, whether they are published or not. The documents may come from teaching and research institutions in France or abroad, or from public or private research centers.

L'archive ouverte pluridisciplinaire **HAL**, est destinée au dépôt et à la diffusion de documents scientifiques de niveau recherche, publiés ou non, émanant des établissements d'enseignement et de recherche français ou étrangers, des laboratoires publics ou privés.

THESE DE L'UNIVERSITE DE LYON

Délivrée par

l'Université Claude Bernard Lyon I

Ecole Doctorale de Chimie

DIPLOME DE DOCTORAT

(arrêté du 7 août 2006)

soutenu publiquement le 29 novembre 2012

par

M. Adrien PADIRAC

Tailoring spatiotemporal dynamics with DNA circuits

Jury: Arnaud BRIOUDE, président du jury
Anthony W. COLEMAN, directeur de thèse
Teruo FUJII
Ludovic JULLIEN, rapporteur
Yannick RONDELEZ, codirecteur de thèse
Masahiro TAKINOUE, rapporteur

Abstract

Biological organisms process information through the use of complex reaction networks. These can be a great source of inspiration for the tailoring of dynamic chemical systems. Using basic DNA biochemistry –the DNA-toolbox– modeled after the cell regulatory processes, we explore the construction of spatio-temporal dynamics from the bottom-up.

First, we design a monitoring technique of DNA hybridization by harnessing a usually neglected interaction between the nucleobases and an attached fluorophore. This fluorescence technique –called N-quenching– proves to be an essential tool to monitor and troubleshoot our dynamic reaction circuits.

We then go on a journey to the roots of the DNA-toolbox, aiming at defining the best design rules at the sequence level. With this experience behind us, we tackle the construction of reaction circuits displaying bistability. We link the bistable behavior to a topology of circuit, which asks for specific DNA sequence parameters. This leads to a robust bistable circuit that we further use to explore the modularity of the DNA-toolbox. By wiring additional modules to the bistable function, we make two larger circuits that can be flipped between states: a two-input switchable memory, and a single-input push-push memory. Because all the chemical parameters of the DNA-toolbox are easily accessible, these circuits can be very well described by quantitative mathematical modeling. By iterating this modular approach, it should be possible to construct even larger, more complex reaction circuits: each success along this line will prove our good understanding of the underlying design rules, and each failure may hide some still unknown rules to unveil.

Finally, we propose a simple method to bring DNA-toolbox made reaction circuits from zero-dimensional, well-mixed conditions, to a two-dimensional environment allowing both reaction and diffusion. We run an oscillating reaction circuit in two-dimensions and, by locally perturbing it, are able to provoke the emergence of traveling and spiral waves. This opens up the way to the building of complex, tailor-made spatiotemporal patterns.

Résumé

L'ADN est reconnu depuis longtemps comme une des molécules fondamentales des organismes vivants. Support de l'information génétique, la molécule d'ADN possède aussi des propriétés qui en font un matériel de choix pour construire à l'échelle nanométrique. Deux simples brins d'ADN complémentaires et antiparallèles (c.à.d. de directivité opposée) peuvent, par exemple, s'hybrider s'ils se rencontrent en solution, c'est à dire s'associer l'un à l'autre. La cohésion de la molécule « double-brin » ainsi formée est maintenue par une série de liaisons faibles entre les bases complémentaires de chaque brin. Cette réaction d'hybridation de l'ADN est réversible : un double-brin stable à basse température retrouvera l'état simple-brin à plus haute température.

Notre capacité à lire (séquencer) et écrire (synthétiser) l'ADN est à l'origine de l'émergence du domaine des *nanotechnologies ADN*. Cette capacité à prévoir quantitativement les interactions (cinétiques et thermodynamiques) entre deux partenaires moléculaires quels qu'ils soient est propre à l'ADN : on peut facilement synthétiser deux molécules de même taille et nature, de manière à ce qu'elles interagissent – ou non – selon la séquence qui leur est propre. Il existe aussi toute une batterie d'enzymes capables de catalyser différentes réactions au sein d'un brin d'ADN ou entre deux brins d'ADN, par exemple : une polymérase catalyse la synthèse d'un brin d'ADN à partir de son complémentaire ; une nickase coupe un seul des deux brins d'une molécule double-brin à un emplacement spécifique ; une exonucléase hydrolyse un brin d'ADN en fragments plus courts, tandis qu'une ligase lie deux brins courts en un brin unique, plus long.

En utilisant ces simples réactions (hybridation, polymérisation, coupe spécifique et hydrolyse), il est possible de construire des réactions qui associent des brins d'ADN « input » à des brins d'ADN « output » selon le modèle « input -> input + output ». Si l'output est de la même nature que l'input, il peut servir d'input à une autre réaction. On définit alors qu'à chaque réaction est associé un « module » : par exemple, le module AtoB encode la réaction A -> A + B. Lorsque A s'hybride à AtoB, il est

allongé par une polymérase suivant la séquence du module AtoB, formant ainsi un brin constitué de la séquence de A suivie de la séquence de B. Ce produit est alors coupé entre A et B par une nickase : A et B peuvent alors se détacher du module AtoB. Montagne *et al.* (MSB, 2011) ont démontré qu'en associant trois modules encodant les trois types de réaction « activation » (A -> A+ B), « autocatalyse » (A -> 2A) et « inhibition » (B -> inhibiteur de A), complétées d'une exonucléase hydrolysant inputs et outputs (mais pas les modules), il est possible d'obtenir un oscillateur qui fonctionne dans un tube à essai, mais qui est entièrement constitué de matériel biologique : l'*oligator*.

Dans cette thèse, nous commençons par vérifier que les trois modules de l'oligator (activation, autocatalyse et inhibition) peuvent être réarrangés de manière arbitraire, afin de créer différents circuits de réactions dynamiques. Nous appellerons cette collection de réactions catalysées par trois enzymes (polymérase, nickase et exonucléase) la *boite à outils ADN*. La construction et le contrôle de circuits complexes nécessitent de pouvoir observer les modules désirés de manière spécifique et en temps réel. A cette fin, nous mettons au point une nouvelle technique de fluorescence utilisant une interaction – souvent négligée – entre les bases d'ADN et un fluorophore qui y est attaché : celui-ci émet une fluorescence dont l'intensité dépend de l'état (simple ou double brin) et de la séquence à proximité du fluorophore. Cette méthode, nommée N-quenching (pour nucleobase-quenching), a fait l'objet d'une publication dans *Nucleic Acids Research*. A l'origine, les oscillations de l'oligator étaient observées au moyen d'un agent intercalant de l'ADN dont la fluorescence dépend de la quantité totale d'ADN présente en solution. En utilisant N-quenching, il est possible d'observer de manière spécifique les différents composants de l'oligator, et d'en apprécier les oscillations déphasées : il suffit d'attacher un fluorophore à un module afin d'observer la présence ou l'absence de l'input associé.

Ces outils en main, nous abordons l'assemblage de circuits de réactions plus complexes, en nous intéressant plus particulièrement à la bistabilité. Le phénomène de bistabilité est extrêmement courant au sein des systèmes de régulation de l'expression génétique, ainsi que dans divers systèmes chimiques. Une fois déterminées les caractéristiques requises pour obtenir un système bistable avec notre boîte à outils, nous construisons un circuit dont les deux états de stabilité correspondent à deux modules autocatalytiques qui s'inhibent mutuellement par le biais de deux modules d'inhibition. N-quenching s'avère être un outil indispensable pour discerner sans ambiguïté les deux états stables du bistable. Nous avons ensuite montré qu'il est possible de donner de nouvelles fonctions au bistable en le connectant à d'autres modules ou sous-circuits : c'est ainsi que nous avons assemblé un circuit « mémoire » pouvant être mis à jour au moyen de deux « inputs » externes, puis une mémoire flip-flop capable de

switcher entre ses deux états stables au moyen d'un unique input externe. Les résultats de ce travail ont été publiés dans *Proceedings of the National Academy of Sciences*.

Les connections entre différents modules de nos circuits de réactions sont basées sur un système d'adressage chimique: c'est la reconnaissance entre deux brins d'ADN qui structure le réseau et nous travaillons donc dans l'espace des séquences. Il est aussi envisageable d'utiliser l'espace réel, c'est à dire de passer d'un système en zéro dimension à un système – par exemple – en deux dimensions ou chaque molécule possède désormais des coordonnées spatiales (en plus d'une adresse chimique). On s'intéresse alors à l'évolution spatiale de nos réactions. Nous avons mis au point un dispositif fluidique permettant d'enfermer hermétiquement nos circuits de réactions sous la forme d'une fine couche de liquide de la forme désirée. Le système est alors observé au moyen d'un microscope pour résoudre les composantes spatiales: nous y installons un oscillateur biochimique et montrons qu'en contrôlant réaction et diffusion, il est possible d'observer l'émergence de motifs spatio-temporels complexes.

De par la nature du matériel les constituant (ADN et enzymes), nos systèmes se situent à l'interface directe entre le vivant et le non-vivant. Notre boîte à outils s'inspire (quoique de manière très schématique) de la régulation de l'expression génétique : elle forme par conséquent une sorte de modèle expérimental permettant l'étude des relations entre la structure du circuit d'une part et sa fonction, d'autre part, telles qu'elles pourraient être au sein du vivant. Ces circuits pourraient aussi être utilisés pour diriger des nanorobots ADN *in situ*, supprimant ainsi le besoin de stimulus externe commandant leurs mouvements. D'autres applications potentielles incluent le transfert de ces systèmes *in vivo*, à des fins thérapeutiques par exemple (médicament intelligent). Cela reste cependant un défi, dont la première étape sera d'améliorer la robustesse de ces circuits afin qu'ils puissent fonctionner dans des milieux plus hostiles qu'un tube à essai.

Acknowledgments

First of all, I would like to express my gratitude to my supervisor, Yannick Rondelez, who was a great mentor, and gave me a wonderful image of scientific research. Even in his busiest time, Yannick was fully available, with a never exhausting battery of wise advices, clever ideas and great teachings. I thank my Senpai (elder colleagues) of the Molecular Programming team: Kevin Montagne, who taught me precious DNA techniques and gave me many advices for both experiments and english language, Anthony Genot for his sharp but good writing advices, as well as my Kohai (junior colleagues): Nathanael Aubert and Alexandre Baccouche who are as lucky as I was, to have Yannick as a supervisor.

I thank my thesis committee members: Arnaud Brioude, Anthony Coleman, Yannick Rondelez and Teruo Fujii, as well as my two referees who carefully read this thesis, Ludovic Jullien and Masahiro Takinoue.

Thanks also to all the Fujii Lab. members, who hosted me and were always available when I needed advices. In particular, thanks to Christophe Provin, who first showed me around the lab, and taught me micro-fabrication, Jiro Kawada, who started his PhD at about the same time as me, Shohei Kaneda who countless times helped me out finding the reagents in the busy chemicals shelves, Soo Hyeon Kim who taught me most of the microscopy techniques I used, and Hervé Guillou for good discussions about important things in life and carefully reading our papers.

I am especially grateful to Dominique Collard for managing the 3-years stipend from the CNRS that allowed me to do this thesis, and Teruo Fujii who hosted me in his laboratory all this time. Thanks also to all the administrative staff of both LIMMS and Fujii Laboratory, who helped me much with everyday administrative issues.

I would also like to thank two visiting researchers who helped me quite a bit in my research: Kazuhito Tabata for teaching me enzyme expression and purification and André Estévez Torres for motivating me spatializing our reaction circuits.

As a child, my father appealed me to Science, and nourished my curiosity with many unreachable, mesmerizing examples. And there I was drawing Miller experiment without a clue of what was happening in this damn good-looking setup. I eventually went on studying systems that may also have implications on our understanding of the Origin of Life, which is a mystery that fascinates me, as it fascinates my father. So, thank you dad. And thanks also to all my family, friends and to my other half, who were the best support - but scientific - during this thesis, and will be so for all what is to come.

Contents

Abstract **2**

Résumé **3**

Acknowledgments **6**

1 Overview **13**

1.1 Introduction . . . 13

1.1.1 DNA . . . 13

1.1.2 DNA computing . . . 14

1.1.3 Mimicking *in silico* computation . . . 17

1.1.4 Mimicking *in vivo* computation . . . 20

1.1.5 Applications . . . 25

1.1.6 Reaction-Diffusion . . . 26

1.2 Outline . . . 28

1.3 Glossary . . . 29

2 N-quenching **32**

2.1 Abstract . . . 32

2.2 Introduction . . . 33

2.3 Materials and methods . . . 35

2.3.1 Oligonucleotides . . . 35

2.3.2 Fluorescence shift measurement . . . 36

2.3.3 Monitoring of DNA reaction circuits . . . 36

2.4 Results . . . 37

2.4.1 Characterization of nucleobase quenching . . . 37
2.4.2 Environmental dependence . . . 38
2.4.3 Monitoring an elementary DNA reaction circuit . . . 39
2.4.4 Monitoring a DNA-based oscillator . . . 41
2.5 Discussion . . . 42
2.5.1 N-quenching sensitivity and quantitative measurement . . . 42
2.5.2 Non-invasive monitoring . . . 43
2.5.3 N-quenching as a general method to monitor position-specific hybridization . . . 44
2.6 Supplementary Information . . . 45
2.7 Additional results . . . 46
2.7.1 C11bt Oligator . . . 46
2.7.2 Impact of a single fluorophore on the production of inhibitor . . . 47
2.7.3 Indirect monitoring using N-quenching . . . 48
2.7.3.1 Reporting module: design & test . . . 48
2.7.3.2 Reporting module: use with an oligator . . . 50
2.7.4 Tracking inhibitors with N-quenching . . . 51
2.7.5 Quantification with N-quenching: calibration curves . . . 52
2.7.6 Fluorophores tested with N-quenching . . . 53

3 In vitro switchable memories 54

3.1 Abstract . . . 54
3.2 Introduction . . . 55
3.3 Materials and methods . . . 58
3.3.1 Oligonucleotides . . . 58
3.3.2 Reaction assembly . . . 58
3.3.3 Fluorescence curve acquisition and normalization . . . 58
3.3.4 Simulations . . . 59
3.4 Results . . . 59
3.4.1 DNA-toolbox: three basic modules . . . 59
3.4.2 Bistable switch: designing the reaction circuit . . . 60
3.4.3 Experimental building of the bistable circuit . . . 62
3.4.4 Two-input switchable memory . . . 65

3.4.5 Push-push memory . . . 68
3.5 Discussion . . . 69
3.6 Conclusion . . . 72
3.7 Supplementary Information . . . 73
3.7.1 Workflow of network assembly with the DNA-toolbox . . . 73
3.7.2 Experimental building of the bistable circuit . . . 73
3.7.2.1 Design rules . . . 73
3.7.2.2 Protection from ttRecJ . . . 74
3.7.2.3 DNA sequences . . . 77
3.7.2.4 Sequence space limitation . . . 77
3.7.3 Model . . . 78
3.7.3.1 Simple Model . . . 78
3.7.3.2 Minimal bistable circuit design: single autoloop . . . 80
3.7.3.3 Simple robustness . . . 82
3.7.3.4 Detailed model construction . . . 82
3.7.3.5 Perturbation of the bistable and switching threshold . . . 84
3.7.3.6 Activation module . . . 86
3.7.3.7 Push-push strategy . . . 86
3.7.4 Reamplification . . . 87
3.7.5 Push-push memory circuit . . . 88
3.7.6 Long-term experiments . . . 90

4 Toward memory circuits 93

4.1 Enzymes activity . . . 93
4.2 Bistable Switch: a design out-of-the-toolbox . . . 94
4.3 Bistable circuits with the DNA-toolbox . . . 96
4.3.1 Working with mesophilic $RecJ_f$ . . . 96
4.3.2 Trials with thermophilic cd-ttRecJ, purified in-house . . . 97
4.3.3 Design and evaluation of autocatalytic modules . . . 98
4.3.4 Design rules for inhibitors . . . 101
4.3.5 Trials with unbalanced autocatalytic modules . . . 104
4.3.6 Working with a new thermophilic exonuclease: full-length ttRecJ . . . 106

4.3.7 On balancing the bistable circuit . . . 106
4.3.7.1 First: charge and inhibit to balance . . . 107
4.3.7.2 Second: inhibit to balance . . . 109
4.4 On switching the bistable: switchable memory circuit . . . 111
4.4.1 Direct injection of inputs . . . 111
4.4.2 "Super-inputs" . . . 112
4.4.3 "Input-makers" . . . 116
4.5 Modeling of the circuit . . . 117
4.5.1 DNA melting experiment . . . 117
4.5.2 Enzymes kinetic parameters . . . 118
4.5.2.1 Exonuclease parameters . . . 119
4.5.2.2 Nickase parameters . . . 119
4.6 Stability on the long-term . . . 120
4.6.1 Buffer additives . . . 121
4.6.2 Template degradation by ttRecJ. . . . 121
4.6.3 Flattening the steady state . . . 122
4.7 Others . . . 123
4.7.1 Tristable circuit and three-switch oscillator . . . 123
4.7.2 Charge / Load . . . 125
4.7.3 Parasite . . . 127

5 Compartmentalization of the reactions 129

5.1 Microfabrication . . . 129
5.2 Self-closing chambers . . . 131
5.2.1 First design . . . 132
5.2.2 Comb design . . . 132
5.2.3 Are the chambers closed? . . . 133
5.2.4 Improving the sealing of the chambers . . . 134
5.3 The impossible compromises . . . 136
5.3.1 PDMS and EvaGreen . . . 136
5.3.2 Coating and Sealing . . . 136
5.4 Droplet microfluidics . . . 137

6 An ecological approach to spatiotemporal patterning 138

6.1 Technical notes . . . 139

6.2 Predator-Prey reaction circuit . . . 139

6.2.1 Basic functioning . . . 139

6.2.2 Adjusting the parameters of the Predator-Prey circuit . . . 140

6.2.3 Long-term oscillator . . . 142

6.3 Enable the reactions for working under the microscope . . . 144

6.4 A simple device to observe the reactions in two-dimensions . . . 144

6.5 Stabilizing the reaction . . . 146

6.5.1 Double layer and coatings . . . 146

6.5.2 Delaying the divergence . . . 147

6.5.3 A commercial alternative . . . 148

6.6 Paraframe . . . 149

6.6.1 Tracking the foxes . . . 152

6.6.2 Spatiotemporal patterns . . . 152

6.7 Mathematical modeling . . . 153

6.8 Extension of this work . . . 154

Conclusion 156

Bibliography 158

A Expression, extraction and purification of cd-ttRecJ 176

B Working at lower temperature 182

C Two-dimensional Bistability 186

D Working in agarose 188

E Nucleic acids for the rational design of reaction circuits 191

F A microfluidic device for on-chip agarose microbead generation with ultralow reagent consumption 199

Chapter 1

Overview

1.1 Introduction

Nucleic Acids may be the informational polymers that jump-started the emergence of life [1]. In the "RNA world" hypothesis, RNA is considered as one of the most primitive informational polymers, probably followed at some point by DNA [2] and proteins. In Life as we know it, Nucleic Acids are the holders of genetic information, which makes them central to all biological organisms. Nucleic acids are also extremely important from a biochemical point of view: DNA and RNAs are - together with proteins - regulating and expressing the genetic information. But more than that, as a molecule, RNA and DNA form an amazing biochemical tool to build things at the nanoscale or to assemble chemical systems.

1.1.1 DNA

DNA stands for DeoxyriboNucleic Acid. The DNA polymer is built from nucleotide monomers. As the fundamental building block of DNA, the nucleotide consists of a phosphate joined to a sugar (deoxyribose), to which a base is attached. The phosphate group of a nucleotide is linked to the sugar of the following nucleotide by a phosphodiester bond (Figure 1.1). Because of the chirality of the sugar, the DNA molecule has a direction, noted 5'->3'. Each nucleotide contains one base: a purine (Adenine or Guanine) or pyrimidine (Thymine or Cytosine). These four bases exhibit a complementary characteristic: A pairs with T, and G pairs with C. Following these two characteristics (directionality and complementarity), two antiparallel, complementary DNA strands (for instance,

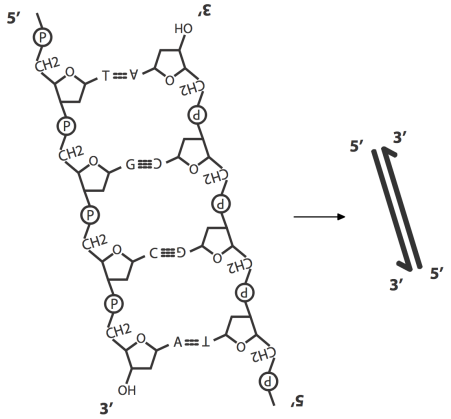

Figure 1.1: DeoxyriboNucleic Acid: DNA. (Left) Structure of a double-stranded DNA molecule showing Watson-Crick base pairing. A pairs to T with 2 hydrogen bonds, and C pairs to G with 3 hydrogen bonds. Circled P corresponds to a phosphate group. (Right) Corresponding schematic representation used in this study for two complementary, anti-parallel, hybridized DNA strands. The arrowhead indicates the 5'->3' direction.

5'-GGTC-3' and 5'-GACC-3') can hybridize to each other. DNA hybridization is reversible: a double-stranded DNA molecule can dissociate under mechanical force or high temperature. As such, each DNA molecule carries information encoded in its sequence, and has the capability to recognize its perfectly complementary sequence, as well as partially complementary sequences with a lower affinity.

With these properties, DNA (along with RNA) is a powerful biochemical tool that can be used to engineer various nanoscale devices. Back in 1959, Richard Feymann pointed out that DNA uses as little as about 50 atoms to store one bit of information (or 1 bit per cubic nanometer for Adleman [3], 2 gigabytes per micromol for Ouyang [4] or 455 exabytes per gram for Church [5]): is there any other information storage more compact? Also, DNA molecules provide an immense address space that can be explored at will. Our capacity to read (sequence) and write (synthesize) nucleic acids (NA) has opened up a wide range of possible applications, and gave birth to the field of NA nanobiotechnology. Researchers first focused on structural NA nanotechnology: 2D [6] and 3D [7] static structures. Then came NA nanomachines [8, 9]: dynamic nanostructures capable of nanoscale movements in response to external stimuli. In this thesis, we will focus on a third sub-field of NA nanobiotechnology: DNA computing, also known as molecular programming.

1.1.2 DNA computing

In 1994, Leonard Adleman [3] showed that it was possible to compute directly with molecules, as he used DNA to solve a Hamiltonian path problem (Figure 1.2). Such problem was known to require much

computing power when solved *in silico*, because there exists no algorithm that can shortcut the search of the solutions: one can only adopt a brute-force approach that consists in exploring all possibilities, one by one. DNA appeared to be an alternative of choice in this specific case. Adleman's *in vitro* implementation of the problem took advantage of the massive parallelism of DNA hybridization: if in a tube, one puts thousands of different DNA strands, all will find their complementary strand and hybridize to it, simultaneously. In other words, instead of manually trying DNA strands one by one to find the matching one, all can be thrown together in a tube, where each strand will find its complementary upon annealing. This breakthrough brought much enthusiasm to the unconventional computing communities and created the field of DNA computing. It was followed by other works also using the parallelism of DNA chemistry to solve "search" type problems [10, 11, 12, 4, 13]. Some were even predicting vast computation speedups over *in silico* computing for similar problems [10, 14]. Such computation however required numerous laboratory steps, resulting in long and laborious processes to harness the computational power of DNA [13]. This issue was somewhat addressed by autonomous DNA computers, which aimed at integrating these numerous steps in all-in-one protocols: as an example, Sakamoto *et al.* [15] solved another "search" problem by using secondary structures of DNA molecules, but this time in a one-step protocol. Advance in this direction was eventually hindered by issues such as the fidelity of DNA hybridization or reactions kinetics, limiting the complexity of the computable problems [16].

A few years later, Yurke *et al.* [9] came up with a DNA machine in which structural changes were obtained by DNA hybridization, and made reversible by a strand-displacement DNA hybridization. This DNA-made, DNA-fueled nano-machine gave a new breath to the field, bringing along the "toehold-mediated DNA strand-displacement" [17, 18] (Figure 1.3). This great tool - thoroughly and quantitatively analyzed by Zhang *et al.* [19] - brought a new dimension to the conception of molecular programming: roughly speaking, an "input" DNA strand can release a related "output" DNA strand by following the scheme of Figure 1.3. Input and output strands can be addressed through their specific DNA sequence, potentially leading to an infinity of possible connections between inputs and outputs, that is, offering the ability to encode various connectivities in circuits of reactions. This powerful concept opened up the way to generalized computation using the DNA.

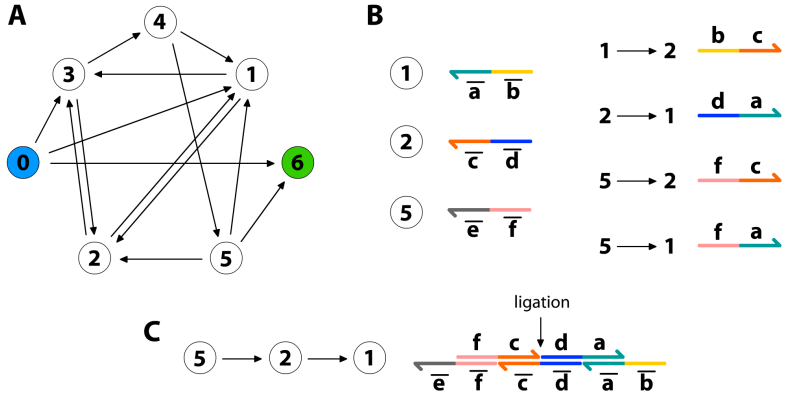

Figure 1.2: Adleman's DNA implementation of a Hamiltonian path problem. (A) Let the circled numbers be cities, the arrows airplane flights. The problem is to find the path that goes from the starting (0) city to the final (6) city, and stops only once in each city. (B) Cities and flights are encoded by DNA strands. $\bar{a}$ is complementary to a, $\bar{b}$ to b and so on. The left (3') site of cities can be considered as the airport arrival terminal, and the right (5') as the departure terminal. (C) Flight strands are connecting the city strands together, and a DNA ligase covalently binds two adjacent DNA strands. The DNA molecule that encodes the Hamiltonian path then has the following properties: starts with the city strand 0, ends with the city strand 6 and contains all the cities: it can be extracted from the pool and read using conventional molecular biology procedures.

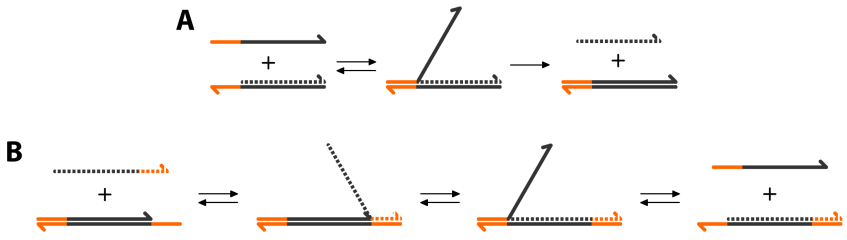

Figure 1.3: Toehold-mediated DNA strand-displacement. Toehold is colored in orange. (A) Irreversible case: the solid strand takes advantage of its toehold to displace the dashed strand from its location. Dashed strands does not have toehold, hence cannot displace the hybridized plain strand. (B) Reversible case: "toehold exchange". A toehold is included at both ends of the bottom DNA strand: both solid and dashed strands have a toehold that allows them to displace the hybridized strand.

1.1.3 Mimicking *in silico* computation

Since the birth of the field, molecular computation using NA has taken various forms, from mimicking *in silico* (logic gates) or *in vivo* (genes regulatory networks) computations to the exploration of more DNA-specific, novel ways of computation, as first proposed by Adleman [3]. In 2002, Stojanovic and coworkers [20] demonstrated logic gates (AND, NOT and XOR) based on deoxyribozymes (DNA-based catalysts [21]). Despite the limitation in the number of gates that could run in parallel, they demonstrated a brilliant molecular automaton capable of playing tic-tac-toe against a human opponent [22], following 19 different game patterns. They later refined their automaton with a perfect strategy, encompassing 76 different game patterns [23]. Other systems encoding logic gates were proposed [24, 25], and soon took as a principle that both input and output were of the same nature, potentially allowing chain reaction system, that is, cascading of logic gates [26, 27].

So far, the most advanced DNA logic gates circuits that have been made are based on toehold sequestering / exchange technology (Figure 1.3-B). In 2006, Seelig *et al.* reported a complete set of boolean logic gates (OR, NOT and AND) powered only by toehold sequestering [27]. Using short DNA strands as inputs and outputs, these gates could be cascaded in a more complex 6-inputs forward circuit (computing "a AND b AND (c OR d) AND (e OR f)"). They successfully performed the experiment at 37°C in presence of high concentration of mouse brain total RNA, suggesting that these logic circuits could potentially be run *in vivo*. However, in order to form a robust cascading circuit, each gate would require a complex signal restoration mechanism ([28] to overcome damping of the signal) and signal thresholding (to avoid leak reactions), thus rapidly increasing the complexity of the circuit. In their example, signal restoration was only introduced at the output of the circuit, a design which would be incompatible with larger scale circuits (due to signal damping during the evolution of the computation). Zhang *et al.* came up with a toehold exchange-based solution for the implementation of catalytic reactions: an "entropy-driven catalytic gate", which allowed the release of more than one output per input [29], making signal restoration a routinely executable task. Such mechanism would insure the modularity of the reactions, that is, the possibility to arbitrarily assemble logic gates in any configuration, and to cascade them at will (Figure 1.5-A).

Then Qian and Winfree proposed the "seesaw" gate [30]: a simple modular gate motif featuring both thresholding and catalytic signal restoration (Figure 1.4), opening the way to large-scale logic circuits. They demonstrated that AND and OR logic gates could be both constructed with two seesaw gates, and proposed a method to translate logic gate circuits into seesaw gate circuits [30].

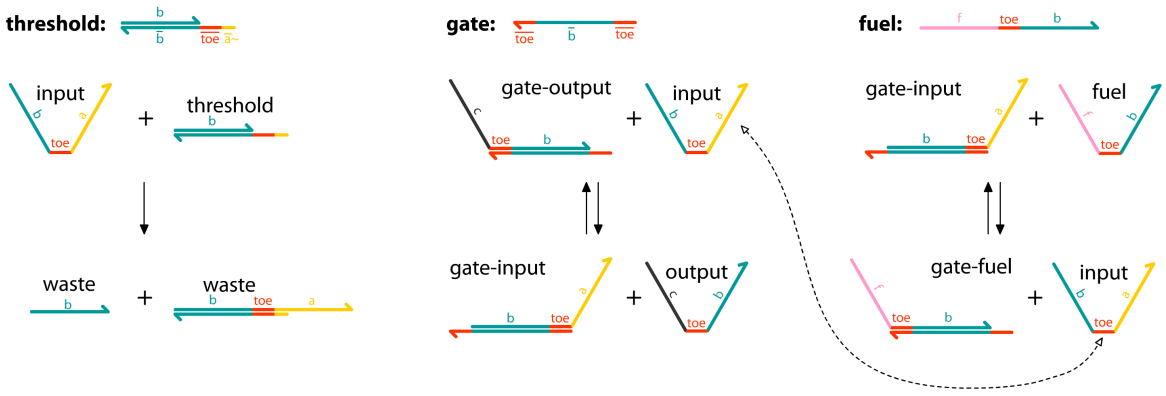

Figure 1.4: Seesaw gate for large-scale DNA logic circuits. Input has a higher affinity for the threshold, and get sequestrated by it. If the concentration of input exceeds that of the threshold, input goes to the gate and displaces the output. In such configuration, the system should equilibrate with roughly the same amount of free input and output (since the output can displace the input from the gate). In the case of cascaded logic gates, this would lead to a quick damping of the signal. However, in presence of fuel, the input (the strand that displaced the output) is "recycled", and can in turn displace another output: one input has the ability to release a number of output that depends on the initial amount of fuel.

They demonstrated the modularity and scalability of the seesaw gate by constructing a 42-gates (plus 16 thresholds) circuit calculating the square root of a four-bit number [31], and a 48-gates (plus 12 thresholds) circuit elegantly mimicking neural network computation [32].

Current logic circuits based on toehold exchange are single-use processes, driven toward equilibrium: once the final output (end-point concentrations of some DNA strands) is reached, the circuit is locked in its thermodynamic trap (Figure 1.5-B). Genot *et al.* recently demonstrated reversible logic circuits that are responsive to changes in their inputs concentrations [33]. They first built a reversible AND gate based on a DNA hairpin that is opened upon cooperative binding of its two inputs. The opened hairpin reveals the hybridization domain of a fluorescent probe, that consequently informs about the current state of the gate. They assembled a logic circuit computing "(a AND b) OR (b AND NOT c)" and demonstrated that it could be reused - if the inputs initially introduced were known: in this case, adding their complementary strands would sequester them, resetting the system for a new computation. However, such system needs to stay close to the equilibrium, which may limit the possibility to cascade the reactions [34]. To maintain time-responsiveness, a system requires a source of energy. In a closed setup, is also requires a kinetic trap to be kept out-of-equilibrium, that is, to be able to exhibit *dynamic* behaviors [35, 36]. In other words, it needs to be continuously traversed by a flux of energy (Figure 1.5-B).

Despite their non-ideal behaviors [37], toehold exchange circuits have been proposed as a universal

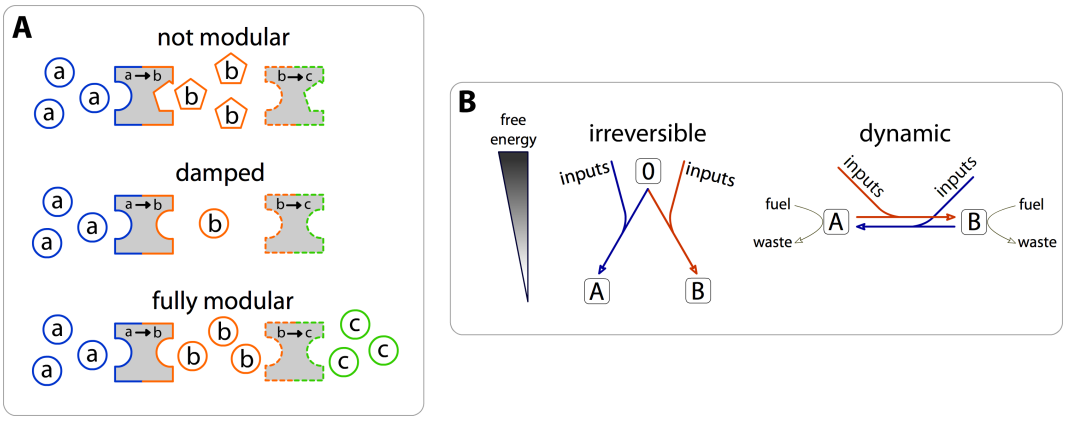

Figure 1.5: Modularity and Dynamism (A) In order to be *modular*, a reaction circuit needs that (*i*) its outputs are of the same nature as its inputs, so that they can themselves play the role of inputs and that (*ii*) an input triggers the production of one or more ouptut, so that the signal is not damped as reactions are cascaded. (B) Irreversible system versus dynamic system. Left: from an initial state (0) and a set of inputs, an irreversible system evolves towards a low-potential equilibrium state that corresponds to the answer of the computation (A or B), and cannot be re-used. Right: a dynamic system continuously consumes energy. Upon reading of a set of inputs (that may be endogenous), it transits from state to state, but does not get trapped in the equilibrium: it can be re-used or perform recursive tasks.

technology for dynamic biochemical circuits [38]. Soloveichik *et al.* demonstrated that, theoretically, they could be used to build an infinity of dynamic behaviors, including limit cycle oscillator, 2-bit counter and chaotic system [38]. The main issue with strand-displacement cascade based systems is that they are driven by a finite number of gates (or gate-output duplexes, see Figure 1.4): as an output is released from a gate, the gate itself becomes a waste. The depletion of gate-output complexes inevitably impacts the kinetics of the system, until its kinetic death (as it runs out of all gate-output). In their theoretical study, Soloveichik *et al.* set an initial amount of gates in regard to the expected time of the reaction, so that it can be considered pseudo-constant during the whole reaction time [38]. This would however be difficult for practical reasons. Another way to overcome this issue in a closed environment was proposed by Lakin *et al.*, with the idea of keeping a constant amount of ready-to-use, "active" gates [39]. They proposed an architecture that works as follows: when an *active gate* is consumed, it is replaced by a *buffered gate* (i.e. inactive), which gets activated by an initializing strand that is released when an *active gate* is consumed. Doing so, each consumed gate is replaced by a fresh one. They theoretically demonstrated the efficiency of these buffered gates to support a long-running three-phase oscillator. Another, more practical possibility to allow strand-displacement cascades to run forever would be to set them up in an open reactor, with a constant flow of fresh gate-output complexes.

A way to achieve dynamic reaction circuits in a closed system is to harness the wonderful catalytic properties of enzymes. For example, dynamic and modular logic computation was proposed with RTRACS (Reverse-transcription and TRanscription based Autonomous Computing System): an autonomous computer modeled after retroviral replication [40]. RTRACS uses RNA as both input and output of a DNA-encoded software that is executed by an enzymatic hardware. It includes a reverse transcriptase, a DNA polymerase, a RNA polymerase, and a RNase that plays the role of chemical sink (to keep the system out-of-equilibrium). In the context of RTRACS, Takinoue *et al.* first experimentally demonstrated an AND gate [40], that was later extended to a NAND gate [41]. Kan and coworkers recently built a general logic gate that should be capable of performing various logic functions (such as AND, NAND, OR, NOR), thus expanding the possible computational power of RTRACS [42]. Using the modularity of RTRACS, it should be possible to build oscillating reactions [43], or even more complex cell-like systems that could be hosted, for instance, in liposomes [44].

1.1.4 Mimicking *in vivo* computation

Cellular information processing relies on dynamic networks of biochemical reactions [45] that continuously recompute their state depending on some exogenous stimuli and the endogenous state of the cell. In these out-of-equilibrium networks of reactions, genes and their products regulate each other in huge assemblies of components and connections. Biological reaction networks seem to be among the most sophisticated information-processing systems that we know, and finding the relations between the cell's function and the underlying reaction network is not an easy task. Characterization of even the simplest systems (e.g. the lactose utilization network [46, 47] or the phage decision switch [48]) requires information that is extremely hard to obtain, including: macroscopic characteristics of the function, molecular understanding of the underlying reaction network, chemical knowledge of the different elements and quantitative kinetic and thermodynamic information concerning their interactions. Synthetic biology provides an other way to progress toward a better understanding of the underlying rules of natural reaction networks. The strategy consists in following a bottom-up approach - that is, to rationally design, construct, run and characterize such reaction networks *in vivo* [49, 50, 51].

Back in 2000, Elowitz and Leiber [52] and Gardner *et al.* [53] first harnessed the cell's machinery to compute synthetic reaction circuits. They showed that the cell could be used as a *hardware* to which one could give a *software* - an artificially designed gene network - that would endow the cell with new, non-natural functions. In contrast to standard genetic modifications, the function is engineered by

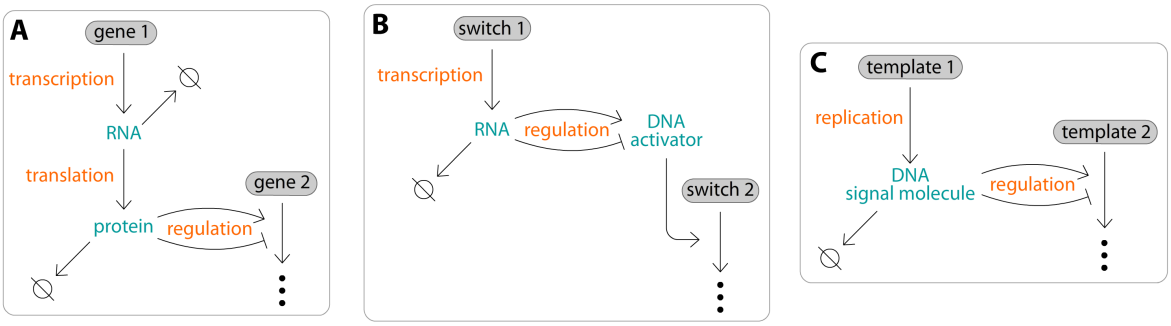

Figure 1.6: Schematic building blocks of *in vivo* reaction networks and *in vitro* analogs. (A) Schematic gene regulation pathway in the cell: a gene is transcribed into RNA, in turn translated into proteins that regulate (activate or inhibit) the activity of another gene. (B) *In vitro* analogy proposed by Kim *et al.* [61]: a DNA "switch" is transcribed into RNA transcripts which sequester or release the DNA activator of another switch. (C) *In vitro* analogy proposed by Montagne *et al.* [62]: a DNA "template" is replicated into DNA signal molecules that directly regulate the activity of another template.

rearranging a few of the cell's known regulatory elements: by doing so, they constructed an oscillator [52] and a bistable function [53]. Following the same approach, other small scale reaction networks encoding elementary functions such as cascades [54], bistability [53, 55, 56, 57] or oscillations [52, 55] have been successfully engineered. Synthetic biologists are however facing some major issues due to the complexity of their platform - the cell. The shortage of known interoperable regulatory elements is one of these issues, as well as the difficulty to harness the cell's machinery: nonlinear effects [58, 51, 59] and unintended interactions between the synthetic network and the cell's housekeeping functions [60] are frequent and difficult to pinpoint.

An attractive alternative is to engineer analogs of gene networks out of the cell, in purposely created - and better controlled - *in vitro* environments [61, 63, 62, 64, 65, 66]. Such cell-free approach eliminates unintended interactions with the natural functioning of the cell, and allows easier quantitative analysis [67]. Figure 1.6 abstracts the *in vivo* gene regulation pathway mechanisms (Figure 1.6-A), as well as two *in vitro* analogs implemented by Kim *et al.* ([61], Figure 1.6-B) and Montagne *et al.* ([62], Figure 1.6-C).

As straight as it can be, Noireaux *et al.* demonstrated cell-free genetic circuit elements in a commercial (modified) transcription-translation extract [68]. They harnessed the full gene regulation pathway (Figure 1.6-A), and showed that positive and negative regulatory elements could be produced *in vitro* [68]. In later studies, Shin and Noireaux produced and characterized a cell-free expression toolbox from *E. Coli* extracts, potentially giving access to many regulatory elements that could be rearranged in *in vitro* synthetic gene circuits [69]. Using this system, they recently constructed a

multiple stage cascades, an AND gate and a negative feedback loop [66]. This complete system stands as the unique *in vitro* implementation allowing the study of transcription-translation reaction networks, which are closely reproducing *in vivo* networks.

In 2006, Kim *et al.* proposed an *in vitro* analogy of gene regulation pathway [61] where, rather than getting translated into protein, RNA transcripts directly regulate transcription from DNA gene analogs (Figure 1.6-B). In their system, a "genelet" is a short double-stranded DNA that contains a nicked promoter (Figure 1.7). The promoter needs to be completed by a DNA activator for the genelet to start emitting RNA transcripts. RNA transcripts make the bridge between genelets, by either sequestering or releasing DNA activators. One or two RNases keep the system out-of-equilibrium by specifically digesting the RNA transcripts. As for the genes in natural *in vivo* reaction networks, genelets can be cascaded: one can arbitrarily decide which genelets will be connected, and what will be their interaction (activation or inhibition). In this way, Kim and Winfree have experimentally constructed a bistable circuit [61], and a number of oscillators [63] by rearranging genelets following different network topologies (Figure 1.7-B and C). As recently demonstrated [70], a single auto-activated genelet can behave as a bistable switch, which is intrinsically autoregulated. They also investigated the load effect, which happens when a genelet needs to load (and drive) a downstream process that uses its RNA transcript [71].

Montagne *et al.* proposed in 2011 an even simpler *in vitro* biochemical implementation of reaction networks [62], where DNA gene analogs (templates) produce DNA signal molecules that directly regulate other DNA templates (Figure 1.6-C). Despite its simplicity, this system is able to reproduce *in vitro* the main architectural features of gene regulatory networks. As a stripped-down *in vitro* genetic machinery, the DNA-toolbox is based on three enzymatic reactions (Figure 1.8-A): short DNA signal molecules hybridize with stable DNA templates in a set of basic reactions that structures the topology of the reaction circuits. Templates are composed of a 3' input site and a 5' output site. Signal molecules come in two types: inputs activate templates whereas inhibitors block templates. An exonuclease specifically degrades DNA signal molecules, thus providing the required chemical sink to build out-of-equilibrium reaction circuits. Templates are fully modular: it is theoretically possible to assemble them following complex reaction circuits topologies (Figure 1.8-B and C). Montagne *et al.* first demonstrated an oscillator (Figure 1.8-C) made with this system [62]; in this thesis, we will construct a bistable function (Figure 1.8-B), and show how the modularity of the reactions allows the building of more complex memory functions.

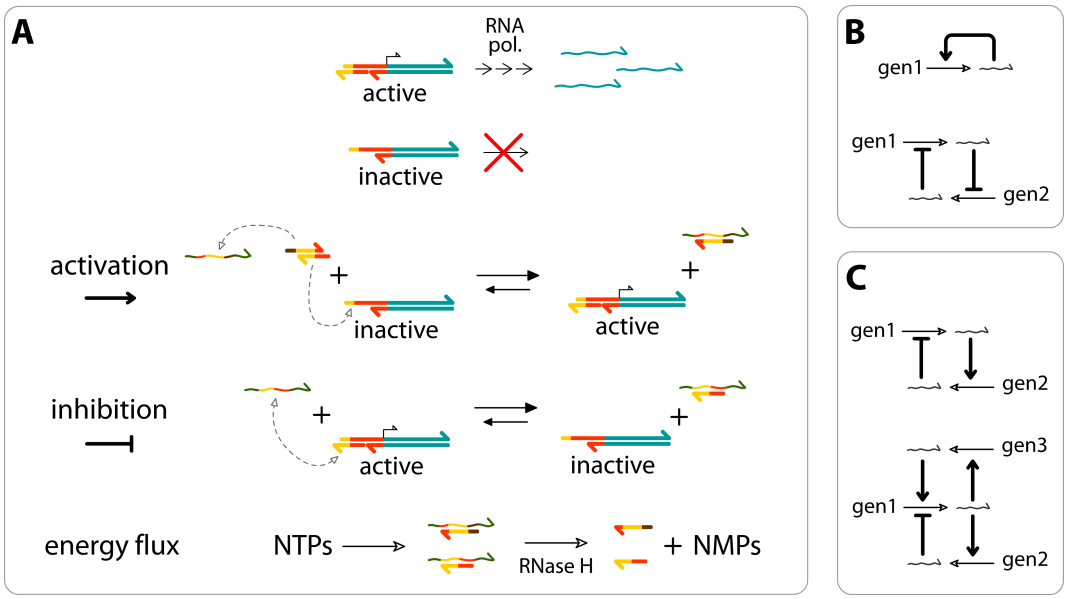

Figure 1.7: The genelet system. (A) Functioning of the genelet system. Genelets are short double-stranded DNA that contain a nicked promoter (in red). When the promoter is complete (genelet indicated as "active"), a RNA polymerase transcribes it into RNA transcripts (thin wavy strands) that establish the connection between genelets. A RNase degrades RNA transcripts, keeping the system out-of-equilibrium. "Activation" is obtained as the DNA activator of an inactive genelet (which promoter is incomplete because lacking its DNA activator) is released thanks the incoming RNA transcript. "Inhibition" is obtained when the incoming RNA transcript sequester the DNA activator of an active genelet, making it inactive. The system is traversed by an energy flux as NTPs are used to produce RNA transcripts that are later on hydrolyzed into waste NMPs. (B) Two circuit topologies that experimentally showed a bistable behavior. Up: a single autoregulated genelet. Bottom: two cross-repressed genelets. (C) Two circuit topologies that experimentally produced oscillations. Up: Two-genelets negative feedback loop. Bottom: Amplification with negative feedback loop.

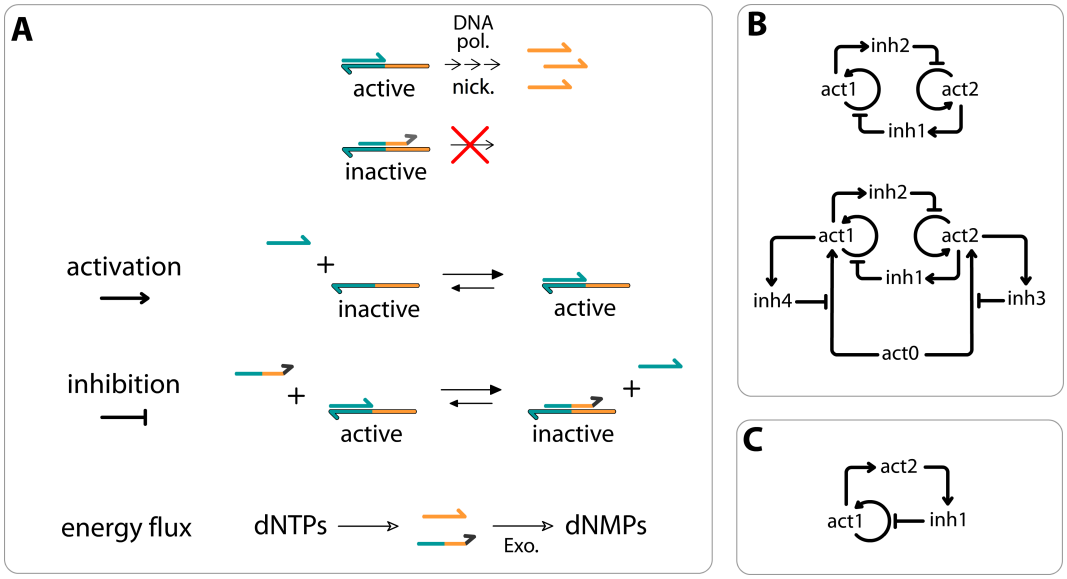

Figure 1.8: The DNA-toolbox. (A) Functioning of the DNA-toolbox. Templates (bottom strands) have an input site (3') and an output site (5'). When their input is hybridized (template noted as "active"), a polymerase and a nickase catalyze the production of outputs. These outputs establish the communication between templates. An output can be either the input or inhibitor of another template. "Activation" is obtained as an input hybridizes to its corresponding template. "Inhibition" is obtained as an inhibitor hybridizes to a template, displacing the activating input. The energy flux is based on dNTPs, consumed by the production of outputs, then hydrolyzed into waste dNMPs by an exonuclease. (B) Up: A topology of bistable function encoded with the DNA-toolbox. Down: a push-push memory circuit (see Chapter 3). Wires represent templates. (C) The Oligator [62], an oscillating circuit made of an amplification with negative feedback loop.

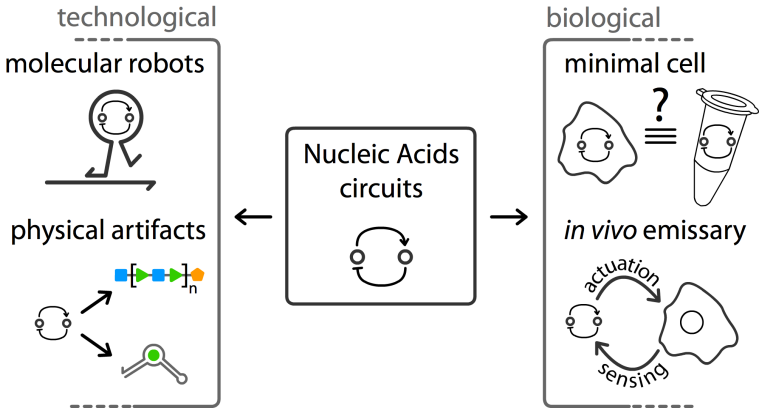

Figure 1.9: Examples of applications of NA reaction circuits

1.1.5 Applications

In vitro NA reaction circuits are enabled to interfacing with all the other constructs of the widening field of NA nanobotechnology. These include static as well as dynamic nanostructures: for example, NA reaction circuits could be used to drive NA robots *in situ*, thus removing the need for exogenous control (Figure 1.9). In this way, Franco *et al.* used a genelet-based oscillating circuit to sequentially drive the opening and closing of DNA tweezers [71]. NA reaction circuits can also be used to drive other processes such as the production of aptamer [71], organic synthesis [72, 73], DNA gels [74] or optical devices [75].

Dynamic reaction circuits provide an experimental model to study the relationships between circuit topology and functions. Because they are shaped by mimicking *in vivo* computation, they may affect our understanding of the complex *in vivo* regulatory processes. Recent *in vitro* works have pointed out the importance of two neglected phenomena on molecular circuits: the competition for enzymatic resources (and complex couplings that may arise thereof) [59] and the "load" effect that appears when a circuit has to drive a downstream process [71]. It is very probable that similar phenomena also happen in natural reaction networks, however, they are generally not considered in the building of biological models [59]. In this sense, engineering *in vitro* analogs is another way of exploring the underlying design rules of the molecular circuits that control cells.

In vivo applications of NA reaction circuits are also burgeoning. Hybridization chain reaction - by which a NA molecule triggers a chain hybridization of metastable hairpin molecules, eventually releasing a final NA product [76] - was used for detection of specific mRNAs within biological samples [77]. It was also successfully translated *in vivo*, and set up as a reaction circuit drug that mediated

the cell death upon detection of a given combination of cancer-specific mRNAs markers [78].

However, it is not trivial to transfer NA circuits designed *in vitro* to a more challenging environment. In recent works, much effort is put on improving the robustness of the circuits for subsequent implementation in non-pristine milieu, where various materials and reactions may interfere with the circuit [79]. NA logic circuits showed to perform well in the presence of excess of random oligonucleotides [80], or mouse brain total RNA [28]. Diehl and coworkers did a careful study of their strand-displacement system in order to improve its robustness for application *in situ* [81]. This proved useful as they used it with DNA-conjugated antibodies for the labeling of endogenous proteins [82]. Other works have also focused on reaction robustness to impurities in the sequences [37], and hybridization robustness over large ranges of temperature and salt conditions [83]. These works may prove extremely useful to assist the transfer of complex NA circuits *in vivo*.

NA reaction circuits stand at the interface between the living and non-living matter: they form a unique bridge that is both conceptual - as an operative model of *in vivo* information processing - and material - as being capable of sensing and actuating *in vivo* functions - (Figure 1.9).

1.1.6 Reaction-Diffusion

Reaction-diffusion (RD) computers can be considered as a thin layer of liquid that is the receptacle of programmed reactions; these reactions transform data; data takes the form of concentrations of reagents. Such liquid computers are capable of amorphous computing: they can be considered as a huge number of identical microvolume processors that are interconnected by diffusion, but do not have any *a priori* knowledge of their spatial location [84]. These microvolume processors continuously and simultaneously recompute their state (i.e. their concentration in reagents) depending on *(i)* their own state, *(ii)* the state of their neighbors and *(iii)* possible external perturbations [85]. This is radically different from regular computers, which are hard-wired assemblies of transistors computing in a serial manner: if one transistor dies, chances are that the computer will also die. In contrast, RD computers are fault-tolerant: if a single unit is damaged, it may not affect the main function of the computer. In this sense, RD computing shares similarities with the distributed computing approach where multiple computers connected over a network are executing different tasks in order to solve a common problem.

RD computers are relevant to biological / natural information processing which seems to be carried out by highly parallel mechanisms [86]. The concept of amorphous computer fits well to local arrays of identical cells that are capable of intercellular communication [87] (even though cells are themselves

complex computing units). Also, neural networks can be considered as networks of simple units that interact with each other, yielding a variety of collective behaviors [86]. Their case can be a bit trickier, since neurons are not only connected to nearest neighbors, but can also have direct connections to more distant areas [88]. Reaction-diffusion models have been proposed to describe various cases of biological patterning phenomena [89] such as, for example, some anatomic features of *Drosophila* acquired during morphogenesis [90, 91, 92], or the reorganizing stripe patterns on the skin of angelfishes [93].

In a different perspective, reaction-diffusion systems can also be used to explain various phenomena such as the complex ecological patterns observed in nature [94], or the spread of infectious diseases [95, 96]. In a more general vision, simple chemical reaction-diffusion systems [97] or cellular automata such as Conway's Game of Life [98] have shown that the key to the emergence of complex patterns lies in the communication capability of simple units.

Note that amorphous computers are not meant to replace conventional, silicon-based computers, and probably cannot [99]. However, our ability to program such systems would expand the list of available substrates that are capable of information processing [84]. Then, one could imagine fantasy applications such as smart materials of which each molecule (or single unit) would behave in conjunction with its neighbors, and would have computational abilities so that the whole chunk of material would sense and actuate in response to its environment.

Mathematically, a reaction-diffusion system can be obtained by simply adding a diffusion term to a set of ordinary differential equations, given that these are of the first order in time [100]. Experimentally, it consists in granting a chemical system the possibility to diffuse. In this way, the Belousov-Zhabotinsky (BZ) oscillating reaction [101] has been extensively studied in zero (well-mixed), then in two (thin layer of liquid) and three-dimensional environments. By setting the BZ reaction in 2D, researchers first discovered traveling waves [102], then spiral waves [103] that emerged from breaking traveling waves (e.g. by a physical perturbation of the front of an expanding wave).

In contrast with conventional chemistry, NA-based biochemistry proposes an easy access to the scaling up of reaction circuits, mainly due to the chemical addressability of NA. We have seen that NA-based chemical reaction circuits are able to emulate *in vitro* the behavior of many dynamic systems with complex time trajectories [63, 62]. Yet, NA-based *in vitro* dynamic RD systems have, so far, not been explored.

1.2 Outline

Montagne *et al.* built a robust DNA-based biochemical oscillator (the *Oligator*) through a rational network design [62]; we will demonstrate that the three basic building blocks they devised (the DNA-toolbox) can be reused in a general and fully modular manner to build more complex DNA reaction circuits.

The oscillations of the oligator could be observed by using a fluorescent intercalating dye reporting on the total (oscillating) amount of DNA strands present in solution. When working with larger scale reaction networks, it is necessary to be able to monitor the reactions at the desired locations in the sequence space, that is in a sequence-specific manner. For instance, a bistable reaction circuit that would output either a strand α or a strand β (but not both at the same time) would require a way to differenciate between these two strands: it would otherwise be impossible to unambiguously check the state of the system (i.e. state $\{\alpha, \beta\} = \{1, 0\}$ OR $\{0, 1\}$). Such reaction circuits thus require dedicated monitoring technique: in Chapter 2, we will address this point by proposing N-quenching, a versatile fluorescent technique for the monitoring of oligonucleotide hybridization.

With the DNA-toolbox and N-quenching in our hands, we will tackle the construction of more complex reaction circuits, and more specifically circuits encoding for bistability and updatable memory functions: we demonstrate in Chapter 3 the construction of a bistable reaction circuit, and improve it into the first *in vitro* updatable memory circuit and 1-bit binary counter. The (long) road that led to these working circuits is presented in Chapter 4, in which we also explore a few other circuit assemblies.

The laboratory hosting us is specialized in microfluidics. Naturally, this spurred us on to combine the possibilities brought by the microfluidic tool with our expertise of DNA biochemistry. First, the idea was to enclose our reactions in tiny reactors - that is to compartmentalize our reactions - and then connect them. In Chapter 5, we explore various (failed) approaches. Eventually, microdroplets appeared to be the best compartmentalization method, if not the most practical in the purpose of connecting them in assemblies of microreactors.

Finally, in Chapter 6, we explore the use of the DNA-toolbox made reaction circuits to build reaction-diffusion systems. For this purpose, we engineer a very simple and cheap device that allows us to observe our reaction circuits in two-dimensions. As a first step toward tailor-made spatio-temporal patterns, we show that locally perturbing an oscillating reaction circuit provokes the emergence of traveling and colliding waves.

1.3 Glossary

- Closed system: is a system that does not exchange matter with its environment. If a flux of energy is not provided, a closed system ultimately reaches its thermodynamic equilibrium. In this study, we deal with closed systems which are emulating openness to allow *out-of-equilibrium* behaviors for a certain lapse of time.

- DNA-toolbox: nickname refers to the modular DNA based chemistry introduced first by Montagne *et al.* [62]. It allows the construction of arbitrary networks of activation and inhibition reactions.

- dNTPs: stands for deoxyribonucleotide triphosphate. dNTPs are activated DNA monomers that are used by the DNA polymerase to polymerize the complementary DNA strand of a *template*.

- EvaGreen: is a DNA-binding dye (such as the SYBR Green I) that intercalates with double-stranded DNA molecules, thus allowing to monitor DNA hybridization in a non-sequence specific manner.

- Fluorophore: is a fluorescent compound (also referred to as dye) that emits light when excited with a light of a shorter wavelength.

- Inhibitor: is the signal molecule produced by an inhibition module. A given inhibitor blocks a target *template* (either an activation or an autocatalytic module) by hybridizing to it, overlapping on its input site and output site. It is longer (hence more stable) than inputs and is able to displace an input hybridized to its *template*.

- Input: are activating the production of other inputs, or inhibitors, by hybridizing to the input site of the associated template.

- Melting temperature: For a stoichiometric mix of two complementary DNA strands (or a DNA strand secondary structure, such as a hairpin), the melting temperature (T_m) is the temperature at which half of the double-stranded complex is dissociated (i.e. in single-stranded form), given its concentration and salt conditions.

- Modular: is said of a system which subunits (or modules) can be arbitrarily connected to other subunits (or modules). Modularity requires that input and output of a subunit are of the same nature, so that output can play the role of input for a separate subunit. It also requires the

amount of produced output to be equal, or greater, than the amount of received input, so that there is no damping of the signal throughout the reactions.

- N-quenching: is the fluorescence technique that we devised to monitor the hybridization of *inputs* in a sequence-specific manner. This technique is detailed in Chapter 2.

- Out-of-equilibrium: refers to a system which is not allowed to relax to its thermodynamic equilibrium. Out-of-equilibrium conditions can be maintained by a flux of matter or energy traversing the system, or by a kinetic trap existing on the thermodynamic track. In the context of the DNA-toolbox, out-of-equilibrium conditions are maintained thanks to the slow spontaneous hydrolysis of dNTPs and the two-step enzymatic catalysis (polymerization-depolymerization) that can accelerate this process.

- Phosphate: In the context of this study, the 3' end of *templates* is modified with a phosphate group, that prevents the DNA polymerase from extending them.

- Phosphorothioates: are backbone modifications of the DNA strand used to protect the *template* from hydrolysis by the exonuclease. The 5' end of *templates* is typically modified with three phosphorothioates.

- Strand-displacement: DNA polymerases display two different modes of polymerization along a template: normal (unobstructed) polymerization, when the template is unoccupied downstream, and strand-displacement, when it has to displace a downstream DNA that occupies the template. In the context of this study, strand-displacement happens when the output site of template being processed is occupied by the output. In this case, the DNA polymerase has to displace the already present output to polymerize a new output. This reaction is taken in account in the detailed mathematical model, as well as the fact that the DNA polymerase we use has a lower activity when working in strand-displacement.

- Template: In general, a "template DNA" is a DNA strand that is transcribed into RNA: it serves as "template" for the RNA polymerase. In this study, a template designates the DNA strand associated to a module of the *DNA-toolbox*. A template strand is composed of an input site and an output site. Templates are modified in 5' with *phosphorothioate* modifications, and in 3' with a *phosphate* of a *fluorophore*.

- Thermocycler: to run *DNA-toolbox* made reaction circuits in bulk, we use real-time PCR thermocyclers. These machines allow to incubate and monitor the fluorescence of up to 96 separate reactions in parallel. We typically use reaction volumes ranging from 10 µl to 20 µl.

- Time-responsive: is said of a system that is reusable. Upon reading of a set of inputs, a time-responsive system gives an answer that is only transient: once the inputs are removed, the system is ready for another computation. Time-responsiveness requires a flux of energy to maintain the system out-of-equilibrium. This is possible in our closed setup by the constant (for a given amount of time) supply of precursors (*dNTPs*) that are consumed as signal molecules are produced. Signal molecules are then degraded into inactivated waste monomers (dNMPs).

Chapter 2

N-quenching

The Oligator [62] was constructed by using three distinct modules (its functioning involves 3 dynamic species, see Figure 1.8), which could potentially be rearranged in various reaction circuit topologies. Yet, one would lack a way to monitor specifically the dynamic of each components of such circuit. The work presented below is our answer to this problem: a fluorescence monitoring technique of DNA hybridization, specific and specially tailored for the use with dynamic reaction circuits. We will present how we came up with the idea of this technique, determined its usability in the context of DNA reaction circuits, and used it to monitor the dephased oscillations of the different components of the Oligator in real-time. The following work was published as: Adrien Padirac, Teruo Fujii, and Yannick Rondelez, Quencher-free multiplexed monitoring of DNA reaction circuits in *Nucleic Acids Research*. We will also explore a few practical applications of N-quenching, with notably a proposition about how to monitor inhibitor species, that cannot be directly monitored with a straightforward use of N-quenching.

2.1 Abstract

We present a simple yet efficient technique to monitor the dynamics of DNA-based reaction circuits. This technique relies on the labeling of DNA oligonucleotides with a single fluorescent modification. In this quencher-free setup, the signal is modulated by the interaction of the 3'-terminus fluorophore with the nucleobases themselves. Depending on the nature of the fluorophore's nearest base pair, fluorescence intensity is decreased or increased upon hybridization. By tuning the 3'-terminal nucleotides, it is possible to obtain opposite changes in fluorescence intensity for oligonucleotides whose hybridiza-

tion site is shifted by a single base. Quenching by nucleobases provides a highly sequence-specific monitoring technique, which presents a high sensitivity even for small oligonucleotides. Compared to other sequence-specific detection methods, it is relatively non-invasive and compatible with the complex dynamics of DNA reaction circuits. As an application, we show the implementation of nucleobase quenching to monitor a DNA-based chemical oscillator, allowing us to follow in real time and quantitatively the dephased oscillations of the components of the network. This cost-effective monitoring technique should be widely implementable to other DNA-based reaction systems.

2.2 Introduction

Various implementations of nucleic acid-based reaction circuits have been demonstrated since DNA was first used as a substrate for *in vitro* computation of a Hamiltonian path in 1994 [3]. DNA was used to encode complex systems such as interactive molecular automata [22, 23], as well as computation mimicking neural networks [32], a square-root calculator [31] and robust chemical oscillators [62, 63]. These information processing systems are composed of many interacting DNA species and yield one or more outputs, typically encoded in the dynamic [62, 63, 38] or end-point concentrations [22, 32, 31] of some oligonucleotides. In order to read out the results of such molecular systems, as well as for the purpose of rationally designing and troubleshooting these DNA reaction circuits, it is desirable to distinguish their different components and monitor the evolution of their concentrations as the reactions proceed.

Methods to observe nucleic acid-based reactions have evolved from post-experiment gel analysis to real-time sequence-specific monitoring. Real-time monitoring of DNA based reactions is possible thanks to the development of fluorescence techniques that allow detection and quantification of nucleic acids. In the case of isothermal conditions - as generally used for DNA reaction circuits -, a further constraint is that the monitoring technique does not interfere too much with the reaction that is monitored. Ideally, the presence or absence of the fluorescent probe has no influence on the kinetics and thermodynamics of the DNA-based reaction circuit under scrutiny.

DNA-binding fluorophores, such as the SYBR family, become highly fluorescent when bound to single or double-stranded DNA. They can be used to monitor DNA amplification reactions such as PCR (Polymerase Chain Reaction). Some of them, like SYBRGreen II or Evagreen [104], can also be used to observe isothermal amplification (EXPAR [105, 106]). However, they only provide sequence-unspecific monitoring; in many cases it is necessary to obtain more detailed information than the total

amount of double-stranded DNA in solution. Probes that are specific to a given, arbitrarily selected sequence are then required.

Sequence-specific monitoring can be obtained with fluorescent probes that hybridize to target sequences, leading to a modification of the intensity of their fluorescence. Such fluorescent probes usually consist in oligonucleotides that are dual-labeled with a "donor" and an "acceptor" fluorophore. Through fluorescence resonance energy transfer (FRET [107]), the acceptor acts as a quencher of the donor, and the quenching efficiency strongly depends on the distance between the two fluorophores. Probes bear the complementary sequence of their target, which allow them to hybridize to it. Hybridization and following reactions lead to the separation of donor and acceptor, subsequently dequenching the fluorescence of the donor. For instance, in the case of PCR TaqMan probes [108], depolymerization of the hybridized probe separates donor and acceptor. For Molecular Beacon [109], donor and acceptor are initially brought close to each other by the probe's hairpin structure. The probe opens as it hybridizes to its target, which increases the distance between donor and acceptor.

Besides classic DNA amplification techniques (such as real-time PCR [108] or EXPAR [105, 106]), other types of DNA systems also require sequence-specific real-time monitoring. This work focuses on DNA reaction circuits that are complex reactive assemblies of many DNA strands able to perform some form of pre-encoded program [32, 62, 63]. Such systems generally require the design of custom monitoring solutions. In some cases, it is still possible to readapt the conventional donor/acceptor pair of fluorophores: DNA-based molecular automaton MAYA [22] uses a fluorogenic substrate with a donor at one end and an acceptor at the other. Cleavage of this substrate separates donor and acceptor, which produces an irreversible dequenching of the donor fluorescence. Also, most DNA-based molecular machines [8, 9] use various donor/acceptor pairs of fluorophores to monitor the molecular motions associated with the machine functioning [110].

Donor and acceptor can also be placed on two separate and complementary DNA molecules. In this case, hybridization of the two strands brings donor and acceptor close to each other, which quenches the fluorescence of the donor [111, 19, 31, 32]. However, this technique significantly impacts the thermodynamics of the labeled complementary strands [112].

The most complex DNA reaction circuits are out-of-equilibrium systems that are able to display emergent behaviors like oscillations [62, 63], multi-stability [61] or - theoretically - chaotic trajectories [38]. Such circuits display non-monotonous concentration evolutions and generally require reversible fluorescence reporting. Moreover, labeled probes can be difficult to use in these systems because some

DNA strands are continuously produced and destroyed [62]: therefore, a simple, general and non-disruptive monitoring technique would be a welcome addition to the field of molecular programming.

Direct quenching by adjacent nucleobases is a somehow neglected effect where the fluorescence of a single DNA-bound fluorophore is modulated by interactions with the neighboring DNA sequence [110, 113, 112]. Each nucleoside has a different quenching effect on nearby fluorophores, with guanosine exhibiting the highest quenching efficiency [113]. Moreover, the quenching ability of each base strongly depends on its paired or unpaired status, leading to fluorescence changes upon duplex formation. Using this property, DNA hybridization [114] and PCR [115, 116] have been monitored.

In this work, we show that nucleobase quenching (referred to as 'N-quenching' hereafter) provides an efficient method for real-time multiplexed monitoring of DNA reaction circuits with complex dynamics. By labeling the 3' end of a 'template' oligonucleotide with a single fluorophore, hybridization and separation of the complementary 'signal' oligonucleotide can be monitored. N-quenching is highly sequence-specific: a non-complementary sequence or a sequence hybridizing a few bases away from the fluorophore is readily distinguished from the target sequence. Regarding short oligonucleotides, N-quenching sensitivity is relatively high compared to DNA-intercalating fluorophores. It is a cost-effective technique that only requires one fluorophore per target oligonucleotide, with no need for additional probes. N-quenching is thus non-invasive and compatible with dynamic DNA reaction circuits. As an implementation example, we monitored the signal oligonucleotides of an autonomous DNA-based chemical oscillator by directly labeling the sequences of interest. N-quenching is a versatile monitoring technique that should be easily implemented to various DNA-based reaction systems.

2.3 Materials and methods

2.3.1 Oligonucleotides

All DNA oligonucleotides were purchased from either Integrated DNA Technologies (IDT, Coralville, IA, USA) or biomers.net (Ulm germany), with HPLC purification. Concentrations were determined by measuring the absorbance at 260nm using a GeneQuant Pro RNA/DNA Calculator (GE Healthcare). Using DinaMelt [117], we checked that all sequences used in this study did not display secondary structures at the working temperatures.

2.3.2 Fluorescence shift measurement

For fluorescence intensity shift curves upon temperature-induced hybridization, oligonucleotides were diluted in a buffer containing 100mM NaCl and 0.1% Synperonic F108 (Sigma-Aldrich) in TE buffer (pH 8.0). Oligonucleotides were used at a concentration of 100nM for labeled 22-bases long 'templates' and 300nM for 11-bases long 'signals'. Hybridization and separation were induced by alternating between temperatures lower and higher than the duplexes' melting temperatures. Temperatures were determined so that NUPACK [118] predicts less than 5% of template strands hybridized at 'high' temperature and more than 95% of template strands hybridized at 'low' temperature. Fluorescence of 20µL samples covered with 15µL of mineral oil was recorded using an IQ5 real-time thermocycler (Bio-Rad).

For the experiment shown in Figure 2.1, a 'template' oligonucleotide (5' - AGATGACTCTC-CTTAGACTCAG - 3') bearing a 3'-terminal TAMRA NHS ester modification was used with either a 'signal' complementary sequence (5'-CTGAGTCTAAG-3') or a non-complementary sequence (5'-AACAGACTCGA-3').

2.3.3 Monitoring of DNA reaction circuits

Reactions were assembled in a buffer containing 10mM KCl, 10mM $(NH_4)_2SO_4$, 50mM NaCl, 2mM $MgSO_4$, 45mM Tris-HCl, 5mM $MgCl_2$, 6mM DTT, 100µg/ml BSA (New England Biolabs), 410mM Trehalose, 1x EvaGreen and dNTPs (100µM each). Bst DNA polymerase, large fragment, Nt.BstNBI nickase and $RecJ_f$ exonuclease were purchased from New England Biolabs, and used at 8, 40, 12 U/mL respectively. Samples of 40µL were observed using an IQ5 real-time thermocycler (Bio-Rad) set at a constant temperature of 38.5°C.

For monitoring the single steady state network, 50nM of template A (5' - CTTAGACTCAG-CTTAGACTCAG - 3') with 3'-terminal TAMRA NHS ester modification was put in presence of an initial concentration of 0.1nM of signal α. In the case of the oscillator, templates A, α*to*β (5' - AGATGACTCTC-CTTAGACTCAG - 3') with 3'-terminal TAMRA NHS ester modification and β*to*iα (5' - TTACTCAGCTTAGAC-AGATGACTCTC - 3') with Alexa Fluor 594 NHS ester modification were used at concentrations of 40, 5 and 20nM. All templates bore two phophorothioates backbone modification at their 5' end to protect them from hydrolysis by $RecJ_f$ exonuclease [62].

2.4 Results

2.4.1 Characterization of nucleobase quenching

We initially observed that adding the complementary strand to a 3'-terminal fluorophore labeled oligonucleotide in solution produced a shift of fluorescence intensity. To further characterize the phenomenon and the possibility to use it in our assay, we selected a 22-bases long oligonucleotide 'template' labeled with TAMRA at its 3' end (Figure 2.1). This template was put either in the presence of a 11-bases long 'signal' complementary sequence or a 11-bases long non- complementary sequence. Signal oligonucleotide hybridized adjacently to the template 3'-terminal dye. We induced hybridization and separation of the strands by applying temperature cycles.

This allowed us to observe the effect of hybridization on the intensity of fluorescence emission of the 3'-terminal dye. Figure 2.1 shows the fluorescence intensity shift obtained by cycling between temperatures higher and lower than the duplex melting temperature. At 'low' temperature, TAMRA showed a 50% drop of fluorescence intensity in the presence of the complementary strand, whereas a non-complementary sequence did not produce any significant shift of fluorescence intensity. Cycling the temperature several times confirmed the reversibility of the phenomenon.

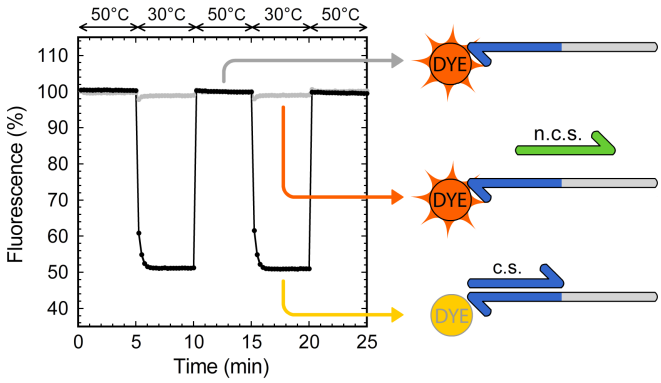

Figure 2.1: TAMRA fluorescence quenching upon temperature induced hybridization/separation. Fluorescence intensity is expressed as a percentage of the fluorescence of TAMRA-labeled template put alone in solution. Presence of the complementary sequence (c.s.) induces a fluorescence shift (black curve) when the temperature is lower than the duplex melting temperature, whereas presence of a non-complementary sequence (n.c.s) does not have influence on the fluorescence of TAMRA (grey curve).

2.4.2 Environmental dependence

The fluorescence intensity shift upon hybridization depends on the direct environment of the fluorophore. We investigated this property by tuning the fluorophore's nearest bases. In the case of TAMRA, Figure 2.2 shows the fluorescence intensity shifts for four combinations of the two bases before the 3'-terminal fluorophore. Depending on these last two bases, we observed either a decrease or an increase of the fluorescence of TAMRA upon hybridization of the two complementary strands: the fluorescence increased for terminal 3'-AG and 3'-TC, and decreased for terminal 3'-GT and 3'-GA. These results globally agree with the trends reported by Nazarenko *et al.* [119] for internally labeled oligonucleotides: the formation of a terminal C-G pair strongly quenches the fluorophore, whereas the hybridization of a complementary strand globally dequenches the fluorophore. We tested other combinations of the last two bases (data not shown), which all produced results consistent with this generalization of the rules reported by Nazarenko *et al.* [119]. While the position of the dye is not really important in our case, the nature of the 3'-terminal bases determines the direction - positive or negative - of the fluorescence intensity shift.

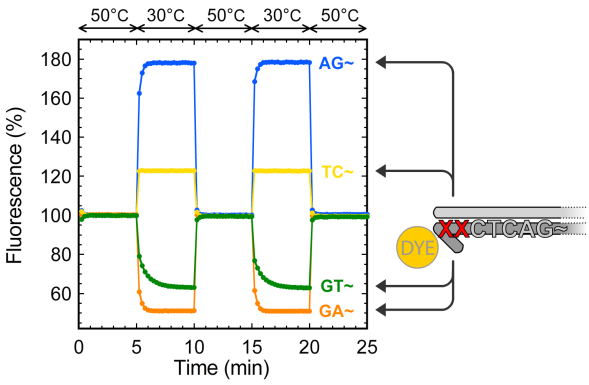

Figure 2.2: TAMRA fluorescence quenching upon temperature induced hybridization/separation for different pairs of 3'-terminal bases. Fluorescence intensity is expressed as a percentage of the fluorescence of the TAMRA- labeled template put alone in solution. Four combinations of the template's two 3'-terminal bases XX (AG, TC, GT, GA) show negative or positive fluorescence intensity shifts upon hybridization of the complementary sequence.

To assess the specificity of N-quenching for the target 11-bases long signal, we compared the shift of fluorescence intensity induced by the target signal (blunt end) to that of a signal strand moved from 1 to 11 bases away (dangling end) from the fluorophore (Figure 2.3). The amplitude of the intensity shift effectively decreased as the distance between the dye and the first base pair increased. As this distance n increased, we observed positive or negative fluorescence intensity shifts depending on the

nature of the dye's nearest base pair (i.e. the terminal base pair). The intensity shift was positive for a terminal A-T, and negative for a terminal C-G base pair. Using the same assay, this trend was confirmed on another sequence (Supplementary Figure 2.6). Following this observation, we could very clearly discern a signal oligonucleotide hybridized at position n=0 (negative shift) from one located a single base away, at position n=1 (positive shift).

We also explored the case of an imperfect match between the template and the 5' end of the signal molecule. As can be seen in Figure 2.3 (red marks), the fluorescence change still primarily depends on the base pair nearest to the fluorophore. Only A-A and G-G mismatches appeared to depart from this rule, with no obvious rationale.

From n=6 to n=11, we observed weak and position- independent fluorescence intensity shifts. We tentatively attribute this to the rigidification of the DNA coil. Our target implementation (described below) only requires distinction between signal molecules that hybridize at the 3' end of the template from those that hybridize 11 bases away. In this configuration, N-quenching provides a reliable sequence- specific monitoring technique.

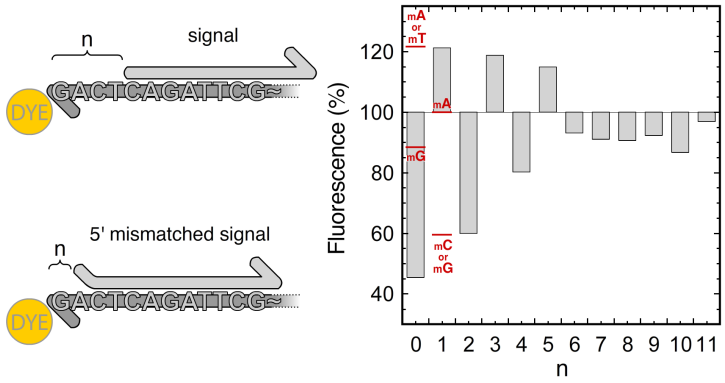

Figure 2.3: Fluorescence intensity shift upon hybridization of a signal oligonucleotide moved from n=0 to n=11 bases away from the template 3'-terminal dye. Red marks show the fluorescence intensities for a signal oligonucleotide hybridizing with a single 5' mismatch (mA, mT, mC or mG). Fluorescence intensity is expressed as a percentage of the fluorescence of the TAMRA-labeled template put alone in solution.

2.4.3 Monitoring an elementary DNA reaction circuit

We used N-quenching to monitor the evolution of an elementary DNA-based dynamic system encoding homeostasis. As shown on Figure 2.4, this network consists of one template 'A' that, in presence of a polymerase and a nicking enzyme, encodes for an autocatalytic amplification of its signal α. In

the additional presence of an exonuclease that specifically degrades signal molecules α [62], but not template A, this circuit becomes a dynamic, out-of-equilibrium system that possesses a single steady state: as long as dNTPs are available, the concentration of α will always evolve toward a given constant value.

To test N-quenching, template A was labeled at its 3' end with TAMRA, allowing us to monitor the concentration of α as it binds to the template. Hybridization of signal α (5'-CT-) on template A induces a quenching of TAMRA fluorescence. Therefore, the template itself becomes a probe for measuring the concentration of α. As a control, we simultaneously monitored the reaction in the presence of an intercalating dye (EvaGreen) whose fluorescence increases when binding to double-stranded DNA. In Figure 2.4, we observe that, as expected, the concentration of α evolves towards a steady state: EvaGreen induced fluorescence increases, TAMRA fluorescence decreases and both eventually reach a plateau that corresponds to the steady state. In this assay, the fluorescence intensity shift observed with N-quenching has twice the amplitude observed for EvaGreen. Also, EvaGreen and N-quenching yielded fluorescent recordings with similar shapes, suggesting that dynamic DNA reaction circuits can be precisely monitored by using N-quenching only.

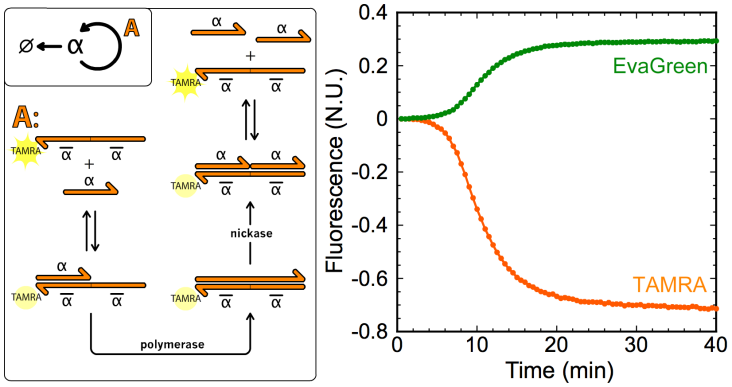

Figure 2.4: Monitoring an elementary DNA reaction circuit. (left) Template A encodes the autocatalytic amplification of signal α, and bears a TAMRA dye at its 3' end. As α hybridizes to the 3' end of template A, it gets elongated by a polymerase. The upper strand of the duplex is then cut in its middle by a nicking enzyme, and signal α and output α are released. The exonuclease specifically degrades single-stranded α. (right) The reaction is triggered with 0.1nM of α and is monitored with both EvaGreen intercalating dye and the 3'- terminal TAMRA of template A. EvaGreen fluorescence intensity increases as α-A duplexes are formed, and TAMRA fluorescence is quenched as α hybridizes to the 3'-end of A. Both fluorescence intensities are normalized with respect to the maximal shift of fluorescence intensity of EvaGreen for the reaction where the TAMRA modification of template A is replaced by a phosphate.

2.4.4 Monitoring a DNA-based oscillator

N-quenching was then used to study a network containing more than one dynamic species. We previously reported a DNA-based oscillator [62] that uses the same enzymes cocktail but is encoded in the sequences of three templates (Figure 2.5). Template A activates the autocatalytic production of signal molecule α. Template α*to*β receives α as input, activating the production of β. Finally, template β*to*iα receives β as input, activating the production of iα. iα closes the negative feedback loop: it inhibits α production by blocking the activity of template A. Overall, this chain of reactions produces oscillations of the three signal molecules α, β and iα.

When this reaction circuit is monitored with EvaGreen as previously reported [62], one obtains real time, but non- specific information about the total amount of duplex DNA in the system. In fact, in this case, EvaGreen fluorescence is mainly induced by iα [62], which mostly prevents the observation of α and β. However, because oscillations are produced by the interplay of the 3 dynamic species, a complete characterization requires individual tracking of α and β concentrations as well. This information is readily obtained using N-quenching: we respectively labeled α*to*β and β*to*iα 3' ends with TAMRA and Alexa Fluor 594, which enabled sequence-specific observation of both α and β. Sequences of α (5'-CTGA-) and β (5'-GAGA-) produced a negative shift of fluorescence intensity upon hybridization (with formation of a terminal C-G base pair). With these two labeled oligonucleotides, we could directly observe the phase shifts between α, β and iα concentration peaks: as expected from the structure of the network, peak of α came first, followed by β and then iα, before the cycle started again. Using N-quenching, we could also extract quantitative information about the concentrations of α and β throughout the reaction. To do so, we built calibration curves for α*to*β and β*to*iα, showing their fluorescence intensity shift as a function of known concentrations of respectively α and β. By comparison with these calibration curves, we found that α and β concentrations do not exceed 30nM and 55nM, respectively, at their peak concentration (see Section 2.7.5 for more details). Also, assuming a linear relationship between the quenching effect and the ratio of hybridized templates, we could deduce that less than 20% of α*to*β and 25% of β*to*iα are in double-strand form at the oscillation peaks.

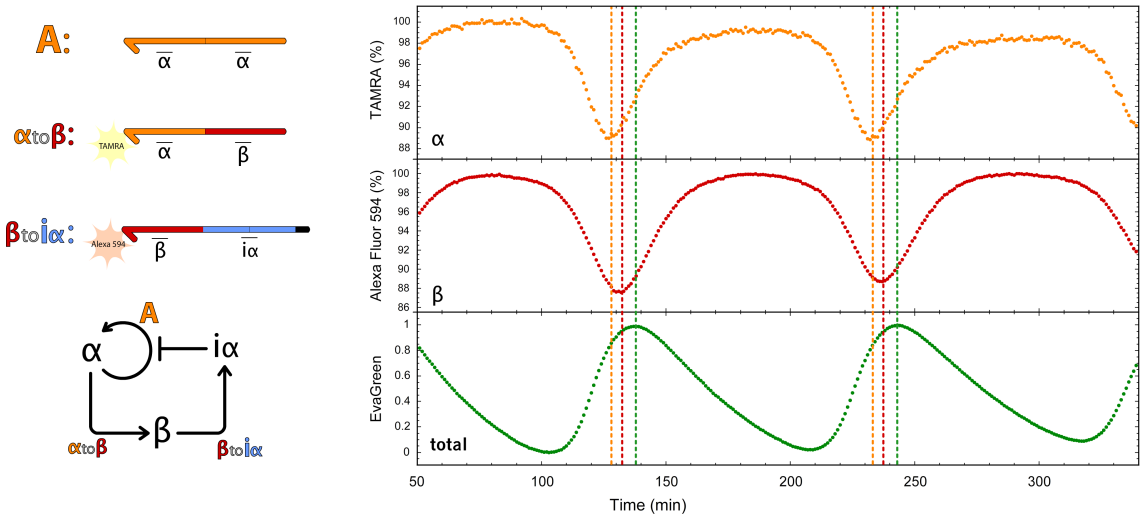

Figure 2.5: Multiplexed monitoring of a DNA-based oscillator. (left) 3-nodes oscillator network and sequence encoding. A is the autocatalytic module of Figure 3. The second template, α*to*β, receives α as input, produces β as output and is labeled in 3' with TAMRA. The third template, β*to*iα, receives β as input, produces iα as output and is labeled in 3' with Alexa Fluor 594. (right) Time evolution of the oscillator in three colors. α is seen with TAMRA, β with Alexa Fluor 594 and EvaGreen shows the total duplex concentration, roughly corresponding to iα concentration [62]. Fluorescence of TAMRA and Alexa Fluor 594 is expressed as a percentage of their respective unquenched fluorescence. Fluorescence of EvaGreen is normalized at 1 for the highest and 0 for the lowest fluorescence intensity. Vertical lines show the peak of each species concentration.

2.5 Discussion

2.5.1 N-quenching sensitivity and quantitative measurement

Using N-quenching, dynamic DNA reaction circuits can be monitored by simply labeling sequences of interest with a single fluorophore. Even though the shifts in fluorescence intensity (up to -50%/+80%) are not as high as those obtained by using donor/acceptor pairs of fluorophores (almost 100% quenching for some donor/acceptor pairs), they were sufficient to observe reactions on 20 or 40µL volumes using a conventional real-time thermocycler (the signal-to-noise ratio in the experiment of Figure 2.1 is approximately 250). In the case of the simple DNA reaction circuit of Figure 2.4, the relative fluorescence intensity shift produced by a 11- bases long oligonucleotide with TAMRA was higher than the one obtained with EvaGreen. One may remark that in these conditions, the fluorescence of EvaGreen is partially quenched by TAMRA [120]. Still, the shift of TAMRA fluorescence intensity is comparable to the one of EvaGreen, using a non- labeled template. This result might be explained by the weak affinity of EvaGreen for short double-stranded DNA [104], and the fact that EvaGreen fluorescence intensity depends on the number of paired bases. Thus, in the case of short DNA strands - here, 11

bases - the sensitivity of N-quenching is comparable to that of EvaGreen intercalating dye. When it comes to monitoring hybridization of strands even shorter than 11 bases, the relative sensitivity should be even greater.

N-quenching allows quantitative measurement of dynamically changing concentrations of target signal molecules. Under the current conditions, we could quantify target signal molecules in concentrations ranging from a few nM up to several hundreds of nM. Because the working temperature is higher than the melting temperature of the target signal molecules, it is possible to quantify concentrations of signal molecule higher than the concentration of labeled template. Moreover, even without calibration, it is possible to quantify the concentration of hybridized template by comparison with the fluorescence of the unoccupied (or saturated) template.

2.5.2 Non-invasive monitoring

In our specific application, single fluorophores are directly attached to the template oligonucleotides that encode the DNA reaction circuit. This way, N-quenching is implemented directly on the circuit rather than being a probe added to the system. Therefore, our expectation was that N-quenching would not significantly interfere with the thermodynamics and kinetics of the system itself.

On the contrary, several studies have reported strong duplex stabilizing effects for donor/acceptor pairs of modifications [111, 112, 121]. For example, Moreira *et al.* [121] reported that, for dual labeled oligonucleotide probes, the presence of the two fluorescent modifications increased the melting temperature of the probe by up to 4.3 °C. In the case of two complementary strands bearing a 5'-terminal donor for one and a 3'-terminal acceptor for the other, an increase of the T_m of the duplex of up to 10 °C was reported [112]. Such thermodynamic alterations are enough to disrupt the functioning of DNA reaction circuits (19). Moreover, these effects are difficult to predict computationally, and may depend on a variety of factors [112]. Therefore, specific strategies need to be devised to circumvent this issue: for example, DNA strand displacement reactions usually use a separate 'probe' complex rather than directly labeling the sequences of interest [32, 31, 19].

By comparison, the maximal Tm increase found for a single 5'-terminal fluorophore was of only 1.6 °C for Cy3 and Cy5 dyes [121]. Compared to monitoring techniques that use pairs of donor/acceptor, the stabilizing effect of a single fluorophore is much lower and less disruptive; however, it should be considered when using N-quenching. In our case, whereas the single fluorophore labeling had quantitative effects on the system, it did not modify its global kinetics: oscillations were obtained both

with or without the fluorescent modifications.

2.5.3 N-quenching as a general method to monitor position-specific hybridization

Some fluorophores exhibited greater fluorescence intensity shifts than others, and some did not show any change in fluorescence upon hybridization, following the trend previously reported [114, 119]. Among the fluorophores we tested, N-quenching worked well for FAM, JOE, TAMRA Alexa Fluor 594, DY-530, DY-636 and DY-681. On the other hand, TEX 615, Atto 633 and Cy5 did not exhibit fluorescence intensity shifts upon hybridization, and were consequently not used for N-quenching (data not shown). The attachment chemistry of the fluorophore also affects the efficiency of N- quenching: for a given sequence, TAMRA exhibited a larger fluorescence intensity shift when conjugated through NHS ester than when attached with a C6 spacer.

In contrast to other quenching methods, the fluorescence intensity shift can be either positive (terminal base pair C-G) or negative (terminal base pair A-T). By tuning the terminal nucleotides, it is possible to distinguish a signal molecule binding adjacently to the quencher from signal molecules binding one or more bases away. This unambiguous detection could be used to cheaply distinguish SNPs (single nucleotide polymorphisms) [122]. It may also be used to distinguish invading strands [9] whose toeholds differ by as little as one nucleotide.

In this work, we devised a monitoring technique that relies on a single fluorophore labeling and quenching by nucleobases. We demonstrated the efficiency of N-quenching by monitoring the hybridization and melting of 11-bases long oligonucleotides in a sequence-specific manner. The sensitivity of N-quenching is lower than that of fluorescent monitoring techniques based on donor/acceptor pairs of fluorophores. However, we showed that it is sufficient to detect nanomolar concentrations of short oligonucleotides in microliter-scale volumes. N-quenching can be easily implemented to dynamic DNA reaction circuits and used to deduce rich quantitative information about the dynamics of the system. Also, by tuning the fluorophore's nearest nucleotides, it is possible to obtain unambiguous position information about the incoming signal oligonucleotide. Moreover, using a single fluorophore is cheaper than using a pair of fluorophore and quencher, and also has a lower impact on DNA kinetics and thermodynamics. Therefore N-quenching should be widely implementable to other DNA-based systems.

2.6 Supplementary Information

On the experiment of Figure 2.3, we observed a pattern of alternating negative and positive changes of fluorescence as the signal molecule was shifted away from the template's 3' fluorophore. This pattern is consistent with the trend observed for signal oligonucleotides hybridizing next to the fluorophore (blunt end): decrease of fluorescence for a terminal C-G and increase of fluorescence for a terminal A-T base-pair. Therefore we may conclude that the unpaired bases in-between the dye and the closest base-pair have only a secondary effect on the quenching.

However, to check unambiguously this result, we performed another experiment with a different sequence. This was done using the same assay as the experiment of Figure 2.3, but with another signal oligonucleotide whose sequence displayed a different alternation of A-T and C-G bases. Supplementary Figure 2.6 shows the results of this experiment: the direction of the fluorescence intensity shifts is not regularly alternated anymore, but follows the pattern of A or T versus G or C in the sequence. As in Figure 3, the shift intensity gradually decreases as the distance increases.

This confirms that as the signal molecule is shifted away from the fluorophore, the fluorescence change upon hybridization still depends on the nature of the fluorophore's nearest base-pair: decrease of fluorescence for a terminal C-G and increase of fluorescence for a terminal A-T.

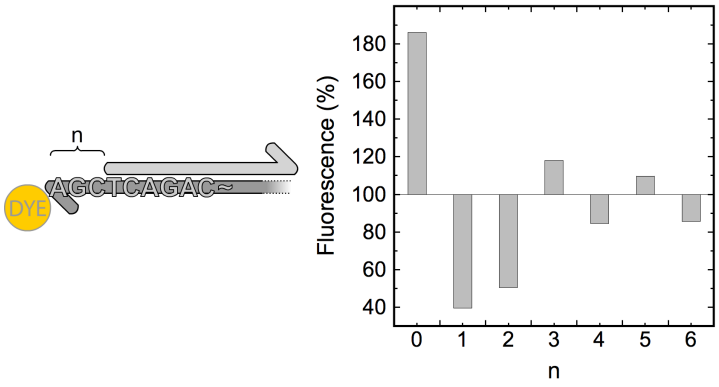

Figure 2.6: Fluorescence intensity shift upon hybridization of a signal oligonucleotide moved from n=0 to n=6 bases away from the template 3'-terminal dye. Fluorescence intensity is expressed as a percentage of the fluorescence of the TAMRA-labeled template put alone in solution. The full sequence of the labeled template is 5'- TTACTCAGCCAAGACAACAGACTCGA-3', with a 3'-terminal TAMRA NHS ester modification.

2.7 Additional results

2.7.1 C11bt Oligator

In this chapter, we worked with an Oligator made of sequences different from the ones used by Montagne *et al.* [62]. The present oligator is based on an autocatalytic module called "C11bt" (hence "C11bt Oligator"), amplifying the input called "T11bt" which was designed with a low melting temperature (33.1 °C against 39.5 °C for "T11" of the original Oligator [62], hence the "bt" that stands for "low temperature" in French). With this low T_m, we were expecting it to have the potential of oscillating faster than the original Oligator. Or at least be able to oscillate at lower temperature, where $RecJ_f$ would be more stable. In practice, C11bt oscillator could run at descent speed at 37 °C (showing periods of about 70 minutes). However, we weren't able to make it run faster than the original Oligator. Figure 2.7 shows a collection of combinations of concentrations of C11bt and I11bt*to*inhT11bt.

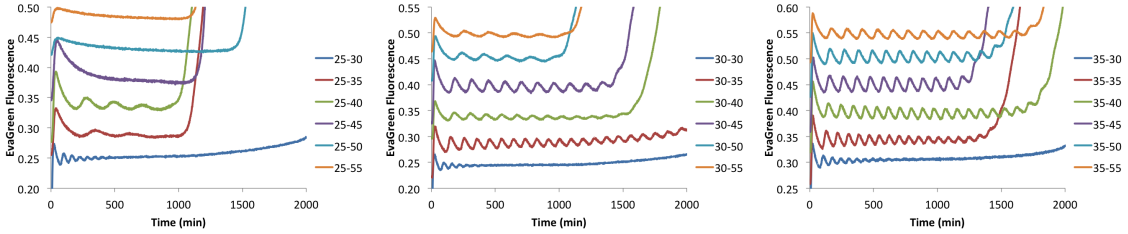

Figure 2.7: C11bt Oligator for various combinations of [C11bt]-[I11bt*to*inhT11bt] (in nM), with a fixed [T11bt*to*I11bt] = 5 nM. Reactions are performed at 38 °C.

The C11bt Oligator is constituted of sequences that do not present any cross-talks with the original Oligator, suggesting that they could potentially be run in the same tube. Due to their difference of design, these two Oligators were originally optimized for very different enzymatic conditions, at different temperatures: finding conditions that would fit both of them required much tuning effort. We eventually managed to get them running together (Figure 2.8), monitoring the reactions with EvaGreen. The resulting fluorescence time plot was not a simple sum of both oscillator running separately, which suggested some complex couplings that may occur - for instance - through competition for enzymatic resources [59]. Unfortunately, this work was done before the completion of N-quenching, which would have provided us with precious hints about the coupling between these two Oligators.

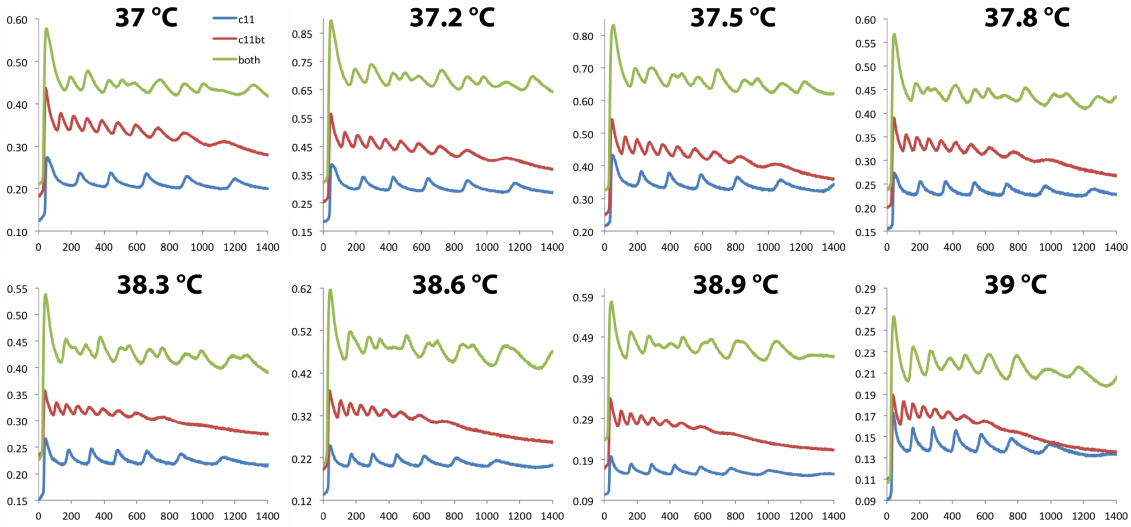

Figure 2.8: Two oligators in the same tube. Fluorescence time plots of EvaGreen, for the original oligator (C11, blue curves), the C11bt oligator (red curves) and the two ran in the same tube (green curves). Time is in minute. Concentrations are as follows (in nM): [C11] = 30, [T11*to*I11] = 5, [I11*to*inhT11] = 30 and [C11bt] = 35, [T11bt*to*I11bt] = 5, [I11bt*to*inh11bt] = 40.

2.7.2 Impact of a single fluorophore on the production of inhibitor

It is known that the melting temperature (T_m) of an oligonucleotide having a 3' and / or 5' fluorophore modification is increased compared to the same unmodified oligonucleotide [112, 121]. Such alteration of duplex stability is likely to hinder the functioning of our reaction circuits. Also, each internal, 5' or 3' modification possibly impacts the way the enzymes recognize and work on the DNA strand. We consequently checked the impact of two different fluorophores (Tamra and Tye665) positioned at the 3' end of separate inhibition modules (respectively T*to*inhV and V*to*inhT) on the linear production of inhibitor (Figure 2.9-A). In the absence of exonuclease, we used EvaGreen intercalating dye to monitor the single stranded inhibitor linearly produced by *Bst* polymerase and NBI nicking enzyme (for a limited concentration of input), and compared the slopes for modified versus unmodifed template (Figure 2.9-B). The amplification occurs in two steps: the first is characterized by a rapid increase of EvaGreen fluorescence that corresponds to the formation of duplex including the inhibition module. The second step corresponds to the accumulation of single-stranded inhibitor, during which the polymerase works in strand-displacement. We will compare the slopes of this second step, because in a running circuit, we expect the inhibition modules to mostly produce inhibitors in strand-displacement. For T*to*inhV with Tamra modification, we found a slope 53% higher than that of the unmodified template. For V*to*inhT with Tye665 modification, we found a slope 80% higher than that of the unmodified template.

These results confirm that the presence of the fluorophore has an impact on the reactions, by probably stabilizing the input on its template, or affecting its recognition by the the enzymes. This impact may seem huge; however, it can be compensated by simply decreasing the concentration of corresponding template. Also, if the labeling or not is determined before starting to assemble a circuit, the involved impact will just be smothered, for that the concerned module will be used as it is. However, one may be careful when changing a labeled module for an unlabeled one (and conversely) in an already assembled circuit: in this case, an adjustment of its concentration may be needed.

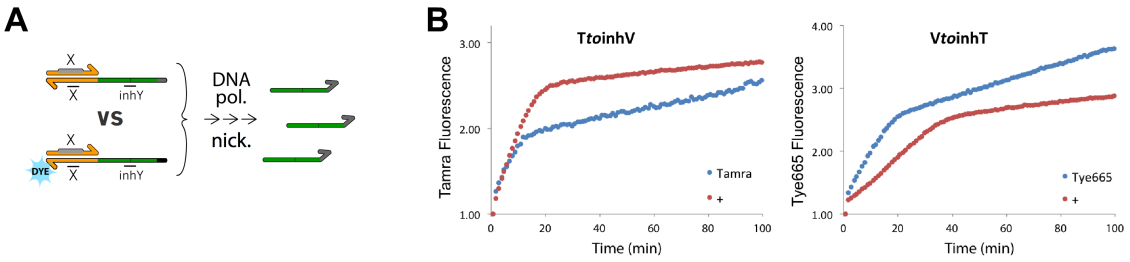

Figure 2.9: Labeled VS unlabeled inhibition module. (A) We compare the production of inhibitor by a "simple" inhibition module versus a labeled one. (B) Inhibition modules (60 nM) are put in presence of 20 nM of input. In the absence of exonuclease, there is a first step of production with a rapid increase of fluorescence corresponding to formation of stable duplex "inhibition module : inhibitor" followed by a second step (slow increase of fluorescence) where the polymerase works in strand-displacement: using EvaGreen, we can observe the accumulation of single stranded inhibitor in solution.

2.7.3 Indirect monitoring using N-quenching

2.7.3.1 Reporting module: design & test

Having observed that the presence of a 3' end fluorophore impacted the activity of the template on which it is attached, we searched for a more indirect way to use N-quenching. That is, deporting the fluorophore on a separate species that would not interfere with the primary function of the monitored input strand. We thought that this would be an elegant method to monitor the components of the reaction circuit without *a priori* affecting its kinetics. This "reporting module" could be connected to any input molecule of the circuit, and report about it in a sequence-specific manner (Figure 2.10).

Experimentally, the reporting module needs to meet several requirements: one has to find a compromise between the intensity of the fluorescent signal and time-responsiveness (Figure 2.11): at the working temperature, if reporting strand *rep* is too short (i.e. not stable on R), no significant fluorescent signal will be induced, whereas if *rep* is too stable on R, time-responsiveness will be lost (*rep* will stay hybridized long after the target molecule will have vanished). Also, one has to consider the load

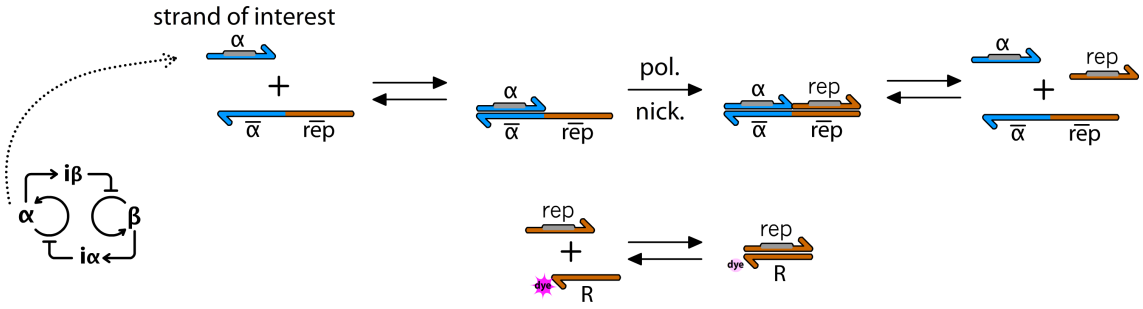

Figure 2.10: (Up) The reporting module receives target input α and produces *rep*. (Bottom) *rep* hybridizes to template R that is labeled with a 3' fluorophore. This results in a change of fluorescence intensity, reflecting the presence of α. By changing only the template α*to*rep (to a template X*to*rep), it is possible to connect the reporting module to another target input (X).

effect [71] on the reported system (see Section 4.7.2 for more details): in the example of Figure 2.10, template α*to*rep will sequester some α, that consequently cannot play its role in the monitored reaction circuit. Thus, the concentration of α*to*rep should be kept low in order to not impact significantly the functioning of the reaction circuit under scrutiny. The presence of the reporting module represents more DNA substrates for the enzymes to work on, which could lead to their saturation more easily.

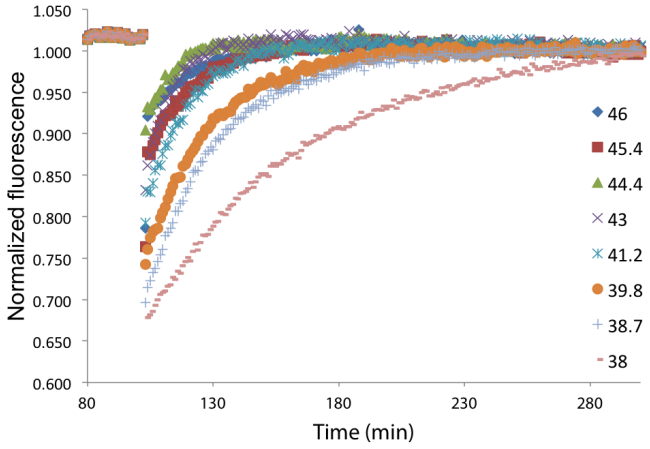

Figure 2.11: Fluorescence change (quenching) of the TAMRA label of template R (60 nM) upon injection of complementary strand rep (100 nM), for temperatures ranging from 38 °C to 46 °C. At high temperature, the injection of *rep* does not induce a big fluorescence change. At low temperature, the fluorescence takes a long time to get back to its initial level. Sequence of R is as follows: 5'-A*G*T*T*CTAGTGTGTC-3'-FAM. Duplex rep:R has a predicted (Dinamelt) T_m of 44.2 °C in the conditions of this experiment.

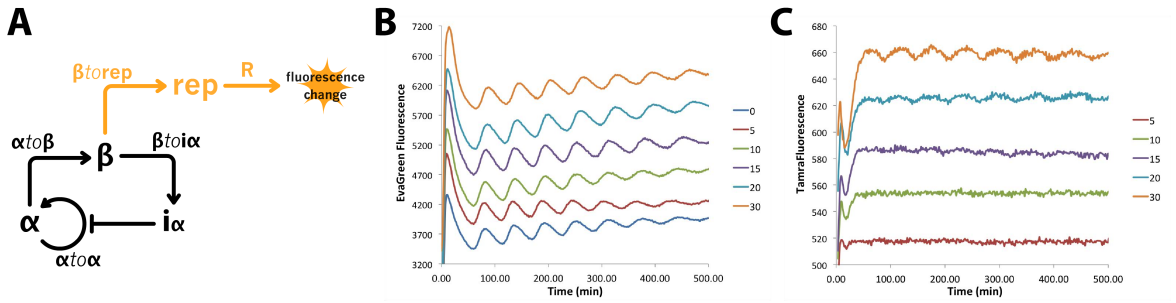

Figure 2.12: Reporting module plugged to the C11bt oligator. (A) Circuit of the oligator (in black) and plugged reporting module (in orange). (B) Fluorescence time plots of EvaGreen intercalating dye for a ramp β*to*rep (0 to 30 nM) and (C) corresponding time plots of Tamra. Curves are offsetted for visibility. The experiment was run at 38.5 °C, with concentrations of templates as follows: α*to*α = 30 nM, α*to*β = 5 nM, β*to*iα = 35 nM and R = 30 nM. Sequence of R is 5'-C*A*A*GTCACATGG-3'-TAMRA. Duplex r:R has a predicted (Dinamelt) T_m of 40.3 °C.

2.7.3.2 Reporting module: use with an oligator

Following the results of Figure 2.11, we designed a new reporting module targeted at the working temperature of the C11bt oligator (38.5 °C). By plugging it to the oligator (Figure 2.12-left), we succeeded in monitoring the oscillating reaction (Figure 2.12-right). Even though the reporting module worked, it only produced a low fluorescent signal. Interestingly, increasing the concentration of β*to*rep seemed to stabilize the oscillations: this may be explained by the fact that β*to*rep slows down (i.e. delays further) the negative feedback loop, which is known to increase the robustness of the oscillations [123] - at the cost of the speed.

Note that the reporting module induces a delay between the monitored fluorescent signal and the actual concentration of target molecule, which potentially makes the analysis more complex. Also, the reporting module appeared to actually - indirectly - have an impact on the kinetics of the reaction circuit under scrutiny - here, seemingly increasing the robustness of the oscillations. We consequently turned toward the simple labeling of the templates with a single fluorophore, allowing a direct monitoring of the target input. Doing so has an impact on the hybridization and kinetics of the corresponding template: however, this impact is still low enough to not disrupt the functioning of the reaction circuits, given some adjustments of the template concentrations. We took this as part of the DNA-toolbox, in which we have many other handles to counterbalance the effect of a single fluorescent modification: for instance, one can decrease the concentration of labeled template if this one seems to be more "active" than the one without fluorescent modification.

2.7.4 Tracking inhibitors with N-quenching

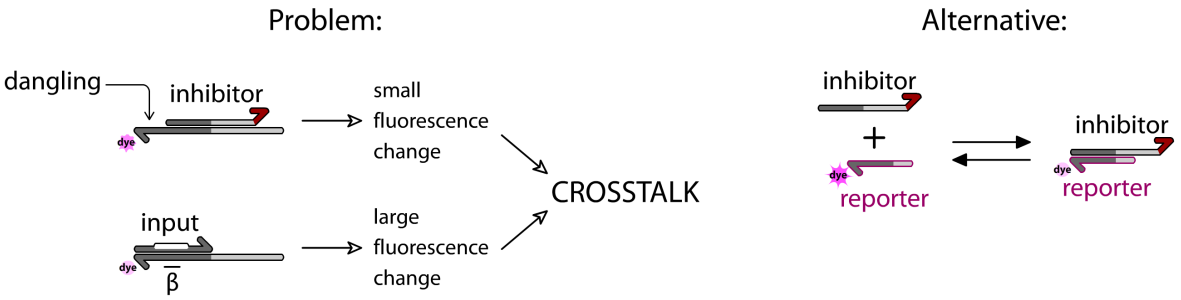

Figure 2.13: (Left) When hybridizing to its template, the input induces a larger fluorescence change than the inhibitor. For this reason, inhibitor strand cannot be directly observed. (Right) A potential solution would be to use a "reporter" of the inhibitor. The reporter is a short DNA strand with a 3'-end fluorophore, that dynamically hybridizes to the inhibitor, inducing a shift of fluorescence intensity. The reporter is designed with in mind to not disturb the circuit functioning: it is shorter than the inhibitor and possibly has mismatches, in order to lower its melting temperature.

In the context of the DNA-toolbox, N-quenching can be efficiently used to monitor the hybridization of input oligonucleotides. However, inhibitors cannot be directly monitored: in fact, inhibitors hybridize in the middle of autocatalytic (or activation) templates, usually leaving the template with a 4-bases dangling 3' end. One might want to label the autocatalytic module in order to monitor its input, but this reveals another problem: the inhibitor hybridizes close enough to the 3'-end fluorophore to induce a fluorescence change (see Figure 2.3), cross-talking with the fluorescence change induced by the template's input (Figure 2.13-left).

In order to specifically monitor the inhibitors, we designed a simple reporter that takes the form of a short strand with a 3' fluorophore (Figure 2.13-right). This reporter is shorter than the inhibitor: in this configuration, the inhibitor has a higher affinity for its target template than for the reporter. This is important to not distract too much the inhibitor from its role in the circuit. Using this method, we could successfully observe the oscillations of inhibitor strand in the C11bt oligator (Figure 2.14). However, the presence of the reporter had an impact on the functioning of the oligator, slowing down its oscillations. Still, this technique stands as our only method to directly monitor the inhibitor, for which the reporting module presented in the previous section could not be used - because the inhibitor doesn't have the nickase recognition site, thus cannot trigger the production of another strand.

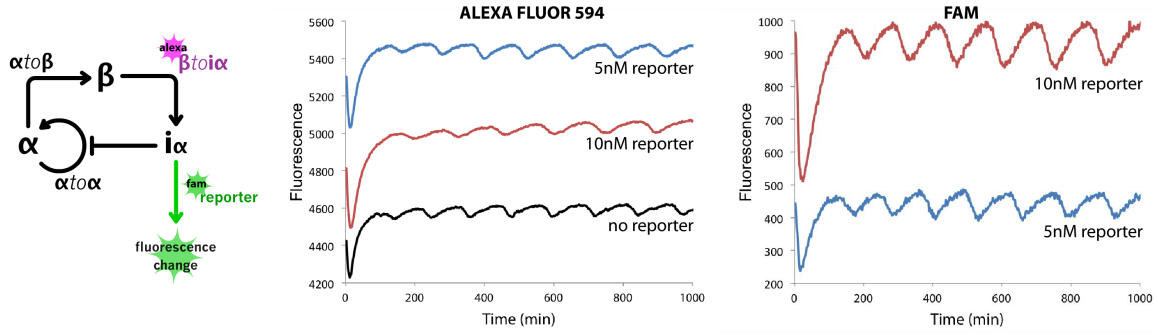

Figure 2.14: Monitoring C11bt oligator with the reporter of inhibitor. (Left) Circuit of the oligator. β*to*iα is labeled with Alexa Fluor 594, thus reporting the presence of β. iα can hybridize to the reporter, which is labeled with FAM. (Middle) Looking at the Alexa channel: the presence of increasing concentration of reporter seems to slow down the oligator (period = 113 min with reporter, 122 with 5 nM and 148 with 10 nM of reporter). (Right) Looking at the FAM channel: the reporter successfully reports on the presence of inhibitor iα. The experiment was run without EvaGreen, at 37.5 °C, and with α*to*α = 30 nM, α*to*β = 3 nM and β*to*iα = 30 nM. Duplex iα:reporter has a predicted T_m of 39.3 °C, to be compared with 46.7 °C for α*to*α-iα. The sequence of reporter is as follows: 5'-C*T*C*AGCTTAGAC-3'-FAM.

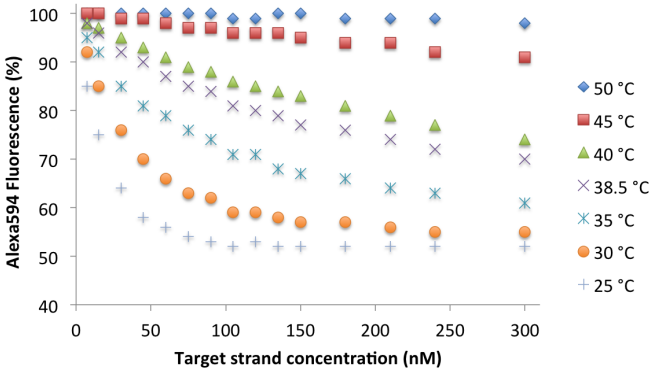

Figure 2.15: Calibration curves of N-quenching for 20 nM of β*to*iα labeled with Alexa 594.

2.7.5 Quantification with N-quenching: calibration curves

When monitoring a reaction circuit with N-quenching, it is easy to get quantitative information about the ratio of hybridized templates if we assume a linear relationship with the quenching effect. Getting further quantitative information, that is, about the actual total concentration of target input in solution, requires to calibrate N-quenching for the reaction conditions (temperature, buffer and concentration of labeled template). Figure 2.15 shows such calibration curves for template β*to*iα at different temperatures. At low temperatures, the fluorescence intensity shift quickly saturates, preventing the quantification of high concentrations of target input. Working at higher temperature allows to mea-

sure concentrations of more than 10 times the concentration of template $\beta to i\alpha$, at the cost of a loss of sensitivity.

2.7.6 Fluorophores tested with N-quenching

As noted in Section 2.5.3, while some fluorophores worked well with N-quenching, some others did not show any change in fluorescence intensity upon hybridization. Table 2.1 recapitulates the tested fluorophores. It is possible to find fluorophores working at any desired emission.

Fluorophore	N-quenching	Excitation/Emission (nm)
FAM	good	494/520
JOE	good	520/548
DY-523XL	good	523/668
DY-530	good	539/561
TAMRA	good	546/576
ROX	intermediate	574/602
Alexa Fluor 594	good	590/617
TEX 615	bad	596/613
Atto 633	bad	629/657
DY-631	intermediate	637/658
TYE 665	bad	645/665
DY-636	good	647/671
Cy5	bad	649/670
DY-681	good	691/708

Table 2.1: N-quenching performance of a few fluorophores. Fluorophores indicated as "good" showed a shift of fluorescence intensity upon hybridization of more than 25 %. The ones indicated as "intermediate" were below 25 %. Fluorophores that showed none or barely no change in fluorescence upon hybridization are indicated as "bad".

Chapter 3

In vitro switchable memories

In the cell, memory is kept by various mechanisms, with bistability potentially being one of the most robust of them [124, 125, 126]. Bistability and oscillations are also believed to be the two major building blocks of the complex networks that carry cellular information processing [127]. In a more general vision, bistability seems to be at the basis of the dynamic behaviors of many non-linear chemical systems, including oscillators [128]. With N-quenching and the three modules of the DNA-toolbox (Figure 1.8) in hands, we tackled this family of memory functions. In the work below, we focused on switchable bistable memory reaction circuits in the context of the DNA-toolbox, and constructed three successive circuits of increasing complexity. In this way, we explored the implementation of relatively large scale dynamic circuits, culminating with a 8-modules circuit encoding for a 1-bit counter. This work was published as: Adrien Padirac, Teruo Fujii, and Yannick Rondelez. Bottom-up construction of in vitro switchable memories in *Proceedings of the National Academy of Sciences*.

3.1 Abstract

Reaction networks displaying bistability provide a chemical mechanism for long-term memory storage in cells, as exemplified by many epigenetic switches. These biological systems are not only bistable, but also switchable, in the sense that they can be flipped from one state to the other by application of specific molecular stimuli. We have reproduced such functions through the rational assembly of dynamic reaction networks based on basic DNA biochemistry. Rather than rewiring genetic systems as synthetic biology does in vivo, our strategy consists in building simplified dynamical analogs in

vitro, in an artificial, well controlled milieu. We report successively a bistable system, a two-input switchable memory element, and a single-input push-push memory circuit. These results suggest that it is possible to build complex time-responsive molecular circuits, by following a modular approach to the design of dynamic in vitro behaviors. Our approach thus provides an unmatched opportunity to study topology/function relationships within dynamic reaction networks.

3.2 Introduction

Cellular information processing relies on dynamic networks of biochemical reactions [45]. For example, genes and their products regulate each other in intricate assemblies that embrace numbers of components and interactions. The function of these assemblies, i.e. the computation that they perform at the molecular level, is encoded both in the structure and in the physical characteristics of the web of chemical interactions that links their components. These in vivo networks are often difficult to identify in their entirety. Indeed, a complete description requires *(i)* a detailed analysis of the macroscopic dynamic behavior, *(ii)* a molecular understanding of the structure of the underlying biological network sustaining the function and *(iii)* a chemical (thermodynamic and kinetic) knowledge of the reactions at hand. For technical reasons, this information can be very hard to obtain, even in the simplest biological cases [129, 130, 47, 48].

Rather than attempting a systematic analysis of natural reaction networks, synthetic biology harnesses cells as a receptacle –the hardware– to implement artificially designed networks [52, 53]. These networks are typically engineered through the recycling of original biological parts, their modification and their reassembly in non-natural architectures, which endow cells with additional functions [49, 50]. This strategy aims at understanding the cell regulatory processes through a bottom-up approach, which is expected to reveal the underlying design rules [51]. In this way, small scale circuits encoding elementary functions such as cascades [54], counters [131], bistability [53, 56, 55, 57] or oscillations [52, 55] have successfully been engineered.

The richness of the cell's inner biochemistry provides a platform that theoretically allows the engineering of an infinity of increasingly complex synthetic networks [132]. It also poses formidable challenges to a rational designer. In practice, only small synthetic networks (compared to their natural models) have been reported [133]. One reason is that synthetic biologists face a shortage of known interoperable units [133, 134]. Also, harnessing the cell's machinery is a complex task: nonlinear effects [51, 59, 58] and unintended interactions between the synthetic circuit and the host housekeeping

functions [60] are frequent and difficult to pinpoint. Moreover, the lack of quantitative knowledge of in vivo processes strongly constrains the predictive power of the in silico models used in the design process [132, 134].

Engineering analogs of gene networks out of the cell, in purposely created and better controlled in vitro environments, provides an attractive alternative [61, 62, 66, 38]. Going cell-free offers a better control of the system parameters, minimizes unintended couplings and allows easier quantitative analysis [67]. Like in vivo gene networks, in vitro analogs are constructed from elementary units, but this time, one is freed from the constraints of the cellular machinery: various, possibly simpler chemistries can be used; toxicity and host interference disappear and stochastic effects can be handled. Still, in analogy with synthetic biology, it is possible to build basic functions like oscillators [62, 63], bistable systems [61, 70] or logic gates [40, 27] through a rational bottom-up strategy. The expectation is that it will be possible to assemble these elementary modules in a wealth of large-scale circuits [31, 135], potentially with life-like behaviors [136].

This paper focuses on in vitro reaction circuits encoding memory functions. In the context of biological circuits, memory refers to the ability to integrate a transient molecular stimulus into a sustained molecular response [137]. In most cases, this information is digitized into a small number of alternative states, which correspond to the multiple steady states of a dynamic chemical system. In the cell, various mechanisms exist to keep memory of an event. Slowly changing protein levels can result in memory-like behaviors transmitted over a few cell generations [138]. Phage-like genetic recombination can be used to reversibly switch one bit of information on the DNA of engineered cells [139], making a passive data storage that can be passed down through generations. Epigenetic switches use bistability to carry a robust, heritable memory [124, 125, 126]. Other bistable switches naturally occur in gene networks, and play important roles in fundamental cell functions [130, 47], cell cycle [129, 140], cell commitment [48, 141] and signal transduction pathways [142].

Such biological memories based on multistability, also require the interfacing with upstream and downstream molecular processes. This includes in particular the ability, given the correct stimuli, to toggle reversibly and sensitively between the reciprocally exclusive stable states [47, 48]. From a chemical point of view, the memory function therefore incorporates a form of antagonism. On the one hand, robust information storage imposes stability against molecular perturbations or noise but, on the other hand, the function also requires a sensitive mechanism to integrate environmental information and – if appropriate – update its state. Synthetic bistable switches constructed so far in vivo have

not yet solved this dilemma: the host cells are typically forced on one state by exposition to strong inducer drugs for the whole switching time [53, 56, 143]. Alternatively, non-molecular stimuli, such as temperature or light, are used. For example, Lou *et al.* [57] have recently reported a synthetic switchable "push-push" bistable circuit in which UV stimulation was used to switch the system back and forth between its two stable states. However, such systems that use non-molecular inputs cannot be cascaded, i.e. integrated in larger circuits. Additionally in this case, extreme photo-toxicity negatively impacts the host cells.

Because the alternative states of a bistable system are all equally stable over time, thermodynamics imposes that multistability is fundamentally an energy consuming, out-of-equilibrium process [144]: switching to the new state requires the complete disappearance or degradation of the constituents of the previous state. This poses a severe constraint for the design of in vitro analogs of biological memory circuits. Nevertheless, a couple of batch bistable systems [61, 70] have been reported, thanks to the use of an enzymatic sink to maintain the dynamic of the system. However, no attempt was made to switch these basic bistable networks after they first reached one of their steady states.

Herein, we use enzyme-catalyzed, DNA-based reactions [62] to rationally construct various in vitro memory circuits. We present a DNA-toolbox composed of 3 modules encoding elementary reactions: activation, autocatalysis and inhibition. These modules can be arbitrarily connected in circuits encoding desired behaviors (SI Appendix, Section 3.7.1). We use these modules to sequentially construct three dynamic reaction circuits implementing memory functions of increasing complexity.

We start with a foundational bistable switch circuit, which always reaches one out of only two possible steady states, depending on the initial conditions. This bistable switch is very robust to perturbation, and making it switchable requires a specific strategy. We use the modularity of the reactions to upgrade the bistable circuit to a two-input in vitro switchable memory circuit. This system comprises 6 modules, and is able to flip between two stable states upon administration of a small amount of the correct, exogenous input. Next, we construct and experimentally characterize a push-push memory circuit that accepts a single external input: depending on its present state, the same input flips it in one direction or the other. This push-push memory circuit culminates at 8 modules, showing the ability of the DNA-toolbox to serve as a tool to rationally construct scaled-up in vitro reaction circuits. All the experimental observations are rationalized by a quantitative mathematical analysis.

3.3 Materials and methods

3.3.1 Oligonucleotides

DNA oligonucleotides were purchased from either Integrated DNA Technologies (IDT, Coralville, IA, USA) or biomers.net (Ulm, Germany) with high performance liquid chromatography purification. All templates have three phosphorothioate backbone modifications at their 5' end to protect them from degradation by the exonuclease. Templates $\alpha to i\beta$ and $\beta to i\alpha$ are modified at their 3' end with respectively FAM and TAMRA NHS ester modification. All the other templates are phosphorylated at their 3' end to prevent any polymerization. Template sequences and concentrations are provided in SI Appendix, Section 3.7.2.3.

3.3.2 Reaction assembly

Reactions were assembled in a buffer containing 10 mM KCl, 10 mM $(NH_4)_2SO_4$, 50 mM NaCl, 2 mM $MgSO_4$, 45 mM Tris–HCl, 5 mM $MgCl_2$, 6 mM DTT, 2 µM Netropsin (Sigma Aldrich), 100 µg/ml bovine serum albumin (New England Biolabs), 0.1 % Synperonic F108 (Sigma-Aldrich) and dNTPs (200 µM each). Exonuclease ttRecJ was a kind gift from R. Masui and used at a concentration of 50 nM throughout this study. Unless otherwise specified, Bst DNA polymerase, large fragment (New England Biolabs) was used at a concentration of 25.6 units/ml. For the Nt.BstNBI nicking endonuclease (New England Biolabs), we noticed a large fluctuation in the activity from batch to batch, and consequently used the enzyme at a concentration ranging from 32 units/ml to 400 units/ml. Experimental adjustment of Nt.BstNBI concentration was done by comparing the activity of a new batch to the activity of the previous batch, by using the assay presented in SI Appendix, Figure 3.11.

Reactions were run at 42 °C (except otherwise specified) in a Bio-Rad iQ5 or CFX96 real-time thermocycler, in a 20 µL volume. Experiments for which the bistable circuit was flipped from one state to the other required administration of an external input (γ or δ), that was diluted in TE buffer and injected in a volume of 0.6 µL while the run was paused for a minimal period of time.

3.3.3 Fluorescence curve acquisition and normalization

Fluorescence cross-talk between FAM and TAMRA was removed by the Bio-Rad built-in thermocycler software. For the experiments requiring an injection of external input, instantaneous signal artifacts at the time of injection (e.g. due to a slight displacement of the tube or the production of bubbles during

mixing) were corrected to keep the curve continuity. "Charge levels" were normalized from fluorescence data: to the high plateau (ON state of the autocatalytic module; if unavailable, a reference tube with the same reacting mix set in the ON state was used) and low plateau (OFF state of the autocatalytic module; if unavailable, the reaction was ran until depletion of dNTPs, thus revealing the OFF state of the autocatalytic module).

3.3.4 Simulations

The simple model of the bistable reaction circuit was analytically analyzed using Mathematica (SI Appendix, Section 3.7.3.1). Detailed models of the bistable circuit, switchable memory and the push-push memory were done with a set of measured and predicted (DINAMelt) parameters, refined by fitting on the experimental curves of the switching memory, using Mathematica (SI Appendix, Section 3.7.3.4). The set of refined parameters was used for all other model predictions.

3.4 Results

3.4.1 DNA-toolbox: three basic modules

Our constructions are based on a stripped-down in vitro genetic machinery based on three enzymatic reactions [62] (Figure 3.1-A): short DNA signal molecules hybridize with stable DNA template molecules in a set of basic reactions that structures the topology of the reaction circuits. Templates are 22 or 26 bases single-stranded deoxy-oligonucleotides composed of a 3' input site and a 5' output site. Signal molecules come in two types: 11-bases long inputs activate templates; on the contrary, 15-bases long inhibitors block them. Reactions take place at a temperature (42 °C) where both inputs and inhibitors are dynamically hybridizing and separating. Note that the short length of the inputs (11 bases) limits the number of available sequences, but the construction of relatively large circuits is still possible (SI Appendix, Section 3.7.2.4).

Templates encode basic reactions following the pattern input -> input + output. When an input correctly hybridizes on the input site of a template, it is elongated by a DNA polymerase, leading to the double-stranded form of the template. Next, a nicking endonuclease nicks the new strand, so that input and output are released from the template. When free in solution, these short oligonucleotides can be degraded by ttRecJ, a single-strand-specific 5'->3' exonuclease [145, 146]. Templates are protected from degradation by a few phosphorothioate backbone modifications located at their 5' end

(SI, Section 3.7.2.2). If not degraded, the input can start another round of reaction, while the output can, for instance, play the role of input for a separate reaction encoded by another template. Templates are thus fully composable, and can be classified into the following three modules, depending on their input and output:

- Activation module if input $\neq$ output (α -> $\alpha + \beta$).
- Autocatalytic module if input = output (α -> $\alpha + \alpha$).
- Inhibition module if output = inhibitor (α -> α + inh).

Inhibitors are longer than inputs, hence more stable when fully hybridized. A given inhibitor targets a template and strongly binds to it, overlapping on the input and output sites of the template. An inhibitor noted iα will target the autocatalytic module αtoα and an inhibitor noted i$\alpha\beta$ will target the activation module αtoβ. Inhibitors do not have the recognition site for the nicking enzyme, hence cannot be cut (SI, Section 3.7.2.1 and 3.7.2.3). They also possess two mismatched bases in 3', which prevents the polymerase from extending them. Therefore, they are able to block the production of output by their target modules.

To observe the dynamics of these reactions, we use N-quenching [147], a versatile fluorescent technique for the monitoring of oligonucleotide hybridization: to follow a given input, the input site of the corresponding template is labeled in its 3' end with a single fluorophore. Hybridization of the corresponding input produces a change in the fluorescence level, whereas hybridization of the templates' output does not (Figure 3.1-B). Therefore, templates themselves serve as specific reporters of the presence of their inputs. This versatile technique eliminates the need for additional probes to monitor the system –which could in turn affect the function of the network through the load effect [71].

Using this toolbox, it is possible to build time-responsive DNA reaction circuits of various topologies, and follow in real time the behavior of some specific sequences within these dynamic systems. We demonstrate next the design and assembly of a bistable switch function.

3.4.2 Bistable switch: designing the reaction circuit

Bistability can be obtained from a variety of elementary motifs [148, 149], all including at least one positive feedback loop, but only a couple of basic designs do not require cooperative binding [150] (and SI Appendix, Section 3.7.3.2). We chose here a symmetrical design [53] where two autocatalytic modules negatively regulate one another: when one autocatalyst is active, it dynamically represses the

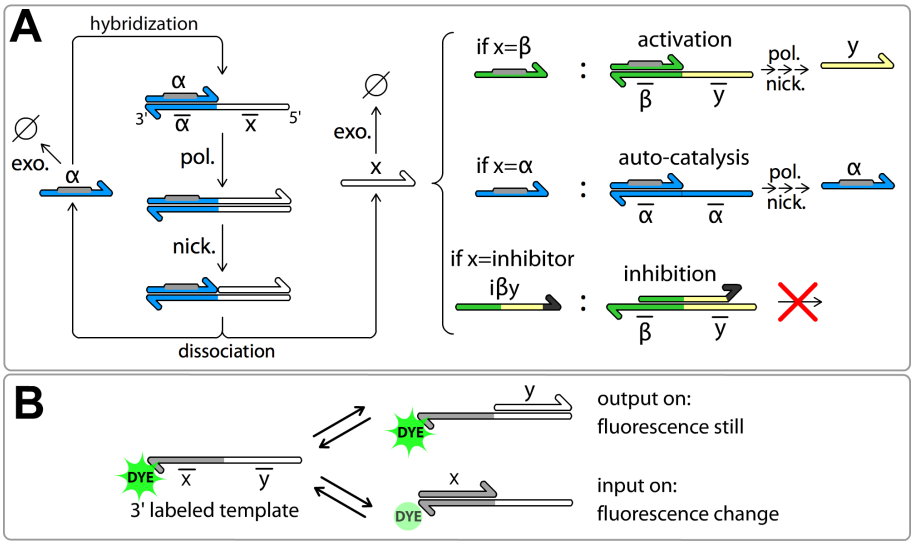

Figure 3.1: The DNA-toolbox uses DNA templates to shape the reaction network performed by a set of three enzymes. (A) Templates (bottom strands) have an input site (3') and an output site (5') and receive signal molecules (upper strands). When an input (α) hybridizes to a template, it is elongated by a DNA polymerase (pol.). Inputs bear the recognition site (in grey) of a nicking enzyme (nick.) that cuts the elongated upper strand between input and output. Input α and output x then dissociate and are free to start another reaction, or be degraded by a single-strand specific exonuclease (exo.). Following this scheme, three types of modules can be obtained depending on the output sites of the template. (B) Nucleobase quenching on the dye-labeled templates allows sequence-specific monitoring of the reactions.

activity of the other (Figure 3.2-A). Given this topology, we decided for two signal strands (α and β), and designed two templates (respectively α*to*α and β*to*β) responsible for their autocatalytic production. In between αtoα and β*to*β are two inhibition modules that encode the cross-inhibition function: inhibition module α*to*iβ takes α as input and produces iβ. It therefore inhibits the production of β when α is present; inhibition module β*to*iα does the opposite job. By combining the 4 templates α*to*α, β*to*β, α*to*iβ and β*to*iα in appropriate ratios and conditions, we expect a system featuring bistability, i.e. where either α or β, but not both, can exist at the steady state.

We started with the building of a simple model to first check the consistency of the design with a bistable function, when implemented within the toolbox. In this coarse-grained model, four equations express the life cycle (production and degradation) of the two inputs and two inhibitors (α, β, iα and iβ, see SI Appendix, Section 3.7.3.1 for details about the model construction). In order to easily find out the control parameters of this bistable circuit design, we put the model in a non-dimensional form (Figure 3.2-B) where productions of inputs and inhibitors are described by Michaelis-Menten equations with maximum rates (t_α, t_β, $t_{i\alpha}$, $t_{i\beta}$) controlled by the concentration of the template encoding the

corresponding reaction. Sequestering of templates by the inhibitors tends to decrease the production rate following a competitive mechanism (enzyme saturation, which would lead to cross coupling terms, is not considered in this simple model). Parameters λ define the relative strength of an inhibitor against the input it is competing with. Degradation is represented by a first order term, with the same degradation rate for all four species.

When looking for the stable equilibria in the $\{t_\alpha, t_\beta\}$ plane, the model suggests that the emergence of bistability is favored by high λ_α and λ_β (i.e. inhibitors stronger than inputs) (Figure 3.2-C). Experimentally, λ_α and λ_β can be adjusted by increasing the binding constants of iα and iβ (for example, making these inhibitors longer). In the case of a non-ideal system (e.g. non symmetrical λ_α and λ_β), the bistability domain in the $\{t_\alpha, t_\beta\}$ plane shrinks (Figure 3.2-D): to be bistable, the circuit needs to be adjusted by, for instance, changing the concentration of α*to*α and β*to*β. Figures 3.2-E & F show the basins of attraction of the two states A and B for an ideal and a non-ideal bistable circuit: for each combination of initial $\{\bar{\alpha}, \bar{\beta}\}$, the bistable circuit tends to one of the two states $\{\bar{\alpha}, \bar{\beta}\} = \{0, 1\}$ or $\{1, 0\}$. One notes that even in the cases where the system is bistable, the basins of attraction of the two states can be very asymmetric.

3.4.3 Experimental building of the bistable circuit

Given these theoretical considerations, we selected the sequences of α and β so that their predicted binding constants were close to each other at the working temperature. We then designed inhibitors so that their predicted binding constants were approximately two orders of magnitude higher than the ones of α and β, i.e. high enough to produce a large bistable state, but small enough to maintain a dynamic binding equilibrium with their target templates (this insures the responsiveness of the circuit). Templates α*to*iβ and β*to*iα are labeled at their 3' end with two different fluorophores (respectively Fam and Tamra), which allows specific and simultaneous monitoring of both α and β (Figure 3.3-A). More details about the design rules are presented in SI Appendix, Section 3.7.2.1.

To assemble the experiment, we combined the four templates and the three enzymes in a consistent buffer containing dNTPs, and incubated isothermally in a closed tube. We first checked for the presence of two stable states, which should be selected depending on the initial conditions. Indeed we found that, if the system is initiated with α only, it evolved to a stable state characterized by a strong shift in Fam fluorescence, but no perturbation in Tamra fluorescence (called state A, see Figure 3.3-B). Initial conditions containing only β produced the opposite fluorescent pattern (called state B). This suggests

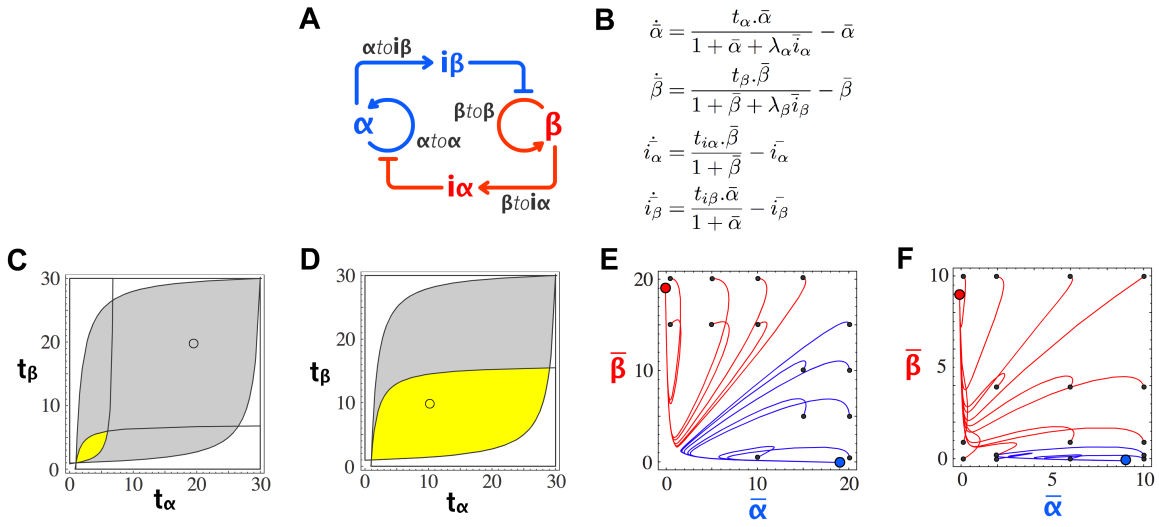

Figure 3.2: Bistable circuit design. (A) A circuit encoding bistability. (B) Non-dimensionalized equations of the simplified model. t_x are the scaled template concentrations and λ_x the ratio of activator over inhibitor binding constant. Periods indicate multiplications. (C) Phase diagram of the bistable circuit in the $\{t_\alpha, t_\beta\}$ plane. Yellow: bistable domain for $\{\lambda_\alpha, \lambda_\beta\} = \{20, 20\}$. Gray: bistable domain for $\{\lambda_\alpha, \lambda_\beta\} = \{100, 100\}$; (D) the same with yellow: bistable domain for $\{\lambda_\alpha, \lambda_\beta\} = \{100, 50\}$; and gray: bistable domain for $\{\lambda_\alpha, \lambda_\beta\} = \{100, 100\}$. (E) Plot of the calculated trajectories of the bistable circuit for different initial $\{\bar{\alpha}, \bar{\beta}\}$ (small black dots). The bistable circuit is evolving to a stable state A (blue dot) or B (red dot). $\{\lambda_\alpha, \lambda_\beta\} = \{100, 100\}$ and $\{t_\alpha, t_\beta\}=\{20,20\}$, corresponding to the small circle in the gray area of C. (F) The same for $\{\lambda_\alpha, \lambda_\beta\} = \{100,50\}$ and $\{t_\alpha, t_\beta\} = \{10, 10\}$ (small circle in the yellow area of D).

that the system possesses only two stable states. Note that working in a closed configuration imposes a limited lifetime for the system: once all the dNTPs are consumed, it will simply die out, toward its unique thermodynamic equilibrium.

To quantitatively assess the bistable behavior of the circuit (i.e. the convergence toward one of these states at the exclusion of any other trajectory), we initiated the reactions with various mixtures of α and β: we observed that, after some transients, the system always stabilized on either stable state A or stable state B (Figure 3.3-C). These experiments also led to a matrix representing the basin of attraction of each stable state, which were initially quite asymmetric (Figure 3.3-D). Even if templates were present in the same concentration and sequences had similar thermodynamic constants (but are still different: dissociation constant of α is more than twice that of β as seen on SI Appendix, Table S3), side A tended to win as soon as α was initially present in significant quantities, irrespective of the initial concentration of β. However, as suggested by the simple model, we could adjust this by tuning the concentrations of templates α*to*α and β*to*β (Figure 3.3-D). Figure 3.3-E shows the trajectories of an adjusted system for different initial input combinations. While the behavior is still not ideal, both

states possess a reasonable basin of attraction.

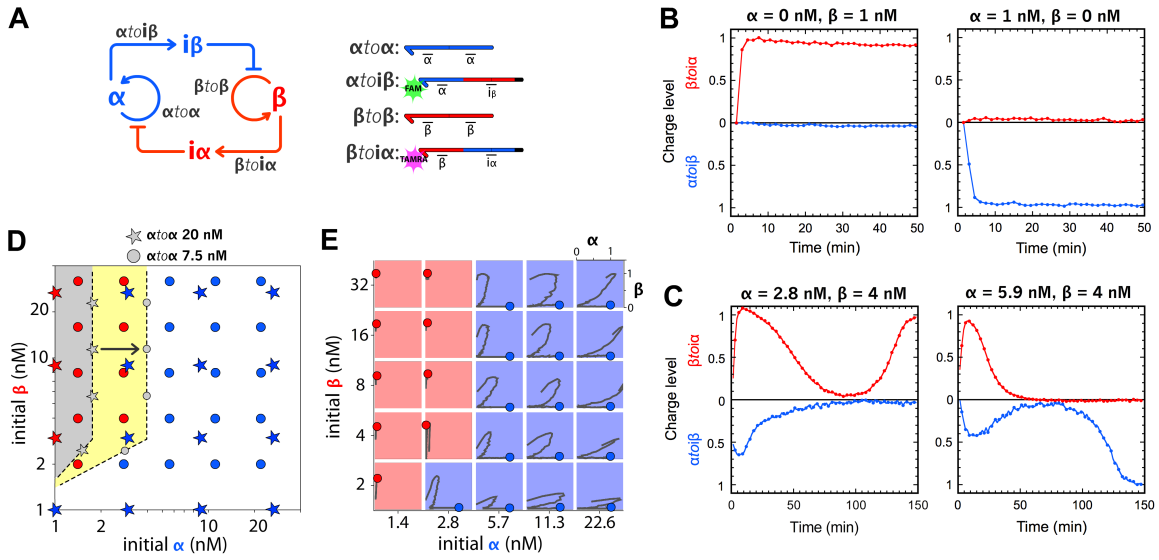

Figure 3.3: Experimental building of the bistable circuit. (A) Topology and templates of the bistable circuit. Templates $\alpha to i\beta$ and $\beta to i\alpha$ are labeled with Fam and Tamra, respectively, allowing multiplex monitoring of the hybridization status of these two templates. (B) Time plots of the "Charge level" of the bistable switch taking either state B (left) or A (right). "Charge level" is the normalized fluorescence at 0 in the absence of the corresponding template's input, and 1 at the steady state of input. (C) Time plots of the Charge level of the adjusted bistable switch for two different initial [α] and [β] combinations. (D) The bistable circuit picks its state (A or B) according to the initial combination of α and β concentrations. With 20 nM of each template, the basin of attraction of state B (grey domain) is small compared to that of state A. Decreasing the concentration of $\alpha to \alpha$ to 7.5 nM results in an expansion of the basin of attraction of state B (yellow domain). Colored stars and dots are experimental points for, respectively, the bistable with 20 nM of each template and the adjusted bistable with 7.5 nM of $\alpha to \alpha$ for 20 nM of $\beta to \beta$. Domain boundaries are drawn to facilitate the plot reading. (E) Experimental trajectories of the adjusted bistable for different combinations of initial α and β. For each trajectory, the X axis corresponds to the charge level of template $\alpha to i\beta$, the Y axis to the charge level of template $\beta to i\alpha$. After some transients, the bistable stabilizes in either state A (blue dot) or B (red dot).

To assess unambiguously and quantitatively the identity of the two states, aliquots were withdrawn from the solution after the system, initiated with {α, β} = {10 nM, 0.1 nM} or {0.1 nM, 10 nM}, reached one or the other stable state. We analyzed the α and β content of these aliquots and found a concentration of 55 nM of α for state A and 40 nM of β for state B (SI Appendix, Section 3.7.4). This similitude between the steady levels of α and β further validates that both sides of the bistable circuit are well balanced, thanks to the tuning of the concentrations of $\alpha to \alpha$ and $\beta to \beta$. At the same time, we measured about 1000 times less of the output of the loosing state. The simple model predicts that the losing side should evolve asymptotically toward 0, but leak reactions not considered therein

probably maintain a small basal level. Combining these results with the fluorescence measurement, we conclude that after having taken a stable state depending on the initial α/β ratio, the bistable system continuously and unambiguously delivers information about its current status.

The simple model predicts that the bistable circuit is robust to perturbations in concentration of α and β as long as they do not exceed the concentration of input currently at the steady-state (SI Appendix, Section 3.7.3.3). Experimentally, we found that the bistable circuit is much more robust than this prediction: for example, when in the stable state A, an injection of a concentration of β (100 nM) twice as large as the steady concentration of α is not enough to flip the bistable circuit to the opposite state (Figure 3.4-A). This discrepancy could be attributed to the fact that the simple model rests on immediate equilibria for all the hybridization reactions. Since the inhibitor strands are stable enough to have slow dissociation constants, this assumption is probably not realistic. We therefore built a detailed mathematical model that takes into account the full set of reactions taking place in the system (SI Appendix, Section 3.7.3.4). Indeed, this new model predicts a higher resilience of the bistable circuit (Figure 3.4-B): when the perturbation is introduced as a single Gaussian spike, a ~20-fold concentration of the opposite input is predicted to be necessary to switch the system to its opposite state (SI Appendix, Section 3.7.3.5). Since this did not appear as a very practical solution to flip the system back and forth, we turned toward an alternative switching strategy.

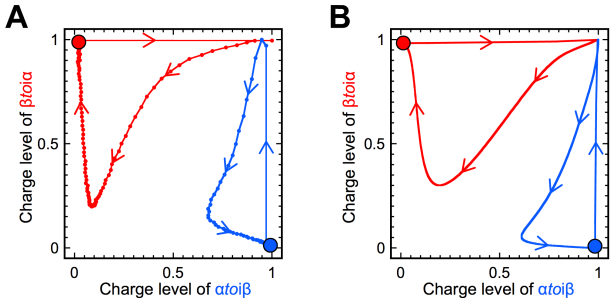

Figure 3.4: Perturbation of the bistable at the steady state. The red dot (charge level $\{\alpha toi\beta, \beta toi\alpha\} = \{0, 1\}$) corresponds to stable state B. The blue dot (charge level $\{\alpha toi\beta, \beta toi\alpha\} = \{1, 0\}$) corresponds to stable state A. (A) Experimental and (B) calculated (using the detailed model) trajectories of the bistable perturbed by 100 nM of the opposite input.

3.4.4 Two-input switchable memory

To obtain an updatable memory circuit, we decorated the bistable circuit with two activation modules that connect this bistable core to two different and specific external signals. Activation modules $\gamma to\alpha$

and δ*to*β take respectively ɣ and δ as inputs to produce a long-lasting pulse of α or β, which should stimulate the bistable core to flip between states (SI Appendix, Section 3.7.3.6).

Experimentally, the width of the pulse of α or β produced by an activation module can be adjusted by changing the concentration of the corresponding template (Figure 3.5). These activation modules therefore provide a handle to push the bistable core toward one state or the other. Correct tuning of the concentration of the activation modules is important: if the concentration is too low, the stimulus will fail to push the bistable core beyond the separatrix, to the basin of attraction of the opposite state (Figure 6B). Conversely, if it is too high, the system will loose in responsiveness (the activation module will stay active for too long). For a concentration of 5 nM of both activation modules, we found that injection of a small amount (30 nM, i.e. even less than α and β at the steady state) of ɣ or δ is enough to flip the memory between its two states.

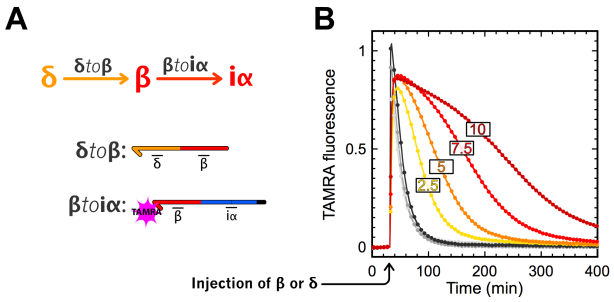

Figure 3.5: Production of β by activation module δ*to*β. (A) Circuit and templates of the system. (B) Experimental time plot of TAMRA fluorescence (baseline removed) produced by the hybridization of β on β*to*iα. Grey curves: injection of 30 to 150 nM of β. Yellow to red: injection of 30 nM of δ in the presence of 2.5, 5, 7.5 or 10 nM of δ*to*β.

The complete switchable memory circuit contains 6 templates (Figure 3.6-A), has two stable states characterized by the exclusive presence of α or β, and can be controlled by the two external inputs ɣ and δ. Figure 3.6-C displays the fluorescence curves of the memory initiated in state A, then switched back and forth once (see SI Appendix, Section 3.7.6 about failed attempts at further switching). When flipping between states, one observes a characteristic biphasic evolution of the charge levels of α*to*iβ and β*to*iα: injection of the external input (e.g. δ) provides the bistable core with a long-lasting pulse of the currently OFF internal input (e.g. β). This pulse charges the inhibition module (e.g. β*to*iα, increase in the red curve) and initiates the inhibition of the ON state. α decreases (slow evolution of the blue curve toward 0), in turn releasing the inhibition of the OFF state. When the external stimulation comes to its end (reversal in the evolution of the red curve), the system has already reached the basin of attraction of B and β ultimately eliminates α (second increase of the red curve

and final decrease in the blue curve): the memory has flipped between states. These curves were used to optimize the parameters of the detailed mathematical model (i.e. all other predictions use this same set of parameters (SI Appendix, Section 3.7.3.4)). They are also plotted as calculated (Figure 3.6-D) and experimental (Figure 3.6-E) trajectories in two dimensions, showing the good agreement between the model and the experiments. The trajectories (from A to B and from B to A) appear to be crossing only because they are a two-dimension projection of a higher dimensional system [151] (see Figure 3.20).

The bistable core takes around 200 minutes to flip between states. This duration is comparable with the period of the oscillator previously reported [62]. Also, switching requires a concentration of external input (30 nM) that is of the same scale as the produced α or β at the steady state (~50 nM). This suggests that the switchable memory circuit could be connected with other circuits made with the DNA-toolbox, in the quest for more complex reaction networks.

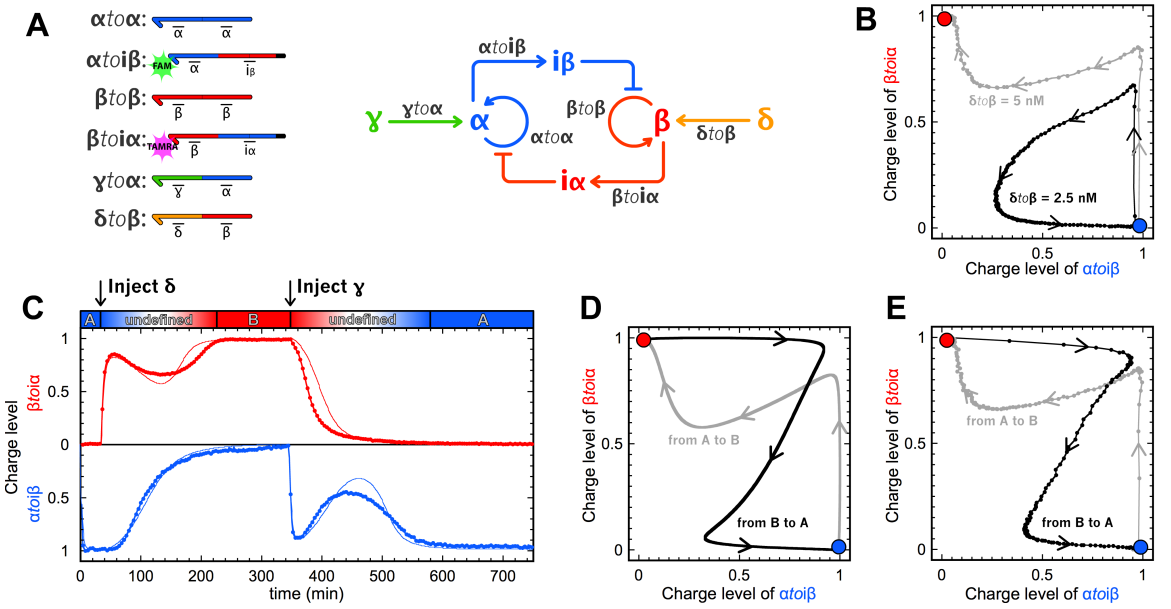

Figure 3.6: Switchable memory circuit. (A) Circuit and templates of the bistable switchable memory. (B) Trajectories of two attempts to flip the bistable memory from A to B, with δ*to*β = 2.5 nM (black, failure) and δ*to*β = 5 nM (grey, success). (C) Experimental (thick line) and fitted model (thin line) time plot of the charge levels of α*to*iβ and β*to*iα. The memory circuit is started in state A, flipped from A to B, then from B to A. (D) Predicted and (E) experimental trajectories of the memory switching reversibly from A to B (grey) and B to A (black).

3.4.5 Push-push memory

The push-push memory is another type of updatable memory element, in which a bistable system is switched back and forth by a unique stimulus (hence the name push-push, in reference to a push-button mechanical switch). A chemical implementation of this function can be obtained by further enriching the previous memory circuit (Figure 3.7-A): the two activation modules (δ*to*α and δ*to*β) now respond to the same external input δ. To carry out the push-push functionality, two additional inhibition modules (α*to*iδα and β*to*iδβ) feed the current state of the bistable core back to the activation modules: when the bistable is in state A, they ensure that the corresponding activation module (δ*to*α) is inhibited, and vice versa. In the presence of the four templates δ*to*α, δ*to*β, α*to*iδα and β*to*iδβ, injection of δ will only trigger the production of the input of the OFF state of the bistable core, whereas the input of the currently ON state will not be produced. This strategy was theoretically validated by a model (SI Appendix, Section 3.7.3.7).

The detailed model suggested that the full circuit would work with the same bistable core and same concentration of activation modules as the memory circuit, in the presence of a few nanomolars of α*to*iδα and β*to*iδβ (Figure 3.7-B). Before assembling the full circuit, we experimentally checked the sub-parts encoding the push-push functionality. Figure 3.8 shows that indeed, a concentration of β*to*iδβ as low as 1 nM is efficiently regulating the pulse of β produced by δ*to*β.

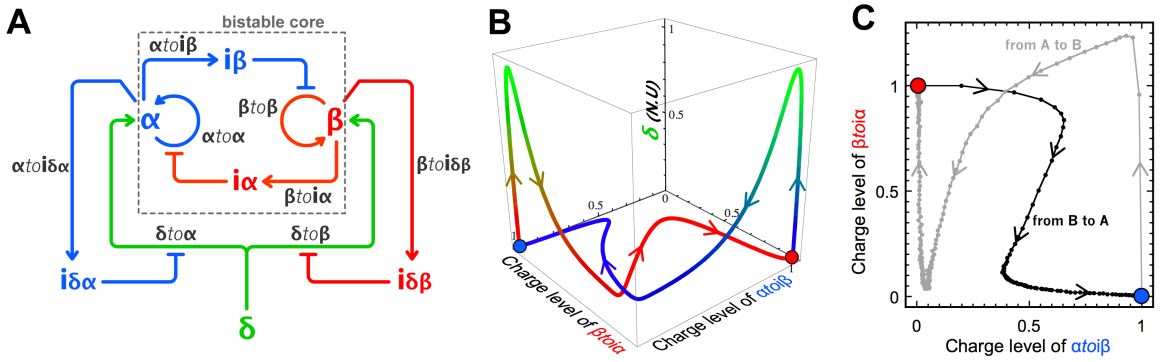

Figure 3.7: (A) Circuit of the push-push memory: a single external input δ controls the bistable core. (B) Calculated 3D trajectories in the space {Charge level of α*to*iβ, Charge level of β*to*iα, Normalized total concentration of δ} for the push-push memory switching from A to B (blue) and B to A (red). Normalized values of δ (injected as a gaussian spike) from 0 to 1 are associated to a color gradient from blue/red to green. (C) Experimental trajectories of the push-push memory circuit showing two independent experiments: one where the system is initially set on the state A, then flipped to B upon injection of 30 nM of δ, and another where the same system is set in state B, then flipped to A upon injection of the same input. The charge level of β*to*iα higher than 1 indicates that the amount of β transiently produced by activation module δ*to*β during switching exceeds the concentration of β at the stable state B.

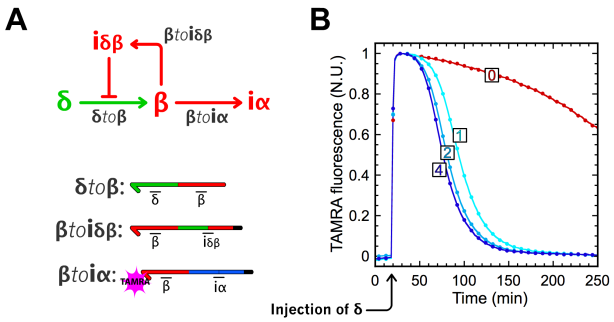

Figure 3.8: Push-push negative feedback. (A) Circuit and templates. Upon injection of δ, production of β is activated. Then, β hybridizes to β*to*iα (resulting in an increase of TAMRA fluorescence) and to β*to*iδβ that, in turn, produces the inhibitor of δ*to*β, stopping the production of β. (B) Experimental time plot of the normalized TAMRA fluorescence (1 at the highest and 0 at the lowest) for different concentrations (0, 1, 2 and 4 nM) of inhibition module β*to*iδβ.

When experimentally assembling the 8 templates of the push-push memory circuit, we had to adjust the concentrations of δ*to*β and β*to*iδβ to strengthen the response of the B side to the exogenous input δ. Note that in the bistable core, state B is less attractive than state A (Figure 3.3-C), which may explain why switching toward B requires a stronger amplification of the external stimulus δ. We therefore kept the concentrations of activation module δ*to*α and inhibition module α*to*iδα proposed by the model (respectively 5 nM and 4 nM), and adjusted the concentration of δ*to*β to 10 nM. This explains the large amount of β produced upon injection of δ (exceeding the concentration of β at the steady state). After fine-tuning of the concentration of β*to*iδβ (we settled on a concentration of 1 nM, see SI Appendix, Section 3.7.5), the push-push circuit could be flipped from state A to B –and from state B to A– by injection of 30 nM of its unique external input, δ (Figure 3.7-C). The corresponding fluorescence time plots are shown on Figure 3.19.

3.5 Discussion

Bistability is a fundamental feature of dynamic systems. Bistable switches have been identified or postulated in a number of important biological circuits [129, 130, 47, 48, 124, 125, 126, 140, 141, 142]. More generally, bistability seems to be at the basis of the dynamic behaviors of many non-linear artificial chemical systems, such as oscillators [128, 152].

Molecular bistability can theoretically be obtained from a great variety of reaction network topologies [148, 149, 153], and the mechanistic requirements for this function have been explored in detail [150, 154, 155]. The presence of a positive feedback loop is a necessary but not sufficient signature

[129, 47, 53, 150]: an isolated single autocatalysis provides bistability only if sufficient non-linearities are included in the loop. In vivo, mechanisms such as ultrasensitivity or cooperative binding –proteins that acquire new regulatory functions through the formation of multimers– typically provide these sources of nonlinearity.

Bistable systems without cooperative nonlinearity can be obtained at the cost of a slightly increased topological complexity of the network [150]. The in vitro toolbox that we use here does not provide a mechanism to introduce cooperative effects; however, it allows easy assembly of relatively large networks. Hence we decided for a robust and symmetrical design that contains two autocatalytic loops responsible for the self-amplification of two cross-repressing species (another design compatible with the chemistry at hand is discussed in SI Appendix, Section 3.7.3.2). The advantages of the present design are twofold: first, both stable states correspond to a high concentration of one out of two species (and not to the presence or absence of a single species), making the reading and interfacing easier; second, the symmetry facilitates the identification of the control parameters for the network behavior. In particular, even for not symmetrical sequences, one can theoretically tune the concentrations of templates to obtain and balance the bistable domain. In practice, this proved to be a useful feature for the construction of the more complex target behaviors.

The requirement to switch from one state to the other poses another design challenge. In the ideal case of a system that adapts immediately to a perturbation, as in the simple model presented in Figure 3.2, flipping from A to B is obtained as soon as the concentration of β is pushed above that of α. This reactivity should not be expected in systems constructed out of complex biochemical transformations, which is typical of biological systems. Slow loops then increase the hysteresis found in the bistable behavior [156]. However, while cellular bistable switches are self-contained and can be exposed to input stimuli over long periods of time [53], it is not the case of our in vitro batch design: by construction, inputs α and β are degradable species, and an injection of α or β will only produce a spike of limited length (Figure 3.5). Therefore, we had to look for an alternative switching strategy: we introduced an additional dimension in the sequence space to provide a switching pathway with a much lowered concentration threshold (see Figure 3.5). The complete system provides a stable memory, able to resist very strong transient fluctuations of its chemical signature, but which also specifically responds to short and dilute spikes of external inputs. Steady state concentrations of outputs α and β (~50 nM) are of the same scale as the external input required to flip the memory (~30 nM), which suggests that the memory circuit is itself modular: it could be used as such in a plug&play manner for the building

of more complex reaction circuits.

The step-by-step assembly of large-scale systems –like the push-push memory circuit presented here– rests heavily on the modularity of the molecular toolbox that we use. By modularity, we refer here to the fact that a priori, any activating or inhibiting relation between two signal molecules (input or inhibitor) can be implemented: one only needs to design the corresponding templates. However, in practice this modularity may be limited by a number of design issues: load effect [71] arises when a downstream module sequesters the product of an upstream module; enzyme saturation can lead to unintended coupling between unconnected modules because of the competition for enzymatic resources [59]; and spurious interactions between non complementary sequences may also lead to some extent of cross-talk [157]. These effects become more prevalent when the size of the system increases [31]. However, their consequences can be circumvented through the emphasis on the robustness of the design, which in turn is identified using toy mathematical models (SI Appendix, Section 3.7.3.1). Then, a complete set of reactions (SI Appendix, Section 3.7.3.4) can be combined to provide a better, quantitative understanding of the consequences of non-modular interactions, which generally lie beyond our intuition. In the end, building and understanding the dynamics of these complex networks strongly rests on the good agreement between the experimental result and the mathematical approach. While this process can be time consuming, one may envision that, in the future, design rules similar to those of engineering disciplines will emerge to directly mitigate or incorporate these complex effects. It is also interesting to note that such design rules may have a direct impact on our understanding of in vivo regulatory processes: for example, in vitro models suggest that competition for enzymatic resources may be an important contribution to the dynamics of cellular circuits [51, 59].

In this paper, reaction circuits were assembled in a closed environment. This stands in contrast to most chemical or biological bistable networks reported so far, which perform in open systems [53, 56, 55, 57, 152]. This closeness imposes specific challenges, for example the presence of precisely controlled internal source and sink energetic pathways. It also implies that each experiment has a limited lifetime, and that true steady states cannot be obtained –because various reaction parameters are modified over time: for instance, dNTP concentration decreases, and enzymes can loose activity. Worse, even though the templates are protected from the exonuclease, they get slowly degraded (SI Appendix, Section 3.7.2.2). These factors may pile up to modify the circuit behavior and explain the loss of function that we have observed after long experimental times (SI Appendix, Section 3.7.6). Still, we were able to obtain satisfying pseudo-steady states and to perform at least one complete cycle

of the two-input memory circuit through its alternative states. For the push-push memory circuit, the longer time required for switching may explain that repetitive operations were not successful. Note that an eventual breakdown is unavoidable considering our closed experimental set-up. We anticipate that if the reactions were performed in an open system (e.g. in a reactor with a constant flow of fresh precursors), they could be run for an infinite amount of time and switched continuously.

3.6 Conclusion

Biological behaviors are built from and controlled by assemblies of biochemical reactions connected in complex networks. Despite the enormous molecular complexity of living systems, we may expect that a correct characterization of the individual components will lead to a rational understanding of the biological organization and dynamics. A critical test for this approach is the man-made rational design of molecular systems reproducing non-trivial biological behaviors. The in vivo version of this idea, synthetic biology, is based on the assumption that biological systems are built from modular, interchangeable sub-elements: cells provide a platform in which exogenous genetic programs can be run. Successes along this systematic line are interpreted as a proof of a correct understanding of the molecular basis of complex, life-like behaviors. However, many studies in this direction have resulted in a significant deviation from this idealized view of a cell as a universal platform. In many cases, interference with the housekeeping functions cannot be neglected; modularity is not provided for free but must be carefully enforced. Our results here suggest that the in vitro approach, which reproduces some of the essential features of biological networks (including universality), but avoids some of their limitations, mitigate these concerns and hence may provide a faster learning curve regarding the potential of reaction networks. Here, the 8 “genes” push-push memory circuit already compares favorably with the largest realizations of in vivo synthetic biology. Moreover, because it is fully modular, it could theoretically be connected to other circuits. For instance, two push-push circuits in series would give a 2-bit binary counter, and one push-push downstream of an oscillator would perform frequency division, oscillating at half the driving frequency.

3.7 Supplementary Information

3.7.1 Workflow of network assembly with the DNA-toolbox

Figure 3.9 shows how to implement a target behavior with the DNA-toolbox.

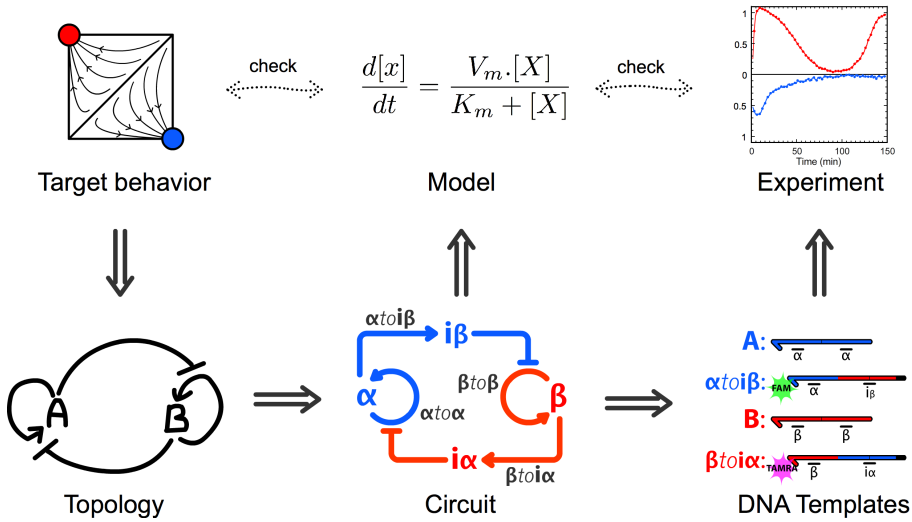

Figure 3.9: Implementation of a target behavior with the DNA-toolbox. A target behavior can correspond to one out of a number of network topologies. These topologies can in turn be translated into an assembly of modules compatible with the toolbox. A simple model of the corresponding circuit allows one to check the consistency of the chosen design with the target behavior, and find out the key parameters or conditions that the circuit must meet in order to perform as expected. The following step consists in the design of the templates that encode the activation, autocatalysis and inhibition modules of the circuit, and the experimental implementation. The experiment should be in good agreement with the simple (or more detailed) model, which can in turn be used to adjust the experimental parameters of the circuit.

3.7.2 Experimental building of the bistable circuit

3.7.2.1 Design rules

To build the bistable, we started with the autocatalytic template included in a recently reported oscillator (template $\beta to \beta$) [62]. We then designed another sequence (α) with several constraints: the sequences must be orthogonal (this also goes for their respective inhibitors), in order to avoid reaction crosstalk. Also, sequences should not exhibit a nicking recognition site at an unwanted location. As suggested by the simple model, we designed inhibitors so that their dissociation constant was about two orders of magnitude higher than that of input strands (Table 3.3). Inhibitors are 15 bases long: 13

bases are matched with the target template, and the last two 3' bases are mismatched, preventing the polymerase from extending the duplex. Inhibitors should not display the nicking enzyme recognition site: to meet this requirement, 7 of the 13 matched bases are on the template input (3') side and 6 on its output (5') side: two partial but no complete recognition sites are then included in these strands (See Table 3.2).

Because of the symmetric topology of the bistable circuit, both autocatalytic modules should be of equivalent "strength". Thus, we designed α and β so that the predicted[1] melting temperatures (T_m) on their templates were as close as possible: even though the T_m alone is not enough to determine the relative "strength" of α and β, it is an accessible parameter to balance the sequences before assembling the circuit. Enzymes have a different affinity for each sequence, and this parameter is not predictable (but has recently attracted interest in the context of isothermal DNA amplification and template dependence [158]), nor controllable for a given sequence. A robust network design should then be as little sensitive as possible to such unpredictable parameters in delivering the target function, and also provide some adjustable control parameters that may be used to mitigate these effects, once the sequences have been decided. Here we have shown that it is possible – in a certain extent – to tune the concentrations of some templates to experimentally "balance" a non-perfect system in order to obtain a robust bistable circuit.

Monitoring of α and β is done by using N-quenching [147]: a single fluorophore is attached at the 3' end of templates α*to*iβ and β*to*iα, where its fluorescence gets modified by the presence of the template's input (i.e. single-strand vs double-strand state). On the contrary, the binding of the output doesn't impact the fluorescence of the template 3' fluorophore [147]. The fluorophores were not attached to templates α*to*α or β*to*β for the following reason: these two autocatalytic modules are the target of inhibitors iα and iβ, which hybridize 4 bases away from the template 3' fluorophore. In this configuration, they might induce a slight fluorescence change when hybridizing [147]. To avoid this unwanted effect, we attached the fluorophores on inhibition modules α*to*iβ and β*to*iα.

3.7.2.2 Protection from ttRecJ

In order to protect template from degradation by 5'->3' exonuclease ttRecJ, templates have several phosphorothioate backbone modifications (PT) at their 5' end. Note that the RecJ exonuclease used here is not the same as the commercially available enzyme from *Escherichia coli* used in Montagne *et*

[1] Using DINAMelt (http://mfold.rna.albany.edu/?q=DINAMelt)

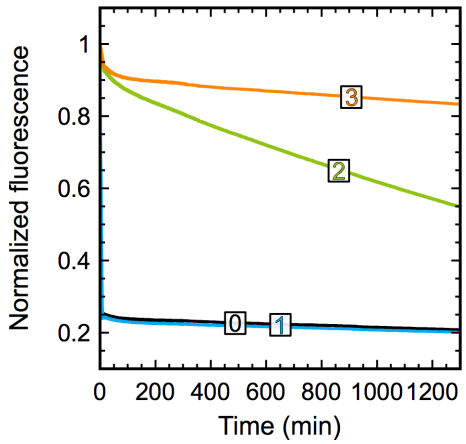

Figure 3.10: Degradation of template β*to*β (400 nM) by ttRecJ in the same buffer, ttRecJ concentration (50 nM) and temperature (42 °C) as for the bistable switch, memory and push-push memory experiments. Template β*to*β has 0, 1, 2 or 3 consecutive phosphorothioate backbone modifications at its 5' end.

al. [62]. Here we used thermophilic analog ttRecJ from *T. thermophilus* [145, 146]. This thermophilic enzyme is more stable than its mesophilic counter part. Therefore it does not require the addition of stabilizing additives in the buffer and extends the range of available working temperatures.

However the activities of the two enzymes are slightly different. Figure 3.10 shows the degradation of 400 nM of template β*to*β in presence of the same concentration of ttRecJ as used in the switch experiments reported here. Even with 2 PTs, β*to*β is rapidly degraded, which may prematurely disrupt the functioning of a circuit containing it (this stands in contrast with the mesophilic RecJ, for which two phophorothioates were found to provide a good protection [62]). Three terminal consecutive PTs appear to be necessary to obtain a correct protection, but produce a problematic side-effect: the nicking enzyme cutting speed is divided by roughly a factor of 4 in the presence of the third PT (Figure 3.11-B).

We hypothesized that this was the consequence of a form of competitive inhibition, where the nicking enzyme could bind –unproductively– the recognition sequence on the output side of the template (even if for this pseudo-site, no DNA extends beyond the nicking position). Following this line of thought, we searched for a way to decrease the affinity of the nicking enzyme for the output site. We found that replacing the thymine of the recognition sequence by an uracil (GACUC instead of GACTC) could indeed address the reduced cutting speed issue. In this case, a correct nicking rate was recovered (Figure 3.11-C). In fact, we even observed an increase in the rate of the nicking process, compared to template β*to*β with 2 PT and no dU.

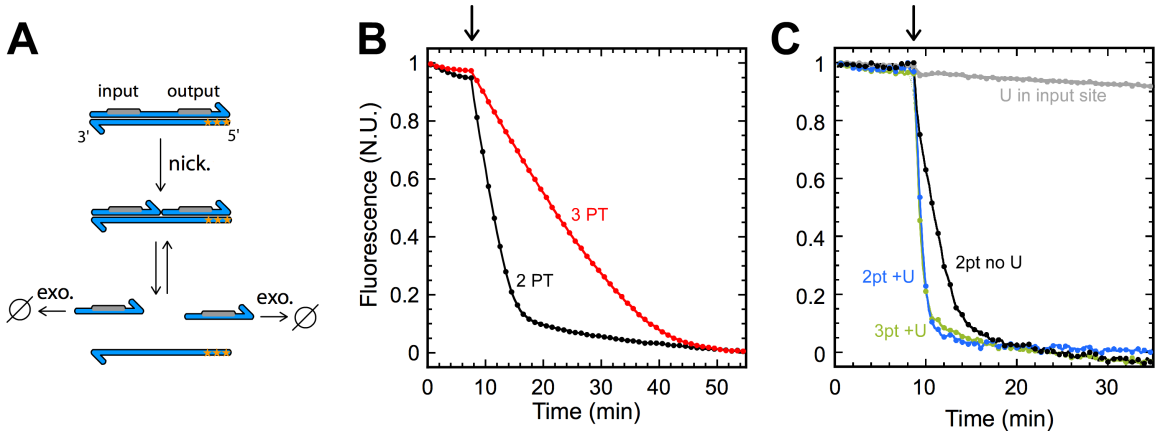

Figure 3.11: Assay for nicking enzyme activity measurement depending on various template modifications. (A) Assay schematic: in the presence of templates in duplex form, the nicking enzyme (nick.) cuts the upper strand between input and output. The two resulting short strands can dissociate from the template and are degraded by an exonuclease (exo.) to avoid the accumulation of products. In the presence of Evagreen (double-strand specific intercalating dye) this reaction results in a global decrease of fluorescence, as template duplexes are converted to single-stranded form. The nicking event is the rate-limiting step. Stars represent phosphorothioate backbone modifications (PT), located at the 5'-end of the template. (B) and (C): Normalized fluorescence records for various templates modifications. The arrow indicates the time for injection of nicking enzyme i.e. the start of the reaction. (B) The presence of 3 PTs slows down the reaction, even if they are very far from the actual nicking site. (C) With a U in the nicking enzyme output recognition site (i.e. the one that has no function), 2 PTs (blue) or 3 PTs (green) do not slow down the enzyme activity. U-containing templates are even faster than the template with 2 PT and unmodified output recognition site (black).

Also, when a U was placed in the input (3') site of the template, the nicking enzyme was mostly unable to cut the duplex anymore (Figure 3.11-C): this confirms that in these conditions, a modified recognition site is poorly processed by the nicking enzyme. Altogether, these observations strongly support the previous hypothesis about competitive inhibition. For a more complete analysis of the effect of dT->dU modifications on various endonuclease activities, see the work of Mazurek and Sowers [159].

Note that we are discussing about dT->dU modifications, and not the dynamic incorporation of dUTP instead of dTTP, as in other PCR-related strategies [160]. The presence of these modifications on the templates will not affect the other toolbox-related processes because i) T->U has only a small effect on duplex stability, and ii) many DNA polymerases -except archaeal [161]- simply ignore the difference between dT and dU on the template and reliably incorporate a dATP at this position. We thus adopted this strategy: all activation and autocatalytic templates have three PTs at their 5'-end, and a U in their output recognition site.

3.7.2.3 DNA sequences

Template	Sequence (5'->3')	Experimental concentration in adjusted reaction circuit (nM)		
		Bistable	Memory	Push-Push
α*to*α	C*C*A*AGACUCAG-CCAA**GACTC**AG	7.5		
β*to*β	A*A*C*AGACUCGA-AACA**GACTC**GA	20		
α*to*iβ	T*T*A*CTCGAAACAGAC-CCAA**GACTC**AG	20		
β*to*iα	T*T*A*CTCAGCCAAGAC-AACA**GACTC**GA	20		
ɣ*to*α	C*C*A*AGACUCAG-GCAT**GACTC**AT		5	
δ*to*β	A*A*C*AGACUCGA-CACT**GACTC**CT		5	10
δ*to*α	C*C*A*AGACUCAG-CACT**GACTC**CT			5
α*to*iδα	T*T*A*CTCAGCACTGAC-CCAA**GACTC**AG			4
β*to*iδβ	A*A*A*CTCGACACTGAC-AACA**GACTC**GA			1

Table 3.1: Templates and concentrations used in this study. Stars stand for phosphorothioate backbone modifications. Templates are separated in two parts, corresponding to input and output binding sequences, respectively. Nicking enzyme recognition sites are in bold. Uracilated pseudo-sites are in gray.

input / inhibitor	Sequence (5'->3')
α	CT**GAGTC**TTGG
β	TC**GAGTC**TGTT
ɣ	AT**GAGTC**ATGC
δ	AG**GAGTC**AGTG
iα	GTCTTGG-CTGAGTAA
iβ	GTCTGTT-TCGAGTAA
iδα	GTCAGTG-CTGAGTAA
iδβ	GTCAGTG-TCGAGTTT

Table 3.2: Input and inhibitors used in this study. Inhibitors are overlapping on both input and output site of their target template. Nicking enzyme recognition sites are in bold, and partial recognition sites (on inhibitors) in gray.

DNA templates used in this study, and their concentrations, are shown in Table 3.1. Input and inhibitors (i.e. the species that are dynamically produced and degraded) are shown in Table 3.2.

3.7.2.4 Sequence space limitation

With the DNA-toolbox, 11-bases long inputs and 15-bases long inhibitors can be arbitrarily wired in reaction networks following any desired network topology. The shortness of these oligonucleotides is limiting the available sequences: on the 11 bases of an input, 5 are required for the nicking enzyme recognition site (in bold on Table S2), leaving 6 bases to choose among 4 nucleotides. That is $4^6 = 4096$ combinations. With a conservative estimate of 2-5 % of them viable (to exclude sequences with

secondary structures, G repeats, cross-talks or other issues (e.g. parasitic nicking site)), this leaves about 80-200 sequences. This last number should be compared with the 3 basic sequences needed to build the push-push memory circuit, giving an idea of the maximal circuit complexity that one could construct with the DNA-toolbox (in homogeneous, well mixed conditions).

In order to overcome this limitation, that is, to increase the number of viable input species, one might consider working with longer oligonucleotides (and therefore at higher temperature to maintain the dynamic exchanges). Also, it should be possible to work with another nicking enzyme having a shorter recognition site: this would further increase the available bases for designing inputs with orthogonal sequences.

3.7.3 Model

3.7.3.1 Simple Model

Assuming a Michaelis-Menten mechanism for the DNA amplification step of an activation template T = x*to*y :

$$x + T \underset{k_{-1}}{\overset{k_1}{\rightleftarrows}} xT \overset{k_2}{\rightarrow} x + y + T$$

we obtain:

$$\frac{dy}{dt} = \frac{k_2.T.x}{K_x + x}; K_x = \frac{k_{-1} + k_2}{k_1}$$

where T and x are the total concentrations of the corresponding species. Note that this is not formaly valid: the second (k_2) reaction involves two complex enzymatic reactions besides mutiple de-hybridization, and thus barely corresponds to the classic Michaelis-Menten assumptions. However, for modelling purposes with minimal mathematical complexity, we can still expect the Michaelis-Menten expression to correctly describe the saturable production of y as a function of x. From the arguments above, we would also expect $k_2 << k_{-1}$, and K_x becomes roughly equal to the dissociation constant of x on the template T. Moreover, assuming that the inhibiting strand i_{xy} acts as a competitive inhibitor, and noting K_{ixy} the dissociation constant of i_{xy} and k_x the k_2 of activator x we obtain:

$$\frac{dy}{dt} = \frac{k_x.T.x}{K_x(1 + \frac{x}{K_x} + \frac{i_{xy}}{K_{ixy}})}$$

For the bistable system as shown in Figure 3.3-A, and assuming the same first order degradation rate D for all species[2], we can then generalize the previous equation (with obvious notations) to write the complete system as:

$$\begin{aligned}
\frac{d\alpha}{dt} &= \frac{k_\alpha.T_\alpha.\alpha}{K_\alpha(1+\frac{\alpha}{K_\alpha}+\frac{i_\alpha}{K_{i\alpha}})} - D.\alpha \\
\frac{d\beta}{dt} &= \frac{k_\beta.T_\beta.\beta}{K_\beta(1+\frac{\beta}{K_\beta}+\frac{i_\beta}{K_{i\beta}})} - D.\beta \\
\frac{di_\alpha}{dt} &= \frac{k_{i\alpha}.T_{i\alpha}.\beta}{K_\beta(1+\frac{\beta}{K_\beta})} - D.i_\alpha \\
\frac{di_\beta}{dt} &= \frac{k_{i\beta}.T_{i\beta}.\alpha}{K_\alpha(1+\frac{\alpha}{K_\alpha})} - D.i_\beta
\end{aligned}$$

We non-dimensionnalize by setting $\tau = t.D$, $\bar{\alpha} = \alpha/K_\alpha$, $\bar{\beta} = \beta/K_\beta$, $\bar{i_\alpha} = i_\alpha/K_\alpha$, $\bar{i_\beta} = i_\beta/K_\beta$ and $t_\alpha = k_\alpha.T_\alpha/K_\alpha.D$, $t_\beta = k_\beta.T_\beta/K_\beta.D$, $t_{i\alpha} = k_{i\alpha}.T_{i\alpha}/K_\alpha.D$, $t_{i\beta} = k_{i\beta}.T_{i\beta}/K_\beta.D$, $\lambda_\alpha = K_\alpha/K_{i\alpha}$ and $\lambda_\beta = K_\beta/K_{i\beta}$.

$$\begin{aligned}
\dot{\bar{\alpha}} &= \frac{t_\alpha.\bar{\alpha}}{1+\bar{\alpha}+\lambda_\alpha\bar{i_\alpha}} - \bar{\alpha} \\
\dot{\bar{\beta}} &= \frac{t_\beta.\bar{\beta}}{1+\bar{\beta}+\lambda_\beta\bar{i_\beta}} - \bar{\beta} \\
\dot{\bar{i_\alpha}} &= \frac{t_{i\alpha}.\bar{\beta}}{1+\bar{\beta}} - \bar{i_\alpha} \\
\dot{\bar{i_\beta}} &= \frac{t_{i\beta}.\bar{\alpha}}{1+\bar{\alpha}} - \bar{i_\beta}
\end{aligned}$$

It can be checked that the fixed point $\{\bar{\alpha}, \bar{\beta}\} = \{0, 0\}$ is unstable as soon as one of the autocatalytic templates reach a threshold concentration ($t_\alpha > 1$ or $t_\beta > 1$). The two fixed points that can give rise to bistable behavior are then $\{\bar{\alpha}, \bar{\beta}\} = \{t_\alpha - 1, 0\}$ and $\{0, t_\beta - 1\}$. They obviously exist only for t_α and t_β superior to unity. Moreover, for the first point, the eigenvalues of the associated Jacobian matrix are $\{-1, -1, (1-t_\alpha)/t_\alpha, -1+t_\alpha.t_\beta/(t_\alpha+\lambda_\beta.t_{i\beta}.(t_\alpha-1))\}$ so this point is stable for $t_\alpha > \lambda_\beta.t_{i\beta}/(1-t_\beta+\lambda_\beta.t_{i\beta})$. Similarly, the second point is stable for $t_\beta > \lambda_\alpha.t_{i\alpha}/(-t_\alpha+1+\lambda_\alpha.t_{i\alpha})$. In the case of a perfectly equili-

[2]This is, of course, not realistic, as inhibitors form more stable duplexes than activators, and are "protected" from the exonuclease when in duplex form. Also, note that the exonuclease has different Michaelis constants for inhibitors and activators (SI Appendix, Section 3.7.3.4). However, in the non-dimensional form of the equations, introducing a different D would come down to scaling $t_{i\alpha}$ and $t_{i\beta}$ and the respective inhibitors concentrations. Therefore it would not change the global dynamic behavior.

brated switch $t_\alpha = t_\beta$ and $\lambda_\alpha.t_{i\alpha} = \lambda_\beta.t_{i\beta}$, they may coexist for $\lambda_\alpha.t_{i\alpha} = \lambda_\beta.t_{i\beta} > 1$. Then, the overlapping areas of stability (i.e. the bistable range) will increase with increasing $\lambda_\alpha.t_{i\alpha} = \lambda_\beta.t_{i\beta}$. Finally, a fourth root in the positive quadrant, corresponding to the coexistence of the two dynamic species, can be stable when the two previous inequalities are simultaneously violated (and thus produces a monostable system).

Therefore, the insights brought by this simple model are as follow (see also Figure 3.2):

- As soon as their templates reach a threshold concentration, both autocatalytic loops produce a non-trivial steady state in α or β.
- Bistability can occur with asymptotic elimination of one species, but a minimum strength of the inhibitory link is necessary, and the concentrations of the autocatalytic templates must both be within a finite range (below which no species is produced and above which the system is monostable with a single species or two coexistent species).
- The bistable area, which can be interpreted as a quantification of the robustness of the function, increases with increasing inhibiting strength.
- This can be obtained both by increasing the binding constant of the inhibitor or the concentration of the template that produces it. Note however that both cases could result in a breakdown of the assumption used in the model (i.e. inhibitors would not dynamically hybridize anymore or the enzymes would become limiting and the production rate of β would not linearly follow the template concentration).
- The most robust behavior is given by the symmetric (ideal) system, as defined above. However, chemical dissymmetry (for example $k_\alpha \neq k_\beta$) can be compensated by adjusting the concentration of the template responsible for the production of each species.

3.7.3.2 Minimal bistable circuit design: single autoloop

In a system lacking cooperative nonlinearities, bistability can still emerge in the presence of at least one autocatalytic module [150, 153]. By using the simple model, we wanted to check if such compact circuit design (one autocatalytic module instead of two) would be deemed feasible in the context of the DNA-toolbox, and if so, how robust would it be compared to the design with two autocatalytic modules.

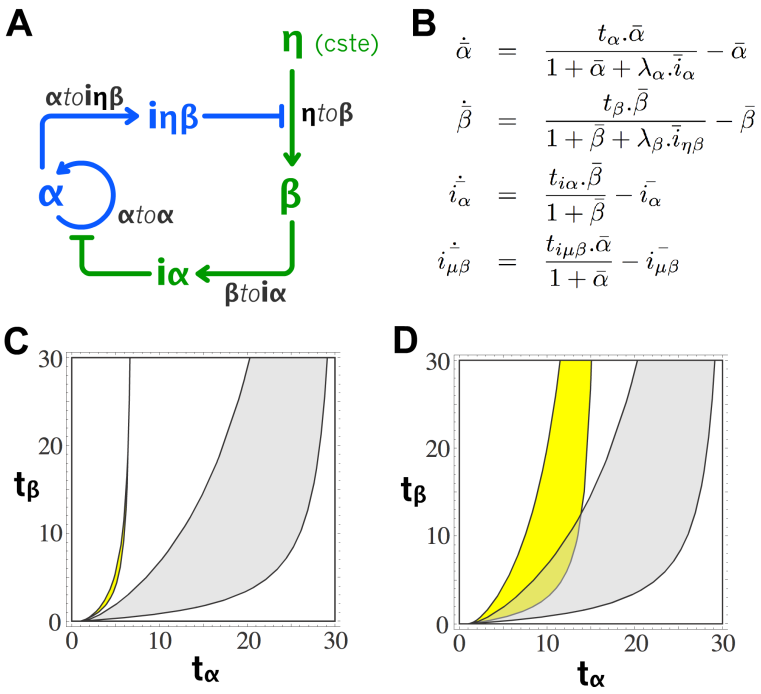

Figure 3.12: (A) Single-autocatalytic module circuit encoding bistability. (B) Non-dimensionalized equations of the simplified model. t_x are the scaled concentrations of template producing x and λ_x the ratio of activator over inhibitor binding constant. Periods indicate multiplications. (C) Phase diagram of the bistable circuit in the plane $\{t_\alpha, t_\beta\}$, with $\{t_{i\alpha}, t_{i\eta\beta}\} = \{0.3, 0.3\}$ and $\bar{\eta} = 1$. Yellow: bistable domain for $\{\lambda_\alpha, \lambda_\beta\} = \{20, 20\}$. Gray: bistable domain for $\{\lambda_\alpha, \lambda_\beta\} = \{100, 100\}$. (D) Idem with yellow: bistable domain for $\{\lambda_\alpha, \lambda_\beta\} = \{50, 100\}$; and gray: bistable domain for $\{\lambda_\alpha, \lambda_\beta\} = \{100, 100\}$.

Experimentally, it should be possible to build a bistable circuit with a single autocatalytic module (Figure 3.12-A), provided that the concentration of one input species (η) is kept constant (this could be obtained by simply adding phosphorothioate backbone modifications at the 5'-end of η, thus protecting it from degradation by the exonuclease). In the network of Figure 3.12-A, constant input η activates the production of β, which in turn triggers the production of $i\alpha$, inhibitor of $\alpha to \alpha$. On the other side, $\alpha to \alpha$ autocatalytically produces α, which triggers the production of inhibitor $i\eta\beta$. The latter is targeting template $\eta to \beta$, thus inhibiting the production of β.

We constructed a simple model of this circuit (Figure 3.12-B) and analyzed it the same way as the model of the bistable circuit with two autocatalytic modules (i.e. with the same values of t_{ix}, λ_x and the same ranges of $\{t_\alpha, t_\beta\}$). The phase diagrams of this bistable circuit in the plane $\{t_\alpha, t_\beta\}$ (Figure 3.12-C and D) suggest that in the context of the DNA-toolbox, and using similar design rules, this single-autocatalytic module design is less robust than the design containing two autocatalytic modules (analyzed in Figure 3.2). Moreover, it does not deliver a symmetric output to signal its current state.

3.7.3.3 Simple robustness

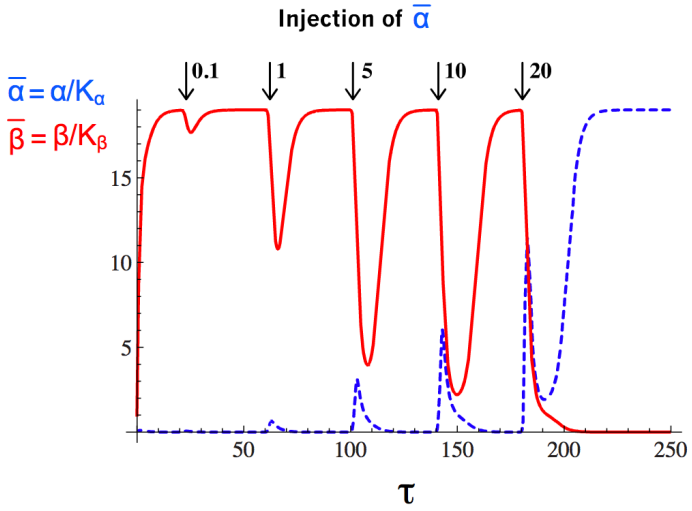

Figure 3.13: Assessing the response of the bistable switch: successive Gaussian spikes of increasing amount of $\bar{}\alpha$ are added to the system in the B state. $\bar{\beta}$ (red line) responds by a decrease as $\bar{\alpha}$ (blue dashed line) is injected. Eventually, injected $\bar{\alpha}$ transiently exceeds the amount of $\bar{\beta}$ at the steady state: the bistable flips from B to A. The parameters are $t_\alpha = t_\beta = 20$, $t_{i\alpha} = t_{i\beta} = 0.3$, $\lambda_\alpha = \lambda_\beta = 100$.

Using the simple nondimensionalized model, we assessed the response of the bistable switch to perturbation in its input concentrations. In this simplified, "instantaneous" model (i.e. that strictly relies on the instantaneous concentrations of dynamic species and does not incorporate hybridization / dehybridization dynamics), the bistable flips between states as soon as the injected OFF state input exceeds the ON state input (Figure 3.13).

3.7.3.4 Detailed model construction

Whereas the simple model gives a good insight about the validity of a given circuit design and its steady states, it fails to predict realistically the experimental circuit dynamics. Thus we built a more detailed mathematical model that takes in account all the hybridization and enzymatic reactions that happen in a toolbox-based DNA reaction circuit (as an example, see the detailed set of reactions for a circuit constituted of one autocatalytic module on Figure 3.14), with the following assumptions:

- Association rate of $k_a = 0.06$ $nM^{-1}.min^{-1}$ was taken, as proposed by Zhang and Winfree [19] for short oligonucleotides.
- Also, inhibitors take advantage of a 7 bases (if hybridizing to template-output duplex) or 6 bases (if hybridizing to template-input duplex) toehold: at 25 °C, this should give them a full

hybridization speed [19]. Our working temperature is however higher, and should decrease the efficiency of these toeholds, but, since we are about 1 or 2 °C higher than the T_m of inputs, and inhibitors bind about 100x tighter than inputs, we still make the assumption that inhibitors can hybridize to templates occupied by either input or output with hybridization rate k_a, (i.e. as if hybridizing to an unoccupied template). Then, the rate of the reverse reactions ("input (or output) displacing inhibitor") can be calculated from the equilibrium constant of the reaction, i.e. the difference in affinity between activators and inhibitors, which we approximated for every sequence at toe = 10^{-2}.

- *Bst* DNA polymerase and ttRecJ are processive enzymes, so we assume that there is no accumulation of partially polymerized or partially degraded inputs or inhibitors.
- Enzymes rates and Michaelis constants were kept to the same value for all DNA substrates. When fitting experimental curves, we adjusted (by hand) the specific dissociation rate of each species to compensate for the substrate dependency of enzymatic rates and affinity.

From a first set of measured or predicted parameters, we used the experimental curves of Figure 3.6-E to optimize the enzymatic and thermodynamic parameters (Table 3.3). This set of adjusted parameters was then used for all the simulations presented in this work, including the push-push memory circuit. In this last case, for the two additional inhibitors (iδα and iδβ), we directly used dissociation constants calculated with DINAMelt[3].

In the context of the DNA-toolbox, it is possible to obtain a very good computational estimate of the dissociation constants of the different species: inhibitors iα and iβ were chosen for their predicted dissociation constants (4.8 nM^{-1} for iα and 1.1 nM^{-1} for iβ) that were in the desired range (i.e. about two order of magnitude higher than α and β). These parameters can also be easily measured with a DNA melting experiment, which gave the values used in the detailed model (4.8 nM^{-1} for iα and 1.4 nM^{-1} iβ). Experimental and predicted values are very close, which is a great advantage compared to the system previously reported by Montagne et al., where the presence of trehalose (used to stabilize the mesophilic exonuclease $RecJ_f$) and EvaGreen (intercalating dye) impacted on the melting behavior of DNA duplexes and were hindering the direct estimation of the thermodynamic values using standard algorithms [62].

Enzymatic parameters were measured using the assays previously described in Montagne et al. (23). For ttRecJ, we found similar enzymatic rates for α, β, iα and iβ (300 ± 8 nM/min) and roughly similar

[3]Using DINAMelt (http://mfold.rna.albany.edu/?q=DINAMelt)

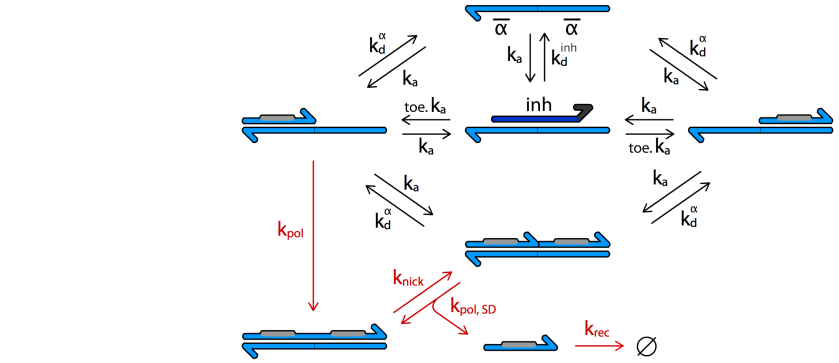

$$A'(t) = k_d^\alpha . (A\alpha(t) + \alpha A(t)) + k_d^{inh} . Ainh(t) - k_a . A(t) . (2\,\alpha(t) + inh(t))$$

$$\alpha A'(t) = k_a . \alpha(t) . (A(t) - \alpha A(t)) + toe . k_a . \alpha(t) . Ainh(t) + k_d^\alpha . \alpha A\alpha(t) - k_a . inh(t) . \alpha A(t) - k_d^\alpha . \alpha A(t) - \frac{k_{pol}\,\alpha A(t)}{K_m\left(\frac{\alpha A\alpha(t)}{K_{m,SD}} + \frac{\alpha A(t)}{K_m} + 1\right)}$$

$$A\alpha'(t) = k_a . \alpha(t) . (A(t) - A\alpha(t)) + toe . k_a . \alpha(t) . Ainh(t) + k_d^\alpha . \alpha A\alpha(t) - k_a . inh(t) . A\alpha(t) - k_d^\alpha . A\alpha(t)$$

$$A\alpha\alpha'(t) = \frac{k_{pol} . \alpha A(t)}{K_m\left(\frac{\alpha A(t)}{K_m} + \frac{\alpha A\alpha(t)}{K_{m,SD}} + 1\right)} + \frac{k_{pol,SD} . \alpha A\alpha(t)}{K_{m,SD}\left(\frac{\alpha A\alpha(t)}{K_{m,SD}} + \frac{\alpha A(t)}{K_m} + 1\right)} - \frac{k_{nick} . A\alpha\alpha(t)}{K_{mn}\left(\frac{A\alpha\alpha(t)}{K_{mn}} + 1\right)}$$

$$\alpha A\alpha'(t) = k_a . \alpha(t) . (A\alpha(t) + \alpha A(t)) - 2\,k_d^\alpha . \alpha A\alpha(t) + \frac{k_{nick} . A\alpha\alpha(t)}{K_{mn}\left(\frac{A\alpha\alpha(t)}{K_{mn}} + 1\right)} - \frac{k_{pol,SD} . \alpha A\alpha(t)}{K_{m,SD}\left(\frac{\alpha A\alpha(t)}{K_{m,SD}} + \frac{\alpha A(t)}{K_m} + 1\right)}$$

$$Ainh'(t) = k_a . inh(t) . (A(t) + A\alpha(t) + \alpha A(t)) - 2\,toe . k_a . \alpha(t) . Ainh(t) - k_d^{inh} . Ainh(t)$$

$$\alpha'(t) = k_d^\alpha . (A\alpha(t) + \alpha A(t) + 2\,\alpha A\alpha(t)) + k_a . inh(t) . (A\alpha(t) + \alpha A(t)) - k_a . \alpha(t) . (2\,A(t) + A\alpha(t) + \alpha A(t) + 2\,toe . Ainh(t)) + \frac{k_{pol,SD} . \alpha A\alpha(t)}{K_{m,SD}\left(\frac{\alpha A\alpha(t)}{K_{m,SD}} + \frac{\alpha A(t)}{K_m} + 1\right)} - \frac{k_{rec} . \alpha(t)}{K_{m,input}\left(\frac{\alpha(t)}{K_{m,input}} + \frac{inh(t)}{K_{m,inh}} + 1\right)}$$

Figure 3.14: Schematic of the full set of reactions relative to a reaction circuit where input α only interacts with template α*to*α, and the corresponding set of ordinary differential equations. α*to*α is noted A for simplicity of notation. Red arrows indicate enzymatic reactions. Periods indicate multiplications. Dissociation rates (in min^{-1}) were calculated as $k_d = k_a/K_d$

Michaelis constant for inhibitors iα and iβ (150 ± 10 nM). However, we found Michaelis constant for input α and β to be higher (440 ± 100 nM), suggesting a higher affinity of ttRecJ for longer substrates (inhibitors). This was also the case for $RecJ_f$ used in Montagne *et al.* [62]. We thus assigned two different parameters for inputs and inhibitors. For Nt.BstNBI, we found Michaelis constants of 30 ± 10 nM for α and β. We however kept one single value for all input species, which would be compensated by adjusting each input dissociation rate during the fitting process.

3.7.3.5 Perturbation of the bistable and switching threshold

As shown in Figure 3.13, the simple model fails to describe the actual resilience of the bistable to perturbation in concentration of its inputs (α and β). We thus used the detailed model of the bistable,

			Starting values	Fitted values	Drift from starting values
Association rate ($nM^{-1}.min^{-1}$)		k_a	0.06	0.06	0
Dissociation constants (nM^{-1})		K_d^{α}	**0.014**	0.013	-8%
		K_d^{β}	**0.006**	0.0045	-25%
		$K_d^{i\alpha}$	**4.8**	5.3	+10%
		$K_d^{i\beta}$	**1.4**	1.3	-8%
		K_d^{γ}	0.007	0.016	+128%
		K_d^{δ}	0.02	0.038	+90%
		$K_d^{i\delta\alpha}$	4.8	4.8	0
		$K_d^{i\delta\beta}$	3.5	3.5	0
Enzymatic maximum rates ($nM.min^{-1}$)	*Bst* DNA polymerase	k_{pol}	**1200***	2100	*
		$k_{pol,SD}$	**40***	420	*
	Nt.BstNBI	k_{nick}	**58 ~ 720**	80	
	$ttRecJ_f$	k_{rec}	**300**	300	0
Michaelis constants (nM)	*Bst* DNA polymerase	K_m	**44***	80	*
		$K_{m,SD}$	**3.5***	5.5	*
	Nt.BstNBI	K_{mn}	**30**	30	0
	$ttRecJ_f$	$K_{m,input}$	**440**	440	0
		$K_{m,inh}$	**150**	150	0

Table 3.3: Set of parameters of the detailed model. Values in bold were experimentally measured. Dissociation constants were otherwise predicted using Dinamelt. *Enzymatic parameters for *Bst* DNA polymerase were measured in different conditions (at 38.5 °C instead of 42 °C and in a different buffer [62]), making irrelevant the calculation of a drift from the starting values. We noticed one order of magnitude fluctuations in the batch-to-batch activity of the commercial nicking enzyme Nt.BstNBI sold by New England Biolabs. Consequently, we needed to adjust the concentration of this enzyme in the interval from 32 to 400 units/mL, in order to get consistent experimental results, using the assay of Figure 3.11 for each new batch. After this experimental adjustment of the concentration of nicking enzyme, we kept a single value of k_{nick} for the simulations.

let it settle on its steady state for 100 minutes, and then added pulses of α or β (as Gaussian spikes). In Figure 3.15, we plot the state (A or B) of the bistable 500 minutes after the injection, as a function of the normalized concentration of injected input, for example α/β_{ss} (ratio of injected α on concentration of β at the steady state) or β/α_{ss} (ratio of injected β on concentration of α at the steady state). Both sides appear to behave relatively symmetrically, and require an injection of opposite input of more than 20-fold the concentration of input at the steady-state, in order to flip between states.

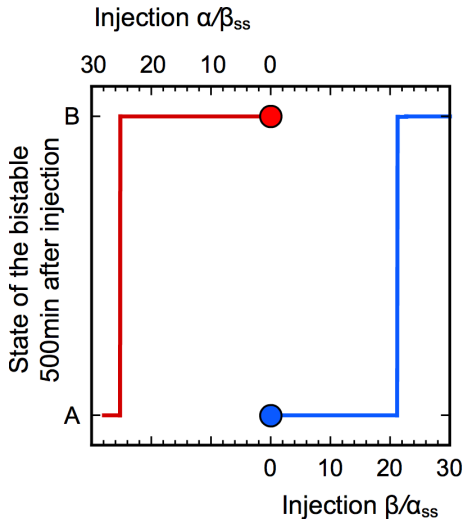

Figure 3.15: Numerical simulation of the switching of the bistable with the detailed model. The system, initially in state A (blue dot) or B (red dot) is perturbed by a Gaussian spike of input of the opposite species, from 0 to 30-fold the current steady concentration. The plot gives the state observed 500 minutes after the injection.

3.7.3.6 Activation module

An activation module is a template that amplifies a short spike of its input into a long-lasting pulse of its output. As an example, activation module $\delta to \beta$ is activated by δ, but also acts as a "refuge" for δ: in hybridized (and elongated) state, δ is protected from ttRecJ that specifically targets single-stranded substrates. δ is thus able to stay in solution for longer than without "refuge" templates, and thus activate the production of a long-lasting pulse of β. Figure 3.16 shows the predicted time plot of α and β concentrations produced by 5 nM of the corresponding activation module, compared to a direct injection of α and β.

3.7.3.7 Push-push strategy

In the push-push memory circuit, the current state of the bistable core is fed back to the two activation modules. This allows the system to decide which internal specie (α or β) to produce upon reading of the single external input δ, depending on its current state. We checked the validity of this strategy with the detailed mathematical model. In the absence of autocatalytic modules $\alpha to \alpha$ and $\beta to \beta$ (Figure 3.17-A), we impose a fixed concentration (40 nM) of non-degradable internal input α or β, and set a spike of 30 nM of external input δ. Figure 3.17-B shows that the system responds with the production of a large pulse of the species that is initially absent (i.e. β if the system is in A state, and conversely).

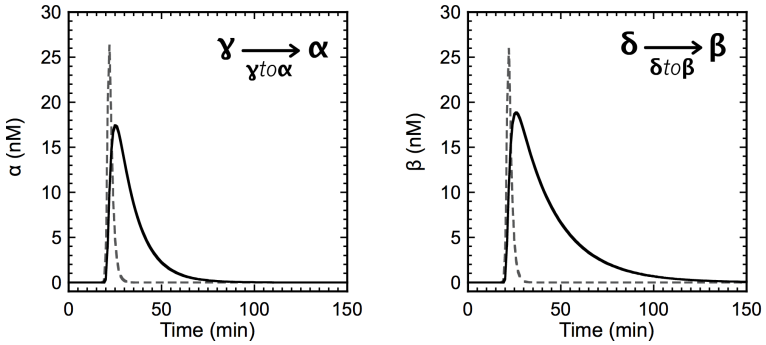

Figure 3.16: Predicted time plots of the concentration of α (left) and β (right) produced by the activation module γ*to*α or δ*to*β (5 nM) upon injection of 30 nM of the corresponding input γ or δ. These curves (plain lines) are compared to direct spike of 30 nM of α or β (dashed lines). These predictions were generated with the detailed model.

Still, the model predicts that the charge level of β*to*iα (for β imposed) and α*to*iβ (for α imposed) is transiently slightly exceeding 1, which indicates a small leak production of the current internal species. Note that no switching is expected here since the state is externally imposed at all times (and no autocatalytic module is present).

3.7.4 Reamplification

	α		β	
Bistable state	A	B	A	B
Sample dilution	1000	100	100	1000
Measured Concentration (pM)	55	0.82	0.68	40
Concentration in aliquots (nM)	55±2	0.082±0.008	0.068±0.004	40±7

Table 3.4: Measured concentrations of α and β at the steady state of the bistable in state A and B.

Here, we used a previously reported method [62] to experimentally measure the concentrations of α and β when the bistable switch is asymptotically converging toward one or the other of its two dynamic stable states.

The system was initiated with {α, β} = {10 nM, 0.1 nM} or {0.1 nM, 10 nM}, and allowed 150 minutes to reach one of its steady states, respectively A or B (as judged by the fluorescence signals). We then withdrew aliquots from the solutions and immediately quenched them by 10x dilution in 95 °C mQ water followed by a 5 minutes incubation at the same temperature. Dilution of these samples were then amplified by isothermal amplification at 50 °C in presence of template α*to*α (20 nM) or β*to*β

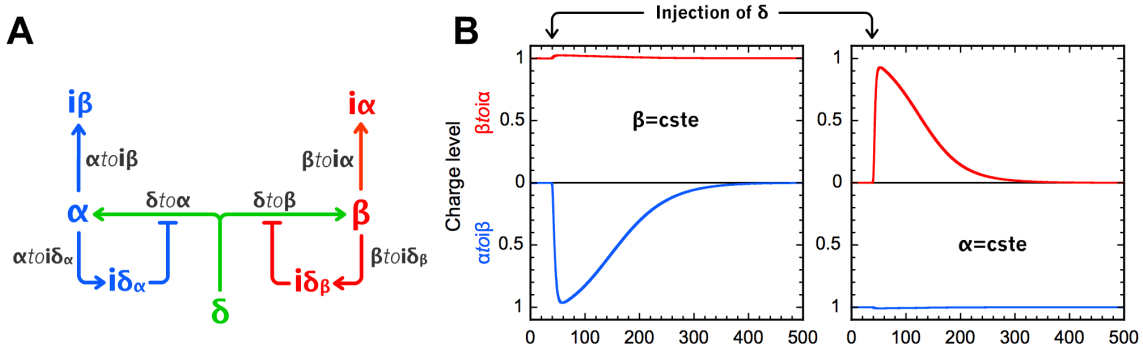

Figure 3.17: Structure and function of the injection layer for the push-push memory system. (A) Inhibition modules $\alpha to i\delta\alpha$ and $\beta to i\delta\beta$ produce respectively $i\delta\alpha$ and $i\delta\beta$, depending on the presence of either α or β. Inhibitors $i\delta\alpha$ and $i\delta\beta$ inhibit the activation modules $\delta to\alpha$ and $\delta to\beta$. In the resulting circuit, in the presence of α, $\delta to\alpha$ is inhibited, and injection of the external input δ will only activate $\delta to\beta$, hence produce β. Conversely, in presence of β, only $\delta to\alpha$ will be sensible to external input δ. (B) Theoretical time traces of the charge level of the templates $\beta to i\alpha$ and $\alpha to i\beta$ either when the constant presence of α is imposed and a short pulse of δ is applied (left), or when the constant presence of β is imposed and the same short pulse of δ is applied (right).

(30 nM) with *Bst* DNA polymerase (8 units/ml) and Nt.BstNBI nicking endonuclease (100 units/ml). The reaction was performed in a thermocycler set at a constant temperature (50 °C) and monitored with 1x EvaGreen intercalating dye as described. Using the built-in software, concentrations of α and β were determined from the shape of the amplification curves by comparison with calibration curves built from UV-calibrated concentrations of pure α or β. Results are displayed in Table S4.

3.7.5 Push-push memory circuit

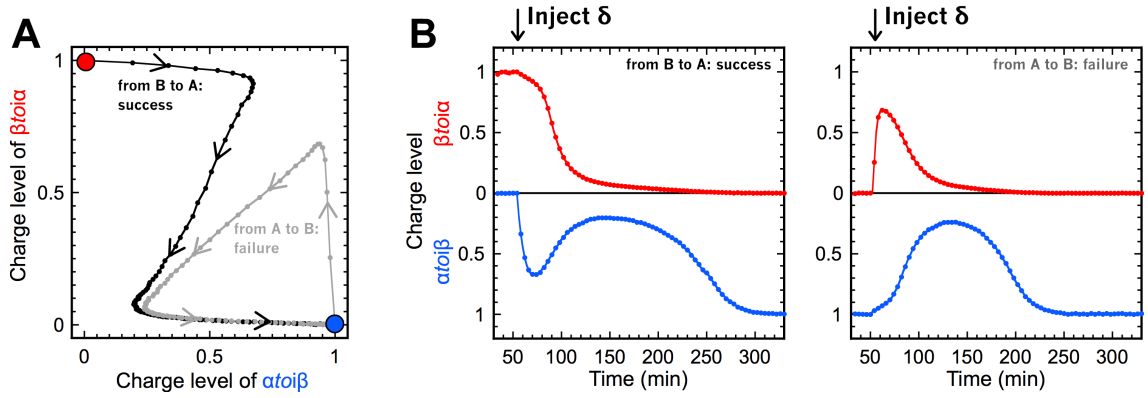

Figure 3.18: Experimental trajectories (A) and time plots (B) of the push-push memory circuit with $\delta to\alpha = \delta to\beta = 5$ nM and $\alpha to i\delta\alpha = \beta to i\delta\beta = 4$ nM. Upon addition of 30nM of δ, the circuit switched from B to A, but failed to switch from A to B.

	Switching from	
[β*to*iδβ] (nM)	A->B	B->A
0.6	✓	
0.8	✓	
1	✓	✓
1.2		✓

Table 3.5: Experimental result of the push-push memory circuit (with δ*to*β = 10 nM, δ*to*α = 5 nM and α*to*iδα = 4 nM) flipping between states for different concentrations of inhibition module β*to*iδβ.

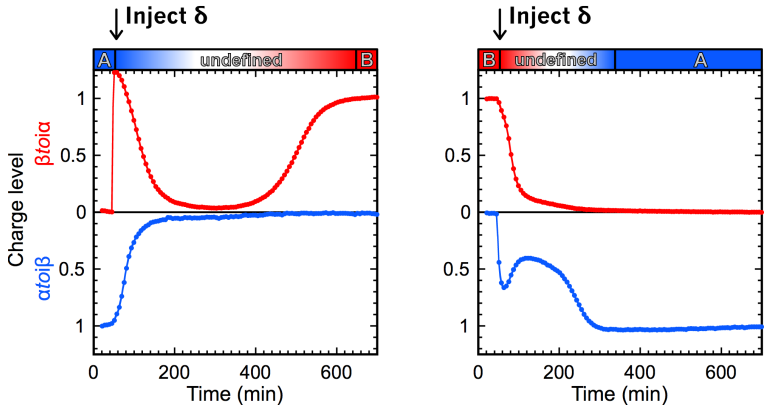

Figure 3.19: Experimental time plots (same data as Figure 3.7) of the push-push memory circuit with δ*to*α = 5 nM, δ*to*β = 10 nM, α*to*iδα = 4 nM, and β*to*iδβ = 1 nM. Upon addition of 30nM of δ, the circuit switched from A to B (left), and from B to A (right).

In the assembly of the push-push memory circuit, we kept the templates of the bistable core at the same concentrations as for the memory circuit and the bistable circuit, and adjusted the concentration of the 4 templates that encode the push-push function. The detailed model suggested that the full circuit would work with concentrations of activation modules δ*to*α and δ*to*β at 5 nM and inhibition modules α*to*iδα and β*to*iδβ at 4 nM. In these conditions, upon addition of 30 nM of δ, the experimental push-push circuit successfully switched from B to A, but failed to switch from A to B (Figure 3.18). This result pointed out that a stronger amplification of input β was required to push the circuit (initially in state A) to the basin of attraction of state B. We consequently adjusted the concentrations of δ*to*β (to 10 nM) and β*to*iδβ to obtain a working point where the push-push memory circuit could switch in both directions. Table 3.5 displays the experimental results of the fine-tuning of the concentration of β*to*iδβ, showing that the strength of the negative feedback (performed by β*to*iδβ) must be carefully adjusted in order to reach a reversible working point. Experimental trajectories of the push-push memory circuit (Figure 3.7) are shown as time plots on Figure 3.19.

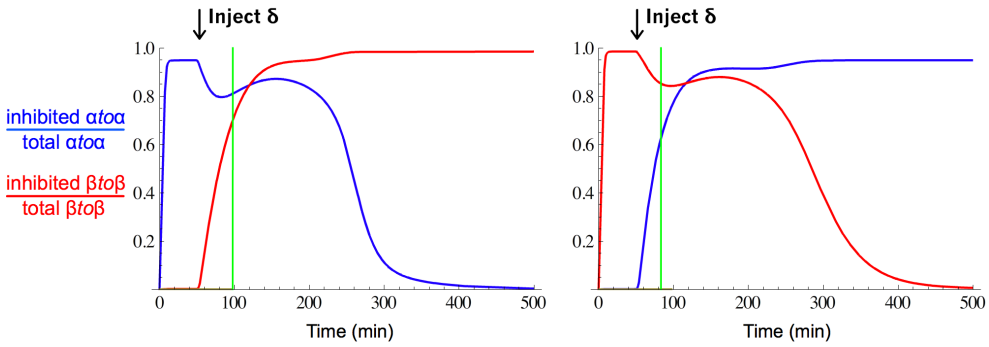

Figure 3.20: Predicted time plots of the proportion of inhibited $\alpha to \alpha$ and $\beta to \beta$ during a switching of the push-push from B to A (left) and A to B (right). The green line shows where the trajectories apparently cross on Figure 3.7: one observes that they in fact correspond to two different proportions of inhibited $\alpha to \alpha$ and $\beta to \beta$.

The discrepancy between the predicted concentrations ($\delta to \beta = 5$ nM, $\beta to i\delta\beta = 4$ nM) and the ones that gave good experimental results ($\delta to \beta = 10$ nM, $\beta to i\delta\beta = 1$ nM) can be explained by the method we used to adjust the model parameters. As detailed in SI Appendix, Section 3.7.3.4, we took the same enzymes parameters for all substrates, then compensated the substrate-dependent enzymatic rates and Michaelis constants by adjusting the specific dissociation rate of each input and inhibitor.

This method worked well in the case of the two-input memory circuit, where each input activates only one activation module. In the push-push memory circuit, however, δ activates both $\delta to \alpha$ and $\delta to \beta$, forming two substrates for which polymerase and nickase are likely to display different rates and affinities. These won't be possible to equilibrate as we adjust a single parameter for δ. In reality, δ might also have two different binding constants for $\delta to \alpha$ and $\delta to \beta$: ideally, one would have to independently measure the hybridization / dissociation kinetics of all duplexes, and enzymatic rates and Michaelis constants for all substrates. In the present study, we showed that we could obtain a relatively good agreement between the detailed model and the experiments without going into such details.

3.7.6 Long-term experiments

One Figure 3.6 of the main text, we showed that the two-input memory circuit could be switched from one state to the other, then back to the initial state. However, further switching was not successful. Similarly, re-activating the push-push system after a first switch did not result in a complete switching. These observations should probably be attributed to the very long time that is necessary to perform such experiments: in the case of the two-input memory circuit, each switching event takes about 200 minutes (Figure 3.6) and in the case of the push-push network, up to 600 minutes (Figure 3.19-left).

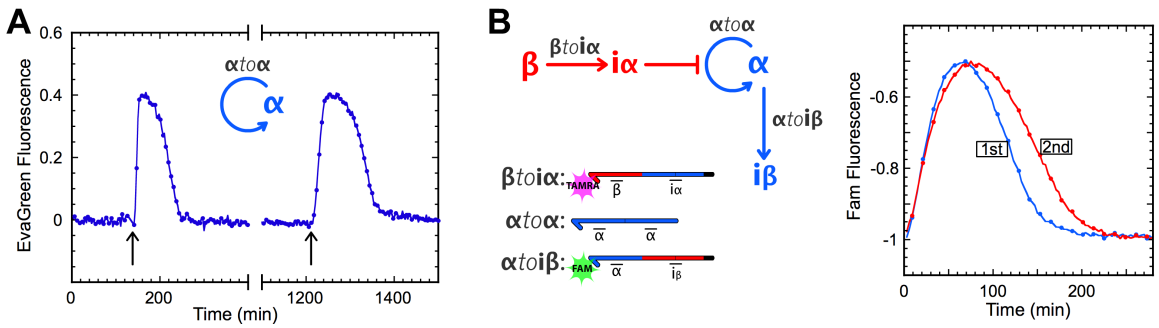

Figure 3.21: Checking the viability of the circuit over time. (A) Autocatalytic module α*to*α (20 nM) is given dNTPs (20 µM) and input α (1 nM) at the times marked by an arrow: first at t = 140min, then at t = 1220 min. After having consumed all dNTPs, it stops producing α: fluorescence level gets back to the baseline level. Reaction is monitored with EvaGreen intercalating dye that reports on the total amount of double-stranded DNA in solution. (B) Autocatalytic module α*to*α (5 nM) is inhibited by iα produced by β*to*iα (20nM) upon injection of β (80 nM). Reaction is monitored with the FAM label of α*to*iβ (20 nM): fluorescence increases as α*to*α is inhibited. Following a first inhibition (blue curve) a second is triggered 500 minutes later (red curve).

Over this extended time, dNTPs will unavoidably deplete, enzymes loose activity and template strands decrease in concentration. Our best hypothesis to explain these experimental observations is that one of these changes, or possibly a combination of some of them, will ruin the delicate balancing of the various reactions, which is necessary for the correct functioning of the circuit[4]: one may imagine that a decreased, say, nicking activity may favor one side of the switch over the other, and this would drive the system away from its bistable area. Moreover, because the bistable core is continuously active over the course of the reactions (continuously producing –and degrading– new oligonucleotides), it is possible that side reactions, even with low probability or very slow rates, may ultimately produce deleterious effect on the circuit.

This hypothesis is supported by experiments showing that the activity of various subparts of the networks do change over time, and not necessarily in a proportional or predictable manner. Two such simple experiments are presented on Figure 3.21. On the experiment of Figure 3.21-A, autocatalytic module α*to*α is activated once upon administration of a small quantity of dNTPs, and is then left in the presence of the three enzymes, but no dNTPs, for a thousand minutes. When activated again with the same amount of dNTPs, αtoα does not amplify as sharply and takes more time to consume all the

[4]With this hypothesis, the fact that the *Oligator* of Montagne *et al.* could still oscillate after 4000 minutes could be attributed to a higher robustness of the network design, which does not rest upon the delicate balance of two symmetrical nodes. It is also probable that the complete switching between two autocatalytic modules that happens in the bistable circuit (i.e. extinction of one and establishment of a steady state of the other) puts more strain on the system than a complete cycle of the Oligator (where the autocatalytic module never gets to 0 nor to its steady state concentration, but oscillate around a value somewhere in between). The fact that the operation of the two-input memory circuit requires repetitive additions of small volumes of input (hence changes in concentration of the constituents of the system) may also have an impact on the long-term functioning of the system.

dNTPs. The experiment of Figure 3.21-B shows two successive inhibitions of α*to*α: here also, αtoα is more strongly inhibited during the second inhibition. On the one hand, this suggests a loss of activity of α*to*α, but on the other hand, this shows that β*to*iα is still handling well its function. These two experiments suggest that it may indeed be some variation in the relative "strength" of the subparts that leads to the loss of function of the global system.

Below, we tentatively discuss one of the many mechanisms that may lead to such evolution over time and possibly hinder the long-term performance of the circuit.

One issue may lay in the slow degradation of the templates by the exonuclease (Figure 3.10). In Section 3.7.5 of the SI, we have seen that the push-push memory circuit was very sensible to a variation in template concentration: the circuit worked for 1 nM of β*to*iδβ, but its ability to switch in both directions was lost when this value was increased or decreased by 20%. As a circuit is running, the exonuclease may slowly degrade all the templates, potentially disrupting the ratios of templates concentrations in the circuit; it turns out that we have not found a perfect protection against ttRecJ. Besides, the actual behavior of ttRecJ with respect to phosphorothioate (PT) linkages (used to protect the 5' end of all templates) is not known.

PT linkages are inherently chiral: Yang et al. [162] reported that Exonuclease III stops on R isomers, but digests S ones. If ttRecJ was to behave the same, we would have, roughly, 50% of intact templates, 25% of templates with 1 base missing, 12,5% of templates with 2 bases missing, and 12,5% of templates entirely digested. In the case where PT linkages would just slow down ttRecJ, all templates would be degraded little by little throughout the reaction. Given the results of Figure S2, we might be facing both behaviors at the same time: degradation curves for 2 PT and 3 PT display an initial quick decrease, then a slower linear slope.

In any case, templates are likely to loose activity because of (i) decrease of their concentration, (ii) loss of one or two bases in 5', which would results in the production of truncated output (with one or two bases missing in 3'), less stable on their target template (i.e. weaker activators). Then, an explanation for the results shown on Figure 3.21-B (i.e. inhibition module β*to*iα still properly handling its function) would be that inhibition modules spend most of their time in duplex with the inhibitor that they produce (iα has a predicted T_m of 51.3 °C on βtoiα): in this duplex form, they are protected from the single-stranded specific exonuclease and consequently degrade more slowly.

Note however that the mechanism discussed above would not explain the difference in durability of two similar templates like α*to*α and β*to*β, but more a departure from the general balance of the system.

Chapter 4

Toward memory circuits

In this chapter, we present the progression that led to a better understanding and harnessing of the tools forming the DNA-toolbox, and ultimately to the work presented in the previous chapter. This progression was littered with challenges that ranged from hunting for the good exonuclease to finding a good strategy to assemble circuits displaying bistability. Amongst others, we sought for different designs of bistable circuit, as well as a good way to reversibly update their state, but also worked on the roots of the DNA-toolbox, defining the design rules for autocatalytic and inhibiting sequences, and tried to stabilize on the long-term these reactions occuring in a closed system.

4.1 Enzymes activity

Enzymes are able to catalyze a variety of reactions within a DNA strand or between two separate DNA strands. The reactions of the DNA-toolbox are catalyzed by three enzymes: a polymerase (*Bst* DNA Polymerase, Large Fragment), a nicking endonuclease (Nt.BstNBI) and an exonuclease ($\mathrm{RecJ_f}$, which we eventually replaced by ttRecJ). With the exception of ttRecJ, all enzymes are commercial ones, and we noticed a large difference in activity from batch to batch (we experienced up to a 10x difference for Nt.BstNBI and a 100x difference for $\mathrm{RecJ_f}$). Our systems are very sensible to the activity of enzymes, and the readjustment of enzymes conditions demanded numerous experiments. More than just a variation in their activity, batches sometimes presented some not characterized parasitic activity that hindered the global functioning of our systems. Figure 4.1 shows two example experiments: a simple comparison between two batches of Nt.BstNBI for a simple amplification reaction, and a ramp

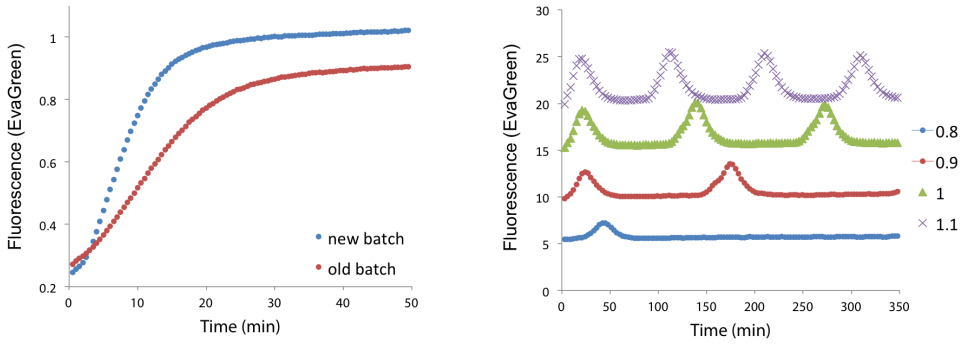

Figure 4.1: Left: Simple amplification of T11 (5'-TCGAGTCTGTT-3') in presence of 100 nM of its associated autocatalytic template. The two curves correspond to the same reaction mix to which the same concentration of Nt.BstNBI from an "old" (red) or a "new" batch was added. Fluorescence data of EvaGreen is divided by that of ROX reference dye, removing machine-related variation of fluorescence intensity. Amplification performs at a different rate, and the reactions reach a different steady state, which suggests a difference in the activity between these two batches. Right: Ramp of *Bst* DNA Polymerase on the oscillating system further presented in chapter 6. Curves were offseted for visibility. A variation of 10 % of polymerase concentration dramatically modifies the kinetics of the system.

of concentration of polymerase for oscillations.

We had to change from one batch of enzyme to an other a large number of times, and number of experiments were done to find the "good" enzymes conditions for a given system. Moreover, the experiments presented in this chapter were performed over a long period of time, with many different batches of enzymes displaying changing activities. In consequence, the concentrations of enzymes for each experiment do not seem to be a relevant information, and will be omitted in this chapter.

4.2 Bistable Switch: a design out-of-the-toolbox

In this design, two autocatalytic modules swA and swB are repressing each other without intermediary sequences (Figure 4.2-A). This bistable switch relies on some form of bifunctionality: the same strand is able to activate its own production and repress the production of an other strand. Such function is not part of the standard DNA-toolbox, and consequently we have to rely on some DNA-related trick.

The functioning of this circuit is clarified on Figure 4.2-B: swA autocatalytically produces strand a, that binds on the input site of swB, thus inhibiting the production of strand b. The same goes for swB, which, when active, inhibits the production of strand a. More precisely, on the one hand, strand a binds with a low affinity on the input site of swA (the 5' end of strand a is mismatched on the input site of swA, see Figure 4.2-C). On the other hand, strand b (produced by active swB) binds with a

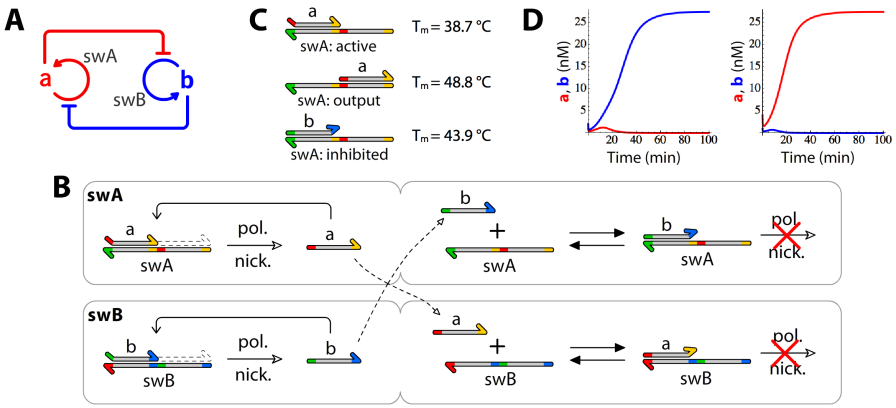

Figure 4.2: A bistable switch out-of-the-toolbox. (A) Topology of the circuit: two templates (swA and swB) are autocatalytically producing signal molecules (respectively a and b) that directly repress the activity of the opposite template. (B) Schematic of the reactions for swA (up) and swB (down). For swA, strand a can bind on the input site with a mismatched 5' end. Through the work of a polymerase and a nickase, it allows the production of another strand a. Strand a can also bind on the input site of template swB with a mismatched 3' end, preventing the polymerase to elongate this substrate. Template swB follows a symmetric scheme. These reactions should encode for "if a then not b" and "if b then not a". (C) Stability of the duplexes calculated (Dinamelt) for swA (5'-T*A*G*T*GACTCTGCC-TAGTGACTCTGGG-3'), swB (5'-A*T*G*T*GACTCTGGG-ATGTGACTCTGCC-3'), a (5'-GGCAGAGTCACTA-3') and b (5'-CCCAGAGTCACAT-3'). Strand b is more stable than strand a on the input site of swA, in order to inhibit the production of a. (D) Calculated time plots of the bistable switch started with {[a], [b]}={1nM, 2nM} (left) and {4nM, 1nM} (right). After some transient, the system finds a steady state of production of either a or b (but not both). These time plots were calculated for a concentration of swA and swB of 20 nM, at 40 °C.

higher affinity than strand a on the input site of swA (Figure 4.2-C). Having its 3' end mismatched on swA, strand b is preventing the polymerase from producing strand a from template swA. In this scheme, we expect strands a and b to be mutually exclusive: at the steady state, either a or b should be produced, but not both.

A simple model (that did not take the saturation of enzymes into account) with the calculated (Dinamelt) dissociation constant of a and b on swA and swB predicted that the system would exhibit a bistable behavior (Figure 4.2-D), provided realistic enzymatic reaction rate, on however a narrow window of carefully chosen concentrations of templates. Experimentally, we could confirm that b was inhibiting the activity of swA and a was inhibiting the activity of swB (in the concentrations of templates and temperature suggested by the model). Assembling the two templates did not, however, produce the expected bistable behavior. Several hypothesis can be done about this failure:

- the model required precisely balanced concentrations of swA and swB to work, which can be hard to obtain experimentally, considering an eventual asymmetry of the dissociation rates and

enzymatic rates and affinities.

- both templates had 4 phosphorothioate backbone modifications in their 5' end, and no U in the output nickase recognition site. We observed later that 3 phosphorothioates were already enough to dramatically decrease the nicking reaction speed (as discussed in Section 3.7.2.2). Four can just be worse.

- the autocatalytically produced strands (a and b) are very stable on their output site because they are matched on both sides (Figure 4.2-C). Thus, at the working temperature, we expect *Bst* DNA Polymerase to only work in strand displacement (it has to displace the hybridized output strand to polymerase a new output strand), making the autocatalytic production reaction slower.

- the relative strength of inhibitor vs activator might not be high enough (only about 5 °C of T_m difference). Yet, we know that in the case of the oligator, a difference of about 10 °C is required.

It should be possible to address these points, and (maybe) make this bistable circuit work properly. However, if ever working, it might still be hard to interface this system that uses some particularities of the oligonucleotides (i.e. the bifunctionality) that are not part of the toolbox and might not be cascadable or generalizable.

4.3 Bistable circuits with the DNA-toolbox

To construct a bistable with the DNA-toolbox, we selected a symmetric repressor-repressor design, where two autocatalytic modules repress the activity of each other through two inhibitor modules (Figure 3.2). We first designed a bistable switch circuit based on the autocatalytic templates of the oligator designed to work at lower temperature (c11bt, also used in Figure 2.5: 5'-C*T*TAGACTCAG-CTTAGACTCAG-3'), and another autocatalytic template, c11' (5'-A*C*TTGACTCTC-ACTTGACTCTC-3').

4.3.1 Working with mesophilic $RecJ_f$

We started to work using the same enzymes (i.e. *Bst* DNA Polymerase Large Fragment, Nt.BstNBI nicking endonuclease and $RecJ_f$ exonuclease) and buffer as for the original oligator [62]. We designed the two inhibition modules that make the link between c11bt and c11', and tried to monitor the reaction with a TAMRA fluorophore located on the autocatalytic templates, either c11bt or c11' -

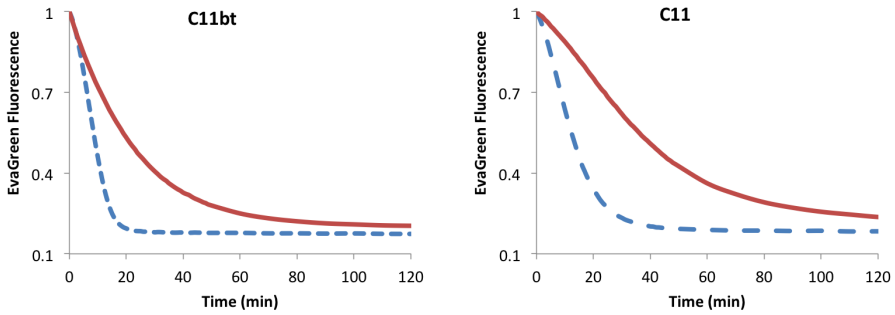

Figure 4.3: Comparison of $RecJ_f$ and cd-ttRecJ. Degradation of two non-protected substrates with $RecJ_f$ (dashed, blue curves) and cd-ttRecJ (red, solid curves). Whereas $RecJ_f$ shows a typical Michaelis-Menten kinetic, cd-ttRecJ seems to have a first order kinetic in these conditions. This reaction was performed at 38 °C with 500 nM of substrate, with a concentration of cd-ttRecJ of about 50 nM.

we realized later that this was causing the weak signal intensity obtained: the input-induced signal is crosstalked with the inhibitor-induced signal hybridizing a few bases away from the fluorophore (see Figure 2.3 in Section 2.4.2). Initially, we thought that the presence of trehalose (used to stabilize $RecJ_f$ at temperature higher than 37 °C) was to blame. This wasn't absolutely wrong: the fluorescence signal of both EvaGreen intercalating dye and attached fluorophore is notably decreased in presence of trehalose. We soon gave up working with mesophilic $RecJ_f$, which was not stable enough (even in the presence of trehalose) to allow the exploration of higher temperatures, where we could expect faster reactions kinetics.

4.3.2 Trials with thermophilic cd-ttRecJ, purified in-house

With the purpose of increasing the temperature of the reactions (thus probably gaining in speed), get rid of trehalose (used to stabilize the expensive $RecJ_f$, but that had also an impact on hybridization kinetics [62], decreased the fluorescent signal intensity and was hard to manipulate because of its viscosity), we looked for an alternative thermophilic exonuclease. Reported by Yamagata *et al.* [163], protein ttRecJ is cloned from the thermophilic bacterium Thermus thermophilus HB8; cd-ttRecJ corresponds to the core domain of ttRecJ and has a 5'->3' exonuclease activity. Reportedly, exonuclease cd-ttRecJ is stable up to 60°C, and shows an increase in activity up to 50°C [163]. With the help of Dr. Tabata (from Noji Lab., in University of Tokyo), we expressed, extracted and purified cd-ttRecJ, a thermophilic exonuclease which plasmid was obtained from Dr. Yamagata [163]. The protocol can be found in Appendix *Expression, extraction and purification of cd-ttRecJ.*

We checked the activity of cd-ttRecJ, which appeared to have a higher K_m than $RecJ_f$ (Figure

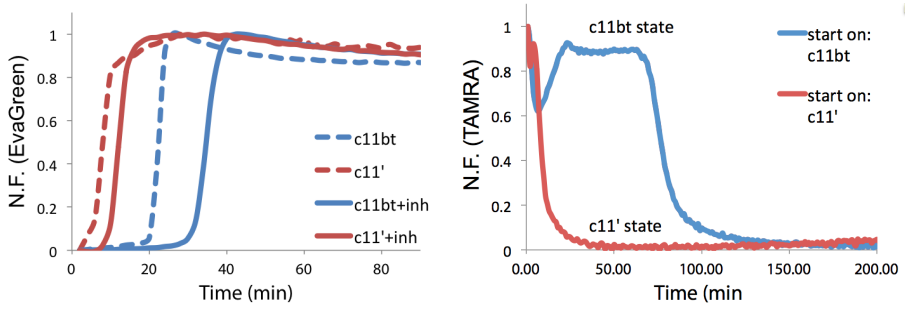

Figure 4.4: Bistable c11bt-c11' (Left) Amplification by c11bt and c11' in the absence (dashed) and presence (plain) of inhibitor strand (present in the same concentration as the autocatalytic module). In presence of inhibitor, the amplification start is delayed. (Right) Complete bistable system. Template c11' is labeled in 3' with TAMRA, which fluorescence is quenched in presence of c11' input. The system started with a small amount of input of either c11bt or c11'. Accordingly, the system takes the c11bt state (high fluorescence) or c11' (low fluorescence). However, after some time (around 70min), the system started on c11bt state self-switches toward c11' state (blue curve). These reactions were performed at 38°C, with concentration of 20nM for autocatalytic modules and 60nM for inhibitor modules.

4.3), as expected from the deletion of the nucleic acid binding domain [145]. We then restarted our experiments on the bistable circuit, this time with cd-ttRecJ. Still using c11bt and c11', we observed that c11' was much "stronger" (i.e. harder to inhibit) than c11bt (Figure 4.4-Left). In the context of the bistable circuit, the system started on c11bt side would spontaneously switch to c11' side after some time, which confirmed that c11bt had difficulties to efficiently inhibit c11' (Figure 4.4-Right).

Another problem arose at this point: as it can be seen on Figure 4.4-Left, the steady-states are not flat. We tentatively attributed their negative slope to a partial degradation by cd-ttRecJ. This was later confirmed (see Figure 4.10): whereas two phosphorothioates provided a good protection against RecJ [62], they were not enough to protect the templates against cd-ttRecJ. One could argue that, in the conditions of experiment of Figure 4.4-Left, templates produce a steady-state of output and are thus most of the time double-stranded (i.e. not targeted by cd-ttRecJ). However, due the working temperature being near the duplexes T_m (or even higher in the case of c11bt), these duplexes are not stable, and probable targets for cd-ttRecJ. We thus went back to the commercial, mesophilic $RecJ_f$ for some time.

4.3.3 Design and evaluation of autocatalytic modules

Having realized that autocatalytic modules (for instance c11bt and c11') could present high variations in amplification efficiency depending on their sequence, we worked at finding theoretical or empirical

rules to design new - potentially better balanced - sequences, and finding a way to evaluate their performance.

By comparing the melting temperature (T_m) of input sequences

Figure 4.5-Up displays the input sequences and experimental time plots of their amplification performed by their respective autocatalytic modules, without exonuclease. In this assay, all sequences do not appear to amplify identically: cS11 seems slower (compared to cZ11 that has a close T_m), cK11 diverges (unknown reason). Only looking at the stability of an input on its autocatalytic template is not a good way to evaluate its amplification performance.

Turnover experiment

In order to easily evaluate the efficiency of a given autocatalytic module, we introduced the "turnover" experiment. The idea is to put the autocatalytic module (with polymerase, nickase and exonuclease) in presence of a given amount of dNTPs, and look at the time it needs to consume them all. As the autocatalytic module runs out of dNTPs, it cannot sustain the steady state production of input/output: fluorescence of EvaGreen returns to the baseline level as input/output degraded by the exonuclease are not replaced by freshly produced ones. Then, using the same enzymatic and buffer conditions (containing the same concentration of dNTPs) for various autocatalytic modules, we could directly compare their turnover. Experiments of turnovers for cT11, cP11 and cZ11 are shown on Figure 4.5-Bottom: not only it reveals different behaviors (cT11 steady-state is never really reached - this will be discussed later on, in Section 4.6.3), but also allows to calculate the production rate of each templates in the experiment conditions. For instance, in the case of Z11, the limiting dNTP is G (Figure 4.5-Left): 5 dGTPs are used for each produced Z11. Thus, with 25 µM of dGTPs initially present, cZ11 can catalyze the production of 5 µM of Z11, that are mostly produced during the steady-state (plateau of the fluorescence curve). The steady-state is kept for about 55 min in the case of 30 nM cZ11, which leads to a production rate of roughly 90 nM/min. If the first order degradation rate (k_{1st}) of the exonuclease is known for this sequence, it is possible to directly extract the concentration of Z11 at the steady state.

Designing a library of autocatalytic modules using rational "design rules"

We then designed new autocatalytic modules following a few rules, for a sequence Ω11 of 11 bases:

	sequence 5'-3'	Tm (°C)
T11	TC**GAGTC**TGTT	39.5
K11	TG**GAGTC**ATCC	39.3
P11	AG**GAGTC**AGTG	39.3
Q11	AG**GAGTC**ACAC	39.9
S11	TG**GAGTC**ACTG	41.1
Z11	TG**GAGTC**AAGG	41

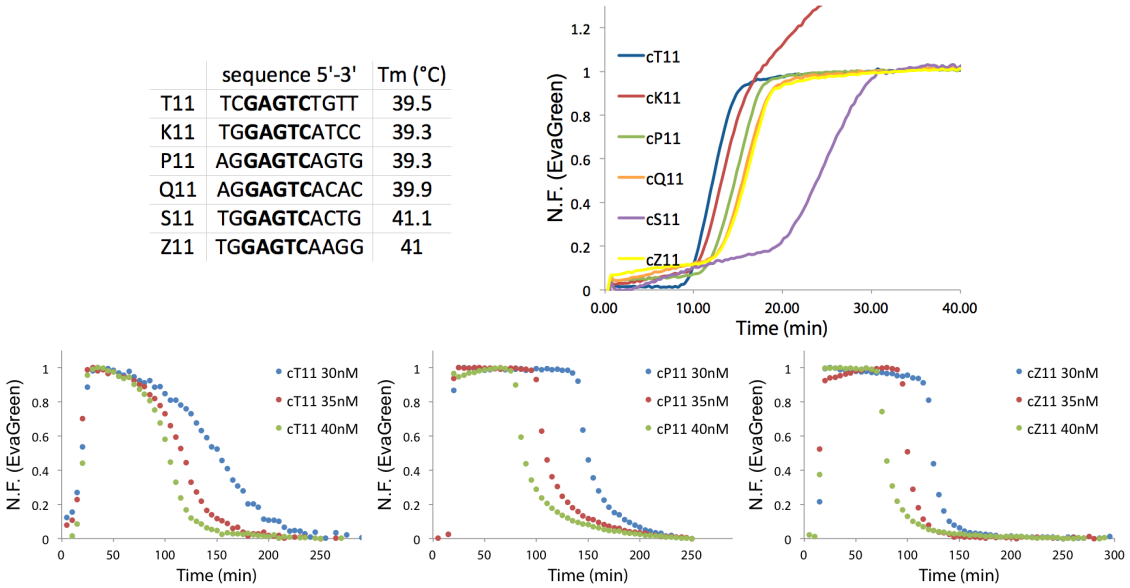

Figure 4.5: (Left) Amplified sequences and calculated T_m. (Right) Fluorescence curves of amplification (self-start, i.e. without primer) at 38.5 °C, in the absence of exonuclease. Templates are present in concentration of 60 nM. (Bottom) Turnovers for cT11, cP11 and cZ11 at 38.5 °C with 25 µM of dNTPs, and three different concentrations of autocatalytic modules.

1. Ω11 has to include the nicking enzyme recognition site.

2. Amplified sequence Ω11 should not end with a G in 3', which would make an unwanted nickase recognition site appearing on the inhibition module Ω*to*inh? in the case of a 8-6 inhibitor (i.e. an inhibitor forming 8 base-pairs on the input site and 6 base-pairs on the output site of the target autocatalytic module).

3. Amplified sequence Ω11 should not end with GA, which would make an unwanted nickase recognition site appearing on the inhibition module Ω*to*inh? in the case of a 7-6 inhibitor (that is, those that we adopted for the final version of the bistable circuit).

4. Ω11 (as well as the corresponding autocatalytic module) should not present any secondary structures (that could lead to self-triggering in the case of a self-fold with a matched 3', or other uncontrolled behaviors) or interactions between two Ω11 (to avoid primer dimer).

5. The melting temperature of Ω11 should be not too high nor too low (i.e. should not be composed of too many C and G or A and T).

6. For the following sequences, we also avoided double C or double G, in order to limit the sequences domain to search.

Scrutinized sequences are shown on Figure 4.6 and 4.7.

Evaluating the new sequences

Evaluation of the new sequences was done by comparison with a previously designed (and efficiently amplifying) autocatalytic module: cX11. We first performed a simple amplification (Figure 4.8-Left). As all sequences seemed to amplify well, we checked their turnover (as defined previously) in presence of 40 µM dNTPs (Figure 4.8-Right). The application of the few design rules presented before proved to be successful: all autocatalytic modules amplified correctly (Figure 4.8-Left), contrarily to some of the ones used in Figure 4.5-Right. These rules were however not sufficient to insure the efficiency of all sequences: the turnover experiment (Figure 4.8-Right) helps finding out which sequences should be discarded. To compare the autocatalytic modules, we can calculate their normalized plateau time with regard to cX11: $S = \frac{N.T}{N_{cX11}.T_{cX11}}$ with N the number of limiting dNTP per polymerized oligonucleotide and T the plateau time. This gives $S_{cW11} = 0.73$, $S_{cE11} = 0.86$, $S_{cR11} = 0.87$, $S_{cX11} = 1$, $S_{cN11} = 1.21$, $S_{cD11} = 2.66$. In the present case, one might want to avoid working with cD11 (which is slow) or cR11 (which shows a tilted plateau).

Sequence dependence of DNA exponential amplification (EXPAR [105]) is still not well understood, but has been the subject of a recent study [158], in which the Qian *et al.* characterized the performance of about 400 templates. They notably observed that GA or AG dimers-rich sequences were poorly performing. Interestingly, one of our "strongest" autocatalytic template (cP11, see Figure 4.5) has very few AG dimer (i.e. a lot in the amplified sequence, as displayed in Figure 4.5). For future design of autocatalytic templates, one may consider including the rules proposed by Qian *et al.* [158].

4.3.4 Design rules for inhibitors

Inhibitor strands are referred to as inhΩ11-ab where "Ω" is the autocatalytic module targeted, "a" is the number of bases that will bind on the input site of the target template, and "b" the number of bases that will bind on the output site. For instance, inhT11-76 targets cT11 and binds with 7 bases on its input site and 6 bases on its output site. Inhibitors should be more stable than inputs in order to block autocatalytic modules. Montagne *et al.* [62] proposed that the T_m of an inhibitor should be about 10 °C higher than that of the target input, which was the case for the oligator. In the case of a bistable circuit, the importance of the inhibitor binding strength can be deduced from the analysis of a simple model of the circuit (as described in Section 3.7.3.1). Roughly speaking, the

Complementary of the amplified sequence	Tm of most stable secondary structure	Tm of amplified sequence	Ordered as
GTCAxxxxxAC	47		
GACTxxxxxAC	25		
GTGAxxxxxAC	60		
GAGTxxxxxAC	59		
CTCAxxxxxAC	21		
CACTxxxxxAC	27		
CTGAxxxxxAC	55		
CAGTxxxxxAC	51		
GTCTxxxxxAC	53		
GACAxxxxxAC	23		
GTGTxxxxxAC	46		
GAGAxxxxxAC	56		
CTCTxxxxxAC	27		
CACAxxxxxAC		38.3	cD11
CTGTxxxxxAC	46		
CAGAxxxxxAC	56		
GTCAxxxxxTC	48		
GACTxxxxxTC	unwanted nickase site		
GTGAxxxxxTC	52		
GAGTxxxxxTC	57		
CTCAxxxxxTC	24		
CACTxxxxxTC		37.2	
CTGAxxxxxTC	52		
CAGTxxxxxTC	51		
GTCTxxxxxTC	53		
GACAxxxxxTC	25		
GTGTxxxxxTC	31		
GAGAxxxxxTC	59		
CTCTxxxxxTC		36.1	
CACAxxxxxTC	24		
CTGTxxxxxTC	31		
CAGAxxxxxTC			

Figure 4.6: Designing autocatalysts (first part). Sequences were chosen following the previously defined rules (xxxxx indicates the nickase recognition site, GACTC). All sequences were scanned to discard the ones presenting too stable (or "dangerous", such as a hairpin with a matched 3') secondary structures (checked with Nupack). Among the remaining sequences, a few were chosen, after making sure that the T_m of the amplified sequence was between 37 and 39 °C (calculated with DinaMelt).

Complementary of the amplified sequence	Tm of most stable secondary structure	Tm of amplified sequence	Ordered as
GTCAxxxxxAG	49.4		
GACTxxxxxAG	35.6		
GTGAxxxxxAG	56.1		
GAGTxxxxxAG	59.1		
CTCAxxxxxAG		37.3	cR11
CACTxxxxxAG	47.2		
CTGAxxxxxAG	59.8		
CAGTxxxxxAG	51.2		
GTCTxxxxxAG	54.3		
GACAxxxxxAG		37.3	
GTGTxxxxxAG	31.2		
GAGAxxxxxAG	56.1		
CTCTxxxxxAG	45.2		
CACAxxxxxAG		38.4	
CTGTxxxxxAG	45.8		
CAGAxxxxxAG	60		
GTCAxxxxxTG	49.4		
GACTxxxxxTG	unwanted nickase site		
GTGAxxxxxTG	52.5		
GAGTxxxxxTG	57.3		
CTCAxxxxxTG	44.2		
CACTxxxxxTG		38.4	cE11
CTGAxxxxxTG	58.7		
CAGTxxxxxTG	51.2		
GTCTxxxxxTG	54.3		
GACAxxxxxTG	46.2		
GTGTxxxxxTG	31.2		
GAGAxxxxxTG	61		
CTCTxxxxxTG		37.3	cW11
CACAxxxxxTG	46.2		
CTGTxxxxxTG		38.4	cN11
CAGAxxxxxTG	59.8		

Figure 4.7: Designing autocatalysts (second part).

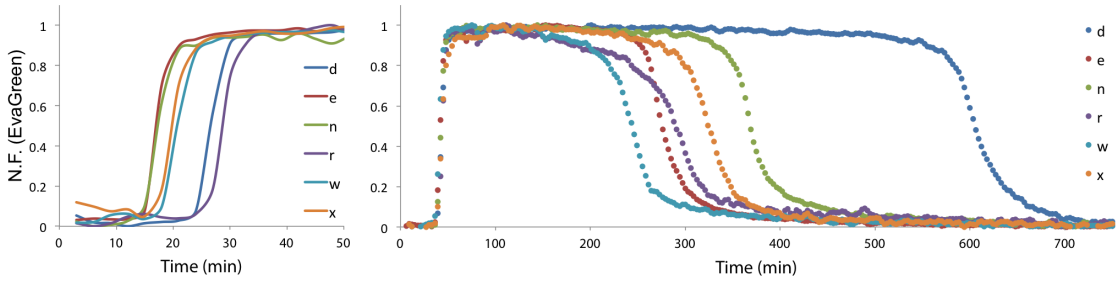

Figure 4.8: Evaluation of new autocatalytic modules (20 nM, 43°C). (Left) Amplification (self-start). All sequences seem to perform amplification efficiently. (Right) Turnovers in presence of 40 µM dNTPs. Limiting dNTP for each template (and number per polymerized oligo): cD11: G(5), cE11: G(4), cN11: A(4), cR11: G(4), cW11: A and G (4), cX11: A (4). Despite consuming more of the same dNTP per polymerized oligo, template cD11 is by far the slowest. Template cR11 presents a tilted plateau: it is never really flat.

stronger the inhibitors are, the larger will the bistability domain be. However, too strong inhibitors are likely to impact the dynamic of the circuit: we are looking for an efficient dynamic inhibition to insure a good responsiveness of the circuit. They would also result in a break-down of the hypothesis of fast equilibrium used to build the simple model (see Section 3.7.3.1).

In the context of the DNA-toolbox, inhibitors must also meet two sequence requirements:

1. They must possess two 3' mismatched bases to prevent the polymerase from extending them as they are hybridized on their target template.

2. They should not present the nickase recognition site, which might lead to disastrous experiments (Figure 4.9): as a consequence, inhibitors cannot cover more than 8 bases on the input site of the target template, and 6 bases on the output site.

In an attempt to make stronger inhibitors that would not have the nickase binding site, we tried to include a mismatch on the output-binding section of the inhibitor: this would allow us to have inhibitors covering more that 6 bases on the output site of the target template, presenting a mismatch in the nickase recognition site, which we hypothesized to be enough to distract the nickase from binding to the mismatched substrate. In practice, the designed inhibitors were targeting cP11, which later appeared to be a "too strong" autocatalytic module: these mismatch-bearing inhibitors did not work against it.

4.3.5 Trials with unbalanced autocatalytic modules

We tried to build bistable circuits with the autocatalytic modules of Figure 4.5-Bottom: cT11, cP11 and cZ11. All three circuits (T-P, T-Z and P-Z) resulted in systems that would eventually set in one single

	Sequence 5'-3'	Tm (°C)
P11	AG**GAGTC**AGTG	39.3
inhP11-67	TCAGTG-AG**GAGTC**TT	48.3
inhP11-77	GTCAGTG-AG**GAGTC**TT	51.1
inhP11-76	GTCAGTG-AGGAGTAT	49.6

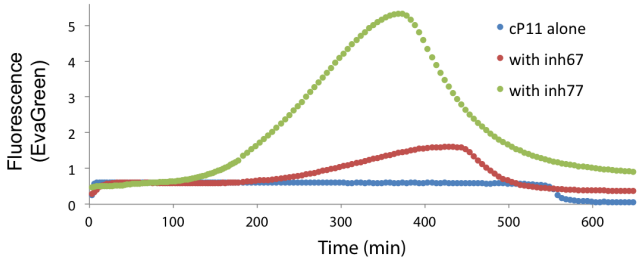

Figure 4.9: Forbidden inhibitors. (Left) Sequence of P11 and three associated inhibitors: inhP11-67 and inhP11-77 have the nickase recognition site (in bold). (Right) Turnover of cP11 (15 nM) alone or in presence of 30 nM of inhP11-67 or inhP11-77 protected against degradation by ttRecJ. The experiment is run at 42 °C with 50 µM dNTPs. In presence of inhibitors that have the nickase recognition site, the reaction produces an unexplained fluorescence trajectory.

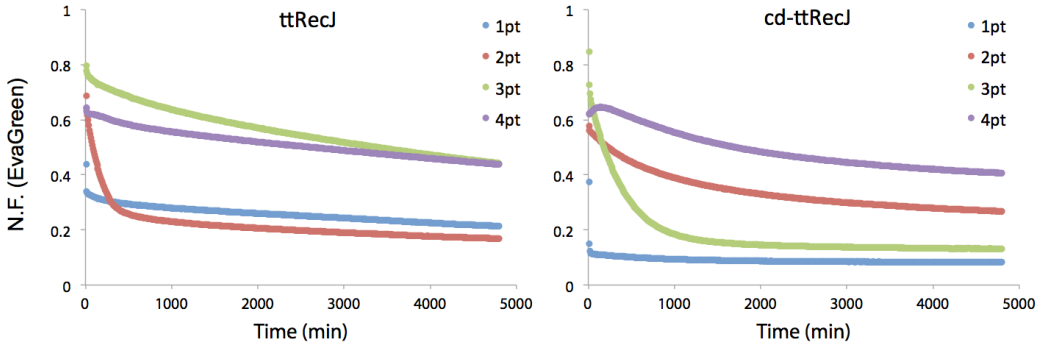

Figure 4.10: Degradation of template c11bt (400nM, 43°C) with 1, 2, 3 and 4 phosphorothioates (pt). Fluorescence intensity of EvaGreen was divided by that of ROX (1x) reference dye, then divided by the fluorescence of the corresponding template in absence of exonuclease. Still, fluorescence level are not perfectly quantitatively comparable, as 0 does not correspond to 0nM of template remaining. (Left) Degraded by ttRecJ (15% of 1/160). Templates with one and two phosphorothioates are quickly degraded. (Right) Degraded by cd-ttRecJ (10%), which behaves quite differently. Interestingly (and unexpectedly), 2pt provide a better protection than 3pt. Also, 2pt and 4pt curves have similar profiles.

state, suggesting a lack of balance between the autocatalytic modules. These failures were also probably due to other problems unrecognized at that time. We were still working with the commercial RecJ_f, usually at temperature as low as 38.5 °C, using EvaGreen that was stabilizing duplexes, and trehalose that was probably slowing down the hybridization kinetics [62]. It is possible that these conditions were increasing the already important gap between the sequences amplification performances. We realized later that cP11 as well as cZ11 were virtually unstoppable in the concentrations then used (>20 nM), even at higher temperatures.

	original	new
exonuclease	$RecJ_f$	ttRecJ
temperature	up to 40 °C	up to 50 °C
stabilizing agents	triton X-100 (0.1 %), trehalose (400mM), BSA (0.1 mg/ml)	synperonic (0.1 %), BSA (0.1 mg/ml)
product inhibition by the nicking enzyme	strong	less
monitoring	EvaGreen (non-specific)	N-quenching (sequence-specific), EvaGreen (non-specific)
template modifications	5': 2 phosphorothioates, 3': phosphate	5': 3 phosphorothioates, 3': fluorophore or phosphate
inhibitors	8-6	7-6

Table 4.1: Status of the DNA-toolbox. The use of thermophilic ttRecJ allows to increase the temperature, and get rid of trehalose. Product inhibition: the use of a dU in the output site of the nickase recognition site decreases the affinity of the nickase for this site (where it would bind without having anything to cut, thus hindering the melting of the output). Monitoring: N-quenching allows to monitor the reactions in a sequence-specific manner, which was not possible with EvaGreen. Inhibitor: we adopted inhibitor 7-6 (with 7 bases hybridizing to the input site, and 6 bases hybridizing to the output site of the target template) instead of 8-6. While still efficiently inhibiting, shorter inhibitors (i.e. less stable), allow a faster recovery of the target template from inhibition.

4.3.6 Working with a new thermophilic exonuclease: full-length ttRecJ

The purified full-length ttRecJ was a kind gift from Dr. Masui (Osaka university), and worked like a charm. Exonuclease ttRecJ proved to be extremely stable, and seemed perfectly usable for our DNA reaction circuits. It however brought a disturbing surprise: the two 5' phosphorothioate backbone modifications that provided a good protection against $RecJ_f$ were not enough against ttRecJ (Figure 4.10-Left). Luckily, 3 or 4 phosphorothioates seemed better, as opposed to cd-ttRecJ for which 3 were worse than 2 (Figure 4.10-Right, still unexplained).

We consequently ordered autocatalytic templates with 3 phosphorothioates instead of 2, but soon found out that these were performing poorly compared to the ones with only 2 phosphorothioates. These results and the solution to this issue are presented in Section 3.7.2.2. Once this problem was solved, we adopted ttRecJ and redesigned our reaction circuits in order to work with this enzyme, potentially at a higher temperature. At this point, the DNA-toolbox had evolved quite a bit (Table 4.1): we kept this status for the rest of this study.

4.3.7 On balancing the bistable circuit

Even carefully designed autocatalytic modules with very close T_m are far from being perfectly balanced: some show a better amplification performance than others. The present symmetric design of bistable

circuit however requires well balanced nodes: as seen in Figure 4.4-Right, two autocatalytic modules of very different strength will result in a monostable rather than bistable system. Consequently, we set out on searching for a way to quantify and compensate these differences, in the context of the chemistry at hand (including buffer, temperature and enzyme conditions).

A first idea - given a working temperature and enzymes concentrations - was to use the turnover experiment (see Figure 4.8), on the two autocatalytic modules, or on the two "semi-switches" (autocatalytic module + inhibition module), for ramps of concentration of autocatalytic module or inhibition module. We would then select the concentrations for which the two sides were consuming dNTPs at the same rate. The problem with this strategy is that it would not take in account a factor that is critical for a proper balancing: the strength of inhibitors on their target autocatalytic module (i.e. the inhibition strength). Still, such experiments revealed the "charge" or "load" effect (as shown by Franco *et al.* [71] for a genelet-based circuit that has to "load" a downstream process): the greater the concentration of inhibition module was, the slower the system was to consume dNTPs (i.e. the weaker was the autocatalytic module that had to charge the following inhibition module, see also Section 4.7.2).

Another idea was to inhibit the semi-switches by using phosphorothoiated inputs (thus protected from the exonuclease) to charge the inhibiting inhibition module, that would consequently produce a steady amount of inhibitor (Figure 4.11-A and B). This would have been an elegant method to evaluate the strength of the fully-charged inhibition module, and select its concentration so that the targeted autocatalytic module would be (just) inhibited. It actually did not work: phosphorothioated inputs were not able to activate the production of inhibitors efficiently (Figure 4.11-C). This may be due to the phosphorothioate backbone modifications, which, as discussed in Section 3.7.2.2, are hampering the work of the nickase: if the nickase is slowed down, the production of inhibitor is also slowed down, which will result in a weaker inhibition of the target template. We tried to use phosphorothioated inputs with longer 5' end, in order to move the phosphorothioates away from the nickase recognition site: this only had a (too) small positive impact. Consequently, this method was not deemed viable to balance the bistable circuit.

4.3.7.1 First: charge and inhibit to balance

The next strategy was motivated by the idea of taking in account both the load on the autocatalytic modules and the relative strength of inhibitors, while trying to have a system as sensitive as possible

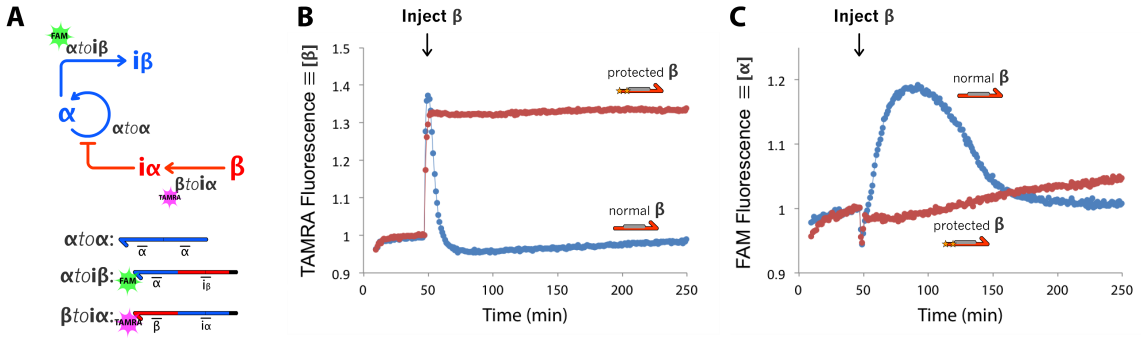

Figure 4.11: Inhibition using protected input. (A) Circuit and templates. [$\alpha to \alpha$] = 10 nM, [$\alpha to i\beta$] = [$\beta to i\alpha$] = 30 nM. 250 nM of either "regular" β or protected β is injected to inhibit autocatalytic module $\alpha to \alpha$. The corresponding reaction (at 42 °C) is monitored with TAMRA (B) (high fluorescence corresponds to high concentration of β) and FAM (C) (low fluorescence corresponds to high concentration of α). Injection of regular β (blue curves) results in a spike in (B) - because injected β is progressively degraded by the exonuclease - and a transient inhibition of $\alpha to \alpha$ in (C). Injection of protected β (red curves) results in an increased fluorescence followed by a plateau in (B) - because protected β is not degraded by the exonuclease - and a very slow and continuous inhibition of $\alpha to \alpha$ in (C).

(which would be easier to flip from one side to the other). This balancing algorithm was as follows, for a bistable switch A-B, constituted of autocatalytic modules $\alpha to \alpha$ and $\beta to \beta$:

1. Choose one or more concentrations of inhibition module: [$\alpha to i\beta$] (10 to 30 nM).

2. Run a first "charge" experiment (ramp of autocatalytic module $\alpha to \alpha$ up to the concentration of $\alpha to i\beta$), in order to determine the concentration of $\alpha to \alpha$ required to correctly charge $\alpha to i\beta$. This determines couples of concentrations of the semi-switch A: [$\alpha to \alpha$] and [$\alpha to i\beta$].

3. Run an inhibition experiment: create a ramp of the opposite inhibition module $\beta to i\alpha$ to find out the required concentration of $\beta to i\alpha$ to completely inhibit the semi-switch A ($\alpha to \alpha$ + $\alpha to i\beta$) upon transient input of β. This determines [$\beta to i\alpha$].

4. Run a second charge experiment for semi-switch B, to determine [$\beta to \beta$] required to charge [$\beta to i\alpha$].

5. Run a second inhibition experiment to determine if the selected [$\alpha to i\beta$] (at step 1) is sufficient to inhibit semi-switch B ($\beta to \beta$ + $\beta to i\alpha$).

6. If it is not, start over from step 1 with another concentration of [$\alpha to i\beta$] (lower for a weaker inhibition and higher for a stronger inhibition).

This method somewhat worked, but required several experiments to complete, and did not warrant 100% success from the first round. Here is a refined version of this method, that should work in a single round (see the example of Figure 4.12):

1. For 10 nM and 20 nM concentrations of inhibition module, run the "charge" experiment, with a ramp of autocatalytic module α*to*α or β*to*β (Figure 4.12-A).

2. Pick one or more couple of [α*to*α] and [β*to*β] that take about the same time to charge their inhibition module.

3. For these concentrations of α*to*α and β*to*β, do an inhibition experiment with a ramp of inhibition module (Figure 4.12-B).

4. Pick concentrations of inhibition module α*to*iβ and β*to*iα that inhibit the opposite autocatalytic module for about the same laps of time.

5. Assemble the bistable circuit.

This refined method worked well, yielding a balanced bistable circuit in two experiments. A remaining problem was that the first charge experiment was done with a fixed concentration (10 or 20 nM) of inhibition module: we have seen that after balancing, it is likely that the chosen concentration of inhibition module will be different. If, for instance, an autocatalytic module has less inhibition module to charge, it will become "stronger" (see Section 4.7.2), i.e. harder to inhibit, which would then require an increased concentration of the opposite inhibition module, further de-balancing the system.

4.3.7.2 Second: inhibit to balance

We then searched for an even simpler way to balance the circuit: a single experiment that would point out the concentrations of the four templates at once. With the insights from previous experiments, we were aware of the load problem: basically, if an autocatalytic module has too much downstream templates to charge, it gets weaker. Having too much to load will also negatively affect its resilience against inhibition. The idea for this new balancing strategy was that if we were fixing the two concentrations of inhibition modules, the only fact of changing the autocatalytic modules concentrations would be enough to balance both sides, while taking in account the load effect. All this, of course, for sequences balanced as much as possible at the design level:

1. Set the same concentrations for the two inhibition modules [α*to*iβ] and [β*to*iα] (20 nM should be enough)

2. Run in parallel these two symmetrical experiments, with [α*to*iβ] = [β*to*iα] = 20 nM: (i) ramp of [α*to*α] from 5 to 20 nM (no β*to*β) with a starting [α] = 1 nM, (ii) ramp of [β*to*β] from 5 to 20 nM

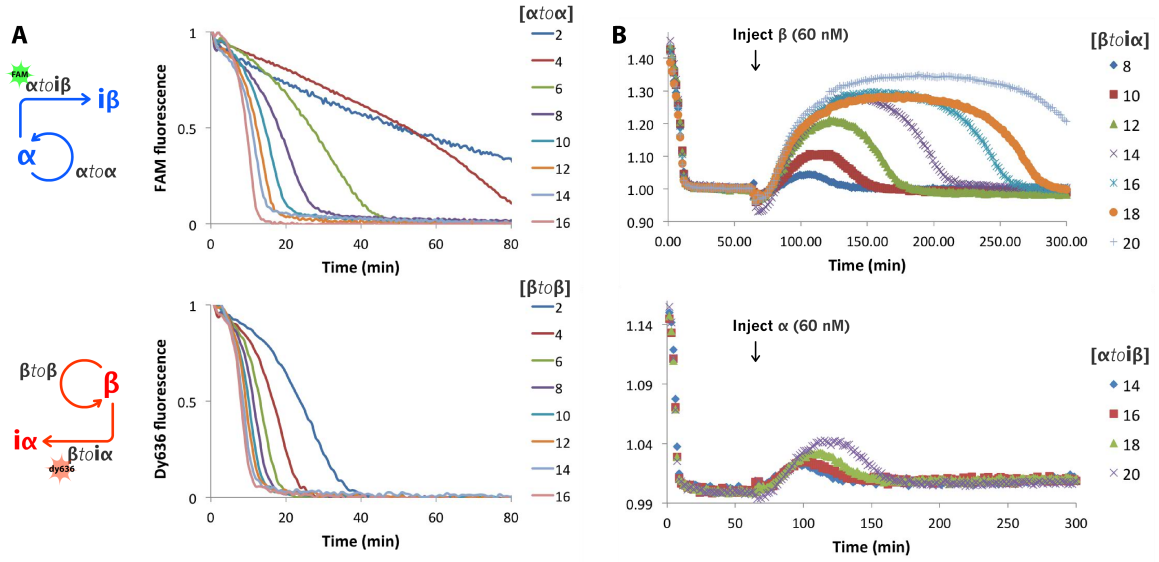

Figure 4.12: Balancing a bistable circuit. Here, we use a different β: 5'-CAGAGTCCAAG-3' which produces a negative fluorescence change as it hybridizes on the dy636-modified $\beta to i\alpha$. (A) Charge of inhibition modules (20 nM) $\alpha to i\beta$ (up) or $\beta to i\alpha$ (down) by respectively $\alpha to\alpha$ or $\beta to\beta$ (ramp of concentration from 2 to 16 nM). In this system, 12 nM of $\alpha to\alpha$ seems to charge $\alpha to i\beta$ in the same amount of time as 6 nM of $\beta to\beta$ charges $\beta to i\alpha$. (B) Inhibition of $\alpha to\alpha$ (12 nM, up) or $\beta to\beta$ (6 nM, down) by a ramp of concentration (from 8 to 20 nM) of the opposite inhibition module (respectively $\beta to i\alpha$ and $\alpha to i\beta$). Here, 10 nM of $\beta to i\alpha$ inhibits $\alpha to\alpha$ for the same time as 20 nM of $\alpha to i\beta$ inhibits $\beta to\beta$. The concentrations to assemble this bistable circuit should then be $[\alpha to\alpha]$ = 12 nM, $[\beta to\beta]$ = 6 nM, $[\alpha to i\beta]$ = 20 nM and $[\beta to i\alpha]$ =10 nM. Reaction were performed at 43 °C, and started with 1 nM of input (either α or β)

(no $\alpha to \alpha$) with a starting $[\beta] = 1$ nM. The samples with concentrations of autocatalytic module that are too low won't reach the steady state before a long time (or might just fail to charge their inhibition module): they should be discarded. When the steady state of production of α or β is reached, inject 30 nM of the opposite input (respectively β or α), that will activate the inhibition of the active autocatalytic module. This experiment will lead to fluorescence curves similar to the ones of Figure 4.12-B: this time, low concentrations of autocatalytic module are more strongly inhibited by the same concentration of inhibition module. Remains to choose the concentrations of autocatalytic module $\alpha to \alpha$ and $\beta to \beta$ that are inhibited for a moderate (and similar) amount of time (i.e. that almost get fully inhibited, but manage to restart and find back their steady state after that).

3. Then, the four concentrations are determined, and the full circuit is ready to be assembled.

This simplified balancing method proved to work nicely: by considering the system at a higher level (i.e. by considering the bistable circuit as made of two "semi-switches" with an inhibitory link, rather than made of four modules with complex interactions), we could abstract the parameters that are hard to balance (in this case, the load problem, see Section 4.7.2), and easily - in a single step - fix the concentrations of all modules. Note that in the case of sequences known to be unbalanced, starting with asymmetric concentrations of inhibition module (i.e. lowering the one that is targeting a weaker autocatalytic module) can prove to be fruitful.

4.4 On switching the bistable: switchable memory circuit

With a bistable circuit constructed and well balanced, the next step would be to give it the ability to be updated. We explored different methods to flip the bistable between states, eventually adopting a DNA-toolbox made solution.

4.4.1 Direct injection of inputs

As described in Sections 3.4.3 and 3.7.3.5, the bistable circuit is robust to perturbation in its input concentration. It should however be possible to force it in one state or the other by successive injections of α or β, given that both sides of the bistable circuit (shown again on Figure 4.13-A) are well balanced. Managing to flip the bistable circuit with this brute-force method would also be a proof that it is possible to update the memory held by the circuit. In the experiment of Figure 4.13-B and C, three

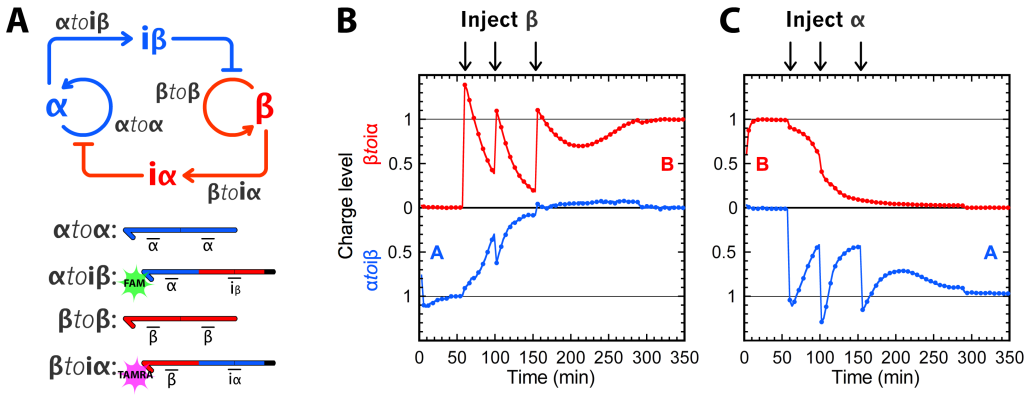

Figure 4.13: Switching the bistable circuit. (A) Bistable circuit and templates. (B) Switching from A to B and (C) from B to A. This experiment was run at 42 °C, with [$\alpha to \alpha$] = 10 nM, [$\beta to \beta$] = 20 nM, [$\alpha to i\beta$] = [$\beta to i\alpha$] =20 nM. The system was administered three shots of 80 nM of α or β before it would eventually switch between states.

successive injections of, respectively, β (to switch from A to B) or α (to switch from B to A) were required to force the flipping of the bistable circuit. For the bistable circuit in state A: the first injection of β primes the inhibition of $\alpha to \alpha$, the second injection continues to inhibit $\alpha to \alpha$, and the third injection allows $\beta to \beta$ to restart, and maintain the inhibited state of $\alpha to \alpha$: the bistable circuit has switched from {A, B} = {ON, OFF} to {OFF, ON}.

This was however far from being practical, and for sure incompatible with the idea of building larger reaction circuits in which the bistable would be a sub-unit. As a matter of fact, the required concentration of input is far larger than what the bistable circuit itself is capable to deliver: the homogeneity between input and output concentrations is lost, and so is the modularity of the bistable circuit.

4.4.2 "Super-inputs"

Consequently, we set on finding a method to switch the bistable memory with a "single shot" of dilute DNA input. We would need to give a chance to the inhibited autocatalytic modules to get rid of the inhibitor blocking them, so that they would start again. To this end, we introduced *super* inputs, which are super-strong versions of the inputs of the bistable circuits: α and β. *Super* inputs are two bases longer than inputs. With these two additional 5' C or G, they bind about as strongly as inhibitors on the input site of the autocatalytic module, which itself has two additional 3' bases to receive them (Figure 4.14-B). Moreover, these additional two bases make them having a 6-bases long toehold to efficiently displace the hybridized inhibitors (Figure 4.14-C).

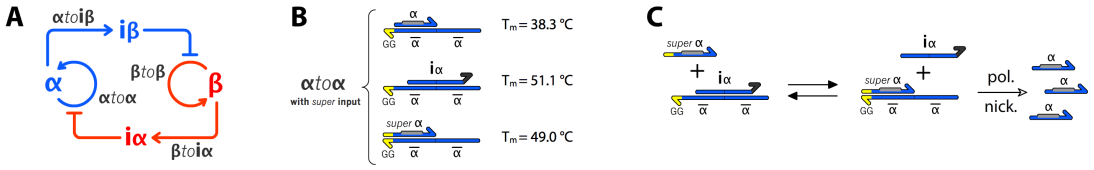

Figure 4.14: *Super* input principle. (A) Bistable circuit. When, for instance, on state B, β is autocatalytically produced and activates the production of iα, that in turn inhibits α*to*α. (B) *Super* input enabled α*to*α has two additional G in 3'. These allow the strong binding of *super* α, that has a T_m close to that of inhibitor iα. (C) With its two additional 5' bases, *super* α benefits from a toehold [19] of 6 bases to displace inhibitor iα and subsequently re-activates autocatalytic module α*to*α.

We first checked that the two additional 3' bases of the autocatalytic modules were not hindering the circuit functioning, as these two dangling bases may have, for instance, a stabilizing effect on the hybridizing "normal" input [164]. *Super* input-enabled autocatalytic modules amplified as their "normal" counterparts. However, when playing the role of input for the inhibition modules, *super* input appeared to activate the production of inhibitor with a rough 20% speed loss compared to simple inputs (Figure 4.15-A). Note that we encountered the same - but stronger - issue as we tried to use protected-elongated inputs (Figure 4.11). We will see that in the case of *super* inputs, this speed loss eventually appeared to not hinder the functioning of the circuit.

We also checked if *super* inputs were inducing a fluorescence intensity shift equivalent to input hybridizing on inhibition modules. Surprisingly, they produced a small intensity shift in the opposite direction of normal inputs (Figure 4.15-B): we would not be able to monitor the presence of *super* input. This small intensity shift can be attributed to the two dangling bases (two C or two G) that modify the direct vicinity of the fluorophore, thus falling out of the N-quenching rules (there is no report concerning the case where the dangling end is on the opposite strand of the fluorophore). Also, whereas we did not observe difference in T_m of α against *super* α on α*to*iβ, there was roughly 5°C degrees of difference between β and *super* β on β*to*iα (Figure 4.15-B).

We then tried to use *super* input-enabled α*to*α and β*to*β in the full circuit. Figure 4.16 shows that the bistable circuit is working pretty well, despite the additional 2 bases on the autocatalytic module: when given a combination of initial concentrations of α and β, it chooses - after some transient - one stable state or the other.

As we gave a shot of *super* input to the bistable circuit at the stable state, the system seemed to respond nicely: the *super* input was, as expected, readily activating the inhibition of the then-ON state, while also reactivating the then-OFF autocatalytic module (Figure 4.17). The bistable

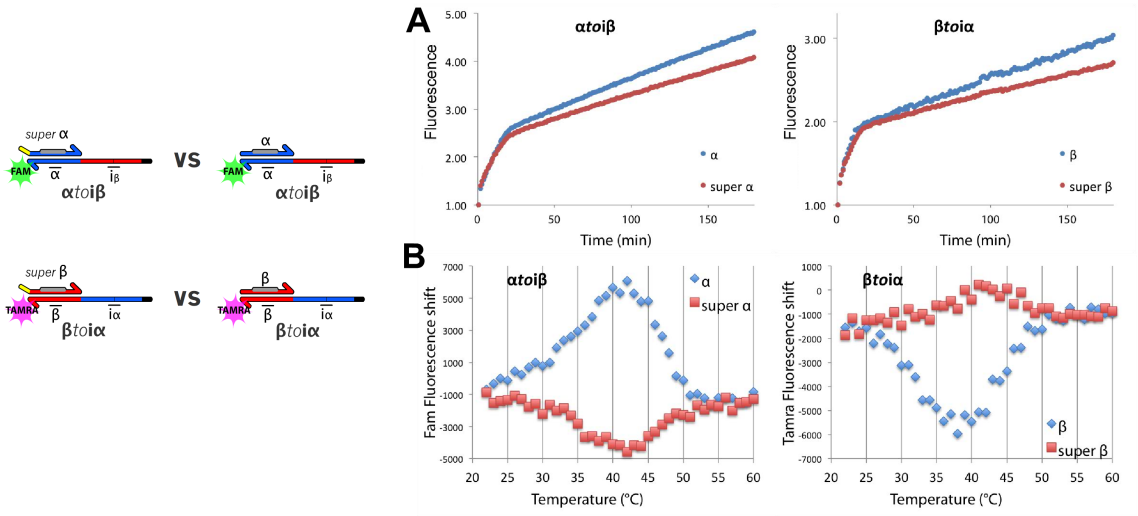

Figure 4.15: *Super* input and inhibition modules. In these two experiments, we compare the production of inhibitor by "normal" input and "super" input, in absence of exonuclease. (A) Production of inhibitor by inhibition module $\alpha to i\beta$ (left) and $\beta to i\alpha$ (right). The reaction is monitored with EvaGreen intercalating dye. Inhibition modules (60 nM) are put in presence of 100 nM of input or *super* input. In the absence of exonuclease, there is a first step of production with a rapid increase of fluorescence corresponding to formation of stable duplex "inhibition module : inhibitor" followed by a second step (slow increase of fluorescence) where the polymerase works in strand-displacement: we can observe the accumulation of single stranded inhibitor in solution. (B) Melting the duplex (50 nM) "$\alpha : \alpha to i\beta$" (left) or "$\beta : \beta to i\alpha$" (right) reveals the fluorescence change upon separation of the duplex (hence opposite to the fluorescence change upon hybridization). Curves show the fluorescence change per degree for the attached fluorophore of the corresponding inhibition module. The highest (or lowest) value roughly (but not exactly) corresponds to the T_m of the duplex.

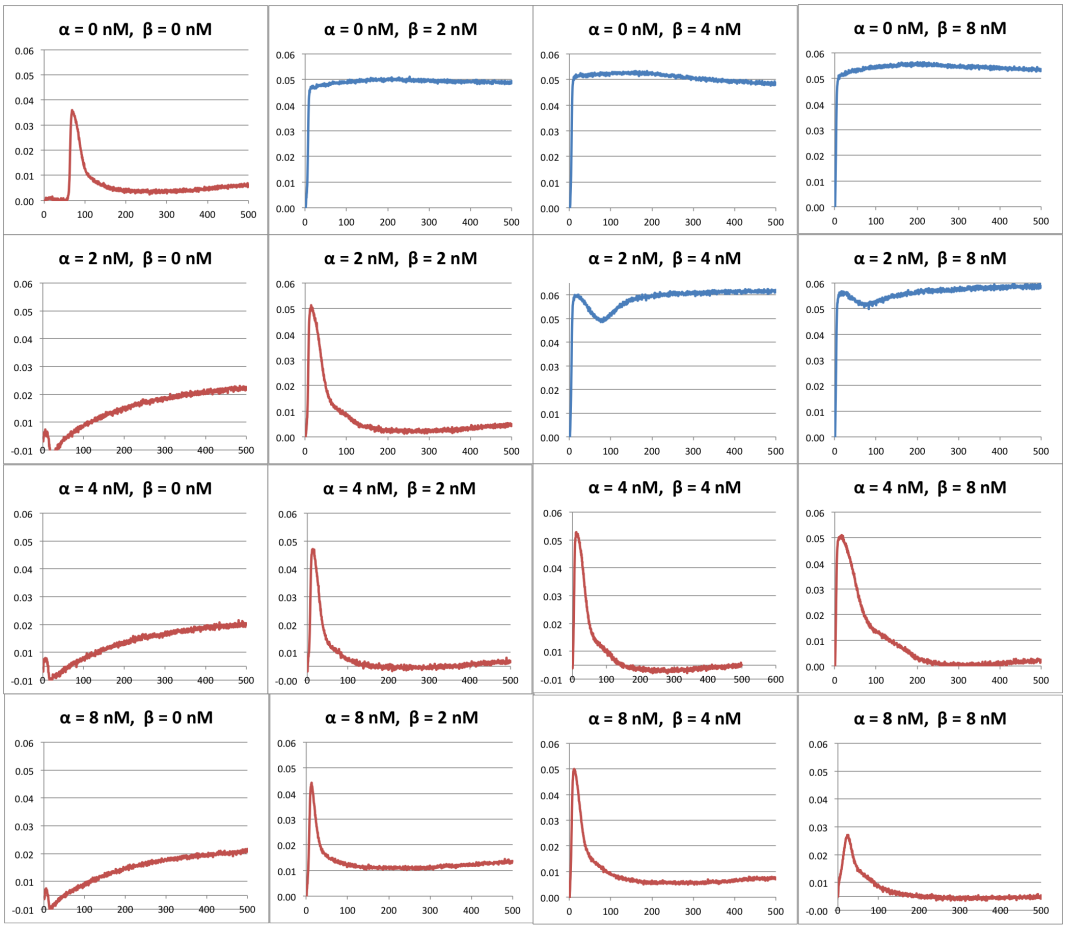

Figure 4.16: Matrix of initial concentrations of α and β on the *super* input-enabled bistable circuit. The experiment is only observed through the Tamra channel: high steady-state corresponds to β*to*β ON (and α*to*α OFF) and baseline level corresponds to β*to*β OFF (and α*to*α ON). As in Figure , it shows the basins of attraction of both states. Concentrations of templates are as follows [α*to*α] = [β*to*β] = 10 nM, [α*to*iβ] = [β*to*iα] =20 nM

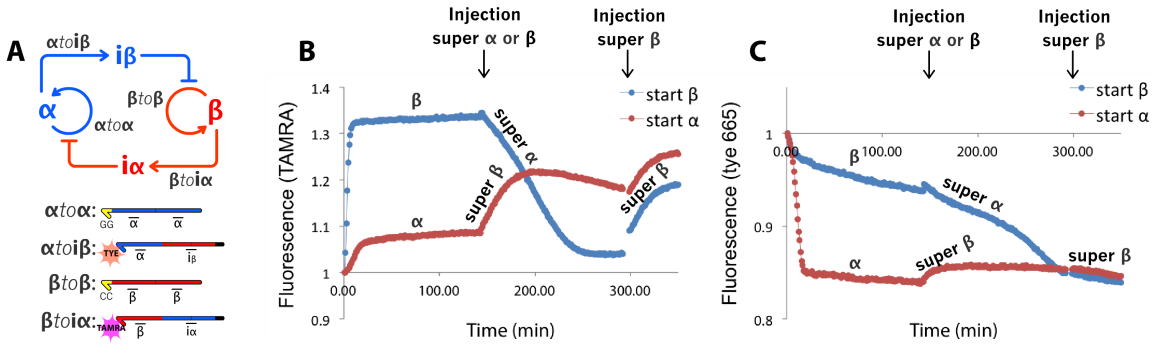

Figure 4.17: Flipping the switch with *super* input. (A) Bistable circuit and templates: α*to*α has two G (and β*to*β, two C) in 3' to receive its *super* input. Fluorescence of TAMRA (B) and tye 665 (C), respectively monitoring β (high fluorescence corresponds to high [β]) and α (low fluorescence corresponds to high [α]). The same reaction mix is initiated with either α (red curve) or β (blue curve). At t = 150 min, an injection of 30 nM of either *super* α or β triggers the switching process. The system initially in state B (blue curve) flips to the A state: fluorescence of TAMRA decreases (inhibition of β*to*β), that of tye 665 also decreases (reactivation of α*to*α). However, the system initially in state A (red curve) doesn't flip to state B, but seems to end up in an alternate state where both α*to*α and β*to*β are partially active. At t = 300 min, an injection of *super* β confirms that the system is not responsive anymore.

circuit seemed to have flipped from one side to the other. When trying to switch backwards, however, the bistable circuit did not behave as expected, and ended up in an intermediate state with both states half active -which is of course forbidden by the bistable topology of the circuit. In other word, once flipped using *super* inputs, the bistable circuit was somewhat stuck in a "*super* activated" state. We tentatively attributed that to the slow melting of *super* inputs, which, once hybridized to the autocatalytic modules, might not move much: the system is not responsive anymore. This system might benefit from running at a higher temperature (it was only tried at 39 °C), where *super* input should still be stable enough to do there job, while being unstable enough to eventually melt and be digested by the exonuclease.

4.4.3 "Input-makers"

Our next attempt, and also the most successful, came straight out of the DNA-toolbox. It consisted in using an activation module (say, x*toy*), that would amplify an exogenous spike of its input (x) into a long lasting pulse of its output (y). The latter would simply be connected to the bistable circuit (y = α or β), stimulating the OFF side of the bistable to make it switch ON. More details are given in Section 3.4.4. By connecting two activation modules to the two nodes of the bistable circuit, it became a two-input switchable memory circuit, able to be switched from one state to the other, and directly

connectable to other circuits made with the DNA-toolbox.

4.5 Modeling of the circuit

Mathematical modeling of the bistable circuit is explained in details in Section 3.7.3, for both "simple" and "detailed" models. Construction of the detailed "realistic" model requires various parameters that can be classified in two categories: oligonucleotides hybridization parameters and enzymes parameters. In this section are presented the techniques used to determine these parameters.

4.5.1 DNA melting experiment

Each input and inhibitor has a different dissociation constant: as mentioned in Section 3.7.3.4, it is possible, in the context of the DNA-toolbox, to obtain a very good computational estimate (for instance using DINAMelt, knowing the concentrations of DNA strands and cations Mg^{2+} and Na^{+}) of the dissociation constant of each species. Nonetheless, chances are that the real value departs from the computed one. Luckily, dissociation constants are easy to measure by doing a DNA melting experiment. This experiment consists in putting two complementary strands in stoichiometric concentrations (in the case of two separate strands, the melting temperature depends on the concentration of species) in the desired buffer (in our case, the reaction buffer without dNTPs), anneal them, then "melt" them by slowly increasing the temperature while measuring the absorbance at 260 nm: denaturation of a duplex is accompanied by an increase of absorbance of about 15 to 20% (hyperchromism). We want to be slow enough to leave time to the sample to reach the thermodynamic equilibrium between duplex / simplex, but avoid staying too long at high temperature (evaporation + DNA depurination).

As an example, we will take the melting temperature of the inhibitor of c11bt (inhbt3) on c11bt, with and without EvaGreen intercalating dye. Curves were acquired with a V600bio spectrophotometer (Jasco), with 1 µM of each oligonucleotide, in the reaction mix without dNTPs nor enzymes (total volume: 700 µL), a stirrer (600 rpm), temperature sensor in the cell, which was closed with Parafilm to avoid evaporation:

1. Denature: sample is brought to 50 °C.
2. Anneal: from 50 °C to 20 °C (slope: 2 °C / min). Low temperature: watch out for condensation!
3. Melt: from 20 °C to 80 °C (slope 0.6 °C / min). High temperature: watch out for evaporation!

4. Plot raw curves (temperature in K). Extract upper (simplex) and lower (duplex) linear baselines (Figure 4.18-A).

5. Plot the fraction of hybridized oligonucleotides: $\theta = \frac{baseline(simplex) - absorbance}{baseline(simplex) - baseline(duplex)}$ as a function of the temperature in Kelvin (Figure 4.18-B).

6. Select $0.03 < \theta < 0.97$ and calculate the constant of affinity $K_a = \frac{\theta}{[concentration(Mol)].(1-\theta)^2}$.

7. Plot $ln(K_a)$ as a function of $\frac{1}{Temperature(K)}$ (Figure 4.18-C).

8. Then we have the Gibbs Free Energy $\Delta G = -R.T.ln(K_a) = \Delta H - T.\Delta S$ which lead to the following linear fit: $slope = -\Delta H/R$ and $Y intercept = \Delta S/R$ with R = 1.985 cal/K/mol.

In the present case, we find with EvaGreen ΔH = -101 kcal/mol and ΔS = -284 cal/K/mol. Without EvaGreen, ΔH = -119 kcal/mol and ΔS = -342 cal/K/mol.

Additional points of interest:

- Association rates: they are roughly constant for all oligonucleotides (inputs and inhibitors) used in the context of the DNA-toolbox [62]. As detailed in Section **??**, we used a single association rate k_a = 0.06 $nM^{-1}.min^{-1}$for mathematical modeling of reaction circuits.

- Derivative: the maximal value of the first derivative (is close to but) usually doesn't correspond to the T_m of the duplex, except for intramolecular denaturation (i.e. internal structure / self-folding / hairpin). The T_m can however be accurately calculated from the extracted ΔH and ΔS with the following formula: $T_m(°C) = \frac{\Delta H}{\Delta S + R.ln([oligo])} - 273.15$. Which, in the present case, leads to a T_m of 46.5 °C with EvaGreen, and 45.0 °C without: this confirms that EvaGreen stabilizes the duplexes.

- Stability: the most stable structure at a given temperature is not the one that has the highest T_m, but the one that has the lowest ΔG at that temperature.

4.5.2 Enzymes kinetic parameters

In the context of the DNA-toolbox, enzyme kinetics can be satisfyingly described by the Michaelis-Menten model. It is an approximation of the multi-step reaction that happens between an enzyme and its substrate: for instance, an exonuclease first binds to its substrate, then cleaves nucleotides one by one (for the construction of the simple model in Section 3.7.3.1, we further simplified the amplification

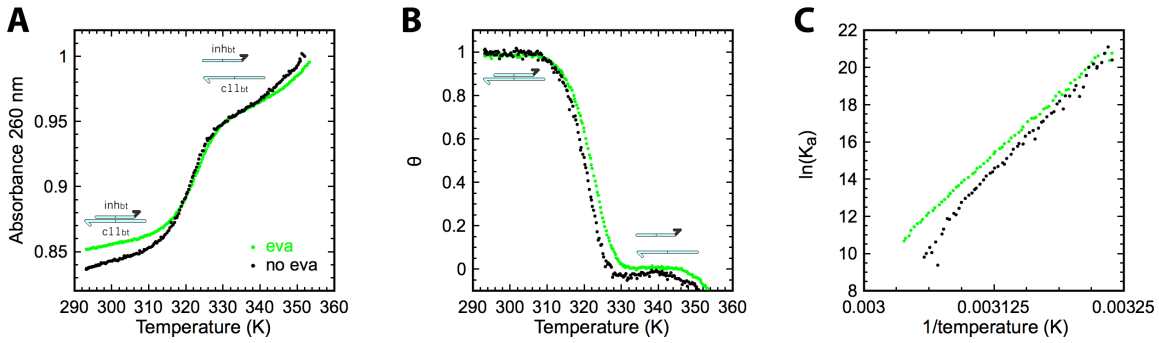

Figure 4.18: Melt curve analysis of c11bt and its inhibitor. (A) Raw melt curve with and without EvaGreen. (B) Fraction of hybridized duplex as a function of the temperature. (C) The linear fit of these two lines contains ΔH and ΔS of the reaction.

mechanism - catalyzed by the polymerase and the nickase - in a single Michaelis-Menten equation). Enzymes can have different rate and Michaelis-Menten constant for each substrate. These can be experimentally measured by setting up a specific assay for each enzyme. By fitting the integrated form of Michaelis-Menten equation to the experimental curves, one can extract k_{enz} (Michaelis rate) and K_m (Michaelis constant) for a given substrate, in a given buffer, at a given temperature, given that the measured enzymatic reaction is actually the rate-limiting reaction. In the case of first-order kinetics, an exponential fit will give the $k_{1st} = k_{enz}/K_m$of the enzyme in given conditions.

4.5.2.1 Exonuclease parameters

The kinetic parameters of ttRecJ are the easiest to measure. One has to put the target signal species (input or inhibitor) in presence of EvaGreen and a low concentration of ttRecJ, and monitor the decreasing fluorescence of EvaGreen that is due to the hydrolysis of target single-stranded species (Figure 4.19). Then plot the Time t (min) as a function of the Fluorescence x, and fit the integrated Michaelis-Menten equation: $-\frac{1}{V_m}\left(\frac{x}{r} - [oligo] + K_m.ln\left(\frac{x}{r.[oligo]}\right)\right)$ with r corresponding to the fluorescence units per mole of oligonucleotide, and $[oligo]$ the initial amount of oligonucleotide in mole.

4.5.2.2 Nickase parameters

The kinetic parameters of Nt.BstNBI can be measured for each template (activation, autocatalytic and inhibition modules) using the following assay. The principle is to have a given amount of double-stranded uncut substrate for the nickase, that will be cut and will consequently melt away. The two separated signal strands will then be degraded by the exonuclease (and the template stays intact, see Figure 4.20-A). The *sine qua non* is that the reaction is set up so that the cutting step is the rate-

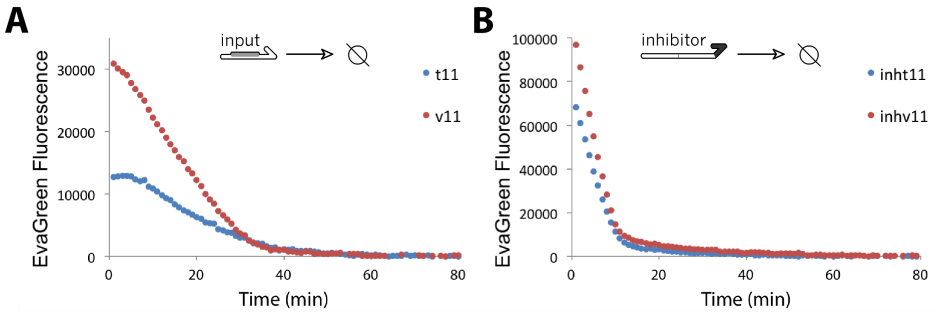

Figure 4.19: Digestion of (A) 2 µM of input t11 (blue) or v11 (red) and (B) 500 nM of inhT11-76 (blue) or inhV11-76 (red), at 42 °C, with 1x EvaGreen and 0.4 % of ttRecJ/160. Baseline removed.

limiting step. This requires: a high concentration of exonuclease (so that as soon as they are cut and melt, signal strands are degraded) and a low concentration of nickase (so that it does not cut faster than the rate of the other reactions -melting and degradation). Figure 4.20-B shows curves for three different concentrations of Nt.BstNBI. In order to make sure that we are looking at what we want, an idea is to check the linear portion of the different curves: if the cutting reaction is the rate-limiting one, then the slope should be double for a double concentration of nickase. This is what we can observe in the inset of Figure 4.20-B for the red (0.05 % of Nt.BstNBI) and the green (0.025 % of Nt.BstNBI) curves. These two can thus be used to fit the integrated Michaelis-Menten equation (as presented in the previous section). This is not the case for the blue (0.1 % of Nt.BstNBI), which slope is not twice that of the red curve: the cutting step might be too fast compared to the dissociation-degradation step (or substrate inhibition may occur and slow down the nicking enzyme).

4.6 Stability on the long-term

Because we are working in a closed system, each experiment has a limited lifetime (typically driven by the initial amount of dNTPs). Also, various reaction parameters are modified over time: enzymes can loose activity, templates can be degraded and so on. These issues are discussed in Section 3.7.6; here we present a few additional results to flesh out the discussion about the stability on the long-term of circuits made with the DNA-toolbox in a closed setup.

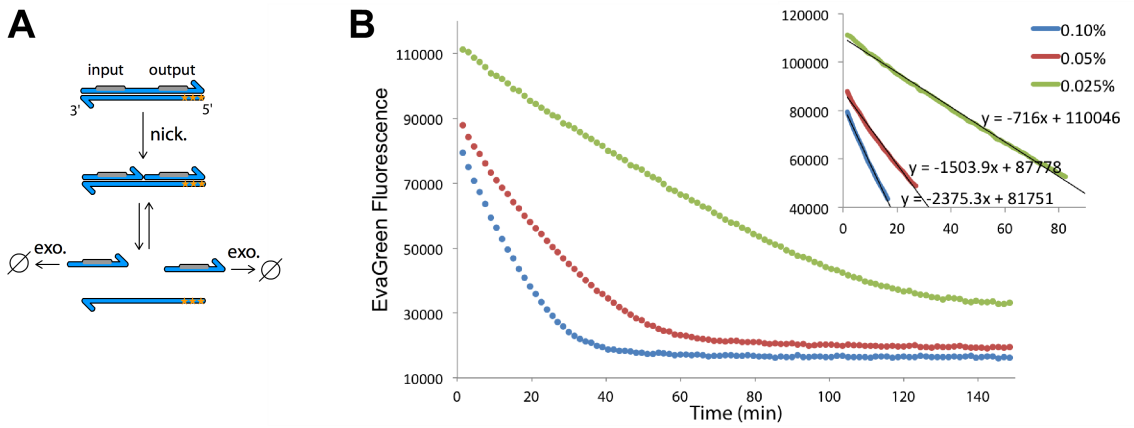

Figure 4.20: Measuring Nt.BstNBI parameters for cT11. (A) Schematic of the reaction: the template and its complementary strand are initially hybridized. The nickase cuts the complementary strand in its middle, and since the two products are shorter, they melt and are then digested by ttRecJ, resulting in a decrease of fluorescence of EvaGreen. The presence of a U in the output site of the template prevents the nickase to stick to it, which would hinder the melting of the output strand. (B) Experiment for cT11 (100 nM) with its complementary (110 nM) at 42 °C. Exonuclease is in excess (4 % of ttRecJ/160), and Nt.BstNBI is present in low concentration (0.1 % (blue), 0.05 % (red) and 0.025 % (green)). The linear portion of the curves is also displayed in inset, with the corresponding linear fit: slope of (0.05 %) is twice that of (0.025 %). However, the slope of (0.1 %) is lower than twice that if (0.05 %), meaning that the cutting reaction is not the speed limiting one anymore: this curve cannot be used to extract the kinetic parameters of Nt.BstNBI.

4.6.1 Buffer additives

Reaction buffer contains several additives, such as BSA (Bovine Serum Albumin) used to stabilize enzymes and their interactions with surfaces (we will see later on that the increase of the surface / volume ratio requires an increased concentration of BSA), Synperonic F108 (a surfactant) and DTT (Dithiothreitol), which is a reducing agent used to stabilize enzymes activity. As an example to illustrate the need for these additives, Figure 4.21 shows a repetitive turnover reaction (such as the one shown in Section 3.7.6) with and without DTT. Indeed, DTT is necessary for the reaction circuit to still be viable after some time.

4.6.2 Template degradation by ttRecJ.

As detailed in Section 3.7.2.2, two phosphorothioate modifications were not enough to efficiently protect the templates against hydrolysis by ttRecJ. We found that putting three phosphorothioates was providing a good protection: here we investigate this a little further. In the experiment of Figure 4.22, autocatalytic module $\alpha to \alpha$ is inhibited by $\beta to i \alpha$ after having been "aged" (i.e. left free in solution with enzymes but without dNTPs) for 0, 2 or 4 hours. This experiment allows us to simulate the effect

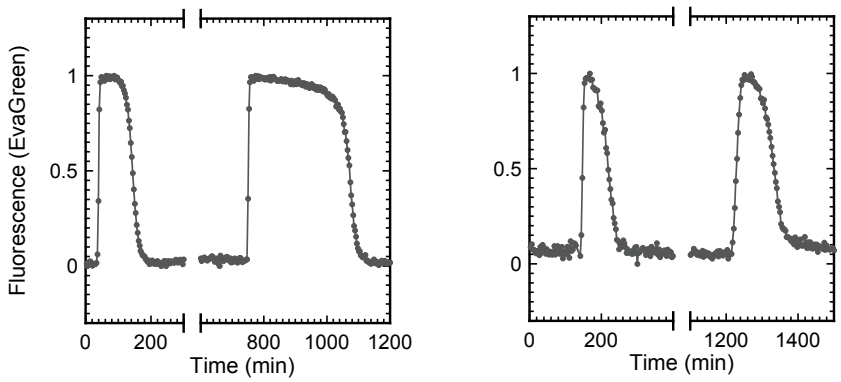

Figure 4.21: Repetitive turnovers of cT11 (20 nM) with 20 µM dNTPs at 42 °C. (Left) Low concentration of DTT (1 mM): production of T11 by cT11 reaches the steady state, and requires more time to consume the second shot of dNTPs (injected at 750 min). (Right) Intermediate concentration of DTT (6 mM): cT11 produces T11 faster, an doesn't have the time to reach the steady state. The second shot of dNTPs (injected at about 1200 min) is consumed in about the same laps of time as the first one.

on long-term experiments of the slow degradation of the template by ttRecJ. It turns out that the activity of $\alpha to \alpha$ does not significantly decrease upon 4 hours of aging. Note that even for the earliest inhibition, $\alpha to \alpha$ does not recover from its inhibition as sharply as in Figure 4.12-B: this may mean that in the present conditions, the "viable" amount of autocatalytic module is not the parameter that limits the rate of amplification: one may want to perform this experiment again in different enzymes conditions.

4.6.3 Flattening the steady state

All autocatalytic modules behave differently, for that enzymes have a different affinity for each sequence. Such phenomenon is usually hard to explain intuitively: still, we investigated this issue a little further, for autocatalytic modules that we knew were free of defaults such as secondary structures or unwanted nickase recognition site. When analyzing a turnover experiment (with a low amount of dNTPs), some templates reach a nice (i.e. flat) steady state (for instance cP11 and cZ11 on Figure 4.5) whereas others (such as cT11 on Figure 4.5) show a not-flat steady state. It turns out that the amplified sequences that have such problem are the ones for which dTTP is the limiting dNTP (i.e. the one present in the biggest number in the sequence): for instance, cT11 (5 T) or cV11 (4 T). On the contrary, amplified sequences having a low number of T (for instance cX11 (1 T), cP11 (2 T) and cZ11 (2 T)) exhibit a nice steady state. Autocatalytic modules cV11 and cX11 are compared in Figure 4.23-Left. We found that adding dTTPs to the reaction mix is improving the flatness of the steady

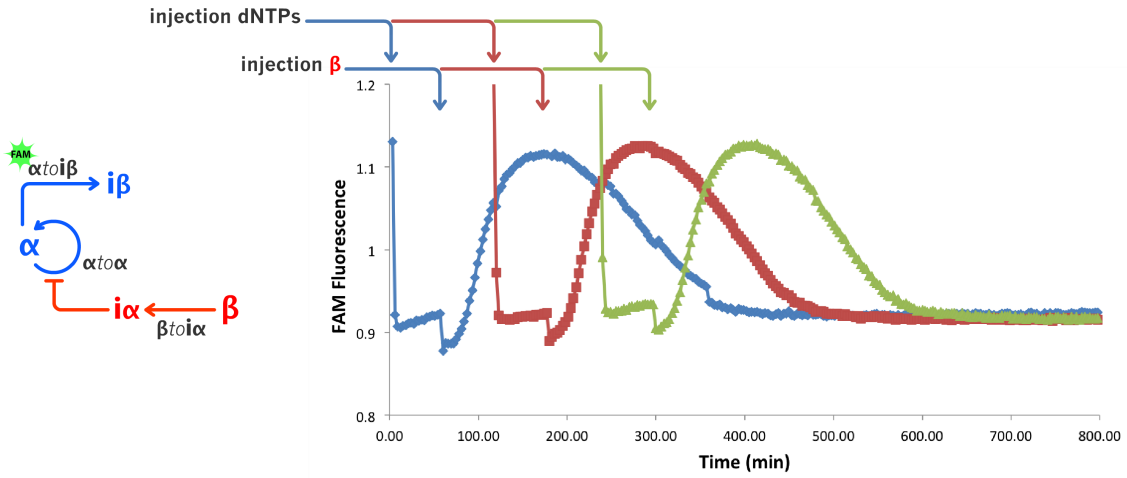

Figure 4.22: Inhibition of α*to*α (cV11, 10 nM) by β*to*iα (20 nM) after aging α*to*α for 0 (blue), 2 (red) or 4 hours (green). As dNTPs are injected, α*to*α starts amplifying (decrease of FAM fluorescence) reaches the steady state. After one hour, an injection of β (30 nM) activates the production of iα, that inhibits α*to*α. This experiment was run at 43 °C.

state of templates such as cT11 of cV11 (Figure 4.23-Right). This may be due to a lower affinity of the polymerase for dTTPs than for other dNTPs (we however did not find any literature about such a phenomenon concerning *Bst* Large Fragment).

4.7 Others

4.7.1 Tristable circuit and three-switch oscillator

Bistability is a frequently observed phenomenon in chemical and biological systems. Tristability, however, has only rarely been reported [152, 165, 166]. Yet, following a topological approach similar to that followed for the bistable circuit described above, a tristable system seems easy to build with the DNA toolbox: it consists of three autocatalytic modules representing the three states, each of them inhibiting the two others through two inhibition modules (Figure 4.24-A). We built this 9-modules circuit, attaching three different fluorophores to observe the three inputs of the circuit: α (FAM) for state A, β (dy636) for state B and ɣ (JOE) for state C. The main challenge when assembling this system was that each autocatalytic module had to be strong enough to inhibit two autocatalytic modules, yet had to be weak enough to be easy to inhibit. This, added to the fact that the three autocatalytic modules were of different strength, made such system tricky to balance. Experimental fluorescence time plots of Figure 4.24-A show the system properly taking each of its three stable states.

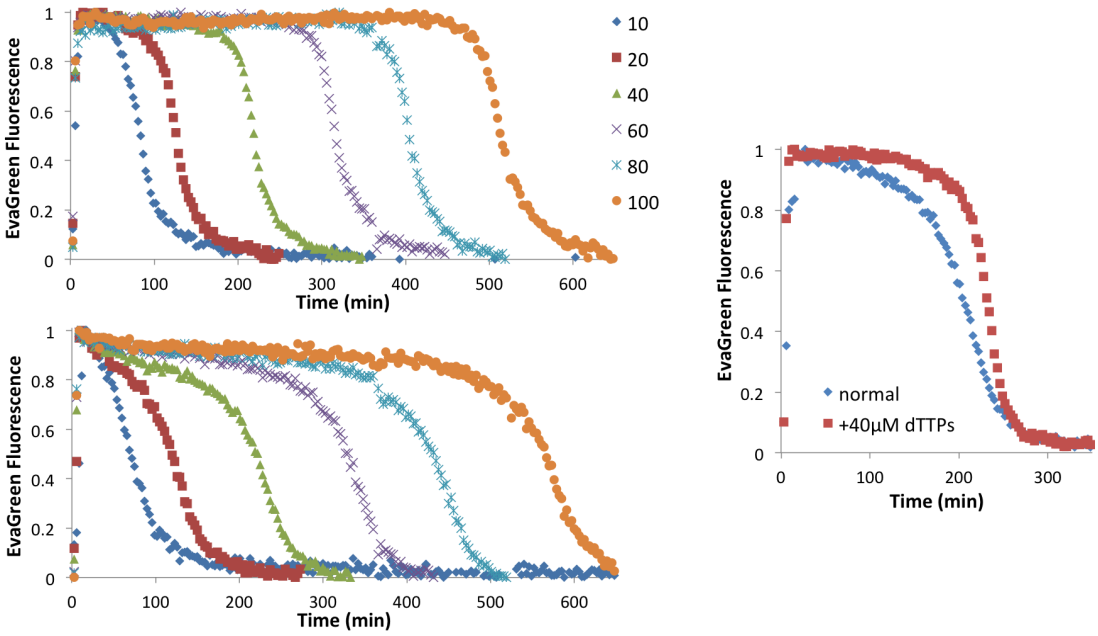

Figure 4.23: Improving the flatness of the steady state. (Left) Turnover of cX11 (up) and cV11 (down) with a ramp of initial concentration of dNTPs (from 10 to 100µM). Whereas cX11 reaches a nicely flat steady state, cV11 does not, especially for the low concentrations of dNTPs. (Right) Turnover of cV11 for 40 µM of dNTPs. Adding dTTPs to the reaction mix improves the flatness of the steady state. Experiments were run at 43 °C with 20 nM of autocatalytic module.

States A and B had, however, very small basins of attraction: as soon as ɣ was initially present in a concentration of even a tenth of that of that of α or β, the system inevitably settled in state C.

By using only half of the inhibition modules on a clockwise pattern (α*to*α inhibits β*to*β that inhibits ɣ*to*ɣ that inhibits α*to*α) or a counterclockwise one (α*to*α inhibits ɣ*to*ɣ that inhibits β*to*β that inhibits α*to*α), one should obtain an oscillator in which autocatalytic modules get activated one after the other (Figure 4.24-B). A mathematical model of the circuit for perfectly equilibrated sequences indeed predicted a robust oscillating behavior. After some tedious balancing of the three sides, we managed to experimentally obtain a single cycle of oscillations (Figure 4.24-C). Autocatalytic module ɣ*to*ɣ appeared, once again, to be stronger than the two others: the system eventually settled in a state where ɣ*to*ɣ only was active and leaving not chance to α*to*α and β*to*β to restart.

4.7.2 Charge / Load

When working in the "right" conditions (i.e. for which the enzymes are not limiting the reaction speed), the rate of amplification by an autocatalytic module is initially correlated to its own concentration and the concentration of amplified input, as shown on Figure 4.25-A and B. Furthermore, when an autocatalytic module has to provide input to a downstream module, it undergoes the "load" effect. This is characterized by a weakened amplification of the module undergoing the load (Figure 4.25-C). This can be intuitively explained by the fact that the module "to load" is sequestering outputs from the "loading" module, and in the case of an autocatalytic module, outputs are also inputs: having a lower concentration of input, the autocatalytic module is slowed down.

Such effect has to be considered during the assembly of circuits in which autocatalytic modules have to charge one or more modules: this can be done by establishing an appropriate balancing strategy, such as the one we have described for the bistable circuit in Section 4.3.7. This can however be trickier for larger reaction circuits such as the the tristable circuit or the push-push memory circuit, in which each autocatalytic module has to load two inhibition modules (for the push-push memory circuit, one module inhibiting the opposite autocatalytic module, and another one feed-backing the current state of the bistable core to the push-push function). In this latter case, the assembly of the full circuit benefited from a robustly balanced bistable core. A strategy against the load effect would be to introduce intermediate activation (amplification) modules (as "insulator" [71]). However, increasing the total concentration of templates may also result in a problem by transferring the load on the enzymes (i.e. moving the system in the saturated regime of the enzymes).

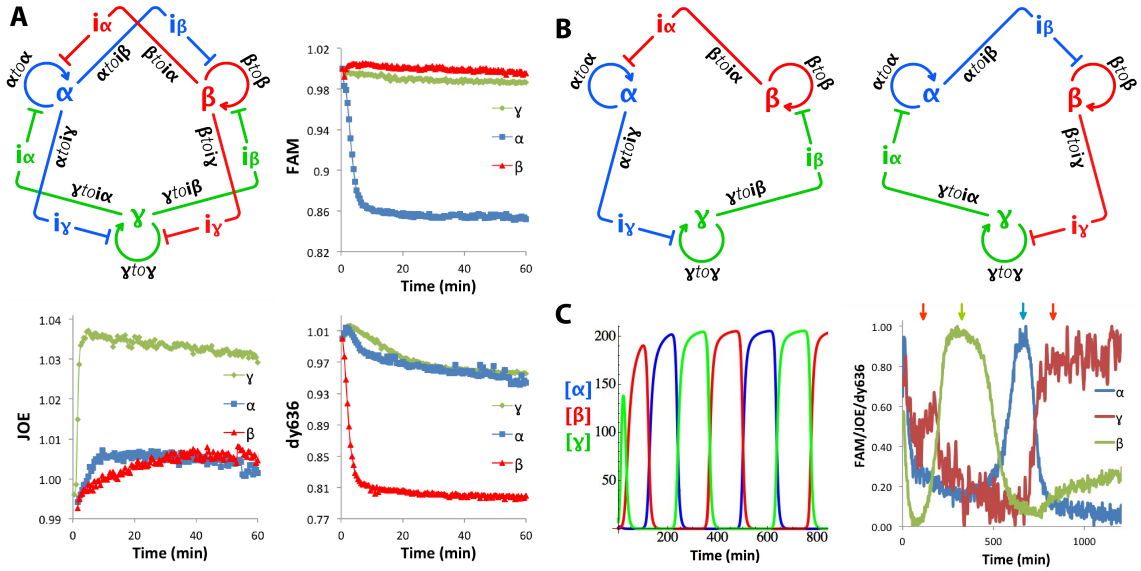

Figure 4.24: Tristability and three-switch oscillator. (A) Tristable circuit. Templates α*to*iβ and α*to*iɣ are labeled with FAM to monitor α (negative fluorescence intensity shift upon charge); β*to*iα and β*to*iɣ are labeled with dy636 to monitor β (negative fluorescence intensity shift upon charge); ɣ*to*iα and ɣ*to*iβ are labeled with JOE to monitor ɣ (positive fluorescence intensity shift). The system initiated with 1 nM of either α, β or ɣ stabilizes in each corresponding state A, B or C, characterized by a shift of fluorescence intensity of, respectively, FAM, dy636 or JOE, as one can observe in the fluorescence time plots of each dye. Concentrations are: [α*to*α] = [β*to*β] = 15 nM, [ɣ*to*ɣ] = 10 nM, all inhibition modules at 20 nM. (B) Three-switch oscillators oscillating counterclockwise (left) and clockwise (right). (C) Left: model (concentration of free α (blue), β (red) or ɣ (green)) for perfectly equilibrated sequences all present in a 20 nM concentration. Right: experimental fluorescence (normalized, and reversed for FAM and JOE whose fluorescence change upon hybridization is negative) time plot for a system with [α*to*α] = 20 nM, [β*to*β] = 5 nM, [ɣ*to*ɣ] = 5 nM, [α*to*iβ] = 10 nM, [β*to*iɣ] = 7.5 nM and [ɣ*to*iα] = 5 nM. This latter concentration explain the poor signal induced by ɣ. The reaction was initiated with [ɣ] = 5 nM and [α] = [β] = 1 nM. Colored arrows indicate the successive spikes of input species: first comes a spike of ɣ, then β, then α, after which ɣ reactivates and the system stalls forever. Sequences are as follows: α: CTGAGTCTTGG, β: CAGAGTCCAAG, ɣ: AGGAGTCACAC.

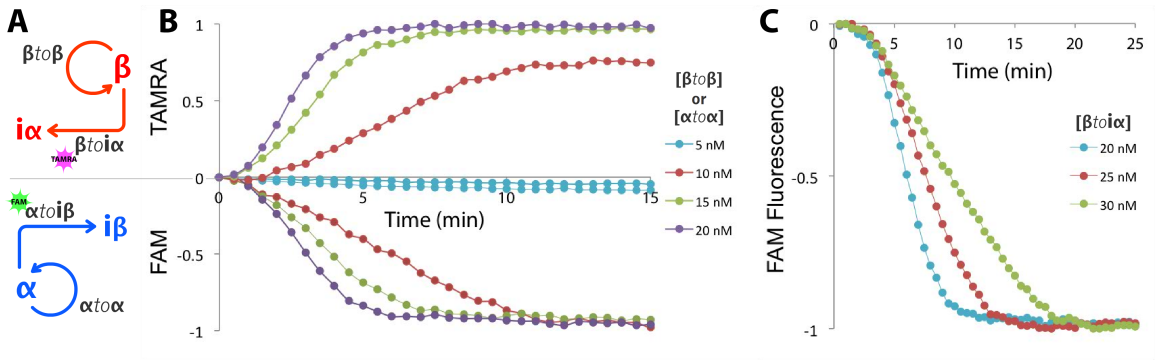

Figure 4.25: The load effect. (A) Circuits used for (B) experiments: (Up) Charge of $\beta to i\alpha$ by $\beta to\beta$ for a ramp of $[\beta to\beta]$. (Down) Charge of $\alpha toi\beta$ by $\alpha to\alpha$ for a ramp of $[\alpha to\alpha]$. The higher the concentration of autocatalytic module is, the faster the associated inhibition module is charged (and the fluorescence reaches the steady state). For both sides, 5 nM of autocatalytic module is not enough to charge the inhibition module, in these (enzymatic and temperature) conditions. Also, $\alpha to\alpha$ and $\beta to\beta$ do not take the same time to charge their respective inhibition modules ($\alpha toi\beta$ and $\beta toi\alpha$). This can be interpreted as an indicator of the respective strength of the autocatalytic modules: one would want to work with autocatalytic modules that amplify at the same rate. (C) $\alpha to\alpha$ (15 nM) charges $\alpha toi\beta$ present in 20 (blue), 25 (red) and 30 (green) nM. As the amount of inhibition module to load increases, the time needed to reach the steady state also increases.

4.7.3 Parasite

Monday, October 17th, 2011, experiments stopped working. This had happened before and was usually due to a change of batch of enzyme (batch to batch variation of enzymes activity are further discussed in Sections 3.3.2 and 3.7.3.4). This time, however, experiments were not simply "not working", and adjustments of enzyme concentration had no positive effect. There was more to it: the bistable circuit was showing some never-seen, and hopefully never-to-be-seen-again dynamics (Figure 4.26). Bistable circuits (cV11-cX11 as well as cT11-cV11) were oscillating, swinging, dying, showing everything but bistability, all by themselves.

Putting a small concentration of EvaGreen intercalating dye in the reaction mix allows us to monitor the accumulation of species otherwise not seen with the dyes attached to $\alpha toi\beta$ and $\beta toi\alpha$. EvaGreen signal impressively increased at the time where the fluorescence of the attached dyes started showing weird fluctuations. This revealed that an unknown species was taking over and at the same time disrupting the functioning of the system. This unknown, parasitic species was maybe related to sequences present in the system [167]. If, for instance, the parasite sequence was including a few bases that would match the fluorophore's nearby bases, this would explain the weird fluorescence fluctuations showed in Figure 4.26. The parasite might also have had a totally unrelated sequence [106], however sequestering (and saturating) the enzymes, leading to the disruption of the functioning of the system.

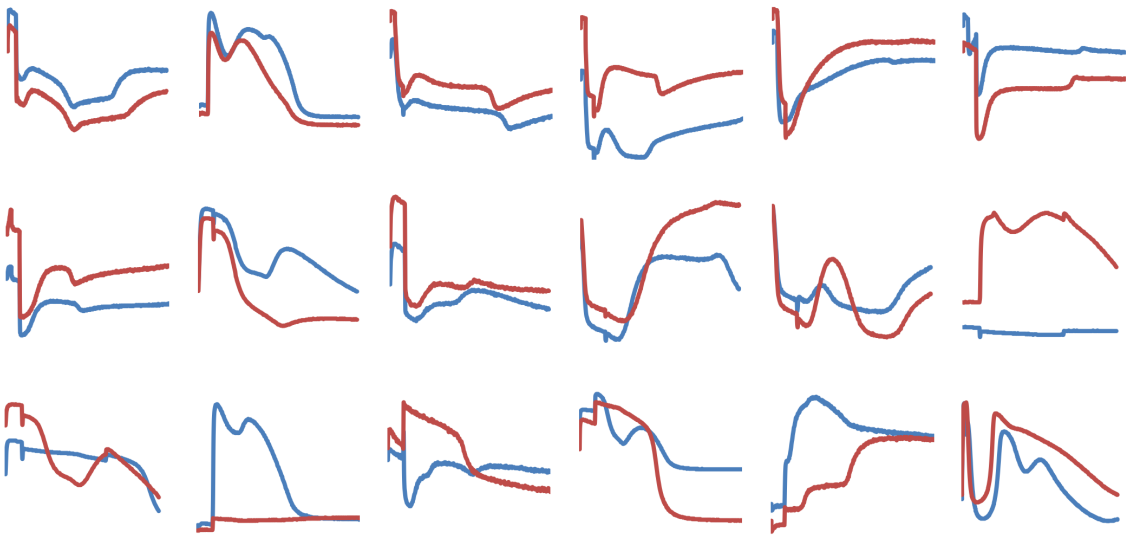

Figure 4.26: Swinging Curves. These are a selection of "crazy" bistable circuits obtained during a few months, seen through FAM, TAMRA of dy636 channels, depending on the bistable system (cV11-cX11 or cT11-cV11).

This parasite first appeared in a separate system (using a different nicking endonuclease, see chapter 6, but soon contaminated all our reactions, as such "monster" is known to have the ability to [168]. In order to get rid of the parasite (or at least delay its emergence) we cleaned all our pipettes and thermocyclers, threw away tubes, buffers, enzymes, and found that using Netropsin, an oligopeptide binding to AT-rich double-stranded sequences [169], was effectively delaying the emergence of the parasite in each reaction. From this time, Netropsin (2 µM) was added to the reaction buffer. We have never sequenced the parasite, nor done any gel analysis (by fear of further spreading the parasite), and maintain the habit to discard, without opening, any tube in which it is suspected to have appeared. It would however be interesting to try and understand the features that make it appear and duplicate that efficiently in our systems.

Chapter 5

Compartmentalization of the reactions

Compartmentalization in micro-reactors can be interesting for many applications. It can allow high-throughput analysis of a given system in various conditions. If small enough, micro-reactors can be used to study the statistical variations in molecule numbers between each units, as well as the dependency of the reaction on its volume. Micro-reactors could then be connected together, allowing one to control the diffusion - that is, the communication - between each computing unit.

By using microfluidic technologies, it is relatively easy to construct two-dimensional arrays of micro-chambers. Remaining challenges are (*i*) to find a way to fill and close them properly (*ii*) to get the reactions to work inside. These challenges do not have obvious solutions, as we will see in this chapter. We will find more success with the use of micro-emulsions, that can be cleanly generated by using microfluidic tools. This will allow us to set up a single-module reaction circuit in mono-disperse micro-droplets, opening good perspectives for the study of our reaction circuits in tiny compartments.

5.1 Microfabrication

Using soft lithography to build a simple microfluidic device first consists in making the *mould master* of the device:

- One has first to draw the design of the microfluidic device, using a vector drawing software (such as Adobe Illustrator) or dedicated software (such as AutoCAD).
- The drawing is then patterned in positive photoresist (e-beam etching) spincoated on a chrome-coated glass. After development of the photoresist, the exposed chrome is etched away (with a

chrome etchant solution): this transfers the drawing of the device to the chrome coating. The remaining photoresist is removed with acetone, thus revealing our *chrome mask*.

- The regular method then consists in using a silicon wafer as a substrate for the device *mould master*. The silicon wafer can first be cleaned using a *piranha* solution (mixture of hydrogen peroxide and sulfuric acid). This however makes the surface of the wafer hydrophilic, which is not wanted for the following spincoating of photoresist. The hydrophobicity of the wafer can be recovered by immersing it in BHF (Buffered Hydrofluoric Acid) for a few minutes. In the case of a freshly produced wafer, this cleaning process is not required.

- Next, negative photoresist is spincoated on the wafer. The thickness of the film of photoresist will roughly be the thickness of the microfluidic channels. Relationship between film thickness and spincoating speed is given by the photoresist maker (for a new photoresist).

- Then, Soft Bake (SB) is carried out: temperature and time depend on the thickness, for a given photoresist.

- The mould is then photo-exposed in the near UV, for a time that depends on the thickness and lamp power.

- Next comes the Post Exposure Bake (PEB), for a time that depends on the thickness of photoresist. This step is extremely important, since it controls the diffusion of the photo-activated compounds that will trigger the reticulation of the resist. If the PEB is too short, there will be a loss in sensitivity of the photoresist (not enough vertical diffusion of the photo-activated compounds), whereas if it is too long, there will be a loss in resolution (too much lateral diffusion of these same compounds).

- The negative photoresist is then developed: the UV-exposed areas, being reticulated, remain on the silicon substrate. We have our *mould master*.

- This mould can be Hard Baked (HB, done at higher temperature than SB and PEB) in order to remove eventual cracks present on the surface of the photoresist.

- Treating the mould master with a Teflon coating (CHF_3) by RIE (Reactive Ion Etching) will insure the resilience of the master mould to repetitive uses.

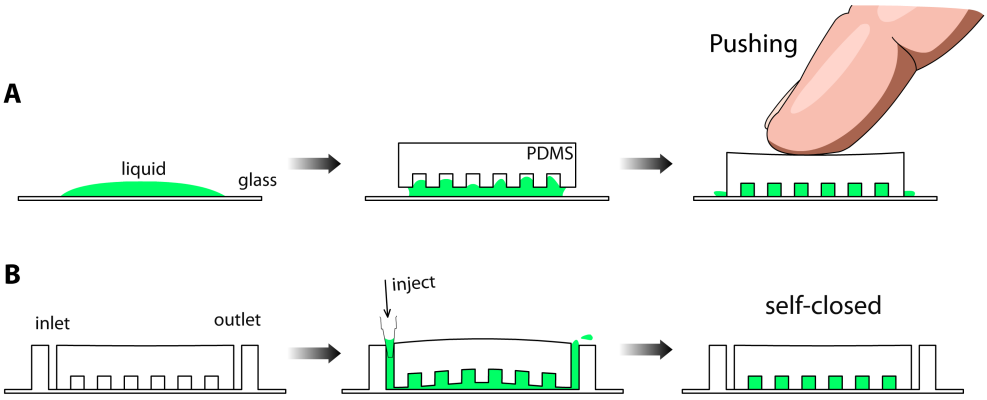

Figure 5.1: Compartmentalization. (A) Pushing technique: a drop of the liquid to enclose is deposited on a glass slide, then covered by the PDMS micro-chambers array, and closed by mechanical pushing. (B) Self-closing technique: liquid is injected in the inlet of a normally closed array of chambers. As the liquid makes its way to the outlet, it opens the chamber and fills them. When the liquid pressure is removed, the device recovers its normally closed state.

If carefully used, a mould master can be reused many times to make reproducible PDMS (Polydimethylsiloxane) devices. PDMS is a polymer chain that can be cross-linked by using different curing agents. It is a cheap, and easy to use material to make microfluidic devices, by following these steps:

- First, mix PDMS and precursor, usually in 10:1 proportion (more precursor is likely to produce a harder PDMS). Once the mix degassed, it is poured on the master mould and degassed again.
- PDMS is typically cured at 75 °C for 90 minutes - which drives the cross-linking reaction of the PDMS - it can be cured longer to obtain a harder PDMS.
- Moulded PDMS devices are then peeled of the master mould, and device inlet and outlet can be punched inside it for subsequent tubing.
- The device can then be directly pasted on a glass slide, or treated with plasma O_2 that forms silanol groups at its surface, allowing covalent bonding to a glass slide or PDMS surface.

This simple moulding recipe can then be repeated again and again, with the ability to make a dozen of small devices at each round.

5.2 Self-closing chambers

We were looking for a way to easily encapsulate large arrays of tiny volumes of liquid, in the purpose to be able to perform highly parallel biochemical reactions. We wanted our device to be as simple as

possible - that is, to avoid multilayer devices with complicated valve structures - because each device would only be used once (to avoid contamination between separate experiments). A common way to enclose liquid in arrays of micro-chambers [170] is to pattern them in PDMS, and press the patterned PDMS array on a glass slide where the liquid to enclose is deposited (Figure 5.1-A). This would require a device to keep the array pressed on the array of chambers.

We thought about a technique that wouldn't need any additional tool: self-closing chambers (Figure 5.1-B). The idea was to set up normally closed chambers, that would get opened by the fluid injected at the inlet of the device. As the liquid injection would stop, the chambers would find back their normally closed state, compartmentalizing the liquid in small separated volumes.

5.2.1 First design

The first design is shown in Figure 5.2-A. We started with an array of about 20000 relatively big chambers (40 µm diameter), patterned in between two inlets (for potential mixing of two reagents) and one outlet. The PDMS layer was covalently bonded to the glass slide, but the chambers array, so that the liquid could flow from the inlet to the outlet. This was done by protecting the chambers array from O_2 plasma with a thin plastic layer, removed before pasting to the glass slide. Using this device was very simple: the liquid was injected in the device with a plastic syringe; when removing the syringe, the chambers would close (Figure 5.1-B and 5.2-B).

This first design was not able to fill out all the chambers: once the injected liquid would have made its way from one inlet to one outlet, the chambers located on the path followed by the liquid would be filled. Then, the other inlets and outlets would stay closed. We tried replacing the inlets split in 5 by a single large inlet, thinking that the whole array would then be filled at once. This however didn't work much better.

5.2.2 Comb design

The best working design (and the progression toward it) is shown on Figure 5.3, for 10 µM diameter chambers. The main idea was to reduce the number of chambers to fill between the inlet and outlet (in order to make sure they would be filled), while keeping a large number of chambers on the device. In the present "comb" channels structure, only 15 to 20 chambers are separating the combs inlet and outlet. The devices shown on Figure 5.3 are still able to hold about 15000 chambers. The main improvement through the successive designs was the increased channels width, which would allow an

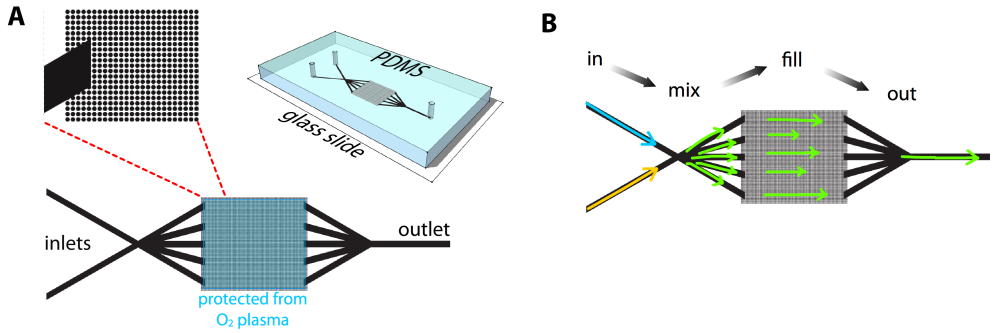

Figure 5.2: First self-closing design. (A) Device layout, 3D view and zoom on the chamber array. The latter is protected from O_2 plasma so that the liquid can make its way from the inlet to the outlet. (B) As the liquid flows from the inlet to the outlet, it fills the chambers.

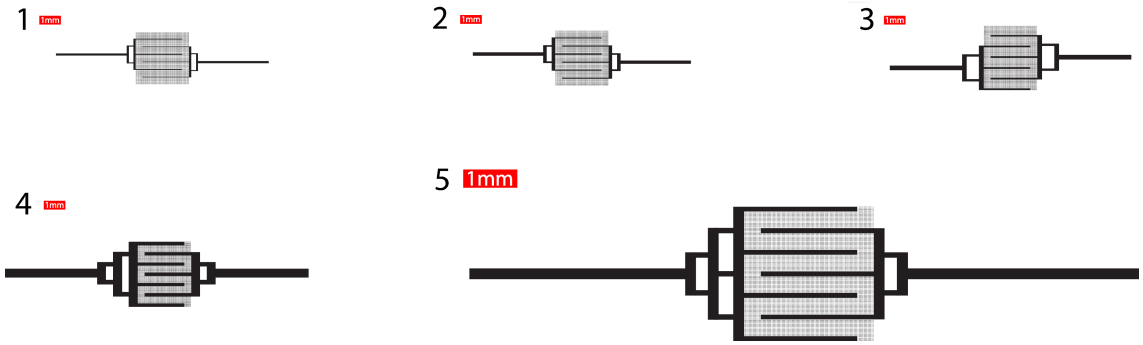

Figure 5.3: Comb design. (1) Initial design, with 15 chambers between the channels that are 70 µm wide. (2) Increased channel width (100 µm). (3) Increased channel width (150 µm) and number of chambers (20 between the channels). (4) XL channels (400 µm), 15 chambers between them and less outlets. (5) Best design: 200 µm wide channels, 15 chambers between them, less outlets than inlets.

easier filling and escape (to the inlets) of the liquid to enclose. For the two following designs, there are less outlets than inlets: this leaves no "dead zone" where the liquid injected would not flow (in the previous designs, the liquid was not able to flow at upper and lower extremities of the array, because bordered by the PDMS rather than an outlet). The chambers array of these devices is about 4 mm wide: this is small enough to allow the fabrication of 4 to 8 device per master mould. This device worked well, allowing the efficient filling and closing of large array of tiny volumes of liquid (Figure 5.4).

5.2.3 Are the chambers closed?

In order to address this important point, we performed a photo-bleaching experiment for each filled device. This test consists in including a fluorescent dye - for instance fluorescein - to the liquid to

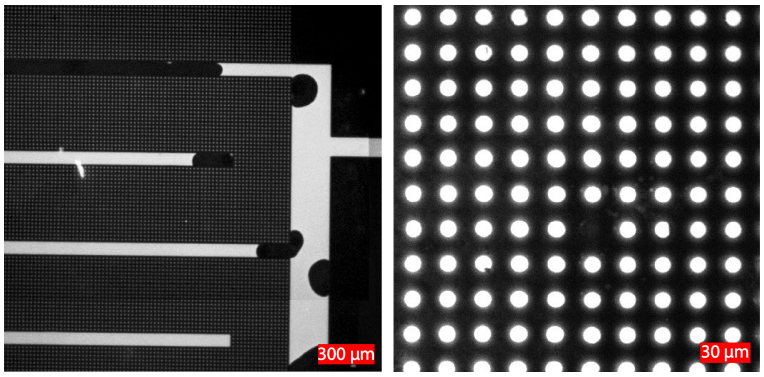

Figure 5.4: Large view of a portion of a filled device (Left). Zoom and bleaching of a single 10 µm chamber (Right).

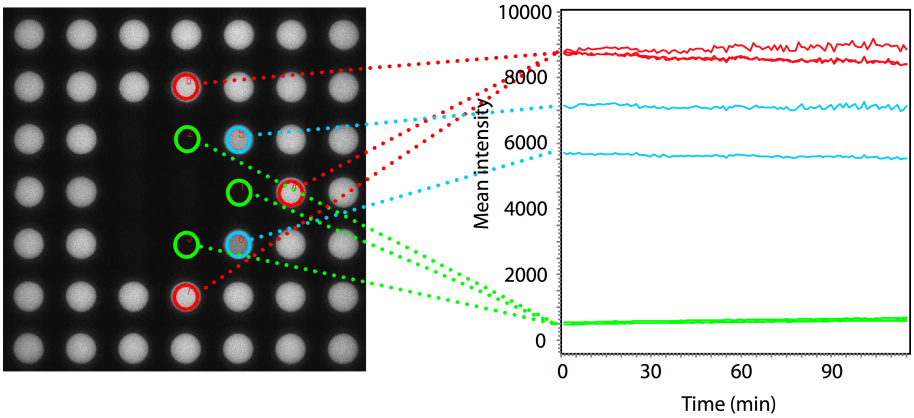

Figure 5.5: Bleaching test with 20 µm chambers. Fluorescein (10 µM) in water is introduced in a self-closing device. After photo-bleaching of the chambers in the middle (using a pinhole, and setting a high UV intensity), the fluorescence recovery is recorded through time. Here, chambers are well sealed: bleached ones do not recover any fluorescence during the 2-hours long time-lapse recording.

enclose; once the chambers seem closed, photo-bleaching one or more chambers - by exposing them to a strong light - then checking if, through time, the bleached chambers recover or not their fluorescence. If they do, this means that they are not properly sealed: there is diffusion of fluorescent dye from the nearby chambers. If they stay dark, this proves that they are well sealed (Figure 5.5).

5.2.4 Improving the sealing of the chambers

Here are a few ideas we tried to improve the sealing of the chambers:

- Making a thicker PDMS layer -> this somewhat worked. While a layer too thin was not allowing a good self-closing, a too thick one was rendering the device hard to fill. The best compromise was a thickness of about 4 mm.

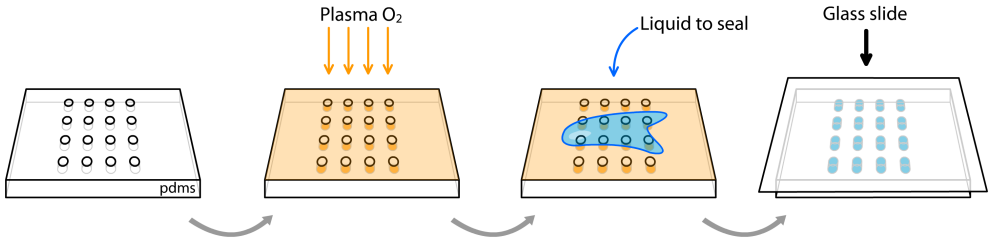

Figure 5.6: Plasma sealing. The PDMS surface containing microchambers is activated with plasma O_2. The liquid to seal is then poured on the surface, and covered with an activated glass slide, that should covalently bind to the PDMS array, thus closing the chambers.

- Increasing the stiffness of the closing layer: this could be done by covalently binding a glass slide on top of the PDMS layer -> this worked for thin PDMS layer, (of about 2 mm). The filling was however quite harder.
- Once the self-closing chambers are filled, applying a constant and negative pressure on the inlet and outlet: the channels will thus behave like suckers, sealing the chambers more efficiently -> this worked. However, the encapsulated liquid dried up more quickly.
- Making smaller arrays of chambers -> this also proved useful, however reducing the number of experiments possible to perform in parallel.

Another idea to close the chambers is presented in Figure 5.6. It consisted in taking a simple layer of PDMS with patterned array of chambers, treating it with O_2 plasma, which would make the surface (and chambers) hydrophilic. A drop of liquid to enclose would then easily get inside the chambers, and would be covered by a glass slide also treated with O_2 plasma. We would then expect the glass slide to covalently bind to the PDMS, efficiently closing the chambers. This technique worked well with simple solution of fluorescein in water, given that the overload of liquid could flow out of the array of chambers, before getting trapped by the covalent binding between the glass slide and the PDMS layer. For that, one would have to start press the device from the middle of the array to the outer sides. This technique however failed at enclosing samples "richer" (e.g. that contain proteins) than just a fluorescent dye in water.

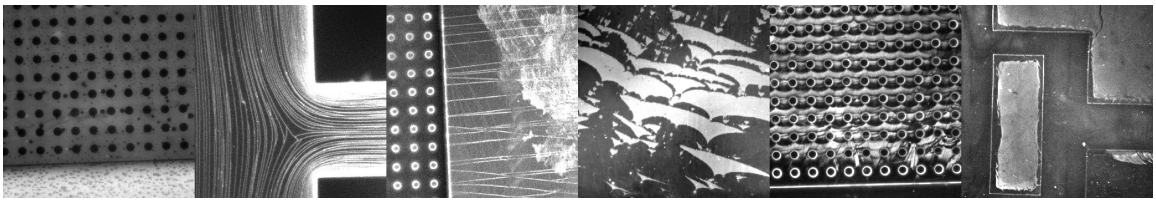

Figure 5.7: Various fluorescence pictures of the PDMS layer after the experiment (after having flushed away all the liquid)

5.3 The impossible compromises

5.3.1 PDMS and EvaGreen

As we started experiments with our reaction mix, we observed odd adsorption phenomena. EvaGreen appeared to be sticking to PDMS (Figure 5.7) which was one major problem: at that time, we were only using EvaGreen to monitor our reactions. We tried various surface treatments, coatings and surfactants: treating the PDMS with O_2 plasma was what appeared to work best. Which was a problem, since the fabrication of the self-closing device required the chamber array to be protected from O_2 plasma.

Adsorption of EvaGreen on the PDMS surface was one of the reasons that motivated the investigation of a different monitoring method: N-quenching. Another solution would have been to change the PDMS for another material, or come up with a device fully made of glass.

5.3.2 Coating and Sealing

As the surface to volume ratio increases, one gets subject to various problems at the interface between the liquid and the PDMS. We are working with chambers of sub-nanoliter volume, and want to enclose in it a buffer that contains DNA and enzymes, which can both have a tendency to adsorb on the surfaces. BSA (Bovine Serum Albumin) is commonly included in biological buffers to avoid DNA and enzymes non-specific adsorption [171, 172, 173] by competitively sticking to the surface. MPC (2-methacryloyloxyethyl phosphorylcholine) coating can also be used to prevent protein molecules adsorption on the surfaces [174, 175, 176]. As well, other surfactants can also be included in the reacting mix [177, 178].

While all these surfactants may be necessary for the reaction to perform in small volumes (in PDMS), they appeared to hinder the sealing of the chambers. We tried combinations of MPC-coated or raw surface with BSA, or BSA added to our reaction mix, and performed the photo-bleaching test

to check if the chambers were properly sealed. We found that sealing was possible with BSA alone (up to 0.5 mg/ml) or our reaction mix alone, but adding BSA to the reaction mix resulted in a failed sealing. As well, MPC coating was negatively affecting the sealing of the chambers.

5.4 Droplet microfluidics

Another way to encapsulate reactions is to use water-in-oil micro-emulsion. Microfluidics is good at producing microdroplets of desired size, in which it is possible to encapsulate things going from simple DNA amplification mixture [179] to single cells [180]. Microdroplets have also been used to compartmentalize the Belousov-Zhabotinsky oscillator and study the coupling (by an inhibitory intermediate of the reaction diffusing in oil) between oscillating droplets in 1D [181] and 2D [182]. Microfluidic droplets technology are readily used in our laboratory, we had the chance to design and try one of our simplest reaction circuits and monitor on-chip its functioning in agarose microdroplets by using N-quenching.

Mono-disperse microdroplets can be generated by using a flow-focusing microchannel network through which the aqueous phase is segmented by the oil phase. We used an innovative "push-pull" technique to produce microdroplets: it consists in pushing the oil phase only, while applying suction at the outlet of the device. By doing so, we could produce microemulsions by using a very low volumes of reagents. Using this setup, we encapsulated a single autocalatytic module blocked by an inhibitor strand (to prevent the reaction from starting during the droplets generation at room temperature), and could perform the reaction it in microvolume droplets, monitored under the microscope. The result of this work was published in *Biomicrofluidics*, and is present in Appendix as *A microfluidic device for on-chip agarose microbead generation with ultralow reagent consumption*. It opens the way to the high throughput analysis of DNA-toolbox made circuits: a next step may be to encapsulate more interesting - such as oscillating - reaction circuits, and observe the possible statistical variations between the encapsulated reactions.

Chapter 6

An ecological approach to spatiotemporal patterning

Ecological systems display complex population fluctuations that can theoretically be described by the century-old Lotka-Volterra Predator-Prey (PP) equations [183]. Also, spatial effects are believed to be responsible for a large part of the dynamic complexity observed among animal populations [94]. In this chapter, we will use a recently reported *in vitro* implementation of the PP relationship [184], and install it in a purposely engineered two-dimensional milieu. Our setup can be considered as a micro-ecosystem, which is able to emulate a two-dimensional *in vitro* PP ecosystem under a microscope. In nature, PP systems are extremely hard to observe because of their large scale in both time and space [185, 186]; our micro-ecosystem enables easy two-dimensional *in vitro* study of PP relationship and its extensive range of dynamics arising, for instance, from environmental perturbations. It could be used to explore the landscape-dynamics relationships for complex PP ecosystems, by implementing different environment topologies (micro-ecosystem shape), or localizing some of the resources at particular positions of the microchip (patchy systems [187]).

We also implemented the bistable circuit presented in Chapter 3 in a two-dimensional environment, and could observe the two stable states "fighting" against each other in various system geometries. These results are presented in Appendix *Two-dimensional Bistability*.

6.1 Technical notes

Otherwise indicated, all reactions were performed with the template G5dy530 (5'-CGGCCGAATG-CGGCCGAATG-3'), refereed to as G (for grass). Reactions were monitored with N-quenching alone (G is labeled with a dy530 in 3', allowing the specific monitoring of rabbits), or completed by EvaGreen intercalating dye (reporting both rabbit and fox concentrations).

For the two-dimensional experiments, we used an inverted IX-71 microscope (Olympus) with a CoolLED light source (pE excitation system) associated with a Semrock Cy3-4040C filter cube (to observe the fluorescence of dy530) . Reactions were monitored with an Andor XION camera, through a 1.25x objective lens with a 0.5x camera adapter. Devices were incubated using a Tokai thermoplate.

Images were typically acquired every minute (using µmanager software) and post-treated as follows, using ImageJ software:

- Optional: moving average on the whole stack, followed by the removal of half of the slices (great gain in signal to noise ratio, for a slight loss in spatial-temporal resolution).
- Calculation of the mean image of the whole stack (from shortly after the beginning to before the emergence of divergence) to get an estimate of the static background.
- Each image was normalized against the background.
- Kalman stack filter (used to reduce signal noise) was applied to the stack of images.

6.2 Predator-Prey reaction circuit

6.2.1 Basic functioning

Predator-Prey (PP) systems can be defined in terms of a set of reactions: preys autocatalytic reproduction (N -> 2N), predation of preys by predators (N + P -> 2P), and decay of both species (N or P -> 0). Initially, Lotka studied this system using the following set of ordinary differential equations [183]:

- For the prey: $\dot{N} = N - N.P$ (The growth of the prey is a function of its own population. Preys are consumed by predators, in relation of the frequency of encounters)
- For the predator: $\dot{P} = N.P - P$ (The growth of predator is a function of its own population and the population of rabbits. Predators decay by natural death.)

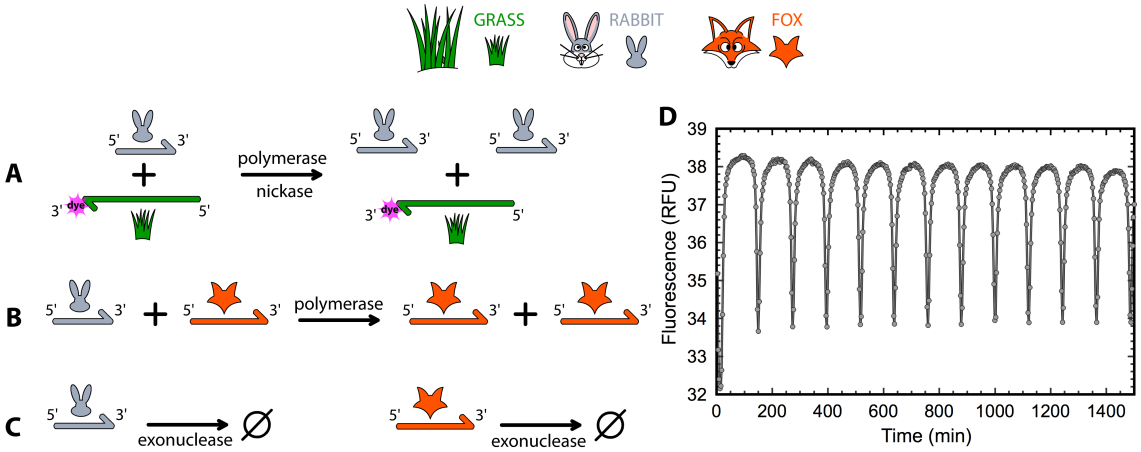

Figure 6.1: DNA-based Predator-Prey system. (A) In presence of the grass DNA template, rabbits autocatalytically reproduce. (B) Predation of rabbits by foxes. (C) Death of both rabbits and foxes. (D) Experimental curve in 0-dimensional milieu (test tube) using N-quenching [147], showing oscillations of rabbit population: a decrease in fluorescence intensity indicates an increase in rabbit concentration.

By using the same set of DNA-based enzymatic reactions as in the DNA-toolbox (based on a polymerase, a nicking enzyme and an exonuclease), it is possible to implement the PP relationship for the simplest ecological system consisting of a single prey and its predator. Predator (fox) and prey (rabbit) are both DNA species, and their DNA sequences define their trophic relationship. Experimentally, DNA-foxes and DNA-rabbits interact in a closed environment: in the presence of grass template, rabbits autocatalytically reproduce (Figure 6.1-A). Grass template is labeled in 3'-end with a fluorescent dye, which allows – through N-quenching [147] – the monitoring of the rabbits as they hybridize to the grass. A fox finding a rabbit produces two foxes (Figure 6.1-B); both foxes and rabbits die (Figure 6.1-C), whereas the amount of grass stays constant across generations. In 0-dimensional (well mixed) conditions, this system is an accurate chemical *in vitro* model of realistic PP equations [183], and displays sustained oscillations of fox and rabbit populations (Figure 6.1-D). We will not get into the detail of the DNA biochemistry behind this system (which is further presented in [184]), but keep in mind that this system only needs a single template (called G) to oscillate, and is fully compatible with the DNA-toolbox.

6.2.2 Adjusting the parameters of the Predator-Prey circuit

The Predator-Prey system can oscillate over a large range of parameters. In this section, we explore its sensitivity to several parameters, from the concentration of enzymes to the temperature. These experiments can then be reused as a calibration model when, for instance, one has to use a new batch

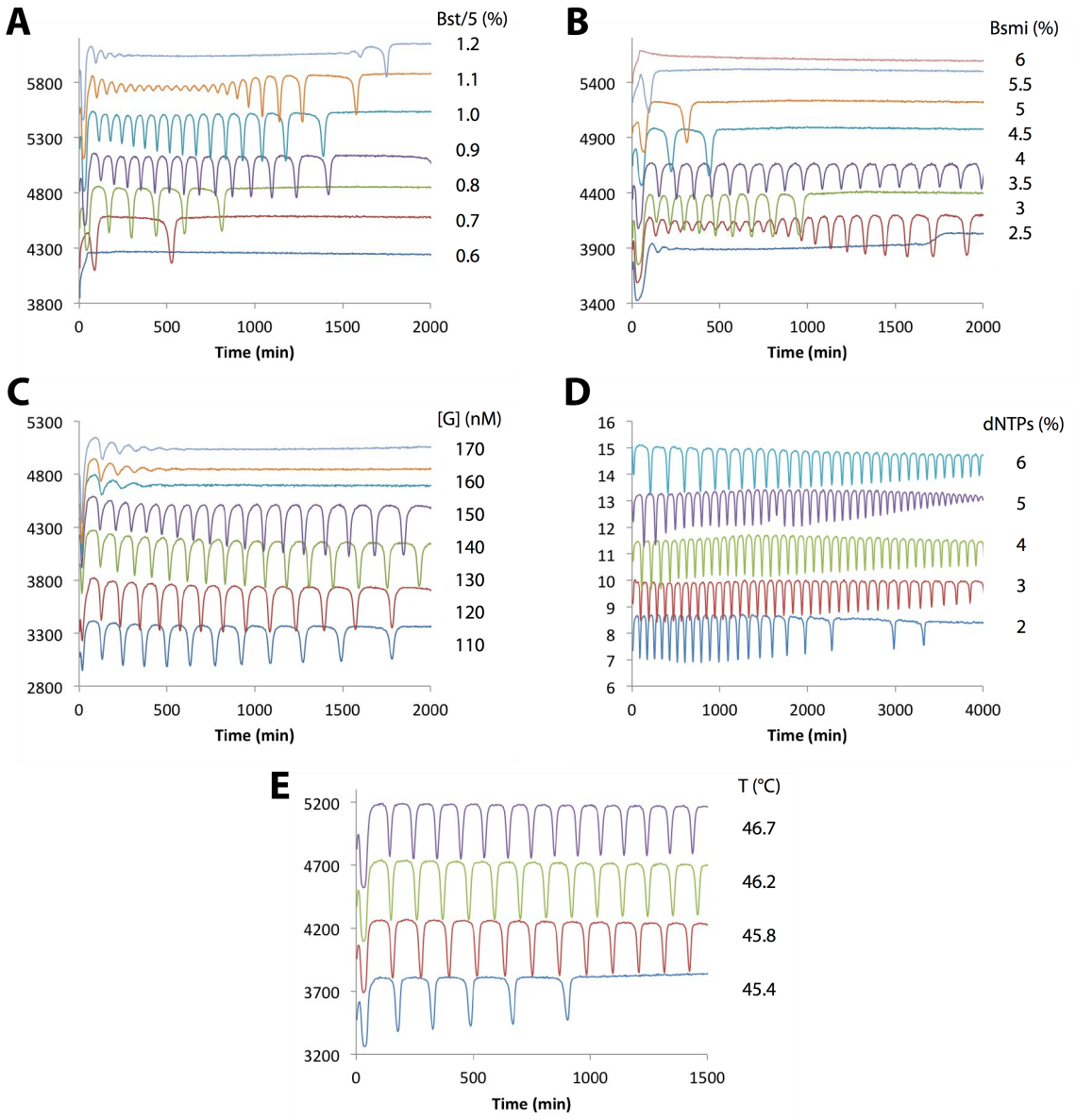

Figure 6.2: (A) Ramp of Bst/5 (percent of the total volume; 1 % corresponds to 16 units/ml) with [G] = 140 nM, T = 44.5 °C, dNTPs = 200 µM. (B) Ramp of Bsmi (percent of the total volume; 1 % corresponds to 100 units/ml) with [G] = 110 nM, T = 44.5 °C, dNTPs = 200 µM. (C) Ramp of [G] (nM) at T = 44.5 °C, dNTPs = 200 µM. (D) Ramp of dNTPs (1 % corresponds to 100 µM of each dNTP) with [G] = 140 nM, T = 46 °C. (E) Gradient of temperature with [G] = 140 nM.

of enzymes (with a different activity), or when one is searching for specific dynamics, such as slower but more stable oscillations, faster and damped oscillations or coexistence of preys and predators. Typical curves for ramps of polymerase concentration, nickase concentration, template concentration, dNTPs concentration and temperature are shown in Figure 6.2.

Changing the concentration of *Bst* polymerase (Figure 6.2-A) gives dynamics ranging from extinction of both species (at low concentration) to damped oscillations followed by coexistence (high concentration). Moving the concentration of Nb.BSMI nicking endonuclease goes reversely (Figure 6.2-B): at low concentration, the nicking enzyme works more slowly than the polymerase, resulting in a too strong growth of both prey and predator, that end up coexisting. At high concentrations, the nickase works too fast: in comparison, the polymerase is not fast enough to support the growth of rabbits. Roughly, changing the concentration of template corresponds to changing the concentration of polymerase (Figure 6.2-C). It is not shown on these curves, but at too low concentration of template, we also observe the extinction of both species. Interestingly, changing the concentration of dNTPs does more than just impacting the life span of the reaction (Figure 6.2-D): at too high concentration of dNTPs, the reaction is initially slower, and accelerates as dNTPs are used throughout the experiment. This can be explained by the binding of Mg^{2+} to dNTPs, making the concentration of free Mg^{2+} dependent on the concentrations of dNTPs. Yet, Mg^{2+} are required for the good functioning of the enzymes. Each "percent" of dNTPs corresponds to 100 µM of each of the four dNTPs, that is, 400 µM. Each percent thus sequesters 5 % of the 8 mM of Mg^{2+} contained in the reacting mix. Alternatively, dNTPs may have a competitive effect by binding to DNA processing enzymes. The temperature also has a complex impact on the kinetics of the reaction: among others, it modifies the activity of enzymes and the stability of duplexes (Figure 6.2-E).

6.2.3 Long-term oscillator

When properly optimized, the Predator-Prey system oscillates for days (Figure 6.3). This proves that we are able to maintain this closed system in quasi-stationary conditions far from equilibrium over a long period of time. We tried to further increase the concentration of dNTPs, but the reactions did not last longer (and actually got slower). After a week, the remaining enzyme activity may just be too low for the reaction to go on. With respect to future applications, it is important that such molecular computers can perform autonomously during such long periods.

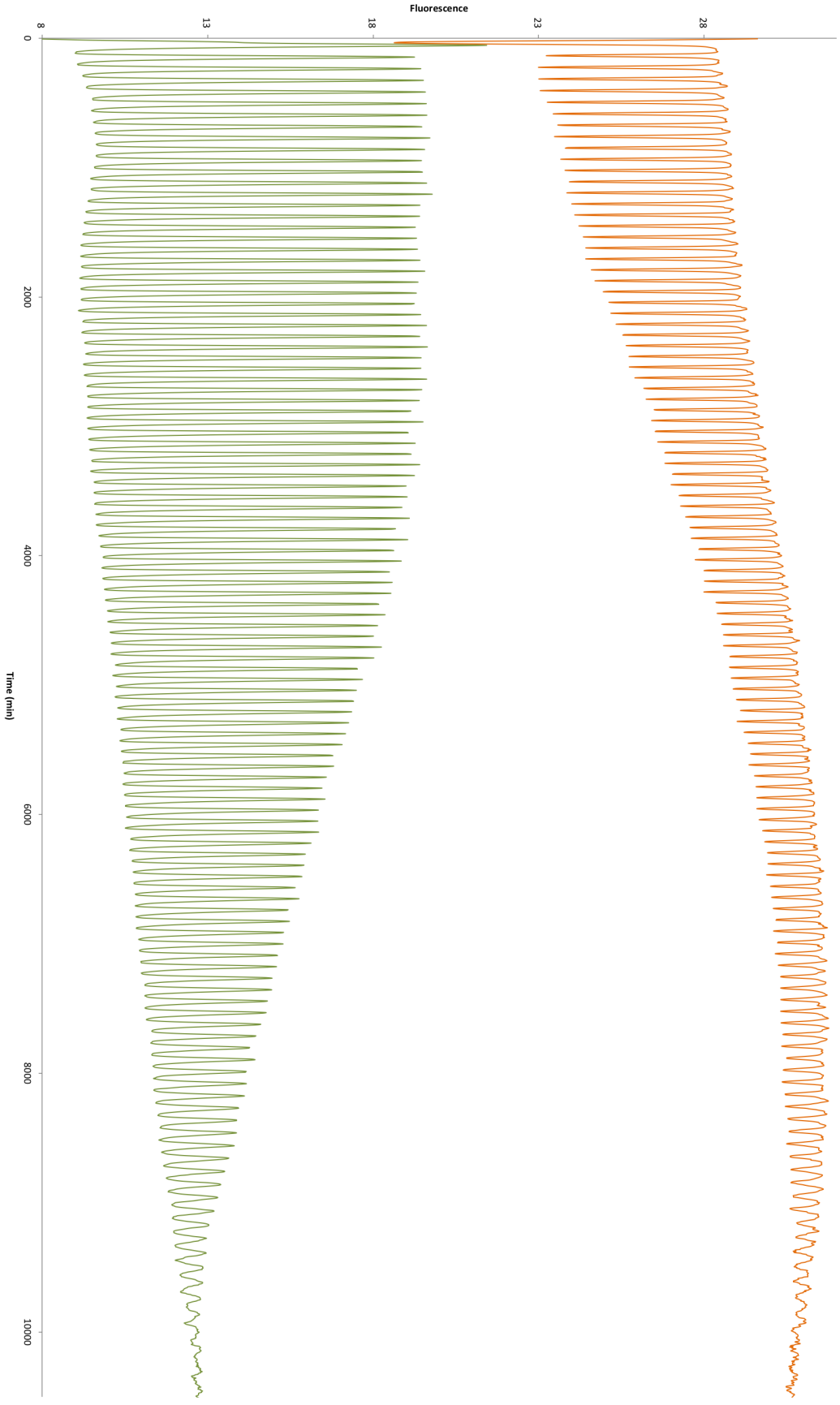

Figure 6.3: An oscillator running for 8 days (showing about 112 oscillations). [G] = 140 nM, T = 45.4 °C

6.3 Enable the reactions for working under the microscope

Our first fear when trying to work in a configuration with an increased surface-to-volume ratio (compared to bulk 0D experiment) was that various components of the system would adsorb on the surfaces of the two-dimensional milieu. During our investigation of PDMS microfluidic devices, we had big troubles with EvaGreen. In consequence, we initially decided to get rid of it. However, EvaGreen is not neutral to the functioning of the system: it is stabilizing the DNA duplexes, as observed in Section 4.5.1, and may also affect the binding of the enzymes to DNA, by competing for the grooves of the helix. Working without EvaGreen, we found good oscillating conditions at 44 °C (which was about 2 °C below the reaction temperature with EvaGreen). N-quenching gave us a signal good enough to monitor the oscillations (Figure 6.1). Enzymes might also adsorb to the surfaces: we could not get rid of them, so we hoped that increasing the two blockers of our reacting mix (BSA and Synperonic) would provide a working solution. In consequence, we checked if increasing the concentration of these blockers was hampering the reactions or not (Figure 6.4). Too high concentrations of BSA or Synperonic seemed to provoke a premature damping of the oscillations. We settled on a concentration of 0.5 mg/mL of BSA (5 times our usual concentration in bulk) and an unchanged concentration of Synperonic (0.1 %).

6.4 A simple device to observe the reactions in two-dimensions

The first device we used was proposed by André Estévez-Torres from CNRS/LPN: a flow-cell made of a simple layer of Parafilm (127 µm) separating two glass slides. By baking the device a few tens of seconds on a hot plate (around 65 °C), the Parafilm strongly attaches to the glass. The sample was then introduced by the "inlet", filling the chamber by capillarity. As initial perturbation, we slightly touched one inlet with a tip filled with rabbit solution. Inlets were closed with grease in order to avoid evaporation. The device was then incubated on the microscope hotplate, in a homemade setup to keep a wet atmosphere: it consisted of a petri dish put upside down on a PDMS joint and sealed with grease. An eppendorf cap filled with water was put next to the device to keep the air around saturated with water. With this simple setup, we could observe three successive waves of rabbits (difficult to distinguish from the background, see Figure 6.5). This was the first time we could observe traveling waves that were emerging from the inlet initially perturbed, and moving toward the opposite inlet. We found a temporal periodicity (when observing the oscillations at a given location) similar to that of

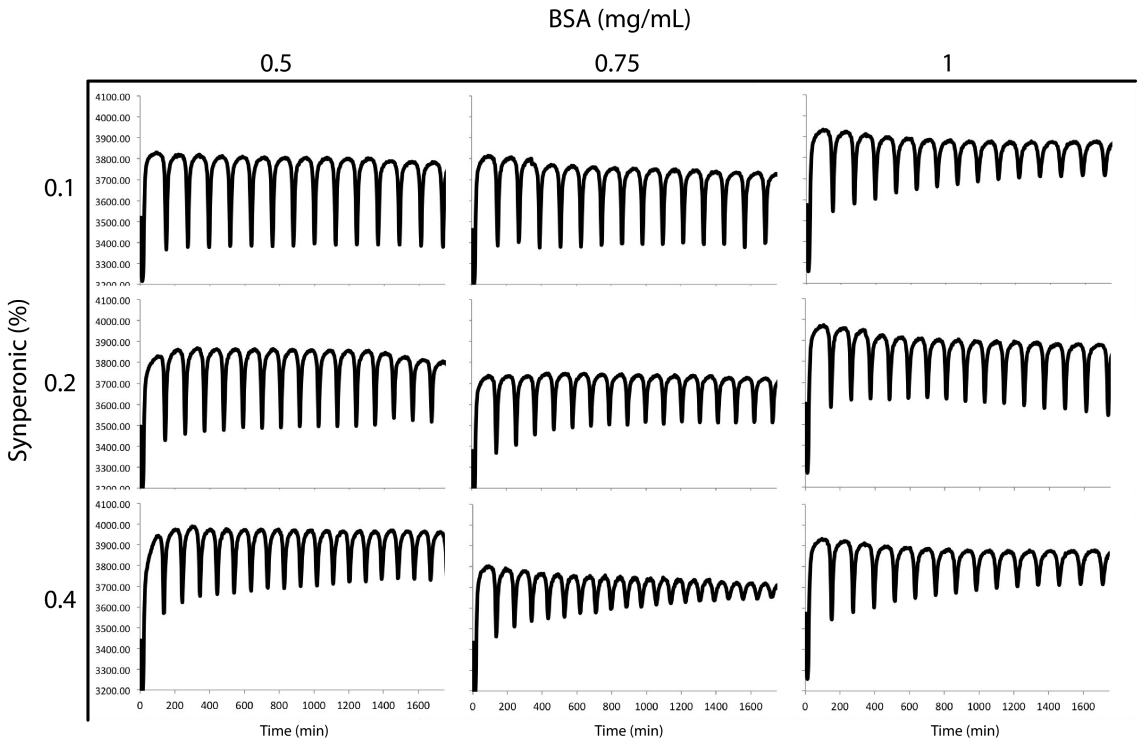

Figure 6.4: Increasing the concentration of BSA and Synperonic. Fluorescence time plots (X-axis: time in minutes, Y-axis: fluorescence of DY-530) for various couples of BSA and Synperonic concentrations. Usual conditions are: 0.1 % of Synperonic and 0.1 mg/mL of BSA. With increased concentrations of BSA or Synperonic, the oscillations tend to damp earlier. The relationship is however not clearcut: there might be some interactions between synperonic and BSA. [G] = 80 nM, T = 44 °C.

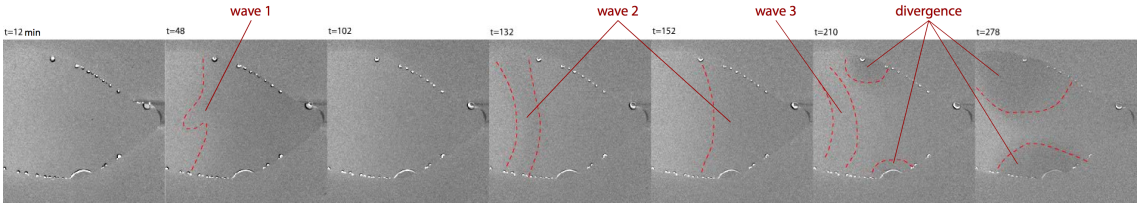

Figure 6.5: Three waves of rabbits going from left to right, arbitrarily delimited for visibility. They are followed by the divergence, emerging from t = 210 min. [G] = 80 nM, T = 44 °C.

the bulk experiment (i.e. a period of about 80 minutes). However, the reaction diverged very quickly, as it can be seen from t = 210 min on Figure 6.5.

In two dimensions, the divergence is characterized by a dark front that moves slowly and ineluctably. It also appears in the bulk experiment - though not as early - and is characterized by a strong decrease of the fluorescence of the attached dye (suggesting that all the templates become part of double-stranded complexes). If EvaGreen is used, one can observe a huge increase of its fluorescence, which indicates an accumulation of double-stranded species (and possibly single-stranded species). We still haven't any steady idea about the mechanism of this divergence, but as an easy example, if an uncut complementary strand of template G was to melt away, it would itself become a template for the production of G. Then, an increasing concentration of G might rapidly cause the system to be saturated with preys, taking away the dynamic balance between the prey and the predator growths. A variety of other autocatalytic mechanisms can be imagined, possibly yielding more complex and/or bigger DNA complexes. Note also that in two-dimensions, the divergence front moves notably (about 4 times) more slowly than the waves of preys, suggesting that its products are longer strands (or bigger complexes) than preys and predators, thus diffusing more slowly.

6.5 Stabilizing the reaction

We set on finding out what was causing the divergence to come so early, as compared to the bulk experiment.

6.5.1 Double layer and coatings

Whereas stable in tube, reactions had a tendency to diverge very quickly in the Parafilm device. Moreover, we had a very bad contrast in the first experiments (Figure 6.5). We solved the bad contrast issue by introducing the double layer device, for a double thickness (254 µm) of reacting mix.

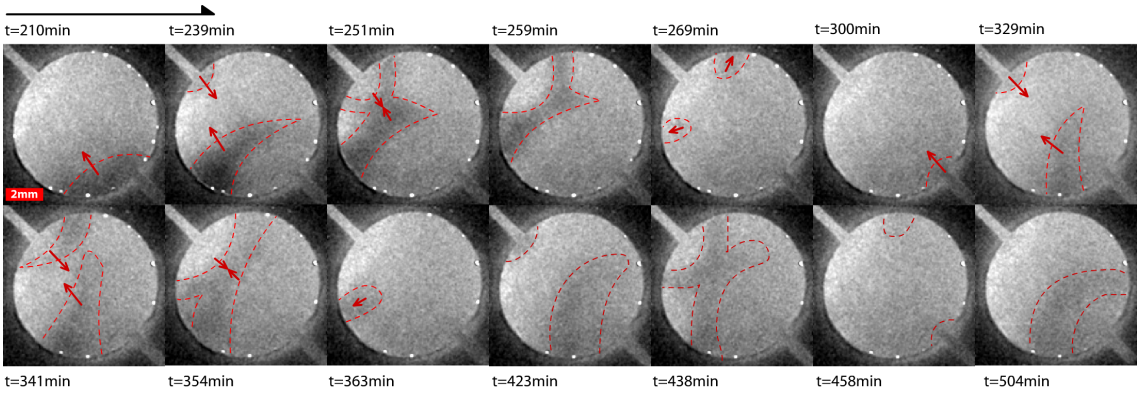

Figure 6.6: Double layer device pre-coated with BSA prior to the experiment. A few colliding waves (arbitrarily delimited for visibility) can be observed. [G] = 80 nM, T = 44 °C.

The device was easier to fill and the fluorescence signal was greatly improved. There is however a limit in thickness for liquid systems as convection effects will appear for a too thick layer of liquid: these are unwanted, for that they would add an uncontrolled complexity to the reaction-diffusion system. Convection effects could be avoided by working in a gel: in this way, we present in Appendix *Working in agarose* preliminary results of a DNA-toolbox made oscillator running in an agarose gel.

Thinking that the premature divergence was caused by some (again) non-specific interactions with the surfaces, we tried to pre-coat the device. Using mineral oil to coat the walls prior to the experiment resulted in some dirty results. MPC [174] coating did not work better. Pre-coating of BSA (1 mg/mL), incubated at 50 °C then flushed prior to the injection of the reaction mix, gave better results (Figure 6.6). We were able to observe our first colliding waves: as two waves of rabbits arriving from both sides of the chamber meet, the rabbits are surrounded by foxes, and the waves vanish. But still, the divergence arrived too soon, after only 4 oscillations.

6.5.2 Delaying the divergence

Looking better a the divergence made us realize that it was always coming from the interfaces with air (or grease). This for a reason that remains unclear: lower local temperature? Accumulation of some reaction components at the air-liquid interface? Any which way, in our device, the only interfaces with air (given that the device is well filled without large bubbles in the chamber) are located at the inlets, from where the front of the divergence slowly advances toward the chamber. In order to verify that these interfaces were the culprits, we made a device with long inlets, which would delay the arrival of the (slowly diffusing) dark divergence in the chamber.

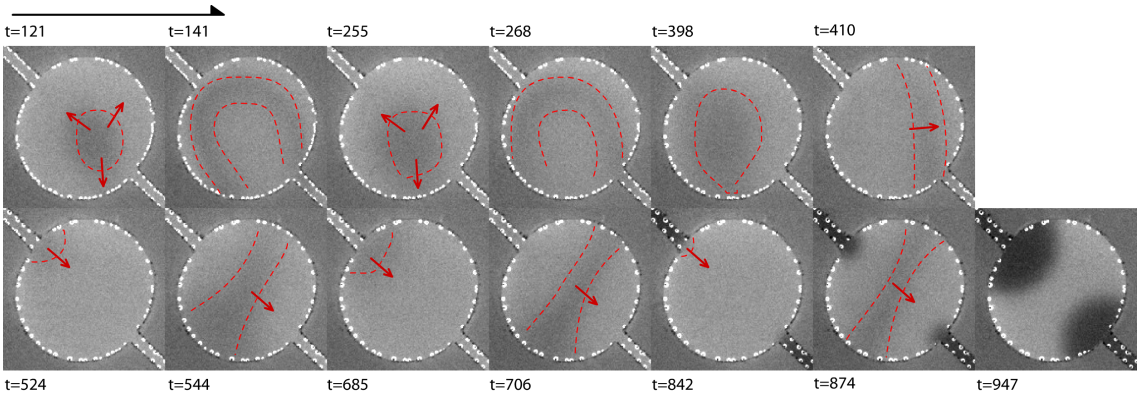

Figure 6.7: Long inlets. The delayed divergence (darker wave) arrives from both inlets. [G] = 80 nM, T = 44 °C.

The experiment of Figure 6.6 was performed in a 8 mm diameter chamber laying on a 24 mm long glass slide, leaving less than 8 mm for the inlets. For the experiment of Figure 6.7, we made the same 8 mm diameter chamber on a 36 mm long glass slide, which resulted in inlets of about 14 mm. Indeed, the divergence took quite longer to arrive in the chamber, where the reaction was otherwise properly performing. We could observe two successive waves of rabbits colliding with the walls of the chambers: in such case, the rabbits get cornered by the foxes that follow them, which results in the extinction of the wave against the wall. After these two waves, the point of emergence of rabbits moved to an inlet, until the eventual divergence of the reaction coming - once again - from the two inlets (Figure 6.7). As a conclusion, getting rid of the divergence meant getting rid of the inlets.

6.5.3 A commercial alternative

Bio-Rad sells Frame-Seal (FS), two-dimensional incubation chambers adapted for PCR reactions, that are vapor-tight and gas-tight up to 97 °C. The frame of FS is pasted on a regular glass slide, and is closed by a plastic sheet. FS allows to set up 65 µL of reacting mix on a 15x15 mm surface (a bit larger than what can be observed with our 1.25x objective lens and 0.5x camera adapter), which makes a thickness of about 290µm. Set up in FS, the reaction got more stable, and we were able to observe some nice spatio-temporal patterns (Figure 6.8). We started the reactions with one or more localized populations of rabbits: this was done by depositing a drop (typically 0.3 µL of rabbits at 1 µM) on the glass slide, and drying it up by heating on a hot plate.

Properly filling the Frame-Seal was tricky, and most experiments were launched with a few bubbles on a side or a corner. Almost every time, the divergence seemed to come from those large bubbles.

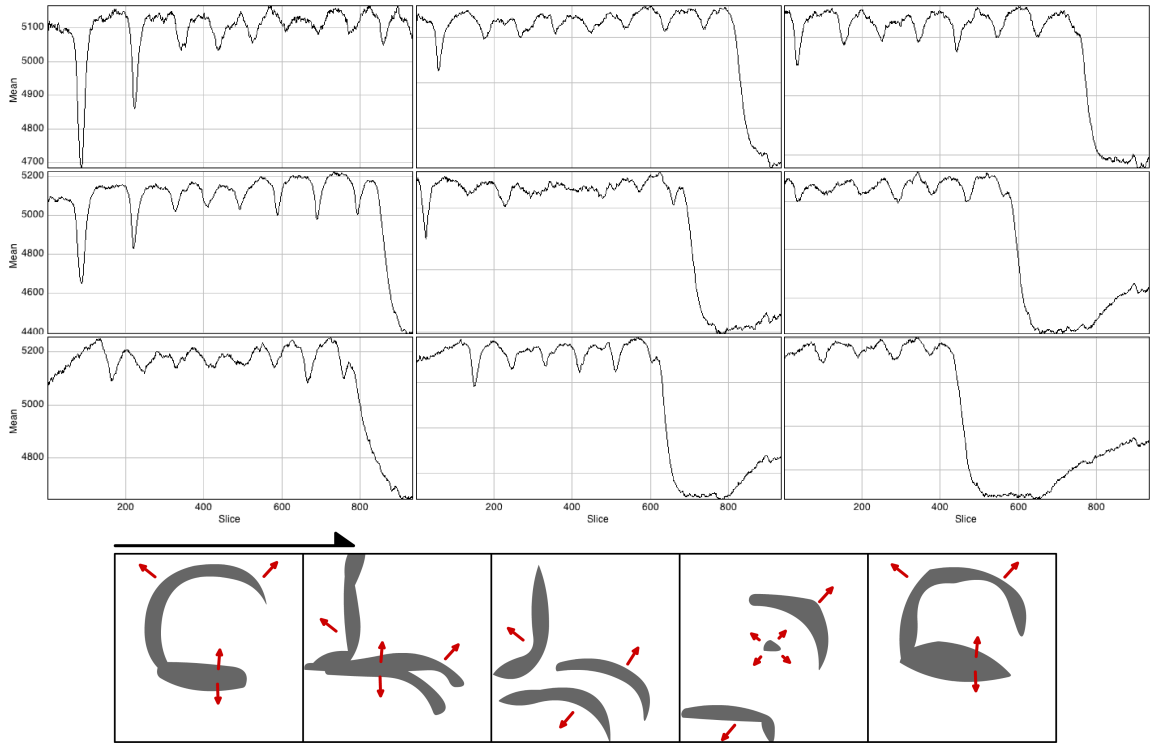

Figure 6.8: An experiment in Frame-Seal. The experiment is started with a population of dry rabbits in the middle of the FS and a smaller population a bit further up-right. (Top) Fluorescence time-plots of 10x10 pixels squares located at their respective locations of the FS (up-left corner, up-middle, up-right corner, and so on) (Bottom) After some transient, the system settled in the pattern tentatively depicted here. [G] = 80 nM, T = 44 °C.

Still, we were able to observe very nice spatio-temporal behaviors for various initial perturbations of the system. We also found good working conditions with an increased concentration of template G (140 nM) which resulted in a better fluorescent signal. FS are, however, all of the same square shape, and mostly impossible to customize.

6.6 Paraframe

The shortcomings of Frame-Seal motivated us to think about a homemade solution. We would need a device simple to produce with any desired shape, however avoiding PDMS (for that - as discussed in the previous chapter - it is far from being a good material when it comes to working with enzymes, and also EvaGreen intercalating dye). This device should avoid interfaces with air, since the premature divergence was always emerging at theses interfaces. As with the Frame-Seal, we wanted to maintain the possibility to localize the initial perturbation of rabbits and/or foxes.

Figure 6.9: Making of Paraframe chambers.

Inspired by Frame-Seal, we upgraded our Parafilm devices. We engineered "paraframe", an extremely simple (and cheap) device that only requires two glass slides and some Parafilm - removing the need for grease (Figure 6.9). Paraframe can be constructed in a few minutes, and only requires to punch or cut the desired chamber shape in a Parafilm double-layer, paste it on a glass slide and bake a few seconds at 50 °C. Then comes the eventual localization of dry rabbits, followed by the deposition of the reacting mix (adding an excess of 1 or 2 µL, as compared to the 20 µl of a chamber of 10 mm diameter). A second glass slide then sandwiches the reacting mix, and the device just needs to be flipped and baked another few seconds on this other side to be firmly closed. Paraframe can then be incubated on a hot plate without need of further closing (it has no inlet nor outlet) or wet atmosphere to avoid evaporation (it holds up well at 46 °C for days). The first experiment was already a great improvement over the "old" devices with inlets and outlets (Figure 6.10). Even in such a roughly shaped device, the reaction showed about 14 oscillations before diverging. The experiment in Figure 6.11 ran for more than two days, demonstrating the ability of paraframe to hold a reaction for a long time, preserved from evaporation.

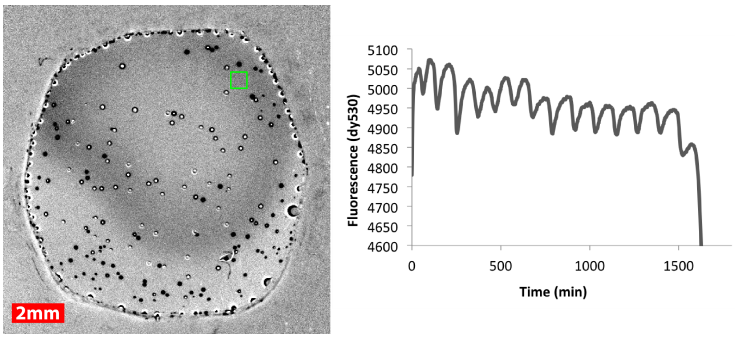

Figure 6.10: First Parafilm device. (Left) Fluorescence image at t = 370 min. Dark area are where rabbits are numerous. Small dots (dark and light) are bubbles. (Right) Time plot of the mean fluorescence in the small square delimited in green on the left image. [G] = 110 nM, T = 44 °C

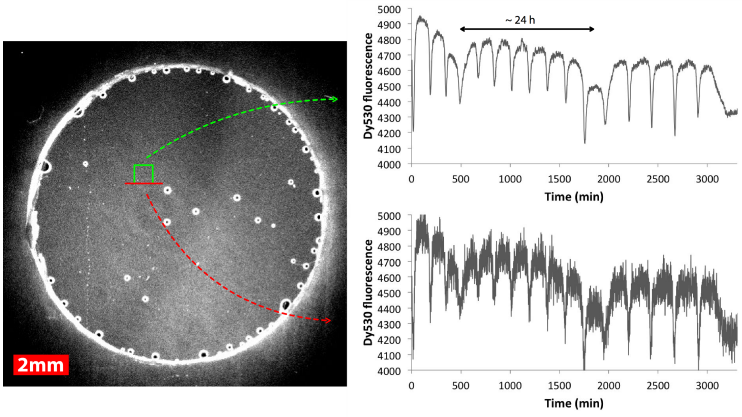

Figure 6.11: PP system with long period (about 200 min) in a round paraframe of 11 mm diameter. (Left) Fluorescence image (dy530) at t = 860 min. (Right) Time plot of the mean fluorescence on 900 pixels (up, corresponding to the green square) and 10 pixels (down, corresponding to the red line). These curves present a global fluctuation of the signal, which period is about 24 hours, which was also observed on longer experiments. We attributed these fluctuations - that mostly appeared in summer - to the variation of the temperature in the experimental room. [G] = 140 nM, T = 43 °C

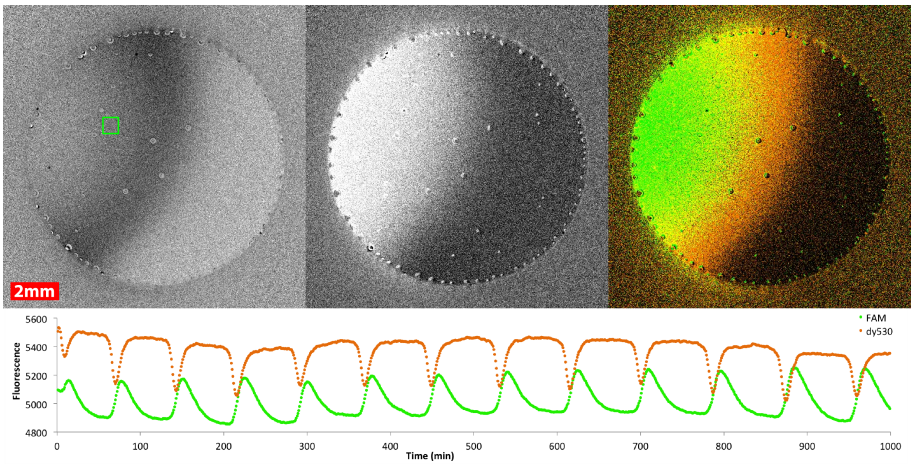

Figure 6.12: Monitoring both foxes and rabbits. (Up) From left to right: fluorescence images of dy530 (rabbits in dark), EvaGreen (foxes + rabbits in bright) and composite image (fake colors) at t = 454 min. [G] = 140 nM, T = 44.5 °C. (Down) Time plot of the mean fluorescence of the square area delimited in green.

6.6.1 Tracking the foxes

After a number of experiments performed without EvaGreen, we tried to use it again in paraframe chambers. Surfaces of paraframe are mostly made of glass, which should not cause much problems regarding the adsorption of EvaGreen - especially with the high concentration of BSA used in our two-dimensional configuration. After a few adjustments of the reaction conditions to work with EvaGreen (that stabilizes DNA duplexes), we ran an experiment in paraframe that, indeed, worked well. Using EvaGreen allowed us to monitor the waves of foxes hunting rabbits (Figure 6.12): the waves of foxes appeared to be wider than the waves of rabbits, and directly following them.

6.6.2 Spatiotemporal patterns

Two experimental videos can be found online at http://www.dailymotion.com/PP-ad

Videos are accelerated 3600 times. Darker (quenched) area are where of the concentration of rabbits is high. If monitored locally, one would expect periods of about 100 minutes.

- *exp2opp*: two starting populations of rabbits are located at two opposite corners of a 15x15 mm square (of which we only see approximately 13x13 mm)
- *exp2col*: the reactions are monitored in two colors: rabbits in orange, and foxes in green (fake colors), in a 11 mm diameter circular chamber (corresponding to the experiment of Figure 6.12)

6.7 Mathematical modeling

As described in [184], the kinetics of the Predator-Prey system is determined by the prey growth, predation (by the predator) and degradation on one side, and by the predator predation (of the prey) and degradation on the other side. As demonstrated in [184], these can be recapitulated in two non-dimensional, coupled ordinary differential equations (for prey n and predator p):

$$\frac{dn}{d\tau} = \frac{g.n}{1+\beta.g.n} - p.n - \lambda.\delta\frac{n}{1+p}$$

$$\frac{dp}{d\tau} = p.n - \delta\frac{p}{1+p}$$

With the following parameters taken from [184]: $\beta = 0.087$, $\lambda = 4.5$, $\delta = 0.39$, $\tau = t/t_c$ with $t_c = 2.6\,min$, $g = G/G_0$ with G being the concentration of template with the scaling factor $G_0 = 53\,nM$. This mathematical model was shown to accurately describe the behavior of this PP system in 0D, for various g (scaled concentration of grass template G). To describe a two-dimensional system, we simply added a diffusion term to the above equations, following Fick's laws of diffusion (with a constant diffusion coefficient D_n for the prey, and D_p for the predator).

$$\frac{dn}{d\tau} = \frac{g.n}{1+\beta.g.n} - p.n - \lambda.\delta\frac{n}{1+p} + D_n\left(\frac{\partial^2 n}{\partial x^2} + \frac{\partial^2 n}{\partial y^2}\right)$$

$$\frac{dp}{d\tau} = p.n - \delta\frac{p}{1+p} + D_p\left(\frac{\partial^2 p}{\partial x^2} + \frac{\partial^2 p}{\partial y^2}\right)$$

Coefficient of diffusion of both species were approximated by following two different rules of thumb found in the literature for short single stranded DNA in water [188, 189]. Both led to diffusion coefficient around 10^{-2} $\mathrm{mm}^2/\mathrm{min}$, and are - once again - approximations: we are not working in water, and at a different temperature. Note also that in our setup, not only preys and predators diffuse, but also the template G, as well as different double-stranded complexes (e.g. prey hybridized to G). Also, predators may have secondary structures or form dimers. Nonetheless, we took $D_n = 1 \times 10^{-2}\,mm^2/min$ for the 10-bases long prey and $D_p = 0.8 \times 10^{-2}\,mm^2/min$ for the 14-bases long predator. With regard to our experimental setup, we set no-flux boundary conditions, and one or more starting populations

of preys, localized as gaussian peaks. The initial population of predators was set as an homogeneous, low concentration on the whole surface. Using this simplified model, we were able to reproduce the important features that we experimentally observed, such as traveling, colliding waves as well as spiral waves.

Three videos of simulations, in a 10x10 mm square, are available online. Dark areas correspond to areas of high rabbit concentration. All the starting populations of rabbits were localized slightly out of the axis or center of symmetry

- *simu1side*: one starting population of rabbits on one side
- *simu2opp*: two starting populations of rabbits at two opposite corners
- *simu3*: three starting populations of rabbits

These can be found at the following link: http://www.dailymotion.com/PP-ad

6.8 Extension of this work

So far, in our two-dimensional setup, all species are diffusing: rabbits and foxes, but also the grass. It would be interesting to study systems for which some species do not diffuse (i.e. patchy systems) by, for instance, localizing inhomogeneous concentrations of grass. In such configuration, the growth of rabbits would be possible only in those patches of grass [187, 190]. A way to experimentally do this is to attach the grass templates to beads, which could be fixed in an gel matrix, where rabbits, foxes and enzymes would be allowed to diffuse. For the gel, agarose could be used: the system may however need some readjustment of the enzymatic conditions, as suggested in Appendix *Working in agarose*.

DNA strands can easily be attached to beads through a biotin-streptavidin link (using streptavidin beads linked to biotinylated DNA strands). We first checked if a biotin attached to the 3' (coupled using a TEG linker) or 5' (coupled using a 2-aminoethoxy-ethoxyethanol linker) end of the grass template was hindering the kinetic of the reactions (Figure 6.13). If performed at the same temperature, and in the same enzymatic conditions as for the system without biotin modification, G with 5' biotin (and a dy530 in 3') showed very fast, damped oscillations (one might try to decrease the concentration of polymerase in order to find stable oscillations), and G with a 3' biotin (and a dy530 in 5') required an increased concentration of template in order to show oscillations.

In conclusion, it should be possible to find optimized conditions for biotin modified templates. The next step would be to attach the template to a streptavidin, then to a bead. Adding a spacer

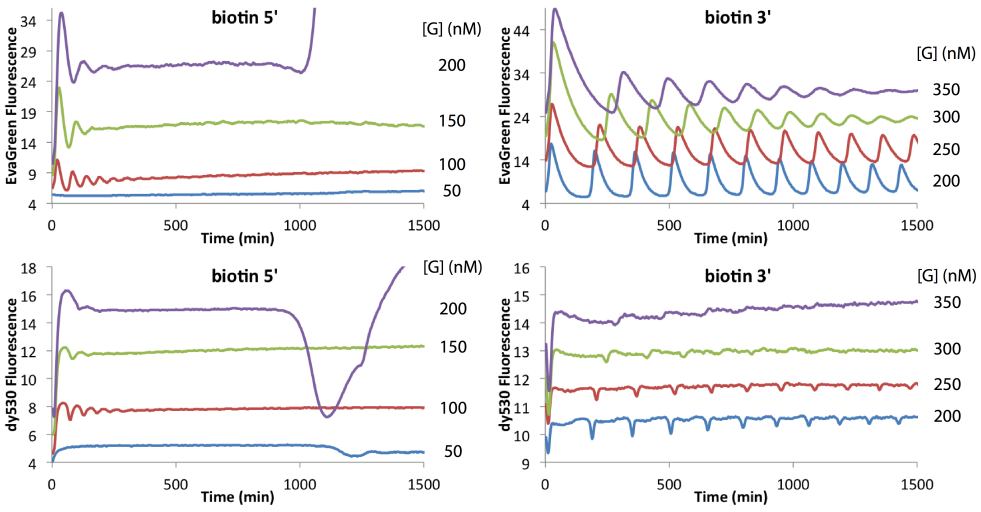

Figure 6.13: Biotinylated G. Fluorescence time plot of the predator-prey circuit for a ramp of [G] (displayed on the right of the curves, in nM), (Left) template G has a biotin in 5' (and dy-530 in 3'). (Right) template G has a biotin in 3' (and dy-530 in 5'). The experiment was performed at T = 46 °C, in the same enzymatic conditions as for G without biotin.

between the template and the biotin modification should help to avoid unwanted interactions between the template and the bead [191, 192]. This should also help the enzymes, which may be affected by the presence of the (big) biotin-streptavidin modification.

Other strategies may also be envisaged on the way for patchy systems: templates could be attached to agarose beads (PCR has been demonstrated in such configuration [193, 194]), or directly patterned on the glass [195]. It may also be possible to localize the enzymes on surfaces [196] (thus preventing their diffusion) or nanoparticles [197] (thus limiting their mobility).

Conclusion

The DNA-toolbox offers the possibility to assemble chemically modular systems that, just like their *in vivo* models, are able to display a plethora of dynamic behaviors. By its relevance to biology, the DNA-toolbox provides an experimental framework to study the network/function relationships within dynamic reaction networks. In this thesis, we expanded the DNA-toolbox with an efficient monitoring technique that was required to develop more complex reaction circuits. We then explored the roots of the DNA-toolbox, improved its buffer and enzymatic machinery and defined several design rules from the sequence level to the rational assembly of modules. By resting on this experience, we tackled the assembly of reaction circuits displaying bistability and switchability. We successfully assembled a robust bistable circuit and two switchable memory circuits. Using the easily accessible DNA hybridization and enzymatic Michaelis-Menten parameters, we built a detailed mathematical model that described extremely well these reaction circuits. Following this direction, it should be possible to explore the construction of even larger circuits with more complex dynamics. Each success along this line will improve our understanding of the underlying design rules of reaction networks, and each failure may hide some still unknown rules to unveil [59].

Nonetheless, perfectly harnessing the DNA-toolbox still presents challenges. Even though its functioning is simpler than the other existing *in vitro* implementations of dynamic behaviors [63, 42, 66], the DNA-toolbox is still a complex molecular system with many unpredictable facets. For instance, enzymes possess marvelous catalytic properties, but are also full of (irritating) surprises. Our circuits are based on three *generalist* enzymes (e.g. the nicking enzyme is expected to cut every recognition site), however, we extensively experienced their substrate dependence, and tried to compensate this issue by a careful –empirical– selection of the DNA sequences and a robust design of our reaction circuits. Yet, various surprises stay unanswered, or are still veiled: for instance, why does cd-ttRecJ degrade more quickly templates with 3 phosphorothioates than the ones with only 2 (Figure 4.10)? Is

their any way to deal with the stickiness of Nt.BstNBI on its substrates (this issue was partially addressed, see Figure 3.11)? Incidentally, sequence dependence of DNA processing enzymes has recently been the focus of a thorough study in the context of EXPAR DNA amplification ([158], using *Bst* DNA polymerase Large Fragment and Nt.BstNBI nicking enzyme). Such study may prove precious on the way to fully master the DNA-toolbox, with the purpose of building more complex reaction networks. Another approach would be to develop enzymatic tools dedicated to the building of reaction networks, instead of reusing not-so-well adapted, naturally occurring enzymes.

Reaction circuits assembled with the DNA-toolbox are starting to make their way towards two-dimensional environments. We now have in our hands a microfluidic tool to make any desired 2D shapes, and the possibility to assemble any desired dynamics: this control of both reaction and diffusion opens up the way to tailor-made spatiotemporal patterning. Still, this is just a burgeoning approach using the DNA-toolbox: perspectives are diverse, as are the technical points to tackle.

On the ecological side, while we observed the evolution of a single pair of predator-prey, many more interesting, complex spatiotemporal patterns can be expected from setting up additional species with arbitrarily chosen relationships in the food web. For instance, two pairs of predator-prey in a single tube have been shown to display chaotic oscillations upon competition for enzymatic resources [184]. What kind of behaviors can we expect from such a system installed in two-dimensions?

On the pattern side, we could observe –in both experiments and simulations– the emergence of spiral waves from the two-dimensional predator-prey oscillator. In the Belousov-Zhabotinsky oscillating reaction, spiral waves are propagating from pacemakers, which are either due to a physical perturbation (such as dust particles) or can emerge from breaking a traveling wave [103]. A technique to locally perturb an already oscillating system would be a good addition to the DNA-toolbox. For instance, we could use a method of photocontrol of DNA duplex formation [198] to locally induce the transient hybridization of an otherwise inactive inhibitor strand.

On the circuit side, we implemented an oscillating and a bistable circuit in our reaction-diffusion setup, but there is still a plethora of reaction circuits that could possibly result in interesting spatiotemporal behaviors. Then, one could think about localizing each circuit in space, by –for instance– attaching DNA templates to the surface, or to immobile beads. This may results in an integrated circuit-like, or a cell array-like surface which computational ability would be driven by both its reaction network components and its spatial arrangement. That is, an array of localized, communicating amorphous computers.

(D)NA and amorphous computers are not meant to replace conventional, silicon-based computers. Shortly after the seminal work by Adleman [3], enthusiasts proposed that molecular computers might surpass silicon-based computers [10]. This eventually did not happen, and surely will not: to date, no man-made molecular computer is capable of programmed calculations that cannot be trivially solved by any notebook. Rather, molecular computers –and amorphous computers– can be seen as new substrates capable of information processing [84]. These should be valued for their specific characteristics (e.g. fault-tolerance, shape independency, massive parallelism), rather than suffer from the comparison of their computational power with that of electronic computers. In this sense, amorphous computers could be envisioned as "smart materials" and two-dimensional reaction-diffusion systems as "smart surfaces". These would be able to sense, compute and actuate in response to their environment.

As molecular computers, Nucleic Acid reaction circuits are wonderful because they form a unique conceptual and material bridge between the living and the non-living matter. In this way, *in vivo* applications of nucleic acid circuits are burgeoning: to this end, more and more effort is put on improving the robustness of various systems [37, 81] and there has been reports of successful *in vivo* implementation of simple systems [77, 78].

The perspective of engineering a minimal, artificial cell as a stripped-down form of life has attracted much attention during the last decade [199, 64, 200]. It has been proposed that the *de novo* construction of such cell could use a liposome as a compartment, membrane proteins to communicate with the outside world, and would host a synthetic "DNA program" commanding its life-like behavior [44, 65]. However, this "DNA program" seems to remain the most complex hurdle of this project [65]. Other approaches concerning the origin of life also emphasize the structuring of reaction networks, rather than some peculiar physical characteristics [201, 202]. May the DNA-toolbox live up to the fascinating challenge of defining the minimal requirements of life?

Bibliography

[1] Powner, M. W., Gerland, B. & Sutherland, J. D. Synthesis of activated pyrimidine ribonucleotides in prebiotically plausible conditions. *Nature* (2009).

[2] Joyce, G. F. The antiquity of RNA-based evolution. *Nature* (2002).

[3] Adleman, L. M. Molecular computation of solutions to combinatorial problems. *Science (New York, NY)* (1994).

[4] Ouyang, Q., Kaplan, P. D., Liu, S. & Libchaber, A. DNA solution of the maximal clique problem. *Science (New York, NY)* (1997).

[5] Church, G. M., Gao, Y. & Kosuri, S. Next-generation digital information storage in DNA. *Science (New York, NY)* (2012).

[6] Winfree, E., Liu, F., Wenzler, L. A. & Seeman, N. C. Design and self-assembly of two-dimensional DNA crystals. *Nature* (1998).

[7] Chen, J. H. & Seeman, N. C. Synthesis from DNA of a molecule with the connectivity of a cube. *Nature* (1991).

[8] Mao, C., Sun, W., Shen, Z. & Seeman, N. C. A nanomechanical device based on the B-Z transition of DNA. *Nature* (1999).

[9] Yurke, B., Turberfield, A. J., Mills, A. P., Simmel, F. C. & Neumann, J. L. A DNA-fuelled molecular machine made of DNA. *Nature* (2000).

[10] Lipton, R. J. Dna Solution of Hard Computational Problems. *Science (New York, NY)* (1995).

[11] Boneh, D., Dunworth, C. & Lipton, R. J. Breaking DES using a molecular computer. *Proceedings of 1st DIMACS Workshop on DNA Computing.* (1995).

[12] Guarnieri, F., Fliss, M. & Bancroft, C. Making DNA add. *Science (New York, NY)* (1996).

[13] Faulhammer, D., Cukras, A. R., Lipton, R. J. & Landweber, L. F. Molecular computation: RNA solutions to chess problems. *Proceedings of the National Academy of Sciences of the United States of America* (2000).

[14] Boneh, D., Dunworth, C., Lipton, R. J. & Sgall, J. On the computational power of DNA. *Discrete Applied Mathematics* (1996).

[15] Sakamoto, K. *et al.* Molecular computation by DNA hairpin formation. *Science (New York, NY)* (2000).

[16] Braich, R. S., Chelyapov, N., Johnson, C., Rothemund, P. W. K. & Adleman, L. Solution of a 20-variable 3-SAT problem on a DNA computer. *Science (New York, NY)* (2002).

[17] Simmel, F. C. & Yurke, B. Using DNA to construct and power a nanoactuator. *Physical review E, Statistical, nonlinear, and soft matter physics* (2001).

[18] Simmel, F. & Yurke, B. A DNA-based molecular device switchable between three distinct mechanical states. *Applied Physics Letters* (2002).

[19] Zhang, D. Y. & Winfree, E. Control of DNA strand displacement kinetics using toehold exchange. *Journal of the American Chemical Society* (2009).

[20] Stojanovic, M., Mitchell, T. & Stefanovic, D. Deoxyribozyme-based logic gates. *Journal of the American Chemical Society* (2002).

[21] Breaker, R. & Joyce, G. A Dna Enzyme with Mg2+-Dependent Rna Phosphoesterase Activity. *Chemistry & Biology* (1995).

[22] Stojanovic, M. N. & Stefanovic, D. A deoxyribozyme-based molecular automaton. *Nature Biotechnology* (2003).

[23] Macdonald, J. *et al.* Medium scale integration of molecular logic gates in an automaton. *Nano Letters* (2006).

[24] Benenson, Y., Adar, R., Paz-Elizur, T., Livneh, Z. & Shapiro, E. DNA molecule provides a computing machine with both data and fuel. *Proceedings of the National Academy of Sciences of the United States of America* (2003).

[25] Benenson, Y., Gil, B., Ben-Dor, U., Adar, R. & Shapiro, E. An autonomous molecular computer for logical control of gene expression. *Nature* (2004).

[26] Takahashi, K., Yaegashi, S., Kameda, A. & Hagiya, M. Chain reaction systems based on loop dissociation of DNA. In *Dna Computing* (2006).

[27] Seelig, G., Soloveichik, D., Zhang, D. & Winfree, E. Enzyme-free nucleic acid logic circuits. *Science (New York, NY)* (2006).

[28] Seelig, G., Yurke, B. & Winfree, E. Catalyzed relaxation of a metastable DNA fuel. *Journal of the American Chemical Society* (2006).

[29] Zhang, D. Y., Turberfield, A. J., Yurke, B. & Winfree, E. Engineering entropy-driven reactions and networks catalyzed by DNA. *Science (New York, NY)* (2007).

[30] Qian, L. & Winfree, E. A simple DNA gate motif for synthesizing large-scale circuits. *Journal of The Royal Society Interface* (2011).

[31] Qian, L. & Winfree, E. Scaling up digital circuit computation with DNA strand displacement cascades. *Science (New York, NY)* (2011).

[32] Qian, L., Winfree, E. & Bruck, J. Neural network computation with DNA strand displacement cascades. *Nature* (2011).

[33] Genot, A. J., Bath, J. & Turberfield, A. J. Reversible logic circuits made of DNA. *Journal of the American Chemical Society* (2011).

[34] Chiniforooshan, E., Doty, D., Kari, L. & Seki, S. Scalable, time-responsive, digital, energy-efficient molecular circuits using DNA strand displacement. *DNA Computing and Molecular Programming* (2011).

[35] Nicolis, G. & Prigogine, I. Self-organization in nonequilibrium systems. *Wiley* (1977).

[36] Kjelstrup, S. & Bedeaux, D. Non-equilibrium thermodynamics of heterogeneous systems. *World Scientific* (2008).

[37] Zhang, D. Y. & Winfree, E. Robustness and modularity properties of a non-covalent DNA catalytic reaction. *Nucleic Acids Research* (2010).

[38] Soloveichik, D., Seelig, G. & Winfree, E. DNA as a universal substrate for chemical kinetics. *Proceedings of the National Academy of Sciences of the United States of America* (2010).

[39] Lakin, M. R., Youssef, S., Cardelli, L. & Phillips, A. Abstractions for DNA circuit design. *Journal of The Royal Society Interface* (2012).

[40] Takinoue, M., Kiga, D., Shohda, K.-i. & Suyama, A. Experiments and simulation models of a basic computation element of an autonomous molecular computing system. *Physical review E, Statistical, nonlinear, and soft matter physics* (2008).

[41] Sakai, Y., Mawatari, Y., Yamasaki, K., Shohda, K. & Suyama, A. Construction of AND Gate for RTRACS with the Capacity of Extension to NAND Gate. *DNA Computing and Molecular Programming* (2009).

[42] Kan, A., Shohda, K. & Suyama, A. A DNA Based Molecular Logic Gate Capable of a Variety of Logical Operations. *DNA Computing and Molecular Programming* (2012).

[43] Takinoue, M., Kiga, D., Shohda, K.-i. & Suyama, A. RNA Oscillator: Limit Cycle Oscillations based on Artificial Biomolecular Reactions. In *New Generation Computing* (2009).

[44] Ayukawa, S., Takinoue, M. & Kiga, D. RTRACS: A Modularized RNA-Dependent RNA Transcription System with High Programmability. *Accounts of Chemical Research* (2011).

[45] Hartwell, L. H., Hopfield, J. J., Leibler, S. & Murray, A. W. From molecular to modular cell biology. *Nature* (1999).

[46] Novick, A. & Weiner, M. Enzyme induction as an all-or-none phenomenon. *Proceedings of the National Academy of Sciences of the United States of America* (1957).

[47] Ozbudak, E. M., Thattai, M., Lim, H. N., Shraiman, B. I. & Van Oudenaarden, A. Multistability in the lactose utilization network of Escherichia coli. *Nature* (2004).

[48] Arkin, A., Ross, J. & McAdams, H. Stochastic kinetic analysis of developmental pathway bifurcation in phage lambda-infected Escherichia coli cells. *Genetics* (1998).

[49] Hasty, J., McMillen, D. & Collins, J. J. Engineered gene circuits. *Nature* (2002).

[50] Guido, N. J. *et al.* A bottom-up approach to gene regulation. *Nature* (2006).

[51] Nandagopal, N. & Elowitz, M. B. Synthetic biology: integrated gene circuits. *Science (New York, NY)* (2011).

[52] Elowitz, M. B. & Leibler, S. A synthetic oscillatory network of transcriptional regulators. *Nature* (2000).

[53] Gardner, T. S., Cantor, C. R. & Collins, J. J. Construction of a genetic toggle switch in Escherichia coli. *Nature* (2000).

[54] Hooshangi, S., Thiberge, S. & Weiss, R. Ultrasensitivity and noise propagation in a synthetic transcriptional cascade. *Proceedings of the National Academy of Sciences of the United States of America* (2005).

[55] Atkinson, M. R., Savageau, M. A., Myers, J. T. & Ninfa, A. J. Development of genetic circuitry exhibiting toggle switch or oscillatory behavior in Escherichia coli. *Cell* (2003).

[56] Kramer, B. P. *et al.* An engineered epigenetic transgene switch in mammalian cells. *Nature Biotechnology* (2004).

[57] Lou, C. *et al.* Synthesizing a novel genetic sequential logic circuit: a push-on push-off switch. *Molecular Systems Biology* (2010).

[58] Mather, W., Bennett, M. R., Hasty, J. & Tsimring, L. S. Delay-induced degrade-and-fire oscillations in small genetic circuits. *Physical review letters* (2009).

[59] Rondelez, Y. Competition for catalytic resources alters biological network dynamics. *Physical review letters* (2012).

[60] Tan, C., Marguet, P. & You, L. Emergent bistability by a growth-modulating positive feedback circuit. *Nature chemical biology* (2009).

[61] Kim, J., White, K. S. & Winfree, E. Construction of an in vitro bistable circuit from synthetic transcriptional switches. *Molecular Systems Biology* (2006).

[62] Montagne, K., Plasson, R., Sakai, Y., Fujii, T. & Rondelez, Y. Programming an in vitro DNA oscillator using a molecular networking strategy. *Molecular Systems Biology* (2011).

[63] Kim, J. & Winfree, E. Synthetic in vitro transcriptional oscillators. *Molecular Systems Biology* (2011).

[64] Noireaux, V. & Libchaber, A. A vesicle bioreactor as a step toward an artificial cell assembly. *Proceedings of the National Academy of Sciences of the United States of America* (2004).

[65] Noireaux, V., Maeda, Y. T. & Libchaber, A. Development of an artificial cell, from self-organization to computation and self-reproduction. *Proceedings of the National Academy of Sciences of the United States of America* (2011).

[66] Shin, J. & Noireaux, V. An E. coli Cell-Free Expression Toolbox: Application to Synthetic Gene Circuits and Artificial Cells. *ACS Synthetic Biology* (2012).

[67] Simpson, M. L. Cell-free synthetic biology: a bottom-up approach to discovery by design. *Molecular Systems Biology* (2006).

[68] Noireaux, V., Bar-Ziv, R. & Libchaber, A. Principles of cell-free genetic circuit assembly. *Proceedings of the National Academy of Sciences of the United States of America* (2003).

[69] Shin, J. & Noireaux, V. Efficient cell-free expression with the endogenous E. Coli RNA polymerase and sigma factor 70. *Journal of biological engineering* (2010).

[70] Subsoontorn, P., Kim, J. & Winfree, E. Ensemble Bayesian Analysis of Bistability in a Synthetic Transcriptional Switch. *ACS Synthetic Biology* (2012).

[71] Franco, E. *et al.* Timing molecular motion and production with a synthetic transcriptional clock. *Proceedings of the National Academy of Sciences of the United States of America* (2011).

[72] Milnes, P. J. *et al.* Sequence-specific synthesis of macromolecules using DNA-templated chemistry. *Chemical communications (Cambridge, England)* (2012).

[73] McKee, M. L. *et al.* Programmable one-pot multistep organic synthesis using DNA junctions. *Journal of the American Chemical Society* (2012).

[74] Xing, Y. *et al.* Self-assembled DNA hydrogels with designable thermal and enzymatic responsiveness. *Advanced materials (Deerfield Beach, Fla)* (2011).

[75] Nishioka, H., Liang, X., Kato, T. & Asanuma, H. A photon-fueled DNA nanodevice that contains two different photoswitches. *Angewandte Chemie (International ed in English)* (2012).

[76] Dirks, R. M. & Pierce, N. A. Triggered amplification by hybridization chain reaction. *Proceedings of the National Academy of Sciences of the United States of America* (2004).

[77] Choi, H. M. T. *et al.* Programmable in situ amplification for multiplexed imaging of mRNA expression. *Nature Biotechnology* (2010).

[78] Venkataraman, S., Dirks, R. M., Ueda, C. T. & Pierce, N. A. Selective cell death mediated by small conditional RNAs. *Proceedings of the National Academy of Sciences of the United States of America* (2010).

[79] Hodgman, C. E. & Jewett, M. C. Cell-free synthetic biology: thinking outside the cell. *Metabolic engineering* (2012).

[80] Zhang, D. Y. Cooperative hybridization of oligonucleotides. *Journal of the American Chemical Society* (2011).

[81] Duose, D. Y. *et al.* Configuring robust DNA strand displacement reactions for in situ molecular analyses. *Nucleic Acids Research* (2012).

[82] Schweller, R. M. *et al.* Multiplexed in situ immunofluorescence using dynamic DNA complexes. *Angewandte Chemie (International ed in English)* (2012).

[83] Zhang, D. Y., Chen, S. X. & Yin, P. Optimizing the specificity of nucleic acid hybridization. *Nature chemistry* (2012).

[84] Abelson, H. *et al.* Amorphous computing. *Communications of the ACM* (2000).

[85] Adamatzky, A., Costello, B. D. L. & Asai, T. *Reaction-Diffusion Computers* (Elsevier Science, 2005).

[86] Hopfield, J. J. Neural networks and physical systems with emergent collective computational abilities. *Proceedings of the National Academy of Sciences of the United States of America* (1982).

[87] Danino, T., Mondragón-Palomino, O., Tsimring, L. & Hasty, J. A synchronized quorum of genetic clocks. *Nature* (2010).

[88] Jirsa, V. K. & Kelso, J. A. Spatiotemporal pattern formation in neural systems with heterogeneous connection topologies. *Physical review. E, Statistical physics, plasmas, fluids, and related interdisciplinary topics* (2000).

[89] Kondo, S. & Miura, T. Reaction-diffusion model as a framework for understanding biological pattern formation. *Science (New York, NY)* (2010).

[90] Bunow, B., Kernevez, J. P., Joly, G. & Thomas, D. Pattern formation by reaction-diffusion instabilities: Application to morphogenesis in Drosophila. *Journal of theoretical biology* (1980).

[91] Lacalli, T. C. Modeling the Drosophila Pair-Rule Pattern by Reaction-Diffusion: Gap Input and Pattern Control in a 4-Morphogen System. *Journal of theoretical biology* (1990).

[92] Papaseit, C., Vuillard, L. & Tabony, J. Reaction–diffusion microtubule concentration patterns occur during biological morphogenesis. *Biophysical chemistry* (1999).

[93] Kondo, S. & Asai, R. A reaction-diffusion wave on the skin of the marine angelfish Pomacanthus. *Nature* (1995).

[94] Briggs, C. J. & Hoopes, M. F. Stabilizing effects in spatial parasitoid-host and predator-prey models: a review. *Theoretical population biology* (2004).

[95] Wilson, R. E. & Capasso, V. Analysis of a Reaction-Diffusion System Modeling Man–Environment–Man Epidemics. *SIAM Journal on Applied Mathematics* (1997).

[96] Riley, S. Large-scale spatial-transmission models of infectious disease. *Science (New York, NY)* (2007).

[97] Pearson, J. E. Complex Patterns in a Simple System. *Science (New York, NY)* (1993).

[98] Gardner, M. Mathematical games: The fantastic combinations of John Conway's new solitaire game "life". *Scientific American* (1970).

[99] Agladze, K., Magome, N., Aliev, R., Yamaguchi, T. & Yoshikawa, K. Finding the optimal path with the aid of chemical wave. *Physica D: Nonlinear Phenomena* (1997).

[100] Kuramoto, Y. *Chemical Oscillations, Waves, and Turbulence* (Dover Publications, 2003).

[101] Zhabotinsky, A. M. A history of chemical oscillations and waves. *Chaos: An Interdisciplinary Journal of Nonlinear Science* (1991).

[102] Zaikin, A. N. & Zhabotinsky, A. M. Concentration wave propagation in two-dimensional liquid-phase self-oscillating system. *Nature* (1970).

[103] Winfree, A. T. Spiral waves of chemical activity. *Science (New York, NY)* (1972).

[104] Mao, F., Leung, W.-Y. & Xin, X. Characterization of EvaGreen and the implication of its physicochemical properties for qPCR applications. *BMC biotechnology* (2007).

[105] Van Ness, J., Van Ness, L. & Galas, D. Isothermal reactions for the amplification of oligonucleotides. *Proceedings of the National Academy of Sciences* (2003).

[106] Tan, E. *et al.* Specific versus nonspecific isothermal DNA amplification through thermophilic polymerase and nicking enzyme activities. *Biochemistry* (2008).

[107] Stryer, L. & Haugland, R. P. Energy transfer: a spectroscopic ruler. *Proceedings of the National Academy of Sciences of the United States of America* (1967).

[108] Holland, P., Abramson, R., Watson, R. & Gelfand, D. Detection of specific polymerase chain reaction product by utilizing the 5'->3'exonuclease activity of Thermus aquaticus DNA polymerase. *Proceedings of the National Academy of Sciences* (1991).

[109] Tyagi, S. & Kramer, F. R. Molecular beacons: probes that fluoresce upon hybridization. *Nature Biotechnology* (1996).

[110] Cooper, J. P. & Hagerman, P. J. Analysis of fluorescence energy transfer in duplex and branched DNA molecules. *Biochemistry* (1990).

[111] Morrison, L. E. & Stols, L. M. Sensitive fluorescence-based thermodynamic and kinetic measurements of DNA hybridization in solution. *Biochemistry* (1993).

[112] Marras, S., Kramer, F. & Tyagi, S. Efficiencies of fluorescence resonance energy transfer and contact-mediated quenching in oligonucleotide probes. *Nucleic Acids Research* (2002).

[113] Seidel, C., Schulz, A. & Sauer, M. Nucleobase-specific quenching of fluorescent dyes. 1. Nucleobase one-electron redox potentials and their correlation with static and dynamic quenching efficiencies. *The Journal of Physical Chemistry* (1996).

[114] Torimura, M. *et al.* Fluorescence-quenching phenomenon by photoinduced electron transfer between a fluorescent dye and a nucleotide base. *Analytical sciences* (2001).

[115] Crockett, A. O. & Wittwer, C. T. Fluorescein-labeled oligonucleotides for real-time pcr: using the inherent quenching of deoxyguanosine nucleotides. *Analytical biochemistry* (2001).

[116] Kurata, S. *et al.* Fluorescent quenching-based quantitative detection of specific DNA/RNA using a BODIPY® FL-labeled probe or primer. *Nucleic Acids Research* (2001).

[117] Markham, N. R. & Zuker, M. DINAMelt web server for nucleic acid melting prediction. *Nucleic Acids Research* (2005).

[118] Zadeh, J. N. *et al.* NUPACK: Analysis and design of nucleic acid systems. *Journal of Computational Chemistry* (2011).

[119] Nazarenko, I., Pires, R., Lowe, B., Obaidy, M. & Rashtchian, A. Effect of primary and secondary structure of oligodeoxyribonucleotides on the fluorescent properties of conjugated dyes. *Nucleic Acids Research* (2002).

[120] Howell, W. M., Jobs, M. & Brookes, A. J. iFRET: an improved fluorescence system for DNA-melting analysis. *Genome research* (2002).

[121] Moreira, B., You, Y., Behlke, M. & Owczarzy, R. Effects of fluorescent dyes, quenchers, and dangling ends on DNA duplex stability. *Biochemical and biophysical research communications* (2005).

[122] Subramanian, H. K. K., Chakraborty, B., Sha, R. & Seeman, N. C. The label-free unambiguous detection and symbolic display of single nucleotide polymorphisms on DNA origami. *Nano Letters* (2011).

[123] Novák, B. & Tyson, J. J. Design principles of biochemical oscillators. *Nature Reviews Molecular Cell Biology* (2008).

[124] Casadesus, J. & D'Ari, R. Memory in bacteria and phage. *BioEssays : news and reviews in molecular, cellular and developmental biology* (2002).

[125] Veening, J.-W., Smits, W. K. & Kuipers, O. P. Bistability, Epigenetics, and Bet-Hedging in Bacteria. *Annual Review of Microbiology* (2008).

[126] Robert, L. *et al.* Pre-dispositions and epigenetic inheritance in the Escherichia coli lactose operon bistable switch. *Molecular Systems Biology* (2010).

[127] Tyson, J., Albert, R., Goldbeter, A., Ruoff, P. & Sible, J. Biological switches and clocks. *Journal of The Royal Society Interface* (2008).

[128] Tyson, J. J., Chen, K. C. & Novák, B. Sniffers, buzzers, toggles and blinkers: dynamics of regulatory and signaling pathways in the cell. *Current Opinion in Cell Biology* (2003).

[129] Yao, G., Tan, C., West, M., Nevins, J. R. & You, L. Origin of bistability underlying mammalian cell cycle entry. *Molecular Systems Biology* (2011).

[130] Monod, J. & Jacob, F. General Conclusions - Teleonomic Mechanisms in Cellular Metabolism, Growth, and Differentiation. *Cold Spring Harbor Symposia on Quantitative Biology* (1961).

[131] Friedland, A. E. *et al.* Synthetic gene networks that count. *Science (New York, NY)* (2009).

[132] Lu, T. K., Khalil, A. S. & Collins, J. J. Next-generation synthetic gene networks. *Nature Biotechnology* (2009).

[133] Purnick, P. E. M. & Weiss, R. The second wave of synthetic biology: from modules to systems. *Nature Reviews Molecular Cell Biology* (2009).

[134] Ellis, T., Wang, X. & Collins, J. J. Diversity-based, model-guided construction of synthetic gene networks with predicted functions. *Nature Biotechnology* (2009).

[135] Simpson, Z. B., Tsai, T. L., Nguyen, N., Chen, X. & Ellington, A. D. Modelling amorphous computations with transcription networks. *Journal of The Royal Society Interface* (2009).

[136] Lincoln, T. A. & Joyce, G. F. Self-Sustained Replication of an RNA Enzyme. *Science (New York, NY)* (2009).

[137] Xiong, W. & Ferrell, J. E. A positive-feedback-based bistable 'memory module' that governs a cell fate decision. *Nature* (2003).

[138] Sigal, A. *et al.* Variability and memory of protein levels in human cells. *Nature* (2006).

[139] Bonnet, J., Subsoontorn, P. & Endy, D. Rewritable digital data storage in live cells via engineered control of recombination directionality. *Proceedings of the National Academy of Sciences of the United States of America* (2012).

[140] Zhang, T., Schmierer, B. & Novák, B. Cell cycle commitment in budding yeast emerges from the cooperation of multiple bistable switches. *Open biology* (2011).

[141] Dworkin, J. & Losick, R. Developmental Commitment in a Bacterium. *Cell* (2005).

[142] Bhalla, U. S., Ram, P. T. & Iyengar, R. MAP kinase phosphatase as a locus of flexibility in a mitogen-activated protein kinase signaling network. *Science (New York, NY)* (2002).

[143] Polynikis, A. *et al.* Design and construction of a versatile synthetic network for bistable gene expression in mammalian systems. *Journal of computational biology : a journal of computational molecular cell biology* (2011).

[144] Vellela, M. & Qian, H. Stochastic dynamics and non-equilibrium thermodynamics of a bistable chemical system: the Schlögl model revisited. *Journal of The Royal Society Interface* (2009).

[145] Wakamatsu, T. *et al.* Structure of RecJ exonuclease defines its specificity for single-stranded DNA. *Journal of Biological Chemistry* (2010).

[146] Wakamatsu, T. *et al.* Role of RecJ-like protein with 5'-3' exonuclease activity in oligo(deoxy)nucleotide degradation. *Journal of Biological Chemistry* (2011).

[147] Padirac, A., Fujii, T. & Rondelez, Y. Quencher-free multiplexed monitoring of DNA reaction circuits. *Nucleic Acids Research* (2012).

[148] Ramakrishnan, N. & Bhalla, U. S. Memory Switches in Chemical Reaction Space. *PLoS Computational Biology* (2008).

[149] François, P. & Hakim, V. Design of genetic networks with specified functions by evolution in silico. *Proceedings of the National Academy of Sciences of the United States of America* (2004).

[150] Widder, S., Macía, J. & Solé, R. Monomeric Bistability and the Role of Autoloops in Gene Regulation. *PLoS ONE* (2009).

[151] Epstein, I. & Pojman, J. A. An Introduction to Nonlinear Chemical Dynamics (2012).

[152] Boissonade, J. & De Kepper, P. Transitions From Bistability to Limit-Cycle Oscillations - Theoretical-Analysis and Experimental-Evidence in an Open Chemical-System. *Journal of Physical Chemistry* (1980).

[153] Siegal-Gaskins, D., Mejia-Guerra, M. K., Smith, G. D. & Grotewold, E. Emergence of Switch-Like Behavior in a Large Family of Simple Biochemical Networks. *PLoS Computational Biology* (2011).

[154] Cherry, J. L. & Adler, F. R. How to make a biological switch. *Journal of theoretical biology* (2000).

[155] Ferrell, J. E. Self-perpetuating states in signal transduction: positive feedback, double-negative feedback and bistability. *Current Opinion in Cell Biology* (2002).

[156] Brandman, O. & Meyer, T. Feedback loops shape cellular signals in space and time. *Science (New York, NY)* (2008).

[157] Zhang, D. Y. & Seelig, G. Dynamic DNA nanotechnology using strand-displacement reactions. *Nature chemistry* (2011).

[158] Qian, J. *et al.* Sequence dependence of isothermal DNA amplification via EXPAR. *Nucleic Acids Research* (2012).

[159] Mazurek, M. & Sowers, L. The paradoxical influence of thymine analogues on restriction endonuclease cleavage of oligodeoxynucleotides. *Biochemistry* (1996).

[160] Pang, J., Modlin, J. & Yolken, R. Use of Modified Nucleotides and Uracil-DNA Glycosylase (UNG) for the Control of Contamination in the PCR-Based Amplification of RNA. *Molecular and Cellular Probes* (1992).

[161] Greagg, M. A. *et al.* A read-ahead function in archaeal DNA polymerases detects promutagenic template-strand uracil. *Proceedings of the National Academy of Sciences of the United States of America* (1999).

[162] Yang, Z., Sismour, A. M. & Benner, S. A. Nucleoside alpha-thiotriphosphates, polymerases and the exonuclease III analysis of oligonucleotides containing phosphorothioate linkages. *Nucleic Acids Research* (2007).

[163] Yamagata, A., Masui, R., Kakuta, Y., Kuramitsu, S. & Fukuyama, K. Overexpression, purification and characterization of RecJ protein from Thermus thermophilus HB8 and its core domain. *Nucleic Acids Research* (2001).

[164] Bommarito, S. & Peyret, N. Thermodynamic parameters for DNA sequences with dangling ends. *Nucleic Acids Research* (2000).

[165] Orban, M., Dateo, C., De Kepper, P. & Epstein, I. Systematic design of chemical oscillators. 11. Chlorite oscillators: new experimental examples, tristability, and preliminary classification. *Journal of the American Chemical Society* (1982).

[166] Tockstein, A. Simple kinetic models for a tristable system in a continuously stirred tank reactor. *Chemical physics letters* (1992).

[167] Bansho, Y. *et al.* Importance of parasite RNA species repression for prolonged translation-coupled RNA self-replication. *Chemistry & Biology* (2012).

[168] Marshall, K. A. & Ellington, A. D. Molecular parasites that evolve longer genomes. *Journal of molecular evolution* (1999).

[169] Zimmer, C. & Wähnert, U. Nonintercalating DNA-binding ligands: specificity of the interaction and their use as tools in biophysical, biochemical and biological investigations of the genetic material. *Progress in biophysics and molecular biology* (1986).

[170] Rondelez, Y. *et al.* Microfabricated arrays of femtoliter chambers allow single molecule enzymology. *Nature Biotechnology* (2005).

[171] Nagai, H., Murakami, Y., Morita, Y., Yokoyama, K. & Tamiya, E. Development of a microchamber array for picoliter PCR. *Analytical chemistry* (2001).

[172] Niu, Z., Chen, W., Shao, S., Jia, X. & Zhang, W. DNA amplification on a PDMS-glass hybrid microchip. *Journal of Micromechanics and Microengineering* (2006).

[173] Giordano, B. C., Copeland, E. R. & Landers, J. P. Towards dynamic coating of glass microchip chambers for amplifying DNA via the polymerase chain reaction. *Electrophoresis* (2001).

[174] Ishihara, K. *et al.* Why do phospholipid polymers reduce protein adsorption? *Journal of biomedical materials research* (1998).

[175] Hirota, K., Murakami, K., Nemoto, K. & Miyake, Y. Coating of a surface with 2-methacryloyloxyethyl phosphorylcholine (MPC) co-polymer significantly reduces retention of human pathogenic microorganisms. *FEMS microbiology letters* (2005).

[176] Goda, T., Konno, T., Takai, M., Moro, T. & Ishihara, K. Biomimetic phosphorylcholine polymer grafting from polydimethylsiloxane surface using photo-induced polymerization. *Biomaterials* (2006).

[177] Shin, Y. *et al.* PDMS-based micro PCR chip with parylene coating. *Journal of Micromechanics and Microengineering* (2003).

[178] Fukuba, T., Yamamoto, T., Naganuma, T. & Fujii, T. Microfabricated flow-through device for DNA amplification—towards in situ gene analysis. *Chemical Engineering Journal* (2004).

[179] Mazutis, L., Araghi, A., Miller, O. & Baret, J. Droplet-Based microfluidic systems for high-throughput single DNA molecule isothermal amplification and analysis. *Analytical chemistry* (2009).

[180] Edd, J. F. *et al.* Controlled encapsulation of single-cells into monodisperse picolitre drops. *Lab on a Chip* (2008).

[181] Toiya, M., Vanag, V. K. & Epstein, I. R. Diffusively Coupled Chemical Oscillators in a Microfluidic Assembly. *Angewandte Chemie International Edition* (2008).

[182] Toiya, M., González-Ochoa, H. O., Vanag, V. K., Fraden, S. & Epstein, I. R. Synchronization of Chemical Micro-oscillators. *The Journal of Physical Chemistry Letters* (2010).

[183] Lotka, A. Undamped oscillations derived from the law of mass action. *Journal of the American Chemical Society* (1920).

[184] Rondelez, Y. Predator-Prey Molecular Ecosystems. *Submitted* (2012).

[185] Okubo, A., Maini, P. K., Williamson, M. H. & Murray, J. D. On the spatial spread of the grey squirrel in Britain. *Proceedings of the Royal Society of London. Series B, Containing papers of a Biological character. Royal Society (Great Britain)* (1989).

[186] Krebs, C. J. *et al.* Impact of food and predation on the snowshoe hare cycle. *Science (New York, NY)* (1995).

[187] Wiens, J. A. Population responses to patchy environments. *Annual Review of Ecology and Systematics* (1976).

[188] Lukacs, G. L. *et al.* Size-dependent DNA mobility in cytoplasm and nucleus. *The Journal of biological chemistry* (2000).

[189] Stellwagen, E., Lu, Y. & Stellwagen, N. C. Unified description of electrophoresis and diffusion for DNA and other polyions. *Biochemistry* (2003).

[190] Michalski, J., Poggiale, J. C., Arditi, R. & Auger, P. M. Macroscopic dynamic effects of migrations in patchy predator-prey systems. *Journal of theoretical biology* (1997).

[191] Nykypanchuk, D., Maye, M. M., van der Lelie, D. & Gang, O. DNA-guided crystallization of colloidal nanoparticles. *Nature* (2008).

[192] Park, S. Y. *et al.* DNA-programmable nanoparticle crystallization. *Nature* (2008).

[193] Kumaresan, P., Yang, C. J., Cronier, S. A., Blazej, R. G. & Mathies, R. A. High-throughput single copy DNA amplification and cell analysis in engineered nanoliter droplets. *Analytical chemistry* (2008).

[194] Zeng, Y., Novak, R., Shuga, J., Smith, M. T. & Mathies, R. A. High-performance single cell genetic analysis using microfluidic emulsion generator arrays. *Analytical chemistry* (2010).

[195] Zammatteo, N. *et al.* Comparison between different strategies of covalent attachment of DNA to glass surfaces to build DNA microarrays. *Analytical biochemistry* (2000).

[196] Mateo, C., Palomo, J. M., Fernandez-Lorente, G., Guisan, J. M. & Fernandez-Lafuente, R. Improvement of enzyme activity, stability and selectivity via immobilization techniques. *Enzyme and Microbial Technology* (2007).

[197] Jia, H., Zhu, G. & Wang, P. Catalytic behaviors of enzymes attached to nanoparticles: the effect of particle mobility. *Biotechnology and bioengineering* (2003).

[198] Asanuma, H., Liang, X., Yoshida, T. & Komiyama, M. Photocontrol of DNA duplex formation by using azobenzene-bearing oligonucleotides. *Chembiochem : a European journal of chemical biology* (2001).

[199] Szostak, J. W., Bartel, D. P. & Luisi, P. L. Synthesizing life. *Nature* (2001).

[200] Jewett, M. C. & Forster, A. C. Update on designing and building minimal cells. *Current Opinion in Biotechnology* (2010).

[201] Eigen, M. & Schuster, P. Stages of emerging life—five principles of early organization. *Journal of molecular evolution* (1982).

[202] Eigen, M. The origin of genetic information: viruses as models. *Gene* (1993).

[203] Chan, S., Zhu, Z., Van Etten, J. & Xu, S. Cloning of CviPII nicking and modification system from chlorella virus NYs-1 and application of Nt. CviPII in random DNA amplification. *Nucleic Acids Research* (2004).

Appendix A

Expression, extraction and purification of cd-ttRecJ

Reagents

10× TB salts (1 liter):

- 23.12 g KH_2PO_4
- 125.41 g K_2HPO_4

Dissolve to a final volume of 1 liter and autoclave.

Terrific Broth (TB) (1 liter):

- 12 g Tryptone
- 24 g Yeast Extract
- 4 ml Glycerol (5 g)

Dissolve to a final volume of 900 ml.

Autoclave and cool down.

Add 100 ml of 10× TB salts, glucose (if required) and ampicillin to 100 µg/ml.

Or, in the case of powder TB (in a 1 liter flask):

For 300 ml TB: mix 14,28 g TB + 300 ml milliQ water. Autoclave

Stock solutions (not sterilized):

- 1 M Tris-HCl pH 7.9
- 5 M NaCl
- 2 M imidazole pH 7.9 (adjust with HCl, watch out over volume)
- 500 mM PMSF in ethanol
- 500 mM EDTA
- 2 M KCl

Method for purification of cd-ttRecJ

Buffer A (200 ml)

- 20 mM Tris-Hcl pH7.9
- 500 mM NaCl
- 10 % glycerol
- 0.5 mM PMSF

Buffer B (50 ml) Next time, try 100 mM imidazole

- Buffer A + 20 mM imidazole

Elution buffer (each 5 ml) Next time, do 150.200.250.300 mM imidazole

- Buffer A + 50 mM imidazole
- + 100 mM imidazole
- + 150 mM imidazole
- + 200 mM imidazole

Buffer C (50 ml)

- 20 mM Tris-HCl pH 7.9
- 100 mM KCl
- 0.1 mM EDTA
- 10 % glycerol

60% Glycerol stock (50ml, autoclaved, kept at room temperature)

LB Agar + Ampicillin plates (2˜3 dishes)

1. One pill of LB Agar for 50 ml of milliQ, autoclave.
2. Once cooled down (to ˜60 °C), add Ampicillin at 0.1 mg/ml. (Watch out gelification at ˜40 °C)
3. Pour in petri dishes.
4. Store upside-down to avoid condensation. Properly saran-wrapped, can be kept 6 months at 4 °C.

Procedure

Verification of expression

1. Plasmid transformed colonies are on a petri dish. Select 6 of them, number them. Number 6 tubes for culture with a large air volume (e.g. 50 ml falcon tubes).
2. Under the hood, with the flame on, insert in each falcon 3 ml of culture medium, 30 µl of IPTG and 3 µl of ampicillin. Use sterile tips.
3. With one tip on a pipetman, pick each numbered colony and put in each numbered falcon tube. Grow at 37 °C overnight.
4. Take 1ml of culture and put in an eppendorf. Centrifugate (˜ 5 min at 6000g), remove supernatant that contains a lot of proteins.
5. Freeze at -20 °C.

Prepare the SDS page with 12 wells comb.

- **Gel:** 1.5M TrisHCl ph 8.3 + 0.4 % SDS 2.6 ml + 40 % acrylamide 3.2 ml + milliQ 4.5 ml + a small spatula of APS, once well dissolved, add TEMED 10 µl. Pour in the frame until ~ 5 mm under the comb. Immediately pour 70 % ethanol on top and wait about 10 minutes.
- **Stacking gel:** 0.5M TrisHCl ph 6.8 + 0.4 % SDS 2.5 ml + 40 % acrylamide 0.75 ml + milliQ 6.6 ml + a small spatula of APS, once well dissolved, add TEMED 10 µl Remove the ethanol and dry with Air Duster, then pour the stacking gel until ~ the top. Insert the comb (watch out bubbles), suck the overload of gel, spray with ethanol. Let it polymerize. Place the gel in the bath, fill with Tris-Glycine SDS buffer. Rinse the wells with the buffer.
- **Prepare the samples (on ice):** Suspend bacteria in 50 µl of milliQ and mix well. Take 1 µl, add 4 µl milliQ and 5 µl SDS sample buffer (blue). Dilute this mix 10 times by taking 1 µl and adding 4 µl milliQ and 5 µl SDS sample buffer. Bring abruptly this final mix at 100 °C for 5 minutes. Then, it can be manipulated at room temperature.
- **Insert the samples in the gel**, slowly, carefully, and rinse the tip in the buffer, at the bottom of the bath.
- Do not preheat the gel; **run in DC**, 40 mA (~350 V) for ~ 30 minutes, until the blue band gets to the bottom of the gel.

Purification

- Take a little bit of the verified culture colony and put in a tube closed not too tight with: 2 ml of LBG, 100 µg/ml ampicillin
- Pre-culture to cd-ttRecJ expression E.coli (over night 37 ℃ with shake).
- For long-term storage at -80 °C: in sterile eppendorf: 60 % glycerol 500 µl + culture 500 µl.
- Heat the inoculation loop until it is red-hot: dip it in the culture solution, then rub on the dish by following the pattern shown on the Figure A.1. Incubate one night, then put at 4 °C until the purification.
- Cultivate for 1 liter TB broth (30 ℃ with shake, 100 µg/ml ampicillin). *(we did 0.5 ml of pre-culture in 300 ml TB, shook 180 rpm for ~3 hours, then started checking OD)*

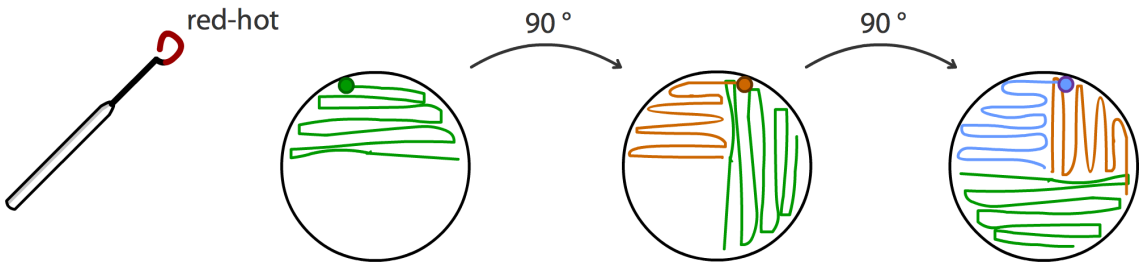

Figure A.1: Pattern to follow.

- Reach an optical density at 600 nm of 0.4 and add to IPTG 0.4 mM.
- Harvest after 3 hours. Induction by centrifugation (8000 rpm, 5 min). *(we did 2 times 500 ml, threw away liquid, then added about 20 ml of [20 mM Tris-HCl + 50 mM NaCl] in centrifuge tube to get the pellet then a bit more to get the remains of the emulsion, put in 50 ml falcon, re-centrifuge, remove liquid)*
- Store the bacteria pellet at -20 ℃.
- Suspend frozen cell (about 10 g) in 80 ml of buffer A. *(we did ~3 g in 20 ml)*
- Sample n°1 for SDS page.
- Disrupt by sonication. *(in beaker, put in ice+water in polystyrene box, ~5 min enough, pulse 1 s off 0.5 s, set amplitude according to sound, once done, set back to 1. Keep cold from now on)* do more than 5min next time
- Sample n°2 for SDS page.
- Heat at 65℃, 30min *(skipped)*
- Centrifuge 40000 rpm for 1 hour. *(we did 70000 rpm 30min, to get a clear solution for his-tag trapping. Be careful to fill the tube completely to avoid explosion. Wipe rotor.)*
- Transfer supernatant and adjust to 5 mM final concentration by adding 2 M imidazole. *(to limit non specific binding)*
- Equilibrate His-Trap column with 20 ml of buffer B. *(don't insert bubbles inside. use lock-type syringe)*
- Add the sample in the equilibrated column.

- Sample n°3 of trash start, n°4 of trash end for SDS page.
- Wash the column with 20 ml of buffer B.
- Sample n°5 at washing end for SDS page.
- Elute from the column with elution buffer (50mM→100mM→150mM→200mM). *(2 samples of 1.5ml for each.)* do 150.200.250.300 mM next time
- Check the eluting fraction by SDS page. Choose the good ones.
- Correct the cd-ttRecJ eluting fraction and (if needed) concentrate by ultrafiltration. *(We took 150-2, 200-1, 200-2, first check that the columns membranes aren't broken: put milliQ in two of them, centrifuge, if mQ is filtered too quickly, that means there is a hole somewhere. We reduced from 4.5 ml to 1 ml. 7500g, enter sample height ~50 mm)*
- Equilibrate desalting column with 25ml of buffer C.
- Apply the sample (1.5 ml) in desalting column. *(We added 0.5 ml of buffer C to get to 1.5 ml)*
- Elute with 2 ml of buffer C. *(exactly 2 ml or other things will get out)*
- Measure the concentration of cd-ttRecJ by absorption at 278 nm (molar extinction coefficient 33400M-1). *(We checked 1x and 1/10x concentrations, 50 µl each. 0.355218/0.0334 = 10.64 µM)*
- Concentrate to (~ 10 mg/ml) by ultrafiltration. *(We concentrated 4 times to ~40 µM)*
- Store at -80°C in 50% glycerol. Freeze small volumes with liquid nitrogen.
- Check the activity of cd-ttRecJ by digestion experiment.

Appendix B

Working at lower temperature

At the time of this study, we were working with the mesophilic exonuclease $RecJ_f$, that we had troubles to stabilize at temperatures higher than 37 °C. The two other enzymes that we were using (*Bst* DNA Polymerase Large Fragment and Nt.BstNBI nicking endonuclease), were thermophilic enzymes, that had a limited activity at 37°C (10 % for Nt.BstNBI according to the producer, New England BioLabs). We consequently asked ourselves if it might be benefic to find a DNA polymerase and a nicking enzyme that would both be mesophilic, that is, working best at 37 °C.

Klenow Fragment

Klenow Fragment (New England BioLabs) is a mesophilic DNA polymerase that has lost its exonuclease domain. It is capable of working in strand-displacement, as *Bst* DNA Polymerase, and works best at 37 °C. We compared Klenow and Bst for a simple amplification: both curves amplified properly, and showed a very similar profile (Figure B.1).

It is probable that in these conditions, the rate-determining step was the cutting by Nt.BstNBI of which we already had to increase the concentration for the amplification to perform properly. Still, Klenow Fragment worked as well as Bst, which encouraged us to search for a nicking endonuclease working best at 37 °C, in order to pair with Klenow.

Nt.CviPII

Nt.CviPII (New England BioLabs) is a mesophilic nicking endonuclease that recognizes and cuts in 5' of the site 5'-CCD-3', with D being A, T or G. According to NEB (New England BioLabs) and Chan *et*

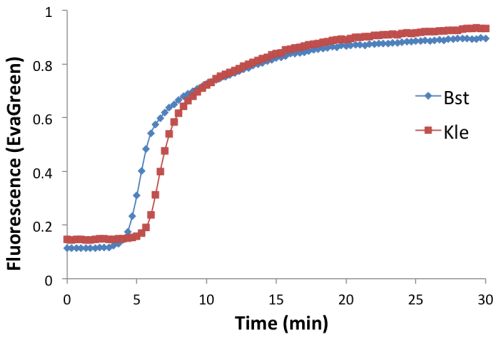

Figure B.1: Amplification of T11 in absence of exonuclease. The reaction is performed at 37 °C, with 0.08 unit/µl of either *Bst* DNA polymerase (blue curve) or Klenow Fragment (red curve). Nicking endonuclease Nt.BstNBI was used (2 %). Autocatalytic module cT11 (60 nM) was initially put in presence of 0.1 nM of T11.

al. [203], the site CCT is cut less efficiently than CCA and CCG, and some CCT sites are not cut at all. We confirmed this with an autocatalytic module (C12vi, amplifying T12vi: 5'-**CCT**AAGATGTAT-3') that did work, however very slowly. One would have to be careful to not use the site CCT.

We then tried with the recognition site CCG with two different autocatalytic modules:

- c11vi-sph, amplifying T11vi-sph 5'- **C**CG**T**CTGCATG*-3', also enabled to work with SphI (NEB), that cuts at the location marked by a star in the site 5'-GCATG*C-3' (Figure B.2)
- c11vi, amplifying T11vi 5'-CCGAGATTGAA-3' (Figure)

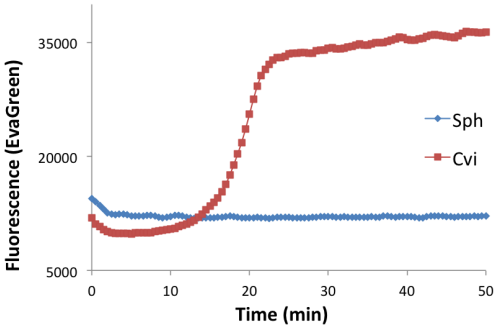

Figure B.2: Amplification of T11vi-sph ([c11vi-sph] = 60 nM) in absence of exonuclease. The reaction is performed at 37 °C, with *Bst* DNA Polymerase, and either nickase SphI (blue curve) or Nt.CviPII (red curve). Whereas the amplification worked well with Nt.CviPII, it did not with SphI.

Curves of c11vi exhibited a weird, sudden decrease of fluorescence after the initial amplification. We investigated this by doing an acrylamide gel analysis of reaction samples taken before and after this sudden decrease. We did the gel analysis for both cT11 (that we know amplify without artifact)

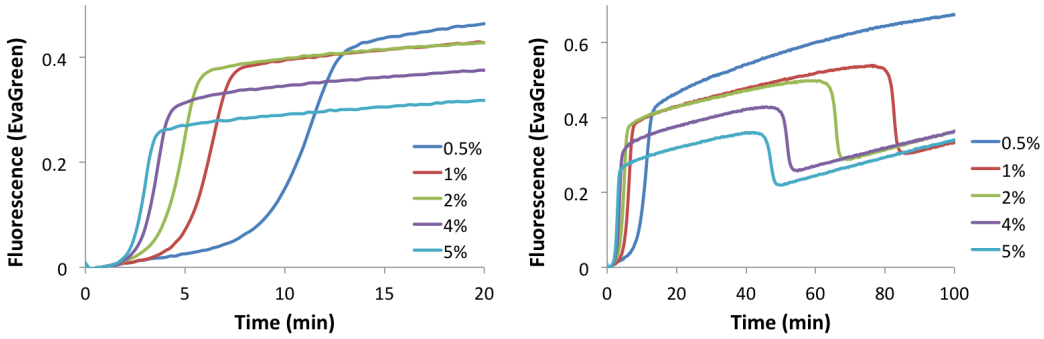

Figure B.3: Amplification of T11vi ([c11vi] = 60 nM) in absence of exonuclease. The reaction is performed at 37 °C, with *Bst* DNA Polymerase, and a ramp of Nt.CviPII from 0.5 % to 5 %. Left: the first 20 minutes. Amplification speed increases as the concentration of nickase increases. Right: after a few tens of minutes, the fluorescence decreases suddenly. This happens earlier for higher concentrations of nickase.

and c11vi. Samples were quenched with EDTA 2 µl, then put on ice, and subsequently frozen until gel analysis. For c11vi, a first sample was taken before the beginning of the amplification, (cycle 0), then at the plateau (cycle 77), then right after the decrease of fluorescence (cycle 253) and finally later on (cycle 403). We can clearly see the emergence of an unknown species (a new band appears on the sample taken at cycle 253) whose concentration increases (the band at cycle 403 is bigger). This new species is longer than T11vi, but shorter than c11vi. Also, it seems that between cycle 253 and 403, the concentration of T11vi has not increased, whereas that of the new species has clearly increased. We could not get to any conclusion with these results alone: T11vi or c11vi do not present any secondary structure or interaction that may lead to unwanted behaviors. A possible star activity of Nt.CviPII may result in such weird behavior; however, we did not find any references going in this direction.

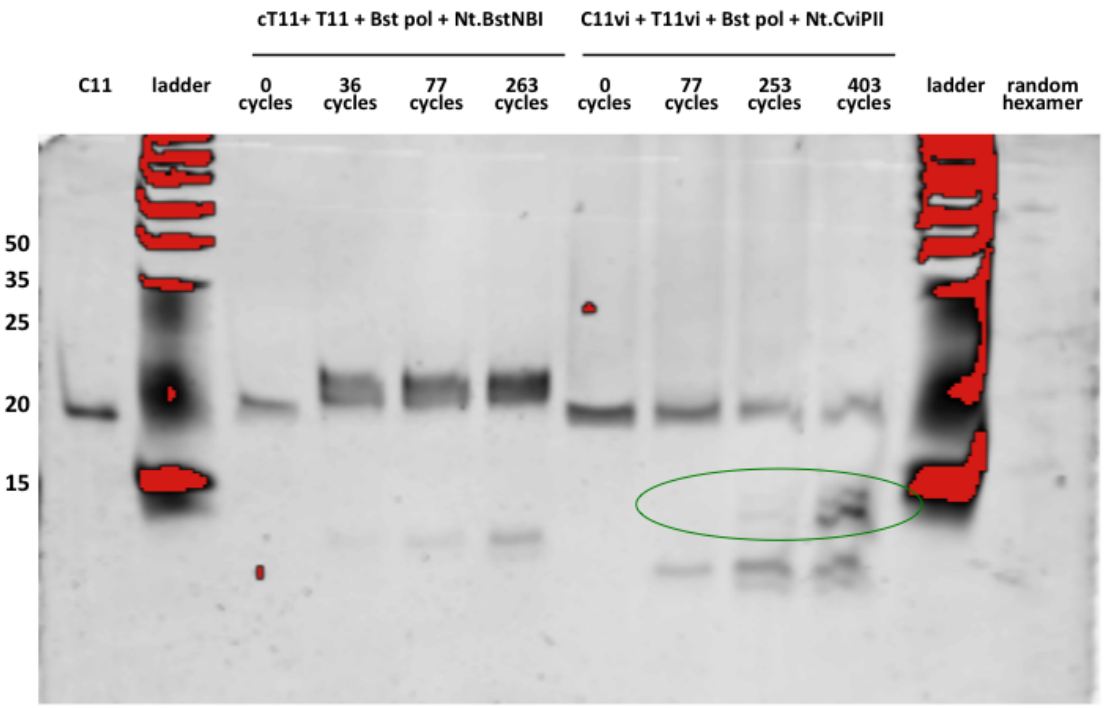

Figure B.4: Poly-acrylamide gel analysis of the amplification of cT11 (left) and c11vi (right). The highest bands correspond to the templates cT11 or c11vi (both 22 bases long). The lower ones correspond to the produced T11 of T11vi (both 11 bases long). In the case of c11vi, a new band appears above that of T11vi, at cycle 253. It becomes darker at cycle 403, suggesting an increase of concentration of this new species.

Appendix C

Two-dimensional Bistability

Using Paraframe, we implemented our bistable circuit in a two-dimensional environment. We were able to appreciate the difference in speed of the moving front in a given state when freely diffusing or when confronting to a front in the opposite state.

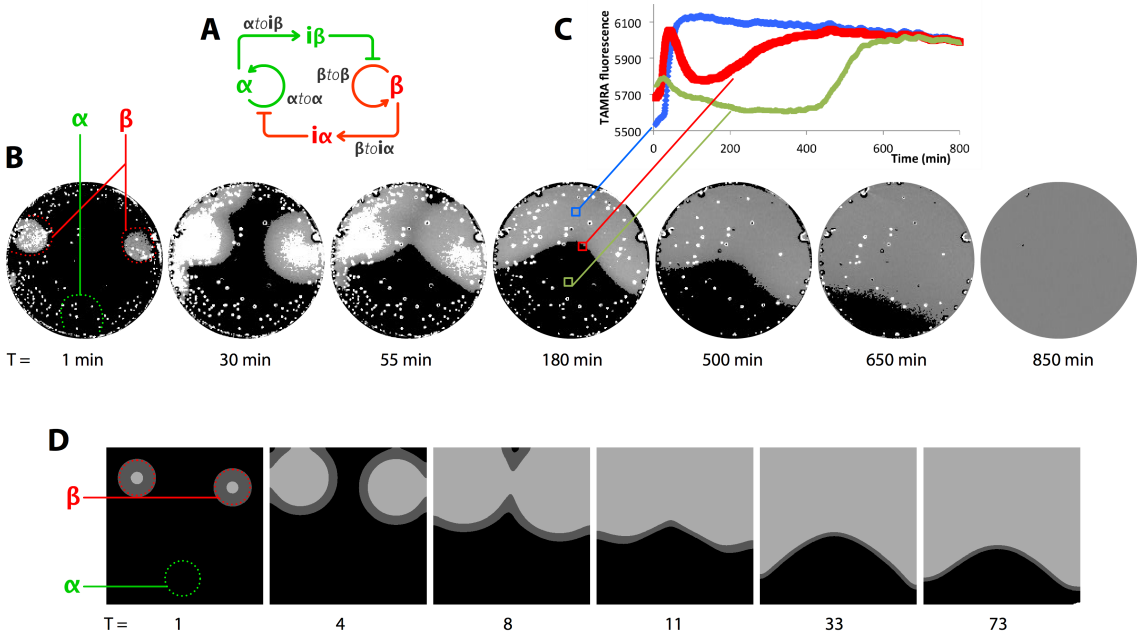

Figure C.1: Bistable circuit in 2D. (A) Bistable circuit. (B) Time-frame of the experiment monitored through Tamra channel. Fluorescence intensity was converted in three levels for visibility (dark, grey and bright). Bright corresponds to high concentration of β. The reaction was started with two localized spots of β and one of α. (C) Fluorescence time-plot at three different locations. The global decrease of intensity suggests that Tamra gets bleached throughout the reaction. The experiment was run at 42 °C, with [α*to*α] =10 nM and [β*to*β] = 20 nM.

In a round chamber

We first tried to run the bistable circuit (Figure C.1-A) in a round paraframe, setting up localized [α] and [β] dried on the glass surface prior to the experiment (Figure C.1-B). In order to get a fluorescence signal high enough, we increased the concentrations of inhibitor modules from 20 nM to 40 nM. We also increased the concentration of BSA to 5 mg/ml (corresponding to the concentration used in Chapter 6). Otherwise, the reaction conditions (enzymatic, temperature and concentrations of autocatalytic modules) were kept the same as in Chapter 2. The front in state B (initiated at the localized spots of β) diffused in tens of minutes to fill the upper part of the chamber, where it did not encounter any resistance. However, front B was confronted to front A on the lower part of the chamber, and took about 800 minutes to finally "kill" the areas in state A. This accounts for the good balancing between both sides (A and B) of this bistable circuits: one would expect an immobile front in the ideal case of a perfectly balanced bistable circuit.

Appendix D

Working in agarose

As detailed in Appendix *A microfluidic device for on-chip agarose microbead generation with ultralow reagent consumption*, both *Bst* DNA polymerase and Nt.BstNBI nicking endonuclease are working well in presence of agarose, gelified or not (we tested up to 2 % on a simple autocatalytic amplification). However, we had trouble using RecJ (both mesophilic $RecJ_f$ and thermophilic tt-RecJ) in agarose.

Oscillator c11bt in agarose: first try

We first tried to run the c11bt Oligator in usual conditions, with or without agarose. This simply did not work (Figure D.1). Warm agarose (3 %) or water was added to the reaction mix, which was then put on ice for gelification before starting the reaction. Note that we were careful not to heat the agarose too much, in order to avoid damaging mesophilic $RecJ_f$.

Degradation by $RecJ_f$ in agarose

We checked the activity of $RecJ_f$ in agarose by doing a degradation experiment: the presence of agarose – gelified or not – clearly impacted the kinetics of $RecJ_f$ (Figure D.2): it decreases $RecJ_f$ speed and seems to increase its K_m. By doing an exponential fit of the degradation curve with 1 % agarose, we found that we would need roughly 5 times more $RecJ_f$ in order to reach the same $k_{1st} = V_m/K_m$ as that of $RecJ_f$ in absence of agarose.

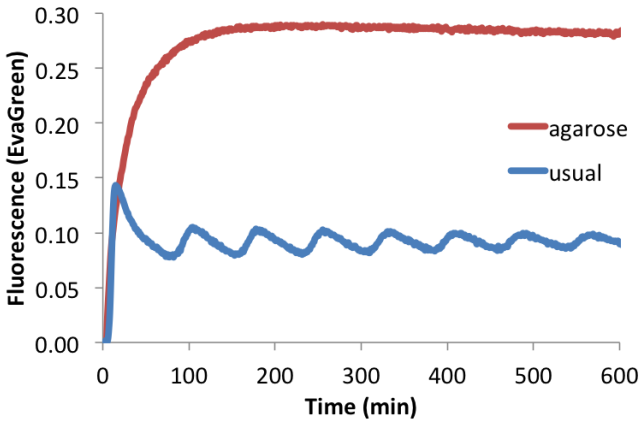

Figure D.1: Oligator c11bt with (red curve) or without (blue curve) agarose 1%. The reaction was performed at 38.4 °C. In presence of agarose, the initial amplification only performs properly. It seems that the exonuclease activity is lost.

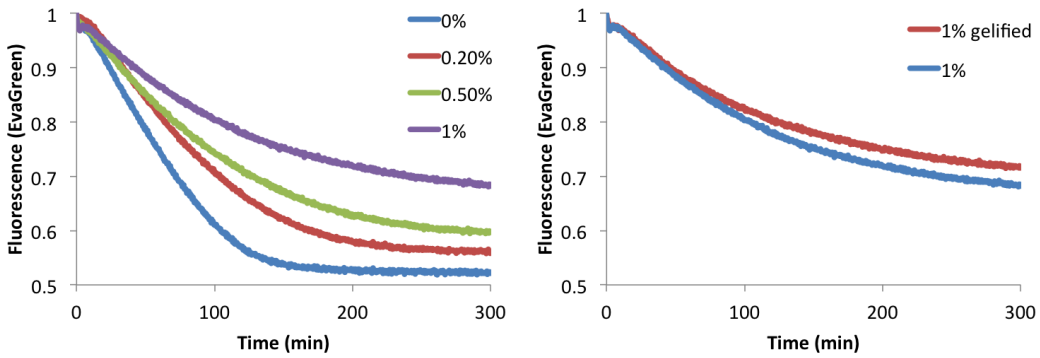

Figure D.2: Degradation of 2 µM of inh11bt3 (5'-GTCTAAGCTGAGTAA-3') by $RecJ_f$. (Left) In presence of 0, 0.2, 0.5 or 1 % of gelified agarose and (Right) in presence of 1 % of agarose, gelified or not. The reaction was performed at 38.4 °C.

Oscillator c11bt in agarose: second try

We then tried again the c11bt Oligator in agarose, with a ramp of concentration of $RecJ_f$. We could observe a few oscillations for higher concentrations of $RecJ_f$ (Figure D.3), confirming that we need to increase its concentration when working in agarose. Agarose probably is a form of competitive substrate for both $RecJ_f$ and tt-RecJ. Supporting this hypothesis, Wakamatsu *et al.* [145] observed that RecJ possesses a domain that has structural similarities to an oligosaccharide-binding fold.

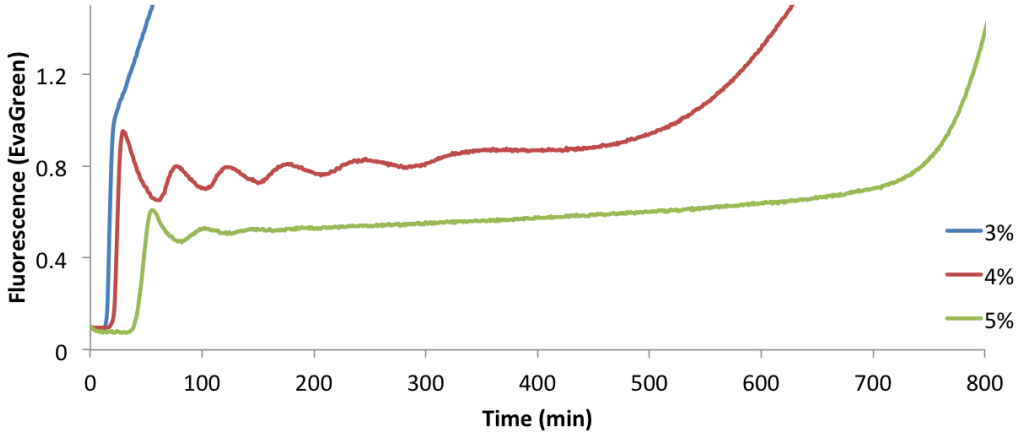

Figure D.3: Degradation of 2 µM of inh11bt3 (5'-GTCTAAGCTGAGTAA-3') by $RecJ_f$. (Left) In presence of 0, 0.2, 0.5 or 1 % of gelified agarose and (Right) in presence of 1 % of agarose, gelified or not. The reaction was performed at 38.4 °C.

Appendix E

Nucleic acids for the rational design of reaction circuits

Nucleic acids for the rational design of reaction circuits

Adrien Padirac[1], Teruo Fujii[1], Yannick Rondelez[1,*]

[1]LIMMS/CNRS-IIS, Institute of Industrial Science, The University of Tokyo, 4-6-1 Komaba, Meguro-ku, Tokyo 153-8505,

*Correspondence to: rondelez@iis.u-tokyo.ac.jp

Abstract

Nucleic acid-based circuits are rationally designed in vitro assemblies able to perform complex pre-encoded programs. They can be used to mimic *in silico* computations. Recent works emphasized the modularity and robustness of these circuits, which allow their scaling-up. Another new development has led to dynamic, time-responsive systems able to display emergent behaviors like oscillations. These are closely related to biological architectures and provide an *in vitro* model of *in vivo* information processing. NA circuits have already been used to handle various processes for technological or biotechnological purposes. Future applications of these chemical smart systems will benefit from the rapidly growing ability to design, construct, and model nucleic acid circuits of increasing size.

Introduction

Nucleic Acid (NA) polymers provide a functional substrate to encode information at the molecular level. When this potential was first harnessed in nanotechnology [1], researchers focused on immobile 2D [2] and 3D [3] nanostructures. These were followed by NA nanomachines: dynamic nanostructures able to perform nanoscale movements [4] upon the reception of external stimuli. NA also proved to be a tool of choice for a specific class of computation: in the mid 90s, Adleman came out with an innovative search strategy for NP-complete problems by exploiting the massively parallel process of molecular recognition inherent to NA hybridization [5].

Computation with NA eventually moved to a more "universal" direction by taking the form of logic gates [6]. Such an approach would allow one to build NA-made Boolean circuits, thereby mimicking *in silico* computation.

In their natural role, NA are the groundwork of biological information managing. DNA carries the genetic information, which is processed within complex reaction networks involving in particular RNA [7]. These *in vivo* circuits can also be taken as a model for artificial NA-based computation. In 2006, Kim *et al.* demonstrated an *in vitro* bistable circuit, modeled after *in vivo* gene regulatory networks [8].

For these various technological approaches, the critical asset of NA is to offer a facilitated access to the modular assembly of a molecular system: simple hybridization rules [9] permit the rational design of molecular recognition; and the polymeric structure of NA allows one to physically link individual domains in order to obtain multifunctional molecular components (e.g. two-input gates [10,11], or input-output modules [12]). Therefore, these modules can be rationally organized into scaled-up reaction circuits. By increasing the size of the circuits [13] –or expanding the set of chemical rules [14-16]– researchers are now addressing increasingly complex computations / behaviors.

In this review, we wish to emphasize the recent breakthrough in the complexity and capabilities of deterministic NA-based molecular circuits. We mostly limit ourselves to experimentally demonstrated systems. Therefore, we do not focus on a number of theoretical works proposing intriguing computation schemes based on stochastic chemical processes, which are less amenable to wet-lab validation [17,18]. We first survey the most advanced irreversible systems, single-use reactive assemblies whose final state is a pre-encoded function of a set of inputs. We then review dynamic systems, out-of-equilibrium assemblies whose convoluted behaviors emerge from the structural features of a *designer* reaction network.

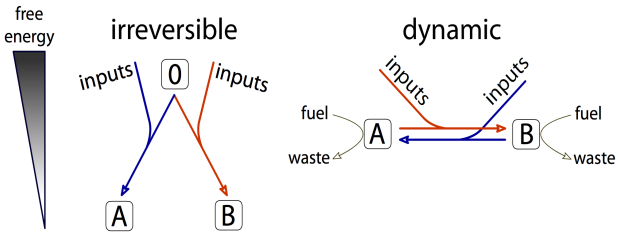

Figure 1: Irreversible system versus dynamic system. (Left) From an initial state (0) and a set of inputs, an irreversible system evolves towards a low-potential equilibrium state that corresponds to the answer of the computation (A or B), and cannot be re-used. (Right) A dynamic system continuously consumes energy. Upon reading of a set of inputs (that may be endogenous), it transits from state to state, but does not get trapped in the equilibrium: it can be re-used or perform recursive tasks.

Finally we discuss the place of these circuits within the field of NA nanotechnology, and their possible links with the biological world.

Toehold based reaction circuits

The first addressable NA nanomachine –the DNA tweezers of Yurke *et al*. [4]– brought the concept of toehold-mediated strand-displacement (TMSD), by which the displacement of an "output" strand, by an invading "input" strand, is controlled by a small single-stranded recognition sequence called "toehold". In 2006, Seelig *et al*. demonstrated the computational ability of TMSD by using it to power a complete set of Boolean logic gates [19]. These hybridization-driven logic gates could be cascaded, yet with several limitations due to a damping of the signal after each layer of logic gates. The authors had to introduce a complicated amplification mechanism to mitigate this effect. The concept of chemical signal restoration to allow deeper cascading was later revisited by Zhang *et al*. [20].

The recent rise in the complexity of toehold-powered reaction circuits was made possible by the "seesaw" gate [11]. Qian and Winfree packed in this compact gate motif the two important features allowing robust modularity, and consequently the scaling-up of reaction circuits: thresholding (robustness against noise) and signal restoration (robustness against damping of the signal). This was nicely demonstrated in two papers showcasing various reaction circuits including up to 40 seesaw gates: one of them able to calculate the square root of a four-bit binary number [13], and another elegantly mimicking neural network computation [21].

However, irrespective of the complexity of the computation they perform, these experimental TMSD cascades are still based on a small thermodynamic driving force. This limits the evolutions of the concentrations of their components to simple trajectories. In other words, they are use-once structures and a new "computer" is required for every computation. Genot *et al*. demonstrated a reversible logic gate design [22] that permanently responds to changes in its inputs. However, such a strategy implies that the system always remains close to the equilibrium, which would forbid signal restoration and limit the cascading of reactions [23]. For classic (deterministic) chemical systems, the only route to non-trivial behaviors -such as oscillations- involves the creation of attractors other than the thermodynamic branch. This is only possible in dissipative chemical systems, i.e. those traversed by a continuous flux of energy [24-26].

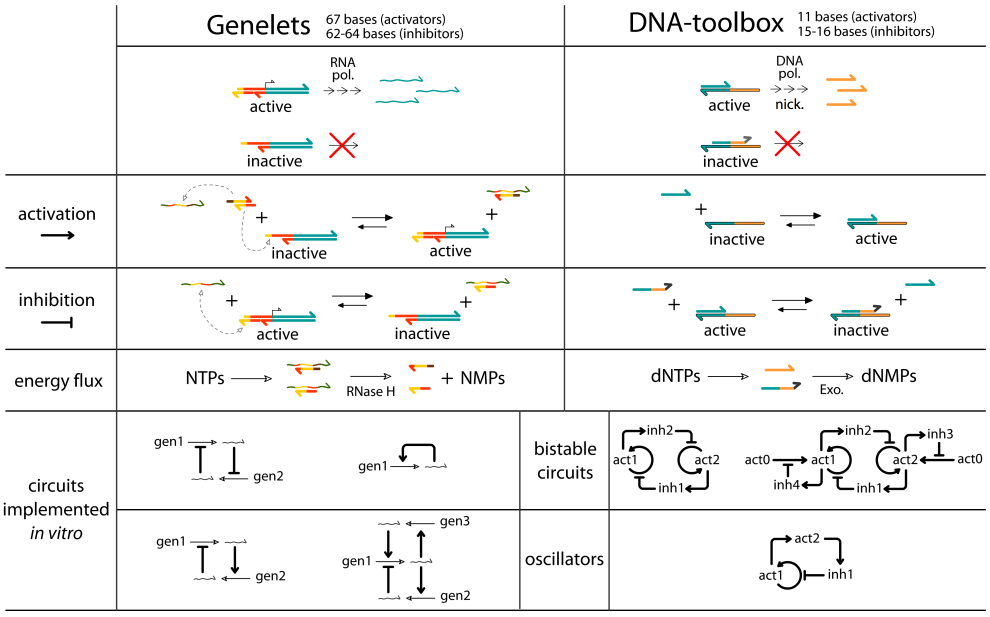

Figure 2: Two systems allowing the rational assembly of dynamic reaction circuits from basic units. Genelets are double-stranded DNA that contain a nicked promoter (in red). When the promoter is complete (genelet indicated as "active"), a RNA polymerase transcribes it in RNA transcripts (thin wavy strands) that establish the communication between genelets. "Activation" is obtained when the sequestered DNA activator of an inactive genelet is released by an activating RNA transcript. "Inhibition" is obtained as an inhibiting RNA transcript binds and displaces the DNA activator of an active genelet, thus inactivating it. A RNase degrades RNA transcripts into NMPs. In the DNA-toolbox, short DNA activators activate DNA templates (bottom strands) that consequently produce other DNA activators or inhibitors and establish the communication between templates. "Activation" is obtained as a DNA activator hybridizes to a DNA template and primes polymerization. "Inhibition" is obtained as a DNA inhibitor hybridizes to a template, thus blocking activators. An exonuclease degrades DNA activators and inhibitors into dNMPs. Both systems led to experimental implementations of various dynamic circuits encoding oscillations and bistability.

Dynamic reaction circuits

In the context of TMSD cascades, building oscillations, chaos or recursive computations [26] would require a theoretically constant concentration of fuel molecules. This could be achieved by working in an open reactor – rather than in a closed tube– with a constant resupply of logic gates. Since closed system are experimentally more practical, another idea would be to have a large amount of "buffered" inactivated gates present in solution, with one buffered gate getting activated as an active gate is consumed [27]. This would allow the system to run with a constant concentration of activated gates, until it runs out of buffered gates. Nonetheless, the building of dynamic or time-responsive behaviors out of TMSD primitives remains an attractive challenge.

Enzymes, with their exquisite catalytic properties, offer an easy access to the implementation of kinetic traps. These provide the separation of time scales that is necessary to turn a closed system into a pseudo-open system [28]. By using catalytic mechanisms with feedbacks to control their rates, it is possible to shape dynamic systems that stay out-of-equilibrium until all precursors have been consumed [29].

RTRACS is an autonomous computer based on RNA polymerase and RNase and modeled after retroviral replication [30]. The modular, time-responsive logic computations use RNA as both input and output of a DNA-encoded software that is executed by the enzymatic hardware. Kan *et al.* recently built a generalized logic gate that should be capable of performing various logic functions (such as AND, NAND, OR, NOR), thus potentially allowing the wiring of larger logic gate circuits [31].

In 2006 Kim *et al*. [8] proposed an *in vitro* analog of gene regulation circuits where, rather than getting translated into proteins, RNA transcripts regulate their own transcription from DNA gene analogs. These *genelets* are short DNA duplexes that contain an incomplete promoter: they require an additional DNA single-stranded *activator* before they can initiate the transcription of their RNA outputs. In turn, these RNA transcripts will either release or sequester the labile DNA activator of other genelets, hence establishing a cross-regulation between different units (Figure 2). One or two RNases [32] provide an internal chemical sink by continuously degrading the RNA transcripts, thereby maintaining the system's boundedness.

As for the genes of *in vivo* reaction networks [33], genelets can be arbitrarily cascaded: one can freely organize the topology of the network, as well as the nature (activation or inhibition) of each vertex. Kim *et al*. first constructed a bistable circuit in which two genelets are mutually repressing each other [8]. It was latter demonstrated that a single self-activating unit can also behave as a bistable switch [32]. The modularity

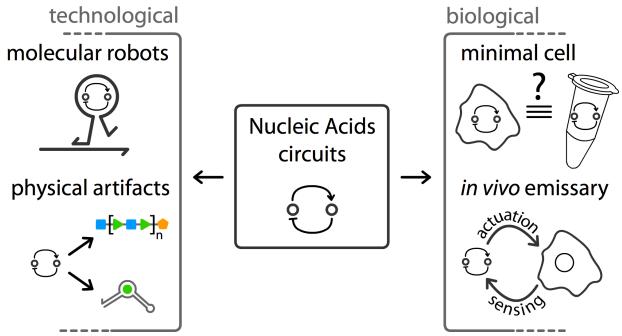

Figure 3: Examples of technological and biological applications of NA reaction circuits.

of these constructs was further explored with several oscillator designs [34], including an analog of the repressilator [35].

Montagne *et al.* abstracted one more step of the gene regulation pathway by removing the need for RNA transcription and described a DNA-only general scheme for the implementation of dynamic circuits: the DNA-toolbox (Figure 2). In this case, pseudo-genes (single strand templates) directly regulate each other by emitting small signal molecules [12]. These DNA signals come in two types: inputs that activate DNA templates and inhibitors that block them. A single-strand specific exonuclease degrades signal molecules, while templates are protected by DNA backbone modifications. Despite its simplicity, this implementation supported reaction circuits displaying oscillations [12,36], bistability and switchable memory [37], all rationally designed and assembled by using the modularity of the reactions.

Interface

In vitro dynamic reaction circuits provide an operative model to study the network / functions relationships with regard to what occurs *in vivo*. Dynamic processes that may be blurred by biological complexity naturally become apparent when one tries to construct *in vitro* analogs [38]. For instance, recent studies have pointed at the possible importance in cellular circuits of two neglected phenomena: the competition for enzymatic resources within a functional motif [39,40], and the "load" effect that appears when a reaction circuit is connected to a downstream process [41].

Some systems that are built *in vitro*, but precisely reproduce the biochemistry of transcription-translation reaction networks, may also be instrumental to bridge the gap with *in vivo* systems [29,42]. In this way, Noireaux and coworkers are developing a cell-free expression toolbox from E. Coli extracts [43,44]. Using this toolbox, they recently constructed a multi-stage cascade, an AND gate and a negative feedback loop [45].

By their nature, reaction circuits built from nucleic acids are at the direct interface with biology. It is however not trivial to transfer a NA circuit designed *in vitro* toward an *in vivo* environment. Efforts in testing and improving the robustness of the circuits are required in order to work in a non-pristine milieu where various materials may interfere with the function of the circuit [46]. Some NA logic circuits have been shown to perform well in the presence of cellular amount of RNA [19], or random oligonucleotides [14,47]. Recent studies also focused on reaction robustness to mutations or impurities in the sequences [47], and hybridization robustness in large range of temperature and salt conditions [48]. Such works may prove precious with respect to the possible implementation of complex NA circuits *in vivo*.

The resilience of strand displacement reactions was specifically studied for *in situ* application [49], and subsequently used with DNA-conjugated antibodies for the labeling of endogenous proteins [50]. Choi and coworkers demonstrated that the hybridization chain reaction [51] –by which a specific DNA molecule triggers a chain hybridization of metastable hairpin molecules– could be implemented with RNA, and tweaked for specific mRNAs detection purposes within intact biological samples. Hybridization chain reaction was also used in living cells, to build circuits that would mediate the cell death upon detection of cancer-specific mRNAs [52].

NA circuits could also play the role of the software controlling dynamic NA robots or motors by sequentially producing the driving molecular stimuli *in situ*, thus alleviating the need for exogenous control. An insight of such application was recently published by Franco *et al.*, who used a genelet-based oscillator to drive the opening-closing of DNA tweezers, as well as the production of an RNA aptamer [41]. This approach could be extended to the control of DNA gels [53], organic synthesis [54,55] or optical devices [56,57]. More complex NA nanorobots [58,59], possibly oriented towards *in vivo* applications [60] could also benefit from an integrated NA circuit-based sensing and driving.

Conclusion

Because they offer a handy solution to the problem of chemical modularity, NA have dramatically accelerated the development of man-made reaction networks with precise structural organization enabling intricate behaviors. Irreversible logic circuits will find applications in therapeutics or smart cellular probes [52,61]. Dissipative architectures have a richer potential from a computational perspective [26]. Moreover their elaboration and study is backed by their relevance to biological examples. Indeed, as regulatory phenomena emerge more and more as the central feature of living systems [62], *in vitro* and generic reaction networking schemes reproducing biological architectures and functions will form a unique conceptual and material bridge between living and non-living matter [63].

1. Seeman NC: **Nucleic acid junctions and lattices.** *J Theor Biol* 1982, **99**:237–247.
2. Winfree E, Liu F, Wenzler LA, Seeman NC: **Design and self-assembly of two-dimensional DNA crystals.** *Nature* 1998, **394**:539–544.
3. Chen JH, Seeman NC: **Synthesis from DNA of a molecule with the connectivity of a cube.** *Nature* 1991, **350**:631–633.
4. Yurke B, Turberfield AJ, Mills AP, Simmel FC, Neumann JL: **A DNA-fuelled molecular machine made of DNA**. *Nature* 2000, **406**:605–608.
5. Adleman LM: **Molecular computation of solutions to combinatorial problems**. *Science* 1994, **266**:1021–1024.
6. Stojanovic M, Mitchell T, Stefanovic D: **Deoxyribozyme-based logic gates**. *J Am Chem Soc* 2002, **124**:3555–3561.
7. Licatalosi DD, Darnell RB: **RNA processing and its regulation: global insights into biological networks.** *Nat. Rev. Genet.* 2010, **11**:75–87.
8. Kim J, White KS, Winfree E: **Construction of an in vitro bistable circuit from synthetic transcriptional switches**. *Mol Syst Biol* 2006, **2**:68.
9. Bindewald E, Afonin K, Jaeger L, Shapiro BA: **Multistrand RNA secondary structure prediction and nanostructure design including pseudoknots.** *ACS Nano* 2011, **5**:9542–9551.
10. Elbaz J, Lioubashevski O, Wang F, Remacle F, Levine RD, Willner I: **DNA computing circuits using libraries of DNAzyme subunits.** *Nat Nanotechnol* 2010, **5**:417–422.
11. Qian L, Winfree E: **A simple DNA gate motif for synthesizing large-scale circuits.** *Journal of The Royal Society Interface* 2011, **8**:1281–1297.
12. Montagne K, Plasson R, Sakai Y, Fujii T, Rondelez Y: **Programming an in vitro DNA oscillator using a molecular networking strategy**. *Mol Syst Biol* 2011, **7**:466.

13. Qian L, Winfree E: **Scaling up digital circuit computation with DNA strand displacement cascades**. *Science* 2011, **332**:1196–1201.

14. Zhang DY: **Cooperative hybridization of oligonucleotides.** *J Am Chem Soc* 2011, **133**:1077–1086.

15. Chen X: **Expanding the rule set of DNA circuitry with associative toehold activation.** *J Am Chem Soc* 2012, **134**:263–271.

16. Genot AJ, Zhang DY, Bath J, Turberfield AJ: **Remote Toehold: A Mechanism for Flexible Control of DNA Hybridization Kinetics**. *J Am Chem Soc* 2011, **133**:2177–2182.

17. Qian L, Soloveichik D, Winfree E: **Efficient Turing-universal computation with DNA polymers**. *DNA Computing and Molecular Programming* 2011, [no volume].

18. Cardelli L: **Strand algebras for DNA computing**. *Natural Computing* 2011, **10**:407–428.

19. Seelig G, Soloveichik D, Zhang D, Winfree E: **Enzyme-free nucleic acid logic circuits**. *Science* 2006, **314**:1585.

20. Zhang DY, Turberfield AJ, Yurke B, Winfree E: **Engineering entropy-driven reactions and networks catalyzed by DNA.** *Science* 2007, **318**:1121–1125.

21. Qian L, Winfree E, Bruck J: **Neural network computation with DNA strand displacement cascades**. *Nature* 2011, **475**:368–372.

22. Genot AJ, Bath J, Turberfield AJ: **Reversible logic circuits made of DNA.** *J Am Chem Soc* 2011, **133**:20080–20083.

23. Chiniforooshan E, Doty D, Kari L, Seki S: **Scalable, time-responsive, digital, energy-efficient molecular circuits using DNA strand displacement**. *DNA Computing and Molecular Programming* 2011.

24. Nicolis G, Prigogine I: **Self-organization in nonequilibrium systems**. *John-Wiley & Sons: New York,* 1977.

25. Kjelstrup S, Bedeaux D: **Non-equilibrium thermodynamics of heterogeneous systems**. Series on Advances in Statistical Mechanics: Vol. 16 *World Scientific: New York,* 2008.

26. Soloveichik D, Seelig G, Winfree E: **DNA as a universal substrate for chemical kinetics.** *Proc Natl Acad Sci USA* 2010, **107**:5393–5398.

27. Lakin MR, Youssef S, Cardelli L, Phillips A: **Abstractions for DNA circuit design.** *Journal of The Royal Society Interface* 2012, **9**:470–486.

28. Li Y, Qian H, Yi Y: **Oscillations and multiscale dynamics in a closed chemical reaction system: second law of thermodynamics and temporal complexity.** *J Chem Phys* 2008, **129**:154505.

29. Goda K, Ito H, Kondo T, Oyama T: **Fluorescence correlation spectroscopy to monitor Kai protein-based circadian oscillations in real time.** *Journal of Biological Chemistry* 2012, **287**:3241–3248.

30. Ayukawa S, Takinoue M, Kiga D: **RTRACS: A Modularized RNA-Dependent RNA Transcription System with High Programmability**. *Accounts Chem Res* 2011, **44**:1369–1379.

31. Kan A, Shohda K, Suyama A: **A DNA Based Molecular Logic Gate Capable of a Variety of Logical Operations**. *DNA Computing and Molecular Programming* 2012, doi:10.1007/978-3-642-32208-2_7.

32. Subsoontorn P, Kim J, Winfree E: **Ensemble Bayesian Analysis of Bistability in a Synthetic Transcriptional Switch**. *Acs Synth Biol* 2012, [no volume].

33. Purnick PEM, Weiss R: **The second wave of synthetic biology: from modules to systems**. *Nat Rev Mol Cell Biol* 2009, **10**:410–422.

34. Kim J, Winfree E: **Synthetic in vitro transcriptional oscillators**. *Mol Syst Biol* 2011, **7**:465.

35. Elowitz MB, Leibler S: **A synthetic oscillatory network of transcriptional regulators**. *Nature* 2000, **403**:335–338.

36. Padirac A, Fujii T, Rondelez Y: **Quencher-free multiplexed monitoring of DNA reaction circuits.** *Nucleic Acids Res* 2012, doi:10.1093/nar/gks621.

37. Padirac A, Fujii T, Rondelez Y: *Bottom-up construction of in vitro switchable memories*. Submitted.

38. Schulman R, Yurke B, Winfree E: **Robust self-replication of combinatorial**

information via crystal growth and scission. *Proc Natl Acad Sci USA* 2012, **109**:6405–6410.

39. Rondelez Y: **Competition for catalytic resources alters biological network dynamics.** *Physical review letters* 2012, **108**:018102.

40. Genot AJ, Fujii T, Rondelez Y: **Computing with competition in biochemical networks**. *Physical review letters*. In Press.

41. Franco E, Friedrichs E, Kim J, Jungmann R, Murray R, Winfree E, Simmel FC: **Timing molecular motion and production with a synthetic transcriptional clock.** *Proc Natl Acad Sci USA* 2011, **108**:E784–93.

42. Chen IA, Nowak MA: **From Prelife to Life: How Chemical Kinetics Become Evolutionary Dynamics.** *Accounts Chem Res* 2012, doi:10.1021/ar2002683.

43. Shin J, Noireaux V: **Efficient cell-free expression with the endogenous E. Coli RNA polymerase and sigma factor 70.** *J Biol Eng* 2010, **4**:8.

44. Karzbrun E, Shin J, Bar-Ziv RH, Noireaux V: **Coarse-grained dynamics of protein synthesis in a cell-free system.** *Physical review letters* 2011, **106**:048104–.

45. Shin J, Noireaux V: **An E. coli Cell-Free Expression Toolbox: Application to Synthetic Gene Circuits and Artificial Cells**. *Acs Synth Biol* 2012, **1**:29–41.

46. Hodgman CE, Jewett MC: **Cell-free synthetic biology: thinking outside the cell.** *Metab. Eng.* 2012, **14**:261–269.

47. Zhang DY, Winfree E: **Robustness and modularity properties of a non-covalent DNA catalytic reaction.** *Nucleic Acids Res* 2010, **38**:4182–4197.

48. Zhang DY, Chen SX, Yin P: **Optimizing the specificity of nucleic acid hybridization.** *Nat Chem* 2012, **4**:208–214.

49. Duose DY, Schweller RM, Zimak J, Rogers AR, Hittelman WN, Diehl MR: **Configuring robust DNA strand displacement reactions for in situ molecular analyses.** *Nucleic Acids Res* 2012, **40**:3289–3298.

50. Schweller RM, Zimak J, Duose DY, Qutub AA, Hittelman WN, Diehl MR: **Multiplexed in situ immunofluorescence using dynamic DNA complexes.** *Angew Chem Int Ed Engl* 2012, **51**:9292–9296.

51. Dirks RM, Pierce NA: **Triggered amplification by hybridization chain reaction.** *Proc Natl Acad Sci USA* 2004, **101**:15275–15278.

52. Venkataraman S, Dirks RM, Ueda CT, Pierce NA: **Selective cell death mediated by small conditional RNAs.** *Proc Natl Acad Sci USA* 2010, **107**:16777–16782.

53. Xing Y, Cheng E, Yang Y, Chen P, Zhang T, Sun Y, Yang Z, Liu D: **Self-assembled DNA hydrogels with designable thermal and enzymatic responsiveness.** *Adv Mater Weinheim* 2011, **23**:1117–1121.

54. Milnes PJ, McKee ML, Bath J, Song L, Stulz E, Turberfield AJ, O'Reilly RK: **Sequence-specific synthesis of macromolecules using DNA-templated chemistry.** *Chem. Commun. (Camb.)* 2012, **48**:5614–5616.

55. McKee ML, Milnes PJ, Bath J, Stulz E, O'Reilly RK, Turberfield AJ: **Programmable one-pot multistep organic synthesis using DNA junctions.** *J Am Chem Soc* 2012, **134**:1446–1449.

56. Zhou M, Liang X, Mochizuki T, Asanuma H: **A light-driven DNA nanomachine for the efficient photoswitching of RNA digestion.** *Angew Chem Int Ed Engl* 2010, **49**:2167–2170.

57. Nishioka H, Liang X, Kato T, Asanuma H: **A photon-fueled DNA nanodevice that contains two different photoswitches.** *Angew Chem Int Ed Engl* 2012, **51**:1165–1168.

58. Gu H, Chao J, Xiao S-J, Seeman NC: **A proximity-based programmable DNA nanoscale assembly line.** *Nature* 2010, **465**:202–205.

59. Lund K, Manzo AJ, Dabby N, Michelotti N, Johnson-Buck A, Nangreave J, Taylor S, Pei R, Stojanovic MN, Walter NG, et al.: **Molecular robots guided by prescriptive landscapes.** *Nature* 2010, **465**:206–210.

60. Douglas SM, Bachelet I, Church GM: **A logic-gated nanorobot for targeted transport of molecular payloads.** *Science* 2012, **335**:831–834.

61. Xie Z, Wroblewska L, Prochazka L, Weiss R, Benenson Y: **Multi-input RNAi-based logic circuit for identification of specific cancer cells.** *Science* 2011, **333**:1307–1311.

62. Gerstein MB, Kundaje A, Hariharan M, Landt SG, Yan K-K, Cheng C, Mu XJ, Khurana E,

Rozowsky J, Alexander R, et al.:
Architecture of the human regulatory network derived from ENCODE data.
Nature 2012, **489**:91–100.

63. Jewett MC, Forster AC: **Update on designing and building minimal cells.**
Current Opinion in Biotechnology 2010, **21**:697–703.

Annotations

•• 12
Montagne *et al.*
A potent strategy for the in vitro assembly of dynamic reaction circuits is presented and demonstrated with a robust oscillator showing tens of periods.

•• 21
Qian *et al.*
The demonstration of large-scale circuits based the seesaw gate motif, mimicking neural networks computation with pattern recognition ability.

• 26
Soloveichik *et al.*
This theoretical paper proposes toehold-mediated strand-displacement as a general mechanism to build dynamic reaction circuits.

•• 34
Kim *et al.*
A transcription-based in vitro scheme is wired into various circuits with oscillatory behaviors.

• 41
Franco *et al.*
A nice demonstration of in vitro reaction circuits driving downstream processes proposes the “load” effect as an important feature of biomolecular reaction circuits.

• 52
Venkatararaman *et al.*
RNA circuits transfected into live cells detect mRNA cancer marker and release a RNA drug to trigger cell death.

Appendix F

A microfluidic device for on-chip agarose microbead generation with ultralow reagent consumption

A microfluidic device for on-chip agarose microbead generation with ultralow reagent consumption

Linda Desbois[1], Adrien Padirac[1], Shohei Kaneda[1], Anthony J. Genot[1], Yannick Rondelez[1], Didier Hober[2], Dominique Collard[1] and Teruo Fujii[1]*

[1]*LIMMS/CNRS-IIS, Institute of Industrial Science, The University of Tokyo, 4-6-1 Komaba, Meguro-ku, Tokyo 153-8505, Japan.*

[2]*Université Lille 2, Faculté de Médecine et CHRU Lille, Laboratoire de Virologie / EA 3610, Loos-lez-lille, 59120, France.*

* *correspondence should be addressed to: tfujii@iis.u-tokyo.ac.jp*

Abstract

Water-in-oil microdroplets offer microreactors for compartmentalized biochemical reactions with high throughput. Recently the combination with a sol-gel switch ability, using agarose-in-oil microdroplets, has increased the range of possible applications, allowing for example the capture of amplicons in the gel phase for the preservation of monoclonality during a PCR reaction.

Here we report a new method for generating such agarose-in-oil microdroplets on a microfluidic device, with minimized inlet dead volume, on-chip cooling and *in situ* monitoring of biochemical reactions within the gelified microbeads.

We used a flow-focusing microchannel network and successfully generated agarose microdroplets at room temperature using the "push-pull" method. This method consists in pushing the oil continuous phase only, while suction is applied to the device outlet. The agarose phase present at the inlet is thus aspirated in the device, and segmented in microdroplets. The cooling system consists of two copper wires embedded in the microfluidic device. The transition from agarose microdroplets to microbeads provides additional stability and facilitated manipulation. We demonstrate the potential of this method by performing on-chip a temperature-triggered DNA isothermal amplification in agarose microbeads.

Our device thus provides a new way to generate microbeads with high throughput and no dead volumes for biochemical applications.

I. INTRODUCTION

Microfluidic technologies are based on the use of liquid flows in small volumes, with the benefit of reducing reagent volume, mitigating sample contamination, and providing a high throughput system for the integration of multiple functions in *MicroTotal Analysis Systems* (μTAS). Water-in-oil microdroplets allow the generation of microreactors (pl to fl volume), which permits the compartmentalization of reactions for multiple chemical and biochemical applications such as protein crystallization[1], organic molecule[2] or nanoparticle synthesis[3], genome sequencing[4], single cell and single molecule analysis[5-7]. With respect to molecular biology operations, previous work showed the efficiency of reagents compartmentalization for PCR[8, 9], single cell analysis[10-12] or transcriptome analysis[13]. Generation of monodisperse microdroplets[12] is one way to carry out high throughput analysis[14] and execute independent reactions in parallel[9].

Recently developed agarose microdroplets have been used to compartmentalize PCR[15, 16] and RT-PCR from cellular mRNA[13]. These reports take advantage of the thermo-responsive sol-gel switching property of agarose to trap amplicons in the agarose gel matrix, allowing the preservation of monoclonality of products within stable agarose microbeads. Actually, long-term stability of microdroplets is an important requirement for their storage and downstream applications, such as FACS analysis and RNA sequencing for single cell transcriptome analysis.

However, usual protocols described in the literature highlight two critical points associated with the generation and use of agarose microbeads. The first one is to avoid unexpected gelation upstream of the droplet formation process. This is typically addressed with a heating system adapted to the reagent syringe[17, 18]. The second one is the delicate operation; imperfectly stabilized droplets can recoalesce [19] during storage, incubation and collection, before they are cooled into microbeads [17] and sent to downstream applications[13, 16].

Here we have developed an integrated device for completely on-chip operations using agarose microbeads. The specific features of our device are *(i)* the "push-pull" microdroplet generation system that drastically downscales reagent consumption and *(ii)* the integration of the heating/cooling system necessary to turn agarose microdroplets into microbeads immediately after their formation. We demonstrate the suitability of our device by performing and monitoring on-chip a DNA isothermal

amplification reaction within the device.

The basic structure is a flow-focusing microchannel network for microdroplet generation. We propose a new way to handle the fluids to generate microdroplets: the "push-pull" operation. The oil mix, on the one hand, is pushed into the device. Suction (i.e. a negative flow rate) is applied at the outlet with a higher rate than the oil inlet flow rate: this induces aspiration of the agarose sample and its segmentation into monodisperse microdroplets. Because there is no tubing associated with the sample inlet, the dead volume is drastically reduced and the consumption of sample can be decreased to only a few microliters.

A pair of copper wires are embedded in the microfluidic chip and connected to a heat sink. After enough agarose-in-oil microdroplets have been formed, this cooling system is used to gelify them into agarose microbeads.

In order to validate our setup for biochemical applications, we prepared a DNA amplification mixture containing 1.5 % agarose and successfully observed temperature triggered DNA isothermal amplification within such microbeads.

This sequence of operations is performed entirely in a single chip and described in more details below.

II. MATERIALS AND METHODS

A. Design and fabrication of the microfluidic device

The microchannel network is designed with AutoCAD software and then reproduced to a chromium mask.

The device mold is made using a standard soft photolithography technique[20, 21]. Briefly, 70 μm SU-8 2050 negative photoresist (Microchem, Japan) is spin-coated on a silicon wafer. The mask is fixed on the top of the photoresist coat which is then photocured by UV exposure. After development, the mold is coated with a Teflon plasma. Then, some Polydimethylsiloxane (PDMS) is poured on the mold and baked at 75 ºC during 1.5 h. The polymerized PDMS sheet is peeled off and cut in rectangular chips. O_2 plasma treatment is performed with a RIE machine to allow PDMS/glass bonding. The PDMS chip with the microchannel network is bonded to a 24 mm x 36 mm x 150 μm glass slide. Silicone connecting tubes are introduced in the inlet and outlet of the PDMS chip, and sealed with PDMS.

B. Agarose microdroplet generation at room temperature (25 ºC)

After 10 min degassing in a vacuum chamber, the device is filled with water. A 1 mL syringe (Terumo, Japan) containing oil mix is connected to the oil inlet, and the continuous phase is pushed into the device. Another 1 mL syringe, containing water is connected to the outlet, and suction is applied to induce the aspiration of the emulsion. Oil mix (Mineral oil, Sigma, Japan), prepared with surfactants to prevent microdroplet coalescence is made with 2 % Silicone based polymeric surfactant ABIL-EM 90 (Goldschmidt, Essen, Germany) and 0.05 % Triton 100 X (Sigma, Japan).

The DNA amplification reagents are suspended in a 1.5 % agarose solution (Ultra-low gelling agarose type XI-A, Sigma, Japan). A small volume of this mix is dispensed in the inlet well with a micropipette (Gilson, France).

The flow-focusing microfluidic device consists of a cross junction with two 25 µm thick oil channels perpendicular to the agarose channel (Figure 1). In the orthogonal nozzle, the oil phase focusing on the aspirated agarose stream segments the disperse phase in regular 55 µm microdroplets.

The generation of these microdroplets is observed with an inverted microscope (Olympus IX 71, Japan) and their diameters are analyzed off-line with the software ImageJ, in order to assess the dispersity of the emulsion (the measurement error is ± 0.5 µm).

C. On-chip agarose microdroplet cooling into agarose microbeads

PDMS is perforated with a needle 550 µm in diameter, at about 500 µm away from the incubation chamber walls, on the device (Figure 3). Two copper wires 550 µm in diameter are introduced in place of the needle in the PDMS. 3 cm, 4 cm, 5 cm, 6 cm, 8 cm, and 10 cm long copper wires have been tested. Once the observation chamber is filled with agarose microdroplets, the syringe pumps are stopped and the wires are cooled at 0 ºC in ice. After agarose gelation has occurred, the microbeads are heated back to 43 ºC with a thermoplate (Tokai, Japan) for DNA isothermal amplification. Because this temperature is below the melting temperature of 1.5 % agarose (60 ºC), the beads remain in the gel state during this process.

D. Temperature measurement in the device

Temperature is measured with a K-type thermocouple (NI USB- TC01 model, National instruments, Japan) inserted in the middle of the incubation chamber (Figure 3). Temperature is measured every minute during 10 min in the device containing either no cooling wires, or a pair of copper wires with a length ranging from 4 to 10 cm. Temperature curves are plotted with Kaleida graph (Synergy software).

The variations of the temperature in the incubation chamber have been simulated with COMSOL multiphysics software and shown in supplemental material[28].

E. DNA amplification reaction

Reactions are done in a buffer containing 10 mM KCl, 10 mM $(NH_4)_2SO_4$, 50 mM NaCl, 2 mM $MgSO_4$, 45 mM Tris–HCl, 5 mM $MgCl_2$, 6 mM DTT, 100 µg/ml bovine serum albumin (New England Biolabs) and dNTPs (100 µM each). *Bst* DNA polymerase, large fragment and NtBstNBI nicking endonuclease are purchased from New England Biolabs and used at 11.2 U/mL and 200 U/mL, respectively.

DNA oligonucleotides were purchased from Integrated DNA Technologies (IDT, Coralville, IA, USA), with high performance liquid chromatography purification. For the amplification reaction, 300 nM of a template strand (5'-AACAGACTCGAAACAGACTCGA-3') with a 3'-terminal TAMRA NHS ester modification is put in the presence of 300 nM of an inhibitor strand (5'-GTCTGTTTCGAGTAA-3') and 0.01 nM of an input strand (5'-TCGAGTCTGTT-3').

Control reactions have been performed in 0.5% to 2% of agarose (Ultra-low gelling agarose type XI-A, Sigma, Japan), and are shown in supplemental material[28].

10 µL of the reaction mixture were introduced in the device for amplification at 43 ºC in agarose microbeads. Another 10 µL were run in a CFX96 real-time thermocycler (Bio-Rad), set at the same constant temperature, for control.

F. DNA amplification monitoring and DNA amplification curve

Microbeads are illuminated with a 490 nm LED light source (CoolLED, pE excitation system, UK). They are observed through a Cy3-4040C filter cube (Semrock Corp.) in order to detect the fluorescence emitted by TAMRA.

Images are recorded with an Andor XION camera, using µmanager software[22].

The fluorescence of 10 drops is measured with ImageJ software, every 2 minutes,

during 120 minutes. The measured fluorescence of the on-chip and control (bulk) reactions is normalized at 0 for the lowest and 1 for the highest fluorescence intensity. For the on-chip amplification, the mean fluorescence of 10 drops ± standard deviation is plotted.

III. RESULTS AND DISCUSSION

Previous reports described the application of the sol-to-gel switching properties of agarose to make agarose microbeads, with applications to RT-PCR from cellular mRNA[13] or cell encapsulation. These reports used a pushing system and the gelation of the agarose was performed off-chip. To mitigate issues associated with droplet coalescence during their manipulation, we investigated the integrated generation of agarose microdroplets at room temperature, and gelation on-chip into microbeads. Our method has the additional advantage of a very low volume consumption of reagents.

A. Agarose microdroplet generation at room temperature with an ultra low volume of sample

In order to check the feasibility of droplet generation at room temperature (25 ºC), we designed a network of flow-focusing microchannels.

The oil mix, containing silicone-based ABIL-EM90 surfactants to avoid unexpected droplet coalescence, is pushed with a syringe pump with a $\overline{Qo}$ = 4 µL/min flow rate. At the same time, 10 µL of 1.5 % agarose solution are deposited onto the reagent inlet. To induce agarose flow focusing in the nozzle, and stream segmentation (i.e. the generation of an emulsion) suction is applied at the outlet with a $\overline{Qe}$ = 5 µL/min flow rate. The applied pulling flow at the outlet induced the aspiration of the agarose solution, stream focusing in the nozzle (Figure 1 (b)) and segmentation by the perpendicular oil stream: thus, the microemulsion is generated.

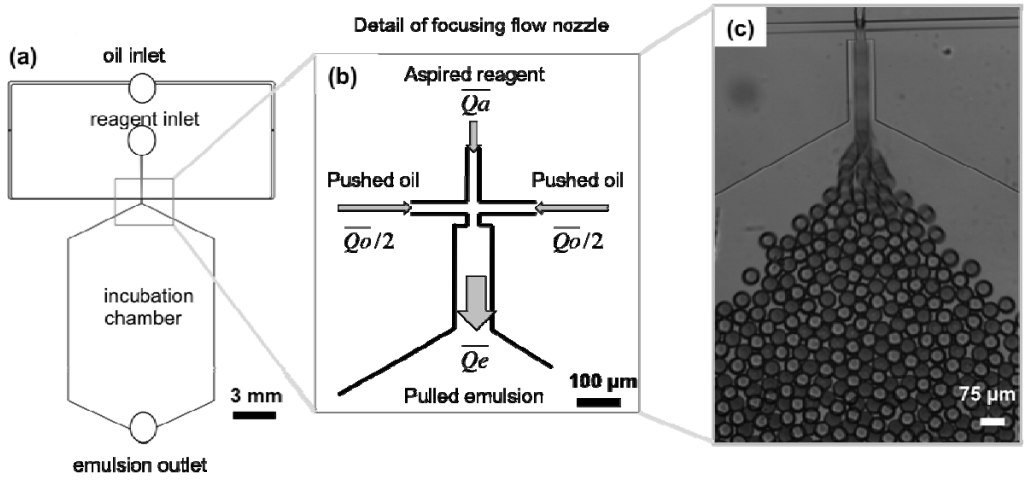

FIG. 1. Microfluidic device for agarose microdroplet generation at room temperature. (a) General view of the device. (b) The oil continuous phase is pushed while the emulsion is pulled. (c) This system induces segmentation of the agarose stream into monodisperse agarose microdroplets.

As shown in Figure 1 (c), highly monodisperse microdroplets 55 µm in diameter are produced. Considering ($\overline{Qa}$) the agarose flow rate ($\overline{Qa} = \overline{Qe} - \overline{Qo}$) and the microdroplet size (55 µm in diameter), we estimated the microdroplet flow generation at 250 Hz.

By tuning the inlet and the outlet flow rates, we could easily control the droplet diameter and the type of droplet regime formation[23]. For example, we could generate microdroplets 20 µm in diameter in the jetting regime at 3900 Hz (Figure 2 (a)). Microdroplets present a uniform diameter of 20 µm ± 3 µm (Figure 2 (d)). We could also generate, in the dripping regime, monodisperse microemulsions with diameters of 35 or 50 µm (Figure 2 (b and c)).

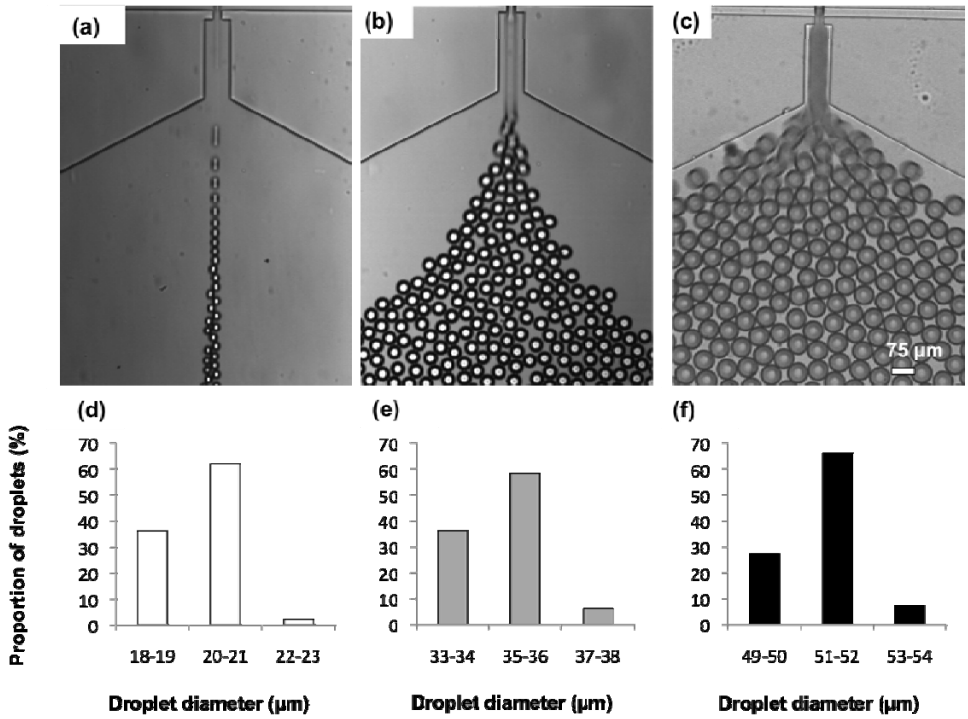

FIG. 2. Different regimes of microdroplet generation and microemulsion polydispersity. By tuning the oil and outlet flow, the diameter of droplets can be changed: (a) 20 µm, (b) 35 µm, (c) 50 µm. In the case of an agarose flow rate of 1 µL/min, the microdroplet generation frequency varies from 3900 Hz for (a) 20 µm microdroplets to (c) 200 Hz for 50 µm microdroplets. (d-f) Polydispersity of microdroplets.

B. On-chip agarose microbead gelation

We investigated a way to cool agarose microdroplets into agarose microbeads on-chip, for easy off-chip collection and direct use for downstream applications.

The 1.5 % ultralow gelling type IX-A agarose melts at 60 ºC and its sol-to-gel switch transition occurs at ≤ 17 ºC. The purpose is to decrease the temperature to this critical gelling temperature in the incubation chamber of the device.

Using the high thermal conductivity of copper, we designed a system to cool the chamber. For this, we introduced two copper wires on both sides of the incubation chamber.

At first, we characterized the temperature in the incubation chamber. We introduced a K-type gauge thermocouple in the incubation chamber as shown in Figure 3. In order to avoid any leakage after introduction, the thermocouple was sealed with PDMS and baked at 75 ºC during 1.5 h.

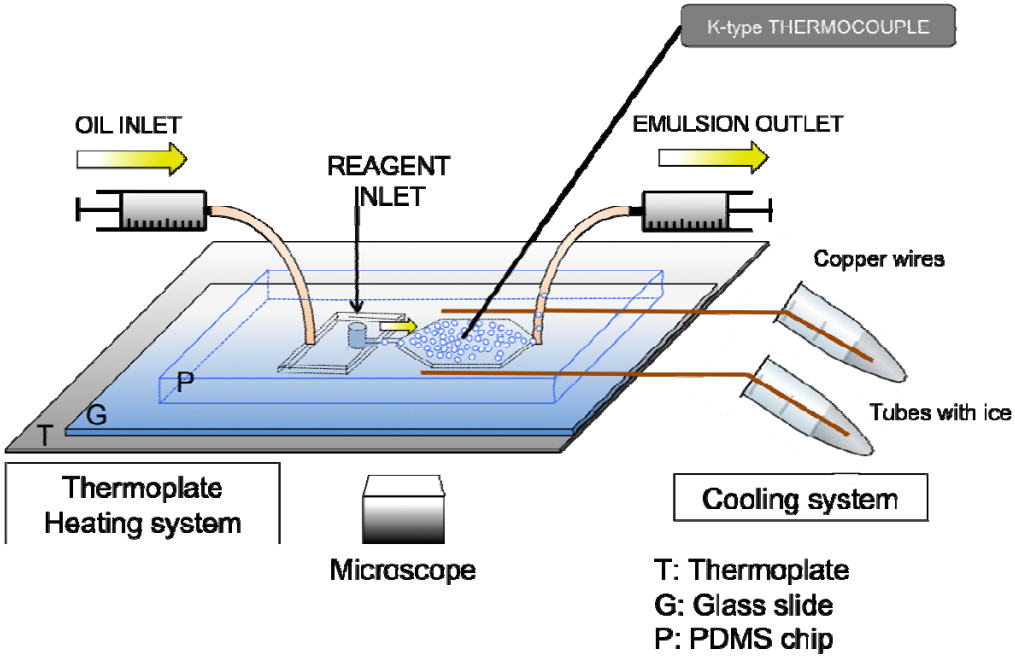

FIG. 3. Device set-up for microbead generation. The "push-pull" method allows the generation of a stable microemulsion. The temperature is measured with A K-type thermocouple, introduced and sealed in the incubation chamber. Heating is done with a thermoplate. Two copper wires, introduced in 1 mL tubes filled with ice are used as a heat sink.

Microdroplets are generated, as mentioned above, at room temperature. When the incubation chamber is filled with microdroplets, inlet and outlet flows are stopped and we proceed to the cooling stage.

For this, the two copper wires are introduced in two 1 mL tubes containing ice (0 ºC). To characterize the thermal behavior of the reactor, cooling was carried out with copper wires of different length, as shown in the Figure 3. The temperature trends are plotted in Figure 4 (a): they reach the steady state in 10 min, irrespective of wire length.

The chamber can be modeled by a thermal capacity, with 2 heat sinks, one associated with room temperature (thermal resistivity: R_{RT}), and the second one with the cooling system. The electro-thermal equivalent is plotted in the insert of Figure 4 (b). The heat transfer with the cold point (ice) is determined by the wire thermal conductivity, serially connected to the wire/chamber resistivity. The evolution of the thermal resistivity of the cooling system with the wire length is plotted in Figure 4 (b), from steady state values shown in Figure 4 (a). The linear dependence of the wire conductivity with its length is clearly obtained, and the slope $(\lambda.S.R_{RT})^{-1}$ allows us the

calculation of the thermal resistances of the models. λ is the thermal conductivity of copper (3.9 W cm^{-1} K^{-1}) and S the wire cross-section (2.5 10^{-4} cm^2). To complete the model identification, the thermal capacitance of the chamber is deduced from the cooling dynamics with a short wire (4 cm), as shown in Figure 4 (c).

Simulations made with COMSOL (see Supplemental Material)[28] show that the temperature in the chamber is homogeneous with a 1.3 ºC variation from the wall chamber to the center (Supplemental material, Fig. S1)[28]. With this set-up, an 16 mm wide chamber can be cooled below 17 ºC (Supplemental material, Fig. S2)[28].

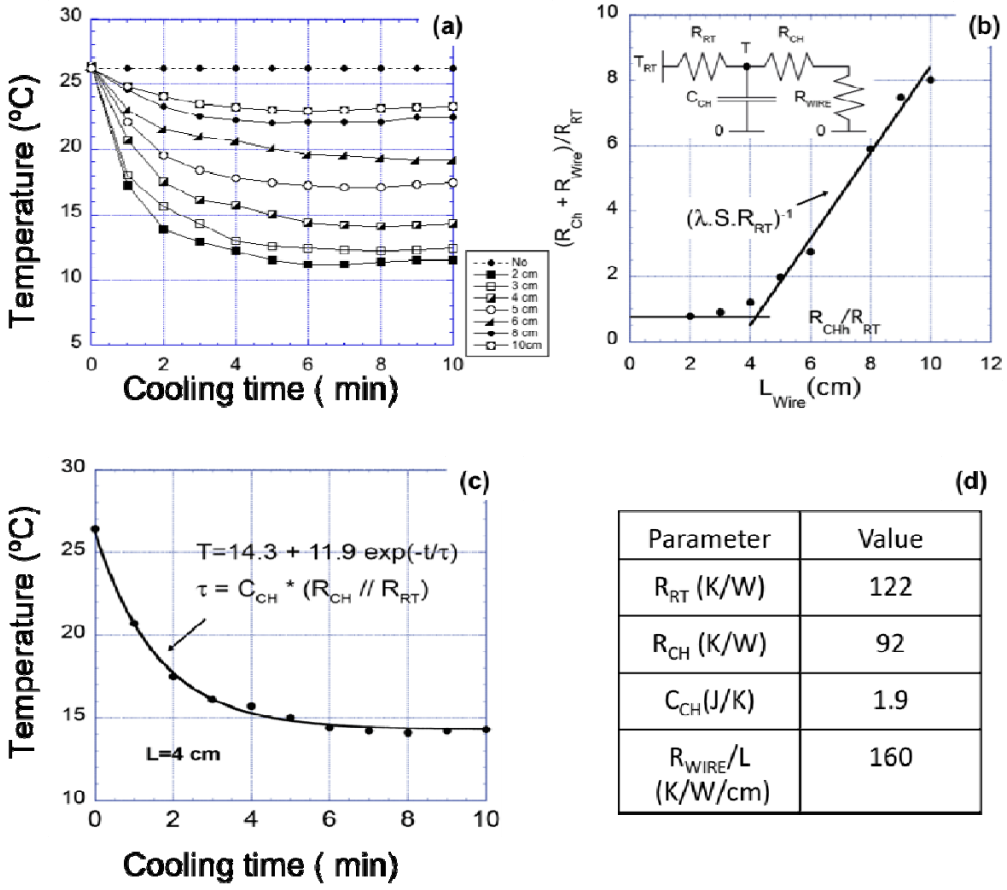

(d)

Parameter	Value
R_{RT} (K/W)	122
R_{CH} (K/W)	92
C_{CH}(J/K)	1.9
R_{WIRE}/L (K/W/cm)	160

FIG. 4. Thermal characterization of the chamber. (a) Chamber temperature transients for various wire lengths. (b) Evolution of the thermal resistivity with the wire length from the steady state temperatures given by (R_{CH}+R_{WIRE})/ (R_{RT}+R_{CH}+R_{WIRE}). (c) Transient temperature cooling with first order extraction for the determination of the response time. (d) Values of the electro-thermal equivalent parameters of the chamber and its cooling system.

This analysis confirmed that we could reach the gelation temperature of agarose within the chamber. We experimentally validated the correct gelation of microdroplets into microbeads by considering the transparency of the microdroplets before and after

cooling. As shown on the Figure 5 (a), after generation, agarose microdroplets were transparent: this limpidity is correlated to the liquid state of the solution[24].

After 15 min of cooling at 14 ºC, the aspect of the microdroplets changed unambiguously and they became opaque as shown in Figure 5 (b). As previously reported, during the gelation process, the turbidity of the gel increases with the apparition of a three-dimensional network of agarose fibers[24]. Considering the temperature of the sol-to-gel transition (≤ 17 ºC) and the fact that agarose gelation increases the microdroplets' opacity, we considered that agarose microdroplets were successfully cooled and agarose microbeads were formed.

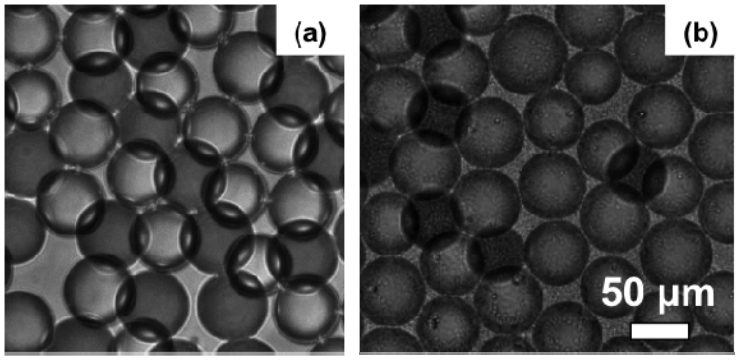

FIG. 5. Agarose microdroplets (a) before and (b) after cooling. After temperature decreases, the microdroplets' opacity increases, suggesting the formation of the agarose mesh (i.e. gelation process).

C. DNA amplification and monitoring on-chip

To confirm the reliability of our system, we used an EXPAR-like isothermal DNA amplification reaction[25]. A "template" strand enables the autocatalytic amplification of the target strand α (Figure 6 (a)). As α hybridizes to the template in 3' position, it is elongated by a DNA polymerase. The elongated strand is then cut in its middle by a nicking endonuclease, releasing two α strands.

We monitor the reaction with N-quenching, a versatile fluorescent technique to observe the hybridization of DNA strands[26]: the 3' end of the template is labeled with a single fluorophore (TAMRA), whose fluorescence intensity increases as α hybridizes to the template as shown in Figure 6 (a).

Such autocatalytic amplification reaction may start at a lower temperature than it is designed for. In order to efficiently block the reaction at 25 °C (i.e. the temperature of droplet generation), we introduced an "inhibitor" DNA strand[27]. The inhibitor is longer than the target α, hence more stable on the template. Also, the 3' end of the inhibitor is mismatched, which prevents the polymerase from elongating it (Figure 6

(b)). As the temperature is raised to 43 °C, the inhibitor is released, α triggers the reaction and is exponentially amplified (Figure 6 (c)).

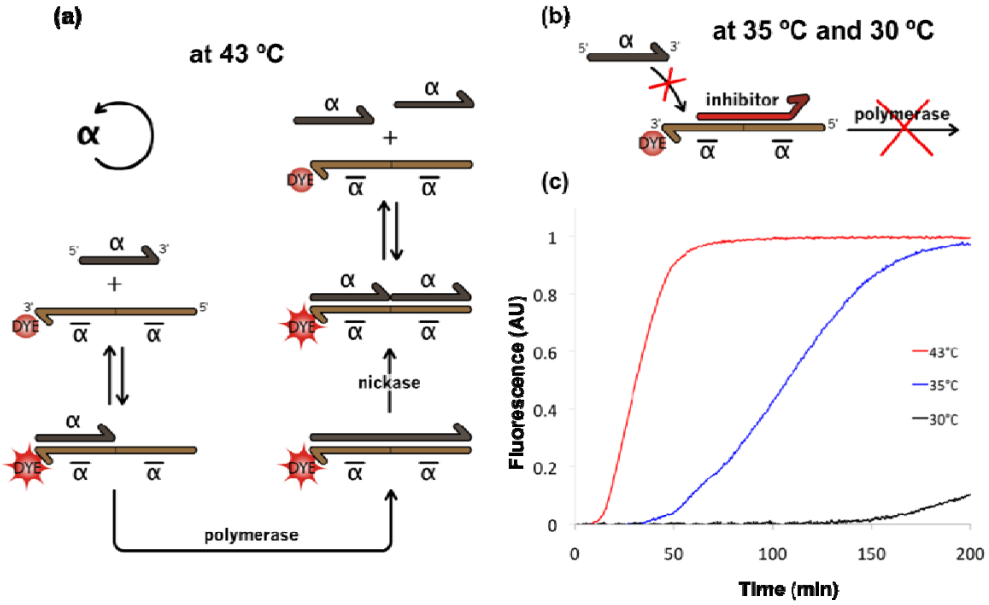

FIG. 6. Autocatalytic DNA amplification reaction in bulk. (a) Schematic of the DNA amplification reaction. At 43 ºC, DNA amplification occurs: as strand α hybridizes to the template, it is elongated by DNA polymerase. The nascent strand is cut in its middle by a nicking endonuclease, releasing two α strands. The template's 3' end is modified with a fluorescent dye, allowing the monitoring of presence of α. (b) At a lower temperature, a stable inhibitor strand blocks the reaction by displacing strand α, and preventing any polymerase activity. (c) Experimental fluorescence time plot of the isothermal DNA amplification in the presence of the inhibitor strand. At a temperature lower than 43 °C, the reaction is slowed down or even blocked by the presence of the inhibitor.

We first checked that agarose gel was not hindering the reaction: DNA amplification performed the same in the presence or absence of gelified agarose (see Supplemental Material, Fig. S3)[28], suggesting that it should be possible to do the reaction in agarose microbeads. A solution premix containing DNA amplification reagents and 1.5 % agarose is prepared at room temperature. Half of the premix is run in a thermocycler as control, and the other part is introduced in the device for microdroplet generation. The premix deposited in the device inlet is segmented into 55 µm microdroplets. When the incubation chamber is filled with microdroplets, the cooling stage is started, as previously described. Once agarose microbeads are formed, we increased the temperature to 43 ºC in order to start the reaction.

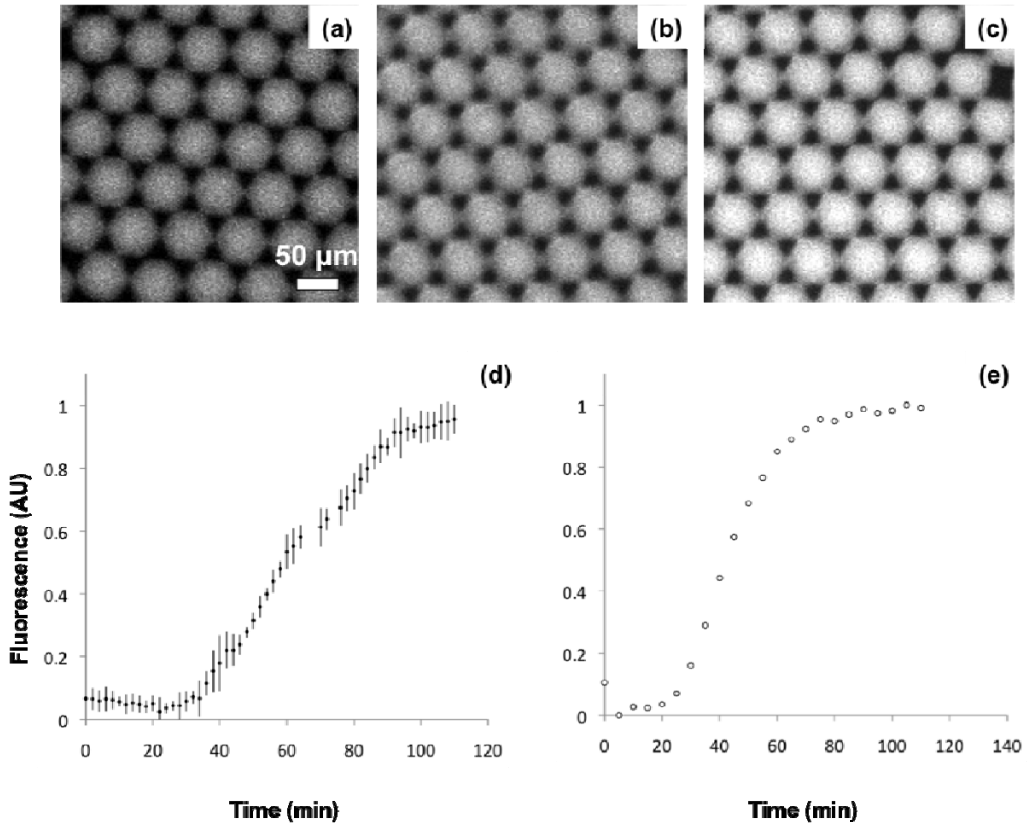

FIG. 7. Autocatalytic DNA amplification in agarose microbeads.

Fluorescence in microbeads at (a) 0 min, (b) 60 min and (c) 110 min. (d) The mean fluorescence ± standard deviation (error bars) of 10 microbeads is plotted to establish a fluorescence variation curve during incubation on-chip. (e) Control experiment (using the same reaction mix) run simultaneously at 43 °C in a thermal cycler.

This reaction can be monitored by an increase in fluorescence, associated with the amplification of DNA (Figure 7).

In both cases (on-chip and control), the reaction starts after 20 to 30 minutes of incubation: the fluorescence increases exponentially and saturates after about 60 minutes. This increase in fluorescence is caused by α strands hybridizing next to the TAMRA fluorophore, and thus represents the amplification of strand α in both microbeads and bulk reaction.

IV. CONCLUSIONS

Agarose microbeads offer a powerful tool for biochemical applications. Previously reported agarose microdroplet generation has been performed by pushing relatively large amount of reagents into the device. Here, for the first time, we have generated

agarose microdroplets by using a "push-pull" system. Because the agarose sample is aspirated in the inlet, a few microliters of sample are enough to generate microdroplets. Moreover, the monodisperse agarose microdroplets can be cooled on-chip into agarose microbeads. This design requires no valves and allows *(i)* biochemical reactions to be performed in microdroplets before or after the gelation process, *(ii)* on-chip monitoring and *(iii)* stabilization of individual droplets into microbeads for facilitated downstream collection and analysis.

As low volumes of sample are required, a potential application of this system could be, by encapsulating single cells, to analyze and sequence the transcriptome.

ACKNOWLEDGMENTS

The authors would like to acknowledge CNRS for financial support, and IIS of Tokyo for laboratory access. The authors would also like to thank Dr Christophe Provin for helpful discussion and advice.

BIBLIOGRAPHY

1. B. Zheng, L. S. Roach and R. F. Ismagilov, J Am Chem Soc **125** (37), 11170-11171 (2003).
2. T. Hatakeyama, D. L. Chen and R. F. Ismagilov, J Am Chem Soc **128** (8), 2518-2519 (2006).
3. I. Shestopalov, J. D. Tice and R. F. Ismagilov, Lab on a Chip **4** (4), 316-321 (2004).
4. M. Margulies, M. Egholm, W. E. Altman, S. Attiya, J. S. Bader, L. A. Bemben, J. Berka, M. S. Braverman, Y. J. Chen, Z. Chen, S. B. Dewell, L. Du, J. M. Fierro, X. V. Gomes, B. C. Godwin, W. He, S. Helgesen, C. H. Ho, G. P. Irzyk, S. C. Jando, M. L. Alenquer, T. P. Jarvie, K. B. Jirage, J. B. Kim, J. R. Knight, J. R. Lanza, J. H. Leamon, S. M. Lefkowitz, M. Lei, J. Li, K. L. Lohman, H. Lu, V. B. Makhijani, K. E. McDade, M. P. McKenna, E. W. Myers, E. Nickerson, J. R. Nobile, R. Plant, B. P. Puc, M. T. Ronan, G. T. Roth, G. J. Sarkis, J. F. Simons, J. W. Simpson, M. Srinivasan, K. R. Tartaro, A. Tomasz, K. A. Vogt, G. A. Volkmer, S. H. Wang, Y. Wang, M. P. Weiner, P. Yu, R. F. Begley and J. M. Rothberg, Nature **437** (7057), 376-380 (2005).
5. M. T. Guo, A. Rotem, J. A. Heyman and D. A. Weitz, Lab Chip **12** (12), 2146-2155 (2012).
6. A. B. Theberge, G. Whyte and W. T. Huck, Analytical Chemistry **82** (9), 3449-3453 (2010).
7. M. Zagnoni and J. M. Cooper, Methods Cell Biol **102**, 25-48 (2011).
8. B. T. Kelly, J. C. Baret, V. Taly and A. D. Griffiths, Chem Commun (Camb) (18), 1773-1788 (2007).
9. R. Tewhey, J. B. Warner, M. Nakano, B. Libby, M. Medkova, P. H. David, S. K. Kotsopoulos, M. L. Samuels, J. B. Hutchison, J. W. Larson, E. J. Topol, M. P. Weiner, O. Harismendy, J. Olson, D. R. Link and K. A. Frazer, Nat Biotechnol **27** (11), 1025-1031 (2009).
10. B. E. Debs, R. Utharala, I. V. Balyasnikova, A. D. Griffiths and C. A. Merten, Proc Natl Acad Sci U S A **109** (29), 11570-11575 (2012).
11. T. Rossow, J. A. Heyman, A. J. Ehrlicher, A. Langhoff, D. A. Weitz, R. Haag and S. Seiffert, J Am Chem Soc **134** (10), 4983-4989 (2012).
12. Y. Zeng, R. Novak, J. Shuga, M. T. Smith and R. A. Mathies, Analytical Chemistry **82** (8), 3183-3190 (2010).
13. H. Zhang, G. Jenkins, Y. Zou, Z. Zhu and C. J. Yang, Analytical Chemistry **84** (8), 3599-3606 (2012).
14. A. Fallah-Araghi, J. C. Baret, M. Ryckelynck and A. D. Griffiths, Lab Chip **12** (5), 882-891 (2012).
15. X. Leng, W. Zhang, C. Wang, L. Cui and C. J. Yang, Lab Chip **10** (21), 2841-2843 (2010).
16. W. Y. Zhang, W. Zhang, Z. Liu, C. Li, Z. Zhu and C. J. Yang, Analytical Chemistry **84** (1), 350-355 (2012).
17. A. Kumachev, J. Greener, E. Tumarkin, E. Eiser, P. W. Zandstra and E. Kumacheva, Biomaterials **32** (6), 1477-1483 (2011).
18. Y. J. Eun, A. S. Utada, M. F. Copeland, S. Takeuchi and D. B. Weibel, ACS Chem Biol **6** (3), 260-266 (2011).
19. J. C. Baret, F. Kleinschmidt, A. El Harrak and A. D. Griffiths, Langmuir **25** (11), 6088-6093 (2009).
20. Y. N. Xia and G. M. Whitesides, Angew Chem Int Edit **37** (5), 551-575 (1998).
21. J. C. McDonald, D. C. Duffy, J. R. Anderson, D. T. Chiu, H. Wu, O. J. Schueller and G. M. Whitesides, Electrophoresis **21** (1), 27-40 (2000).

22. A. Edelstein, N. Amodaj, K. Hoover, R. Vale and N. Stuurman, Curr Protoc Mol Biol **Chapter 14**, Unit14 20 (2010).
23. Z. H. Nie, M. S. Seo, S. Q. Xu, P. C. Lewis, M. Mok, E. Kumacheva, G. M. Whitesides, P. Garstecki and H. A. Stone, Microfluid Nanofluid **5** (5), 585-594 (2008).
24. J. Y. Xiong, J. Narayanan, X. Y. Liu, T. K. Chong, S. B. Chen and T. S. Chung, J Phys Chem B **109** (12), 5638-5643 (2005).
25. G. T. Walker, M. C. Little, J. G. Nadeau and D. D. Shank, Proc Natl Acad Sci U S A **89** (1), 392-396 (1992).
26. A. Padirac, T. Fujii and Y. Rondelez, Nucleic Acids Res **40** (15), e 118 (2012).
27. K. Montagne, R. Plasson, Y. Sakai, T. Fujii and Y. Rondelez, Mol Syst Biol **7** (2011).
28. See supplemental material at [] for the control experiments in agarose and for COMSOL simulation of the temperature in the chamber of the device.

SUPPLEMENTAL MATERIAL

A. COMSOL simulation of the temperature in the incubation chamber

We made simulations of the variation of the temperature in the chamber using COMSOL multiphysics software. We used the constants indicated in the Table SI. The ends of the wires are set to 0 ºC. The device is immersed in air whose temperature away from the device is 26ºC.

The temperature, at the bottom of the chamber (300 μm below the copper wires) varies from 11.9 ºC (near the wall) to 13.1 ºC (4.1 mm away from the wall, i.e. in the middle of the chamber) as shown in Figure S1.

The experimental temperature in the middle of the chamber (14.2 ºC) is in good agreement with the simulation (13.1 ºC). The simulation also indicates that the temperature in the chamber is homogeneous, with a variation of 1.2 ºC between the coldest (walls) and the hottest (center of the chamber) part (Figure S2 (a)).

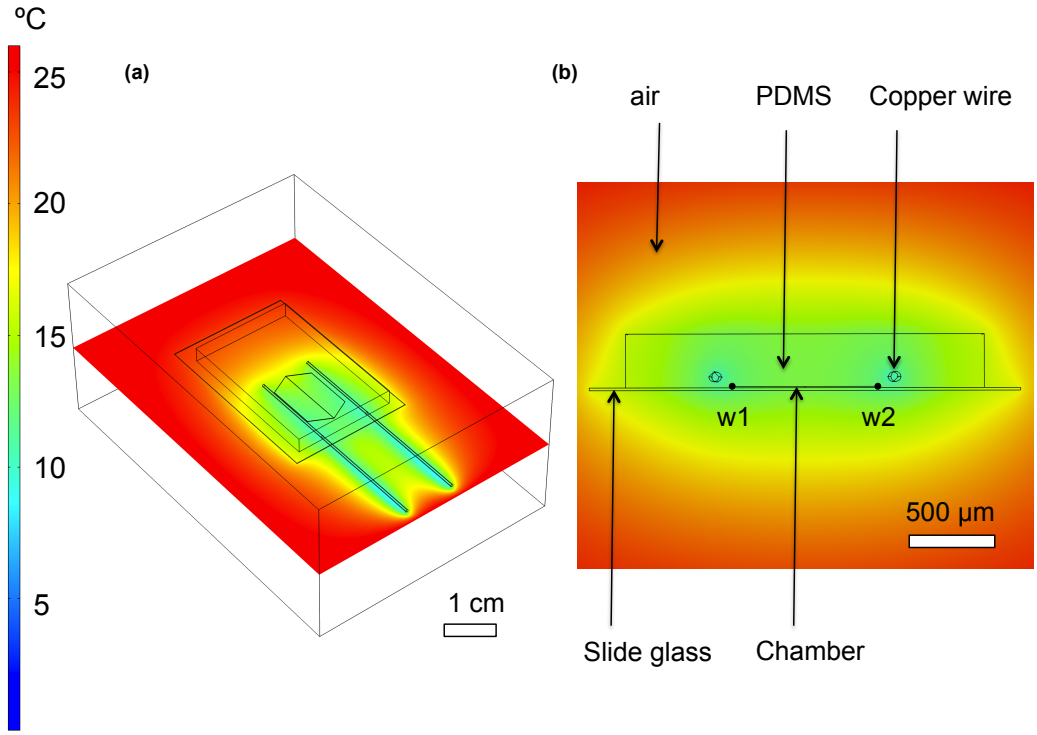

FIG. S1. Simulation of the variation of the temperature inside the chamber. (a) 3D view of the temperature in the device (only the chamber is simulated). The slice shows the temperature at the bottom of the device. (b) Cross section view of the device.

In order to find out the maximal chamber width that can be cooled with this method, we investigate the maximal and minimal temperature at the bottom of the chamber as a function of the chamber width, all other parameters being equal (Figure S2 (b)). The maximal temperature ranges from 10.6 ºC for a 2 mm wide chamber, to 15.7 ºC for a 16 mm wide

chamber. Considering the sol-to-gel temperature of 17 ºC, our cooling system should allow gelation in chamber of the order of 16 mm.

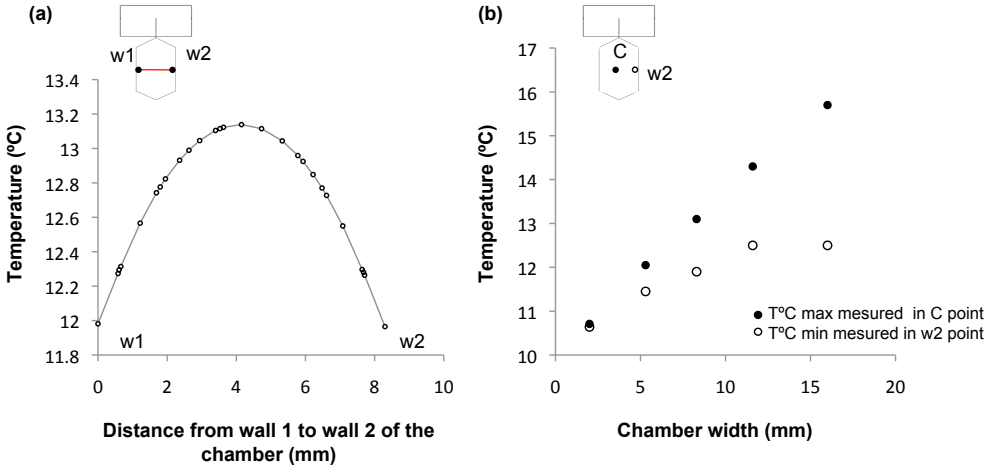

FIG. S2. Simulation of the variation of the temperature inside the chamber. The temperature is chosen at the bottom of the chamber. (a) Temperatures along a line joining the wall 1 (w1) to the wall 2 (w2) of the chamber (the chamber width is 8.3 mm). (b) Variation of the minimum and the maximum temperature as a function of the chamber width. The minimum temperature is measured at the wall 2 (w2). The maximum temperature measurement is done at the center of the chamber ("C" point).

TABLE SI. Values of the constants used in COMSOL Simulation (superscripts refer to the reference used for the parameter)

Materials	Units	PDMS (1/10)	Glass	Mineral Oil
Density (ρ)	Kg/m^3	920[1]	2235[2]	840 $kg.m^3$
Thermal conductivity (k)	W/m.K	0.15[3]	1.13[2]	0.1307[4]
Heat capacity (C)	J/kg.K	1500[5]	710[2]	1670[6]

B. Control experiments for DNA amplification in agarose

The DNA amplification has been performed, for control, in various concentrations of agarose, in bulk format (i.e. in a 20 µL PCR tube). As shown in the Figure S3, the fluorescence increases are comparable in all tubes, whatever the concentration of agarose. These experiments suggest that the agarose gel does not interfere with the reaction.

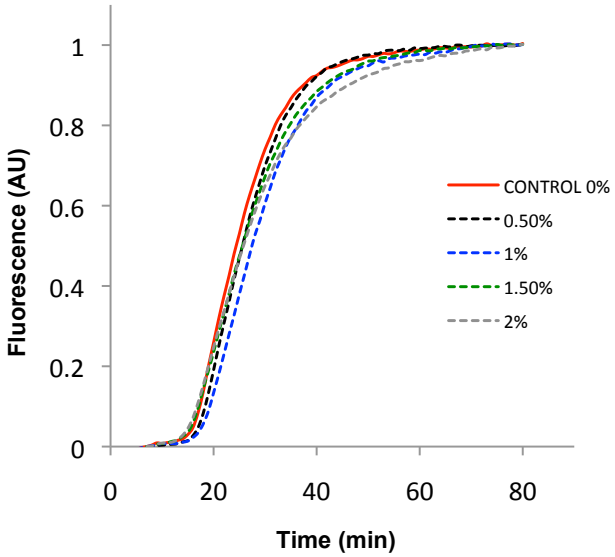

FIG. S3. DNA amplification reaction in the presence of various concentrations of agarose. The DNA amplification mixtures have been prepared with various concentrations of agarose (from 0. 5% to 2 %). They were then cooled at 4 ºC for a few minutes in order to gelify the agarose. After the cooling stage, all tubes have been incubated in a thermal cycler at 43 ºC for DNA amplification. Whatever the agarose concentration, the fluorescence signal increases as fast as the control, i.e. the DNA amplification occurred in all tubes.

BIBLIOGRAPHY

1. D. Armani, C. Liu and N. Aluru, Twelfth IEEE International Micro Electro Mechanical System Conference, 222-227 (1999).
2. I. Wong, S. Atsumi, W. C. Huang, T. Y. Wu, T. Hanai, M. L. Lam, P. Tang, J. A. Yang, J. C. Liao and C. M. Ho, Lab Chip **10** (20), 2710-2719 (2010).
3. O. K. Bates, Ind Eng Chem **41** (9), 1966-1968 (1949).
4. L. H. Huang and L. S. Liu, J Food Eng **95** (1), 179-185 (2009).
5. A. Elliott, J. Schwartz, J. Wang, A. Shetty, J. Hazle and J. R. Stafford, Laser Surg Med **40** (9), 660-665 (2008).
6. C. Xie and J. P. Hartnett, Int J Heat Mass Tran **35** (3), 641-648 (1992).